The MOLLER Project
Measurement **O**f a **L**epton **L**epton **E**lectroweak **R**eaction

An Ultra-precise Measurement of the Weak Mixing Angle
using Møller Scattering

Technical Design Report

The MOLLER Collaboration

February 15, 2024

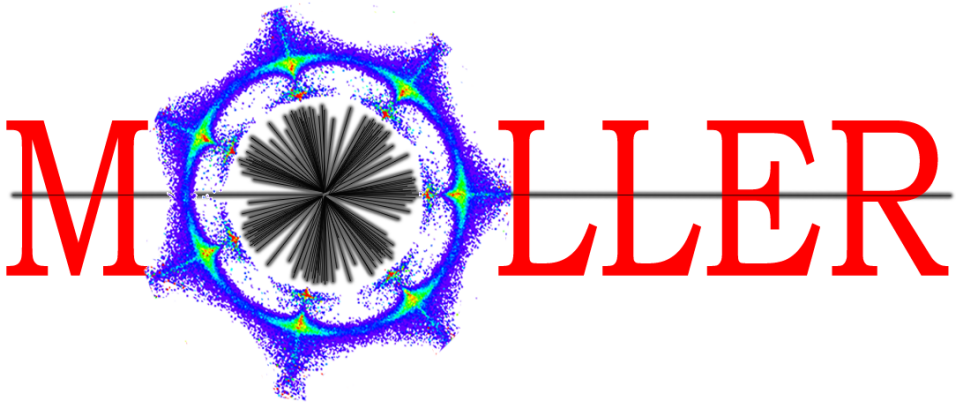

The MOLLER Collaboration

M. Abdullah Mamun, P. Adderley, E. Becker, J. Benesch, V.V. Berdnikov, P. Brindza, J. Brock, D. Bullard, J. Butler, R.D. Carlini, J-P. Chen, E. Chudakov, S. Covrig, M.M. Dalton, P. Degtiarenko, A. Deur, A. DiPette, R. Fair, J. Fast, E. Folts, C. Gal, D. Gaskell, N. Gauthier, A. Gavalya, C. Ghosh, P. Ghoshal, K. Gnavo, J. Grames, S. Gopinath, O. Hansen, W. Henry, C. Hernandez-Garcia, D.W. Higinbotham, A. Hofler, C. Hutton, D.C. Jones, M. Jones, D. Kashy, R. Kazimi, C. Keith, C. Keppel, P. Kessler, K. Krug, H. Liu, S. Malace, M. McGaughan, D. Meekins, R. Michaels, J. Miller, B. Moffit, D. Moser, S. Park, M. Poelker, Y. Roblin, J. Segal, C. Soova, M. Stutzman, R. Suleiman, E. Sun, E. Trovatore, Y. Wang, R. Wilson, R. Wines, B. Wojtsekhowski, D. Young, L. Zana, S. Zhang, C. Zorn
Jefferson Lab

X. Bai, G. Cates, D. Day, D. Di, P. Gautam, N. Liyanage, V.V. Nelyubin, H. Nguyen, K.D. Paschke, S. Premathilake, R. Richards, A. Zec, X. Zheng
University of Virginia

C. Clarke, Z.S. Demiroglu, K. Dehmelt, A. Deshpande, V. Doomra, P. Garg, T.K. Hemmick, W. Li, B. Moran, J. Shirk, T. Ye, W. Zhang
Center for Frontiers in Nuclear Science, Stony Brook University
A. Deshpande
Center for Frontiers in Nuclear Science, Stony Brook University
Brookhaven National Laboratory

A. Gunawardhana, B. Blaikie, P. Blunden, W. Deconinck, M.T.W. Gericke, F. Gorgannejad, H.S. Lee, K. Isaak, T. Kainth, G. Leverick, S. Longo, J. Mammei, M. Laheji, N. Niloy, J. Pan, S. Prabhakar, S. Rahman, W. Rathnakela, N. Roshanshah, W.T.H. van Oers, N.A.C. Venegas
University of Manitoba

V. Bellini, V. Brio, F. Mammoliti, C. Sutera, F. Tortorici
INFN Sezione di Catania and Universita' di Catania

K. Aulenbacher, D. Becker, S. Baunack, N. Berger, J. Erler, , R. Krini, F. Maas, V. Tioukine, M Wilfert, L. Weinstock
Johannes Gutenberg Universitaet Mainz

R. S. Beminiwattha, K. Johnston, N. Simicevic, S. Wells
Louisiana Tech University

D.S. Armstrong, T.D. Averett, K.T. Evans, V.F. Owen, E.W. Wertz
College of William & Mary

S. Chatterjee, A. Hurley, K.S. Kumar [Contact*], R. Miskimen, J. Mott, M.J. Ramsey-Musolf, S. Sarkar, J-Y. Su
University of Massachusetts, Amherst

J. Arrington, A. Cuda, Yu.G. Kolomensky, S. Li, Y. Mei, E. Sichtermann
Lawrence Berkeley National Laboratory and University of California, Berkeley

S. Bhattarai, T.A. Forest, J. Gahley, D. McNulty
Idaho State University

J. Bessuille, E. Ihloff, J. Kelsey, D. Petterson, P. Smith
Massachusetts Institute of Technology

J.A. Dunne, D. Dutta, L. El Fassi
Mississippi State University

R. Mammei, J.W. Martin

University of Winnipeg

D.E. King, J. Napolitano
Temple University

F. Chahili, P. Souder, Y. Tian
Syracuse University

D. Adhikari, A. Gunsch, M. L. Pitt, D. Valmassei
Virginia Polytechnic Institute and State University

P.M. King, J. Roche
Ohio University

F. Meddi, G.M. Urciuoli
Dipartimento di Fisica dell'Universita' la Sapienza and INFN Sezione di Roma

E. Cisbani, F. Garibaldi
INFN Gruppo Collegato Sanita' and Istituto Superiore di Sanita'

A. Ahmidouch
North Carolina A&T State University

A. Aleksejevs, S. Barkanova, M. Ghaffar
Memorial University, Grenfell

C. Palatchi
Indiana University

T. Holmstrom
Longwood University

K. A. Aniol
California State U.(Los Angeles)

D. Bishop, W.D. Ramsay, B. Shaw
TRIUMF

E. Korkmaz
University of Northern British Columbia

D.T. Spayde
Hendrix College

F. Benmokhtar
Duquesne University

A. Del Dotto
INFN, Laboratori Nazionali di Frascati

R. Perrino
INFN Sezione di Lecce

J. Singh
NSCL and Michigan State University

C. Annasiwatta
Ohio State University

L. Bartoszek
Bartoszek Engineering

*kkumar@physics.umass.edu

Contents

List of Figures

List of Tables

Executive Summary

We present the technical design of the apparatus of the MOLLER experiment, which plans to measure the parity-violating asymmetry A_{PV} in polarized electron-electron (Møller) scattering. In the Standard Model, A_{PV} is due to the interference between the electromagnetic amplitude and the weak neutral current amplitude, the latter being mediated by the Z^0 boson. A_{PV} is predicted to be $\approx$ 33 parts per billion (ppb) at our kinematics. Our goal is to measure A_{PV} to an uncertainty of 0.8 ppb. The result will yield a measurement of the weak charge of the electron Q_W^e to a fractional uncertainty of 2.4% at an average Q^2 of 0.0056 GeV^2.

The measurement is sensitive to the interference of the electromagnetic amplitude with new neutral current amplitudes as weak as $\sim 10^{-3} \times G_F$ from undiscovered dynamics beyond the Standard Model. Such discovery reach is unmatched by any proposed experiment measuring a flavor- and CP-conserving process over the next decade, and results in a unique window to new physics at MeV and multi-TeV scales, complementary to direct searches at high energy colliders. Within the Standard Model, the extracted Q_W^e measurement yields a determination of the weak mixing angle $\sin^2\theta_W$ with both precision and accuracy that are unmatched by any conceivable method at $Q^2 \ll M_Z^2$ in the foreseeable future, and matches the uncertainty from the single best such determination from high energy colliders.

The measurement will be carried out in Hall A at Jefferson Laboratory, where a 11 GeV longitudinally polarized electron beam will be incident on a 1.25 m liquid hydrogen target. Møller electrons (beam electrons scattering off target electrons) in the full range of the azimuth and spanning the polar angular range 5 mrad $< \theta_{lab} <$ 20 mrad, will be separated from background and brought to a ring focus $\sim$ 27 m downstream of the target by a spectrometer system consisting of a pair of toroidal magnet assemblies and precision collimators. The Møller ring will be intercepted by a system of fused silica detectors; the resulting Cherenkov light provides a relative measure of the scattered flux.

Longitudinally polarized electrons are generated via photoemission on a GaAs photocathode by circularly polarized laser light, enabling rapid polarization (helicity) reversal and suppression of spurious systematic effects. A_{PV} will be extracted from the fractional difference in the integrated Cherenkov light response between helicity reversals. Additional systematic suppression to the sub-ppb level will be accomplished by periodically reversing the sign of the physics asymmetry by three independent methods.

Simultaneously with data collection, the fluctuations in the electron beam energy and trajectory and its potential systematic effects on A_{PV} will be precisely monitored, active feedback loops will minimize beam helicity correlations, and detector response to beam fluctuations will be continuously calibrated. Background fractions and their helicity-correlated asymmetries will be measured by dedicated auxiliary detectors. The absolute value of Q^2 will be calibrated periodically using tracking detectors. The longitudinal electron beam polarization will be measured continuously by two independent polarimeter systems.

The project team is integrated into a strong collaboration that has extensive experience in previous successful measurements using similar techniques. A comprehensive set of physics requirements led to a conceptual design which was input to the engineering team to develop the technical design articulated in this document. The collaboration is looking forward to construction and deployment of the apparatus and to data collection and analysis at the completion of the project.

1 Physics Motivation

1.1 Physics Context

The MOLLER (Measurement of the Lepton Lepton Electroweak Reaction) experiment [1] has been designed to significantly expand the sensitivity reach to discover new dynamics beyond the Standard Model of electroweak interactions both at low energy scales ($\sim$ 100 MeV) as well as at high energy (multi-TeV). It is one of a small handful of projects worldwide that carry out ultra-precise measurements of electroweak observables well below the scale of electroweak symmetry breaking, and are theoretically calculable to high accuracy. Specifically, MOLLER measures the parity-violating asymmetry A_{PV} in the scattering of longitudinally polarized electrons off unpolarized electrons, using the upgraded 11 GeV beam in Hall A at Jefferson Laboratory (JLab), to an overall fractional accuracy of 2.4%. Such a result would constitute more than a factor of five improvement in fractional precision over the only other measurement of the same quantity by the E158 experiment at SLAC [2].

The purely leptonic Møller PV asymmetry is a rare, low-energy observable whose theoretical uncertainties, especially due to hadronic effects, are well under control. The electron beam energy, luminosity and stability at Jefferson Laboratory are uniquely suited to carry out such a measurement. The 11 GeV JLab beam provides a compelling opportunity to achieve a new benchmark in sensitivity. The physics motivation has two important aspects:

1. New neutral current effective four-fermion interactions are best parameterized model-independently at low energies by the quantity Λ/g, where g characterizes the strength and Λ is the scale of the new dynamics. The proposed A_{PV} measurement is sensitive to interaction amplitudes as small as 1.5×10^{-3} times the Fermi constant, G_F, which corresponds to a sensitivity of $\Lambda/g = 7.5$ TeV. With $g \sim 1$ one probes Λ in the multi-TeV scale with a new and unique sensitivity to 4-electron interactions, while for $\Lambda \sim 100$ MeV, there is extraordinary new sensitivity approaching $g \sim 10^{-3} \cdot \alpha_{QED}$. This would be *the* most sensitive probe of new flavor and CP-conserving neutral current interactions in the leptonic sector until the advent of a linear collider or a neutrino factory, and would have 5σ discovery potential in the discovery space allowed by the existing most precise low energy measurements.

2. Within the Standard Model, weak neutral current amplitudes are functions of the weak mixing angle $\sin^2\theta_W$. The two most precise independent determinations of $\sin^2\theta_W$ differ by 3σ. The world average is consistent with the theoretical prediction for the weak mixing angle assuming the 125 GeV scalar resonance observed at the Large Hadron Collider (LHC) is the Standard Model (SM) Higgs boson. However, choosing one or the other central value ruins this consistency and implies very different new high-energy dynamics. The proposed A_{PV} measurement, which would achieve a sensitivity of $\delta(\sin^2\theta_W) = \pm 0.00028$, has the same level of precision and interpretability: the best among projected sensitivities for new measurements at low Q^2 in the foreseeable future.

1.2 Precision Goal

The parity-violating asymmetry in the scattering of longitudinally polarized electrons on unpolarized target electrons A_{PV} is given by

$$A_{PV} = \frac{\sigma_R - \sigma_L}{\sigma_R + \sigma_L} = mE\frac{G_F}{\sqrt{2}\pi\alpha}\frac{4\sin^2\theta}{(3+\cos^2\theta)^2}Q_W^e \tag{1}$$

where $\sigma_{R(L)}$ are the polarization dependent cross-sections, α is the fine structure constant, E is the incident beam energy, m is the electron mass, and θ is the scattering angle in the center of mass frame.

A_{PV} in Møller scattering is directly proportional to the weak charge of the electron Q_W^e, which is, in turn, proportional to the product of the electron's vector and axial-vector couplings to the Z^0 boson. The prediction for A_{PV} in the current experimental design is $\approx$ 33 parts per billion (ppb) and the goal is to measure this quantity with an overall uncertainty of 0.8 ppb and thus achieve a 2.4% measurement of Q_W^e. Under the assumption of a SM Higgs boson mass of 125 GeV, the MOLLER A_{PV} theoretical prediction will be calculable to better than 0.2 ppb accuracy.

The electroweak theory prediction at tree level in terms of the weak mixing angle is $Q_W^e = 1-4\sin^2\theta_W$; this is modified at the 1-loop level [3–5] and becomes dependent on the energy scale at which the measurement is carried out, *i.e.,* $\sin^2\theta_W$ "runs". At the energy scale of the MOLLER measurement, $\sin^2\theta_W$ increases by approximately 3% compared to its value at the scale of the Z^0 boson mass, M_Z; this and other radiative corrections reduce Q_W^e to 0.0435, a $\sim 42\%$ change of its tree level value of ~ 0.075 (when evaluated at M_Z). This reduction in the numerical value of Q_W^e leads to improved fractional accuracy in the determination of the weak mixing angle, $\sim 0.1\%$, matching the precision of the single best determination from measurements of asymmetries in Z^0 decays in the e^+e^- colliders Large Electron Positron Collider (LEP) and the SLAC Linear Collider (SLC).

A precision (2.4% relative) measurement of a suppressed Standard Model observable ($Q_W^e \sim 0.0435$) results in sensitivity to new neutral current amplitudes as weak as $\sim 10^{-3}\cdot G_F$ from undiscovered dynamics beyond the Standard Model. This remarkable sensitivity to probe of TeV-scale dynamics beyond the SM (BSM) results from the confluence of a very precise experimental goal ($\sim 10^{-3}\cdot G_F$), the low energy scale of the reaction ($Q^2 \ll M_Z^2$), and the ability within the electroweak theory to provide quantitative predictions with negligible theoretical uncertainty. The MOLLER measurement is likely the only practical way, using a purely leptonic scattering amplitude at $Q^2 \ll M_Z^2$, to make discoveries in important regions of BSM space in the foreseeable future at any existing or planned facility worldwide.

An important point to note is that, at the proposed level of measurement accuracy of A_{PV}, the SM prediction must be carried out with full treatment of one-loop radiative corrections and leading two-loop corrections. With the work done over the past few years that investigated several classes of diagrams beyond one-loop [6, 7], the current uncertainty in the theoretical prediction of the electron weak charge Q_W^e is less than 0.3%, a significant improvement on the original estimate during the conceptual design phase [8]. After accounting for small additional uncertainties for spectrometer and detector acceptance, the uncertainty in the predicted A_{PV} will be less than 0.15 ppb or about 0.4%, significantly less than the projected statistical uncertainty. Further, there are ongoing theoretical efforts to address the complete set of two-loop corrections at MOLLER kinematics [7].

1.3 Physics Impact

We now elaborate on the physics impact of the MOLLER measurement, first addressing electroweak physics (bullet 2 of Sect. 1.1), followed by new physics sensitivity (bullet 1).

1.3.1 Electroweak Physics

The weak mixing angle $\sin^2\theta_W$ has played a central role in the development and validation of the electroweak theory, especially testing it at the quantum loop level, which has been the central focus of precision electroweak physics. A key feature of MOLLER is that the A_{PV} measurement will be carried out at $Q^2 \ll M_Z^2$. Since $\sin^2\theta_W$ evolves (so-called "running") as a function of Q^2 due to electroweak radiative corrections, one can use $\sin^2\theta_W$ as a bookkeeping parameter to compare the consistency of the full Q^2 range of weak neutral current measurements, as shown in Fig. 1. The theory error in the low energy extrapolation is comparable to the width of the line in the Fig. [5]. MOLLER A_{PV} would be the first low Q^2 measurement to match the precision of the single best high energy measurement at the Z^0 resonance, with a

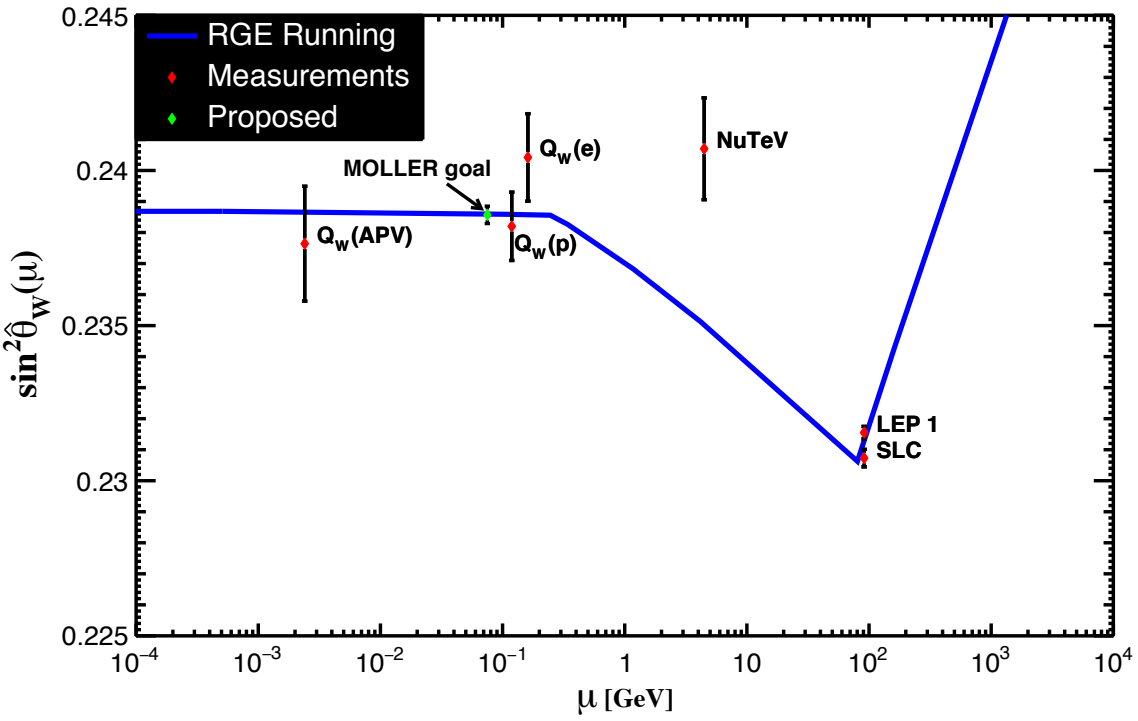

Figure 1: *The four most precise measurements of the weak mixing angle measurements vs. the energy scale μ are shown as red diamonds with error bars; the curve is reproduced from the PDG [9]. The APV point reflects the reanalysis of the original result [10] in Ref. [11]. The $Q_W(e)$ point is the E158 result [2]. The $Q_W(p)$ point is the $Q_{\rm weak}$ result [12]. The NuTeV point is the extracted value from the original publication result [13]. The proposed MOLLER uncertainty (± 0.00028) is shown at the appropriate μ value with the nominal SM prediction as the central value.*

design sensitivity of $\delta(\sin^2\theta_W) = \pm 0.00028$, the most precise such measurement currently proposed over the next decade at low energy.

1.3.2 New Physics Beyond the Standard Model

The MOLLER experiment measures an observable that provides unique complementarity to anticipated results from the LHC in the search for new physics. Meeting our precision goals would result in the most sensitive discovery reach for purely leptonic flavor- and CP- conserving scattering amplitudes in the next decade; see recent reviews that situate the measurement in broader contexts [14–16]. If the LHC continues to agree with the Standard Model with high luminosity running at the full 14 TeV energy, then MOLLER will be a significant component of a global strategy to discover signatures of a variety of physics that could escape LHC detection. Examples include hidden weak scale scenarios such as compressed supersymmetry [17], lepton number violating amplitudes such as those mediated by doubly charged scalars [18–20], and light MeV-scale dark matter mediators such as the "dark" Z [21, 22].

A fairly general and model-independent way to quantify the energy scale of BSM high-energy dynamics (that MOLLER is sensitive to) is to express the resulting new amplitudes at low energies in terms of contact interactions (dimension-6 non-renormalizable operators) among leptons and quarks [23]. Specializing here

to vector and axial-vector interactions between electrons and/or positrons, the interaction Lagrangian is characterized by a mass scale Λ and coupling constants g_{ij} labeled by the chirality of the leptons. For the MOLLER A_{PV} measurement with 2.4% total uncertainty (and no additional theoretical uncertainty) the resulting sensitivity to new 4-electron contact interaction amplitudes can be expressed as:

$$\frac{\Lambda}{\sqrt{|g_{RR}^2 - g_{LL}^2|}} = \frac{1}{\sqrt{\sqrt{2}G_F|\Delta Q_W^e|}} \simeq \frac{246.22 \text{ GeV}}{\sqrt{0.023 Q_W^e}} = 7.5 \text{ TeV}. \quad (2)$$

For example, models of lepton compositeness are characterized by strong coupling dynamics. Taking $\sqrt{|g_{RR}^2 - g_{LL}^2|} = 2\pi$ shows that mass scales as large as $\Lambda = 47$ TeV can be probed, far beyond the center of mass energies of any current or planned high energy accelerator. This allows electron substructure to be studied down to the level of 4×10^{-6} fm.

On the other hand, if the LHC observes an anomaly, then MOLLER will have the sensitivity to be part of a few select measurements that will provide important constraints to choose among possible beyond the Standard Model (BSM) scenarios to explain the anomaly. Examples of such BSM scenarios that have been explicitly considered for MOLLER include: new particles predicted by the Minimal Supersymmetric Standard Model observed through radiative loop effects (R-parity conserving) or tree-level interactions (R-parity violating) [17, 24] and TeV-scale Z's [25] which arise in many BSM theories.

The remarkable feature of the MOLLER sensitivity to four-lepton flavor-conserving contact interactions has been emphasized [26]. Not only does the contact interaction scale reach exceed those at LEP-200, the highest energy electron-positron collider to collect data, but there is unique sensitivity to a specific linear combination of left- and right-handed four electron operators to which all other collider measurements happen to be insensitive. Indeed, in the current global analysis, the E158 result [2] is used to break the degeneracy. The MOLLER measurement will allow the extension of the current limits for these operators from about 2 TeV to more than 7 TeV.

The importance of improving sensitivity over the entire multi-dimensional space of new operators is particularly important if higher sensitivity searches at the LHC yield no new discoveries. For example, in hidden weak scale scenarios such as compressed supersymmetry [17], one of the superpartner masses could be relatively light, likely if the super-partner masses are nearly degenerate. In that scenario, the LHC signatures would be very challenging to disentangle from QCD backgrounds. Another example is a lepton number violating amplitude mediated by doubly charged scalars. The MOLLER measurement is one of the rare low Q^2 observables with sensitivity to such amplitudes, which naturally arise in extended Higgs sector models containing complex triplet representations of SU(2). In a left-right symmetric model, for example, the proposed MOLLER measurement would lead to the most stringent probe of the left-handed charged scalar and its coupling to electrons, with a reach of 5.3 TeV, significantly above the LEP 2 constraint of about 3 TeV. Moreover, such sensitivity is complementary to other sensitive probes such as lepton-flavor violation and neutrinoless double-beta decay searches [18–20].

Finally, the interesting possibility of a light MeV-scale dark matter mediator known as the "dark" Z [21, 22] has been recently investigated. It is denoted as Z_d with mass m_{Z_d}, and it stems from a spontaneously broken $U(1)_d$ gauge symmetry associated with a secluded "dark" particle sector. The Z_d boson can couple to SM particles through a combination of kinetic and mass mixing with the photon and the Z^0-boson, with couplings ε and $\varepsilon_Z = \frac{m_{Z_d}}{m_Z}\delta$ respectively. In the presence of mass mixing ($\delta \neq 0$), a new source of "dark" parity violation arises [21] such that it has negligible effect on other precision electroweak observables at high energy, but is quite discernible at low Q^2 through a shift in the weak mixing angle [22].

In summary, the discovery reach of the proposed MOLLER experiment is unmatched by any proposed experiment measuring a flavor- and CP-conserving process over the next decade. It results in a unique window to new physics at MeV and multi-TeV scales, complementary to direct searches at high energy colliders such as the LHC.

2 Overview of Measurement Technique and Systematic Uncertainties

The MOLLER experimental design and requirements are driven by the need to measure a very small parity-violating asymmetry which requires collection of the scattered electron flux at an unprecedentedly high rate and control over a range of effects that might obscure or produce misleading results. To achieve the scientific impact, the experiment is designed to measure the parity-violating asymmetry in the scattering of longitudinally-polarized electrons from unpolarized target electrons to an overall fractional accuracy of 2.4%, which corresponds to an absolute accuracy of ± 0.8 ppb. In terms of simple counting statistics, this requires the collection of $\sim 4 \times 10^{18}$ scattering events. This design is grounded on the extensive experience gained by the collaboration from other high flux integrating (as opposed to counting individual particles) parity-violation measurements such as MIT-Bates ^{12}C [27], SAMPLE [28], HAPPEX [29], SLAC E158 [2], PREX/CREX [30, 31], and $Q_{\rm weak}$ [12]. In this section, a brief overview of the MOLLER experimental apparatus, including the functional requirements, is given.

2.1 MOLLER Experimental Overview

The MOLLER measurement will be carried out in Hall A at Jefferson Lab, with a 11 GeV longitudinally polarized electron beam incident on a 1.25 m liquid hydrogen target. Møller electrons (beam electrons elastically scattering off target electrons) spanning center-of-mass (CM) polar angles from $60^\circ < \theta_{\rm CM} < 120^\circ$, are separated from background and brought to a focus by a spectrometer system consisting of precision collimators and toroidal magnet assemblies. The Møller scattered events are intercepted by an array of quartz detectors; the resulting Cherenkov light provides a measure of the scattered flux.

The critical factors in the experimental design include a stable beam optimized for asymmetry measurements with high intensity and polarization, incident on a highly stable, long LH2 cryogenic target to achieve high luminosity, and a spectrometer optimized for high acceptance but able to focus Møller scattered events away from background signals onto an integrating detector system capable of deadtime-less measurements at extreme rates. Calibrations must be performed with reduced beam current for tracking individual scattered electrons to characterize the spectrometer acceptance and detector response, while auxiliary detectors in both integrating and calibration modes are required for measuring sources of background.

The MOLLER apparatus consists of:

- Target System - A high power, very stable cryogenic liquid hydrogen target; the system also includes solid targets for calibration;
- Spectrometer – A 7-fold symmetric toroidal magnet system capable of focusing Møller scattered electrons while rejecting backgrounds, collimators to define the acceptance and to reject scattering from the disrupted beam passing through to the beam dump;
- Main Detectors – Detectors employing thin quartz Cherenkov radiators form the main detector element needed by the high-rate, high statistics primary measurement for the experiment;
- Auxiliary detectors - quartz/tungsten sandwich "shower-max" detectors provide a cross-check of the measurement of the Møller flux; other detector systems are optimized to measure pion backgrounds or monitor beam or other background asymmetries;
- Tracking Detectors – Gas Electron Multiplier (GEM) tracking detector planes are used to study backgrounds and verify spectrometer optics in the low-rate "counting" mode;
- DAQ and Trigger – The data acquisition (DAQ) system supports both counting (low rate) and integrating (high rate) modes for the detector systems and beam diagnostic monitors.
- Polarized Beam, Monitoring and Diagnostics - A 65 μA electron beam with 90% longitudinal polarization is used. The polarized electron source supports a polarization reversal frequency near 2 kHz,

with a high level of uniformity in beam trajectory and quality between the complementary polarization states. Beam monitoring and control are sufficient to keep the total correction to the asymmetry to be comparable to the goal for statistical precision.

- Polarimetry - Two independent polarimeters are used for robust, cross-checked measurement of beam polarization at the level of 0.4% precision;
- Hall A Infrastructure and Integration – improvements to electrical power, cooling, and cryogenic systems support the MOLLER apparatus, and additional external radiation shielding is used to protect experimental equipment and meet guidelines on personnel protection.

A list of the nominal parameters that describe the conceptual design of the experiment is shown in Tab. 1. An overview schematic of the experimental apparatus is shown in Fig.2.

Table 1: *Nominal parameters for the conceptual design of the MOLLER experimental apparatus.*

Parameter	Value
E [GeV]	≈ 11.0
E' [GeV]	2.0 - 9.0
$\theta_{\rm CM}$	50°-130°
$\theta_{\rm lab}$	0.26°-1.2°
$\langle Q^2 \rangle$ [GeV^2]	0.0058
Maximum Current [μA]	70
Target Length (cm)	125
ρ_{tgt} [g/cm^3] (T= 20K, P = 35 psia)	0.0715
Max. Luminosity [cm^{-2} sec^{-1}]	2.4·10^{39}
σ [μbarn]	≈ 60
Møller Rate @ 65 μA [GHz]	≈ 134
Statistical Width(1.92 kHz flip) [ppm/pair]	≈ 91
Target Raster Size [mm $\times$ mm]	5×5
Production running time	344 PAC-days = 8256 hours
ΔA_{raw} [ppb]	≈ 0.54
Background Fraction	≈ 0.10
$P_{\rm B}$	$\approx 90\%$
$\langle A_{PV} \rangle$ [ppb]	≈ 32
$\Delta A_{stat}/\langle A_{expt} \rangle$	2.1%
$\delta(\sin^2\theta_W)_{stat}$	0.00023

2.2 Precision Measurement of $A_{\rm PV}$ Using the Flux Integration Technique

High precision measurements of very small polarization-dependent scattering asymmetries require the flux integration technique for detecting and recording particles. MOLLER utilizes this technique, relying on the use of a magnetic spectrometer to direct the Møller elastic scattered electrons onto a detector which produces a response that is strictly proportional to the number of electrons detected. As there is no possibility to identify elastic scattering with features of the individually detected electrons (*i.e.* no timing, amplitude, energy, tracking, etc. information is available), the spectrometer must spatially separate the Møller scattered events from backgrounds.

The goal is to make a measurement that compares integrated flux measurements with opposing beam helicity polarization. The response of this primary detector is integrated over a period with a fixed beam helicity. With the integrated signal proportional to the detected flux rate F in a specific helicity window, the scattering asymmetry is measured for a pair of helicity windows with right- (left-) handed helicity as

$$A_i^{\text{raw}} \equiv \left(\frac{F_R - F_L}{F_R + F_L}\right)_i \simeq \left(\frac{\Delta F}{2F}\right)_i. \tag{3}$$

These measurements are made rapidly, to avoid variations in experimental conditions that might otherwise complicate the interpretation of the integrated signal by changing its proportionality to the detected flux rate. Some conditions which can change rapidly during these measurements – notably the electron beam trajectory, energy, and intensity – must be averaged over the same integration periods and used to correct the measured asymmetry for the changing conditions.

$$A_i = \left(\frac{\Delta F}{2F} - \frac{\Delta I}{2I}\right)_i - \sum_j \left(\alpha_j (\Delta X_j)_i\right). \tag{4}$$

Here, I is the time-averaged beam intensity over the duration of a helicity window, X_j are corresponding average beam trajectory parameters derived from judiciously placed beam position monitors and $\alpha_j \equiv \partial F/\partial X_j$ are coefficients that depend on the scattering kinematics as well as the details of the spectrometer and detector geometry.

In a well-designed experiment the uncertainty in this rapid measurement σ_{A_i} will approximate the counting statistics of the detected flux. Averaging over many (N) such measurements leads to the ultimate statistical uncertainty on the measured asymmetry:

$$\langle A \rangle = \frac{1}{N}\sum_i^N A_i; \quad \sigma_{\langle A \rangle} = \sigma_{A_i}/\sqrt{N}, \tag{5}$$

This measured, beam-corrected asymmetry must then be further corrected to account for background contamination, beam polarization, and other experimental effects, before it can be interpreted as the parity-violating analyzing power of elastic Møller scattering A_{PV}.

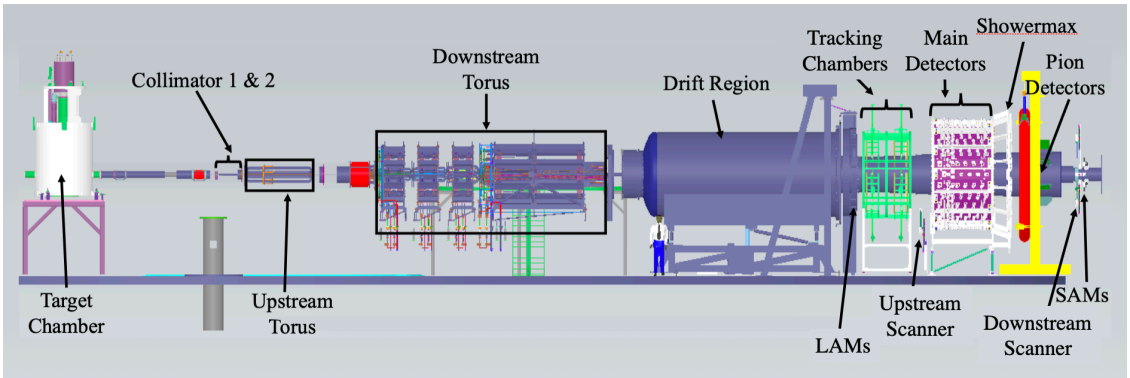

Figure 2: *MOLLER Experimental Apparatus Overview: CAD layout of the target, spectrometer, and detectors.*

2.3 Introduction to the MOLLER Apparatus

This section lists the functional requirements and summarizes the design of the component subsystems of MOLLER.

2.3.1 Target

Liquid hydrogen (LH_2) is the ideal target because it provides the largest electron thickness for the least amount of radiation length. To achieve the required luminosity, more than 8.5 g/cm^2 of LH_2 is needed in a target 125 cm long, with a cryogenic system capable of handling a heat load of 3.1 kW of beam power. This will be the highest-power LH_2 target ever constructed, and it builds on the experience with the operation of the $Q_{\rm weak}$ LH2 target, which successfully operated up to 180 μA with a total power of 2.9 kW [32].

For the precise measurement of a small asymmetry, it is paramount that the target density remains highly stable at the timescale of the helicity flip rate, as fluctuations in density would add statistical noise to the asymmetry measurement. MOLLER requires that target density variation must be $<$ 30 ppm at the millisecond timescale used for the asymmetry measurement, which corresponds to $<$5% excess noise relative to counting statistics. Computational fluid dynamics calculations are used to guide design and characterize the expected performance of the MOLLER target.

A system of solid targets will also be used, with a motion mechanism to swap between the LH2 or various solid targets. These calibration targets will be used at lower beam currents for a number of calibration studies. Details of the target system designed to meet these power and stability performance requirements are presented in Sect. 4.

2.3.2 Spectrometer

The MOLLER spectrometer bends electrons elastically scattered from target atomic electrons away from the primary beam axis, to arrive at a ring-shaped focus about 26.5 m downstream of the target. At the focus, these Møller scattered electrons are well-separated from the unradiated distributions of elastically and inelastically scattered electrons from nuclei in the target, and all electrons scattered into the spectrometer acceptance arrive at this focus at a larger radius than photons radiating from the target. In this way, an array of detectors in the focal plane can collect the Møller scattered electrons with low background contamination, while the nuclear-scattered events that create backgrounds can also be independently studied. Due to the low backgrounds at this focus, it is sufficient for the experiment to detect a single electron from each Møller scattering event.

The spectrometer consists of 5 resistive toroidal magnets with 7-fold symmetry around the beam axis. The upstream magnet and the first 3 subcoils of the downstream magnet set are essentially racetrack coils, and the fourth subcoil in the downstream magnet has a more complicated shape (see Fig. 60). A primary collimator (collimator 2), located upstream of the first magnetic element and about 5 m downstream of the target, defines the acceptance for the Møller signal with a polar angle range of $5 < \theta_{lab} < 20$ mrad. The acceptance is divided into seven identical, equally spaced wedges covering a total of half of the azimuthal angle, with the collimator blocking all flux between these wedges. A primary beam collimator at this position also defines an aperture at 5$\times$ the multiple scattered width of the beam, to allow the exhaust beam to reach the heavily shielded beam dump with minimal interception in the spectrometer. Other collimators, lintels, and shielding enforce a "2-bounce" requirement in which elements with line-of-sight exposure to the target at low angles do not have direct line-of-sight to the region of the detector used to measure the Møller asymmetry. Additional shielding elements are necessary to protect the experimental components, such as the epoxy which surrounds the coils. Two movable collimator-like components, the sieve and blocker, which will be used to calibrate the experimental acceptance and to study backgrounds, are located upstream of the primary collimator.

The maximum figure of merit for the Møller asymmetry occurs at a CM scattering angle $\theta_{\rm CM} = 90^\circ$ where the asymmetry is at a maximum and the cross-section is at a minimum. Møller scattering is identical-particle scattering, so each scattering event results in two electrons at opposing azimuthal angles and symmetric around 90° in the CM frame. The range of laboratory polar angles accepted in the primary collimator corresponds to CM scattering angles in the range 60°-120°. The large and approximately symmetric range of accepted CM polar angle assures that one of the two electrons for each desired Møller scattering event will always lie in the acceptance, even while half the azimuth is blocked to provide space for the magnet framing, services, and coils.

While this approach optimizes the azimuthal acceptance, it motivates an unusual and somewhat complicated magnetic design of the spectrometer, which must focus this required range of small scattering angles, with a corresponding momentum range from $3 \lesssim E' \lesssim 8$ GeV, from a long (1.25 m) target. Resistive magnets are used, as requirements for cryogenic cooling and the challenge of radiative heating at high luminosity preclude comparable performance from a superconducting coil design. The first toroid magnet starts about 5.5 meters from the center of the target and the last magnet ends about 16.3 m from target center. The largest of the coils has a radial size of about 42 cm.

Radial fields near each coil create an "azimuthal defocussing" of electrons, bending electrons away from the center of each sector such that Møller scattered electrons populate a full azimuthal ring at the focal plane. This azimuthal defocussing is greatest for the range of the acceptance with larger polar angle and correspondingly lower scattered momentum. In this way, the average kinematics of the scattered events varies significantly around the azimuthal ring. The ratios of the Møller signal and various background processes also vary across both the radial and azimuthal coordinates.

In summary, the spectrometer system meets the functional requirements for the MOLLER experiment by providing:

- Full azimuthal acceptance for Møller scattering events in the high FOM region (60°-120° in CM polar angle).
- Clean separation of Møller electrons from the primary background of elastic and inelastic electron-proton scattering.
- Collimation such that detectors do not have line-of-sight to the target.
- Clean channel for transport of the degraded beam and the bremsstrahlung photons to the beam dump.
- Minimization of soft photon backgrounds by designing a "two-bounce" system via judiciously placed collimators.

The design and function of the spectrometer is detailed in Sect. 5.

2.3.3 Main Integrating Detectors

The main electron detector system is optimized to achieve high precision on the measurement of the scattered electron flux through integration of the incident signal, rather than counting individual electrons. Each of the main detector elements comprises a quartz Cherenkov radiator held in a gas-filled light guide which transports the Cherenkov light to a larger radius for collection in a photomultiplier tube (PMT). The thickness of the quartz elements is optimized for resolution, balancing photon production against variations in response due to electromagnetic showering. The PMTs and voltage dividers are optimized for a highly linear response to the rate of photon illumination. These are read out using specialized, low noise, integrating electronics. The threshold for Cherenkov light production, low photon conversion, and angular dependence of light collection efficiency all serve to reduce low energy and neutral background contributions.

Radial and azimuthal segmentation of this detector system is required to separately measure the Møller distribution and to quantify the contributions from ep elastic and inelastic scattering. The quartz elements

are located at the spectrometer focus about 26.5 m from the center of the target, where the Møller and elastic ep scattered events are well separated. Taken together, the quartz elements cover the full range of azimuth, starting at a radius of 65 cm from the beamline, which is a slightly smaller radius than the peak of the ep elastically scattered electrons, and extending to a radius of 135 cm, which is slightly beyond the radial location of the Møller scattered peak. The radial segmentation creates six concentric rings around the beamline, with the Møller peak found in Ring 5 and the elastic ep scattering peak found closer to the beamline, in Ring 2. Azimuthal segmentation, with at least 28 elements in each ring, samples the kinematic separation created by azimuthal defocusing through the spectrometer.

These detectors can also be readout in counting mode, with preamplifiers and voltages set to allow for measurements of individual pulses. In this mode, calibration studies with low beam current can be performed in combination with tracking chambers located just upstream, to verify detector alignment, acceptance, and response functions.

The design and performance of the main detector system are described in detail in Sect. 6.

2.3.4 Tracking Detectors

The tracking system provides the diagnostic power to calibrate the primary detectors, the spectrometer optics, and the background processes over the full relevant polar and azimuthal ranges. It also provides the capability of measuring the acceptance function of the primary Møller-scattered electrons, so that the absolute scale of the parity-violating Møller asymmetry can be determined to better than 0.5%. The system primarily operates at lower beam currents for individual particle counting using Gas Electron Multiplier (GEM) detectors and trigger scintillators located downstream of the spectrometer and upstream of the integrating detectors. These detectors will be retracted when high beam current is used, to avoid damage from the high scattered flux and interference with the asymmetry measurement.

The purposes of the tracking system include:

- Verify the optical properties and acceptance of the toroidal spectrometer system.
- Verify the acceptance of the quartz detectors.
- Measure the position-dependent light-output response of the quartz detectors.
- Measure the radial and azimuthal distributions of incident electrons in order to verify the fractional backgrounds from elastic and inelastic ep scattering events in the integrating detectors.
- Study neutral and low-energy backgrounds in the integrating detectors.

The first two items are essential for verifying the expected kinematics of the experiment. The third is useful for searching for radiation damage effects in the main detectors, while the last two contribute to measuring and constraining background contributions.

The functional requirements of the tracking detectors specify that they must cover the full azimuthal and radial extent of the tracks that project to the main quartz detectors. The GEMs much be able to sustain rates of up to 150 kHz/cm^2 with $> 90\%$ single hit efficiency to provide adequate statistics within a reasonable calibration run time. They must provide the reconstructed track position at the thin quartz detectors to within ± 2 mm (RMS). This system is described in detail in Sect. 8.

2.3.5 Auxiliary Detectors

In addition to the thin quartz detectors and the tracking detectors, auxiliary detector systems are used to study neutral and low-energy backgrounds in the detector region, measure the background fraction and asymmetry of charged pions and their optical response in the integrating detectors, test the spectrometer performance, and test for and identify unexpected sources of backgrounds.

Shower-max Detector The Shower-max detector is an array of quartz-tungsten electromagnetic sampling calorimeters downstream of the thin quartz integrating detector array, intercepting the same scattered flux as the main Møller Ring 5. It provides a supplemental, energy-weighted measurement of the Møller signal with less sensitivity to hadronic and low-energy charged backgrounds.

The radial extent of these detectors approximately matches that of the main thin quartz detector ring that measures the Møller electrons (Ring 5). Given the lateral spreading of the showers in these thick detectors, the azimuthal segmentation is less than that of the thin quartz detectors. The individual azimuthal segments require a fractional energy resolution of 25% or better for mono-energetic 3 to 8 GeV electrons, in order to avoid excessive loss of statistical precision; this necessitates at least 4 interleaved layers of tungsten and quartz to reduce sampling fluctuations. The Molière radius of the interleaved stack should be less than 2 cm to minimize edge effects. Like the main detectors, the showermax detectors can be readout in integrated mode or in counting mode. Further details about the Shower-max detector can be found in Sect. 9.1.

Pion Detector In the vicinity of the Møller "peak", there is a possibility of a small ($\sim 0.1\%$) contamination from pions and other charged hadrons. The background could result from processes with a very tiny cross-section with a potentially large analyzing power. It is therefore important to be able to directly measure both the dilution fraction as well as the parity-violating asymmetry of this background.

A measurement (azimuth-averaged) of the pion asymmetry to a 0.10 ppm statistical precision in about 65 days of data-taking is required, for the expected pion fraction of about 10^{-3} of the Møller electron flux. So as not to significantly degrade the statistical width of the asymmetry measurement, a detector pulse-height resolution for through-going charge particles of better than 25% is required. Only the pions incident on the Møller ring need to be measured, so the radial coverage of the pion detectors only needs to provide a fair sample of the extent of main detector Ring 5. There may be significant azimuthal variation in the measured pion asymmetries, due to the combination of a small transverse beam polarization and the possibly large single-spin asymmetries in pion production. Therefore, this detector must instrument the entire azimuth for the pion asymmetry measurement.

The pion detector system consists of 28 identical acrylic Cherenkov detectors, located downstream of both the shower-max detectors and a Pb absorber "donut." It is sufficient for the pion detectors to measure the asymmetry of a roughly equal mix of pions and Møller electrons, so the pion detector system is required to suppress the Møller electrons by a factor of $> 10^3$. Further details about the pion detectors can be found in Sect. 9.2.

Scattered Beam Monitors In order to monitor potential false asymmetries in the background resulting from primary scattered beam interacting in downstream collimators, beampipe, and shielding, scattered beam monitors are needed: a) in locations where the primary target scattered rate is higher than the Møller rate but the expected physics asymmetry is smaller, b) in locations where the expected scattering rate from primary target interactions is small, so the majority of the signal comes from secondary interactions. The first set of requirements is met by the small (SAM) and large (LAM) angle monitors, while the second set of requirements is met by the diffuse beam monitors (DBM). Further details of these detectors are in Sect. 9.3.

Scanner Detectors As described further in Sect. 9.4, there will be two sets of scanner detectors in the experiment. A two-dimensional upstream scanner will be located upstream of the main detector. It is required to provide a map of the scattered particle flux in one septant in a time of less than one hour. This will be used to monitor potential changes in the scattered flux due to such effects as changing beam conditions or long term variations in the magnetic field of the spectrometer. A second scanner system will be located just upstream of the last detector system in the experiment (the small angle monitors). This downstream scanner will use four one-dimensional radial scanners located at various azimuthal positions. With the

spectrometer magnets off and a carbon target, these scanners will map scattered electrons to provide a beam-based confirmation of the position of the acceptance-defining collimator (Collimator 2), with a precision of ± 1 mm transverse to the beam.

2.3.6 Data Acquisition, Trigger, and Analysis

The trigger and data acquisition (DAQ) systems allow for operating the system in both the primary high beam-current integrating mode and low beam-current counting mode. The integrating mode DAQ system primarily interfaces with integrating ADC modules to record the detector and beam monitor signals during the data-taking at high beam current. The integration period is synchronized for these custom, low-noise ADC modules, which will be used to read out the main detectors, beam monitors, and auxiliary detectors.

The counting mode DAQ is used for low beam-current measurements in which individual electron-scattering events can be observed. Triggers will be formed using combinations of main detector elements and scintillators near the GEM tracking detectors. This pulse counting readout will record timing and pulse size information for the GEMs, trigger scintillators, main quartz detectors, and the showermax, pion, and scanner auxiliary detectors.

While MOLLER will make extensive use of scientific computing resources at JLab, a dedicated analysis cluster will be used to assure the required data analysis throughput, which is critical to monitoring the performance of the apparatus. The DAQ, trigger, and analysis systems must meet the following requirements:

- In integration production running, the network and event building systems support a data rate of about 130 MB/s during the production integration mode data collection to maintain 100% throughput without deadtime.
- The counting mode trigger supports trigger decisions based on input rates between 10 kHz and 300 kHz. It has the flexibility to generate triggers from either the dedicated scintillator triggers or from any combination of the quartz detector signals.
- The feedback and real-time analyzers during production running at 1.92 kHz run at nearly 100% throughput without impacting the data acquisition deadtime.
- The online analysis cluster supports sufficient concurrent processes to complete prompt analysis of 100% of the data flow, including correlation analysis and corrections.
- The local disk storage is sufficient to hold at least several days of both the raw data files for staging to the Mass Storage System and the full analysis output files for review.

These systems are described in detail in Sect. 10.

2.3.7 Polarized Beam, Monitoring, and Diagnostics

The MOLLER experiment relies on delivery of up to 70 μA of 90% longitudinally polarized, 11 GeV electron beam. The polarized source will be required to perform the polarization switching at 1.92 kHz, forming a set pattern of 32 complementary pairs organized to cancel 60 Hz line noise.

The polarized electrons are generated using photoemission by circularly-polarized laser light incident on a doped gallium arsenide photocathode, with a fast electro-optic Pockels cell used to toggle the polarization state. MOLLER requires a faster transition between polarization states than has previously been used. The beam quality, in terms of random and helicity-correlated fluctuations, must also meet stringent requirements, well beyond those of previous parity-violation experiments, to achieve the proposed statistical and systematic uncertainties. The stability of the beam position on target should be 10's of microns between the 0.5 msec helicity reversal period, and the beam trajectory difference between the two helicity states must average over the run such that net corrections are at the 1 ppb level. The use of "slow" reversals, with

insertion of laser optics or changes to magnetic settings to change the beam helicity on target relative to the voltages on the Pockels cell, should also be used to reduce potential causes of beam asymmetry between the helicity states.

Section 3 details these requirements, describes the novel implementation of an electro-optic Pockels cell that has been developed to enable the required fast and stable polarization switching, and outlines the techniques that will be used.

The systems that MOLLER needs to measure and control the electron beam properties are also described in detail in Sect. 3. The beam intensity and trajectory must be measured continuously with sufficient precision and accuracy for the 0.5 millisecond helicity states to allow corrections to the detector response for both random and helicity-correlated jitter. Existing beam position monitors based on RF antennae will be used; previous usage has demonstrated the required 3μm resolution at the 1.92 kHz helicity flip rate. Resonant cavity beam position monitors will also be used, with similar resolution. The beam intensity monitor requires a precision of 10 ppm or better; multiple existing RF cavity intensity monitors will be used, with improvements to readout electronics planned to approach this resolution using a single monitor.

A beam modulation system is used to generate controlled variations in the position, angle, and energy of the electron beam to measure the response of the detection system to those variations. As has been used in previous experiments, a system capable of inducing small changes to the beam trajectory/energy at modest harmonic frequencies ≤ 125 Hz is required for this calibration technique.

2.3.8 Polarimetry

Since the measured parity-violating asymmetry is directly proportional to the electron beam longitudinal polarization, it is important to measure the polarization to high precision. The longitudinal polarization of the 11 GeV electron beam is expected to be about 90% and the beam polarization may vary by up to 2% over the duration of a specific photocathode's lifetime. The goal is thus to know the absolute polarization with robust control of systematic uncertainties to 0.4% and to continuously monitor this polarization for significant variations. In addition, the polarization will be oriented to within a degree of longitudinal to avoid an azimuthal scattering asymmetry associated with the transverse beam polarization component.

The techniques for polarization measurements are described in Sect. 11. A Compton polarimeter will be used for continuous measurement of the beam polarization, with independent detection of scattered photons and electrons, providing a pair of measurements with a high degree of independence in systematic errors. The Compton polarimeter will be periodically cross-checked against measurements with a Møller polarimeter using ferromagnetic foil targets. As part of an initiative to upgrade polarimetry in Halls A and C, the Hall A Compton polarimeter will have a new electron detector installed. Upgrades to the Hall A Møller polarimeter will be made to improve its acceptance and optics determination. In operation at lower beam energies, the Møller polarimeter has achieved a precision estimated at $\delta P_b/P_b \sim 0.6\%$, while the Compton polarimeter results have been estimated to reach $\delta P_b/P_b \sim 0.42\%$. Based in part on that previous experience, it is expected that each of these polarimeters will independently achieve or approach the ultimate MOLLER goal of 0.4% precision.

2.3.9 Shielding and Infrastructure

The MOLLER apparatus will require improvements to some infrastructure systems in JLab's Hall A. Upgrades to the Hall A electrical power distribution and low-conductivity water capacities are needed to instrument the series of resistive magnets used by the spectrometer. To satisfy the cryogenic needs of the high power target, a dedicated transfer line is planned, capable of handling the larger flow from the new End Station Refrigerator (ESR-2) which is presently under construction. The MOLLER target location requires modification of the beamline layout and utility platform and routes. The large High Resolution Spectrom-

eters (HRS) previously used in Hall A will remain in place. They will be positioned to avoid interference with the MOLLER apparatus and services, and components of the HRS near the hall center will be removed to allow assembly of the MOLLER spectrometer and shielding in the hall.

New radiation shielding is required around the target, beamline, and electronics racks, with the goal of protecting personnel and equipment throughout the lifetime of the MOLLER experiment. The layout of the MOLLER apparatus in Hall A, with shielding, is shown in Figs. 3 and 4. The shielding and infrastructure considerations for the experiment are described in detail in Sections 12 and 13.

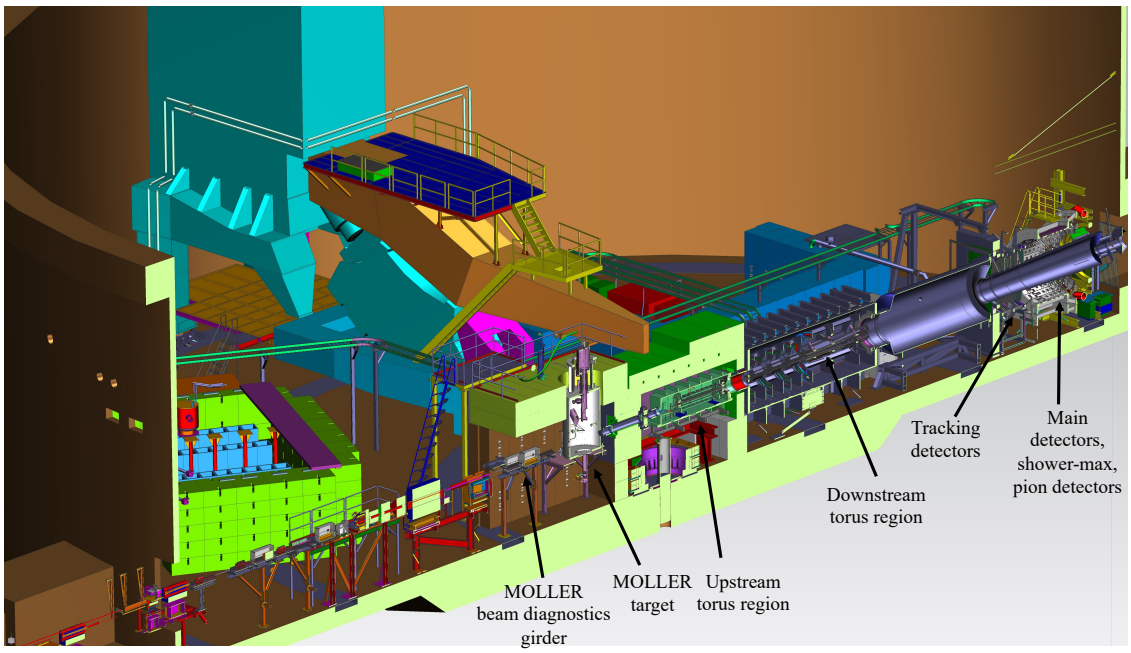

Figure 3: *Overview of the MOLLER experimental apparatus in Hall A with cutaway views and shielding partly removed.*

2.4 Achieving High Precision

MOLLER will measure an asymmetry in the beam-corrected integrated detector yield $\langle A \rangle$, as described in Eq. 5 of Sect. 2.2. This average asymmetry requires additional corrections before it can be interpreted as the parity-violating analyzing power of elastic Møller scattering, $A_{\rm PV}$. First, a correction is required for backgrounds due to other scattering processes. The asymmetry must also be corrected to reflect the incomplete longitudinal polarization of the electron beam $P_{\rm B}$. Assuming, for simplicity, that these corrections are not time dependent, $A_{\rm PV}$ would be calculated from the averaged measured asymmetry $\langle A \rangle$ as:

$$A_{\rm PV} = \frac{R_v}{P_{\rm B}\left(1 - \sum f_i^{\rm bkgd}\right)} \left(\langle A \rangle - A_F - A_{\rm lin} - \sum_i f_i^{\rm bkgd} A_i^{\rm bkgd} \right). \tag{6}$$

Here $f_i^{\rm bkgd}$ is the relative size of the signal from a specific background source i and $A_i^{\rm bkgd}$ is the associated asymmetry. The "false" asymmetry term A_F represents potential experimental asymmetries in the measurement which are not covered by other corrections, while $A_{\rm lin}$ accounts for imperfections ("non-linearity") in the proportionality of the detector signal to the scattered flux. An averaging over the finite experimental acceptance requires a precise determination of the accepted kinematics and an understanding of radiative

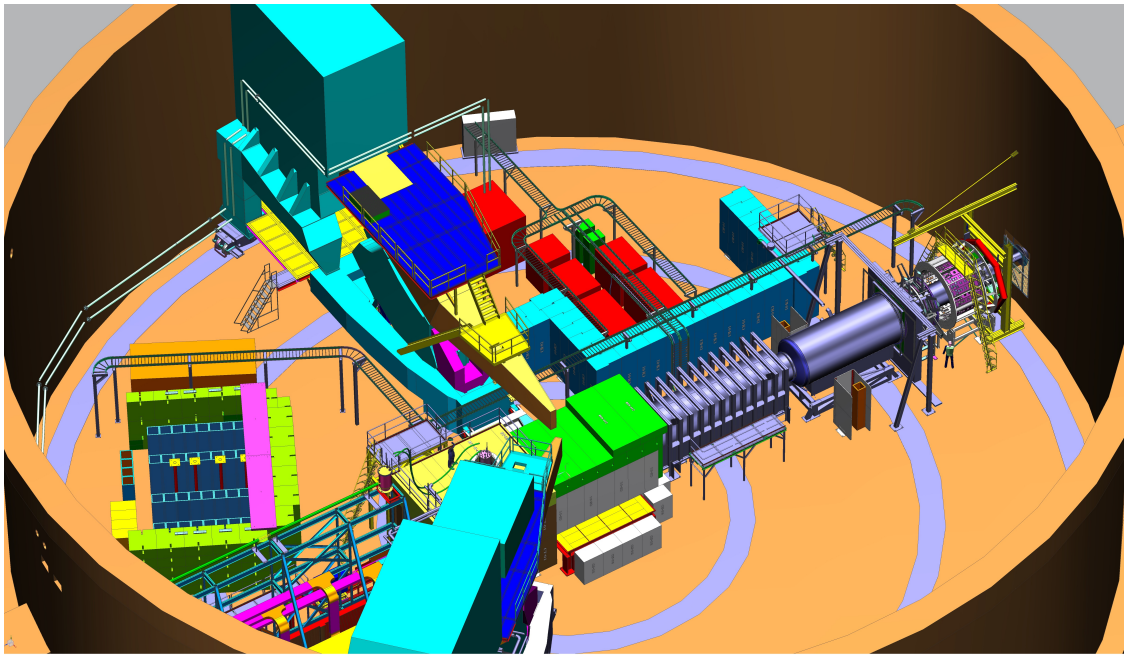

Figure 4: *Overview of the MOLLER experimental apparatus in Hall A with shielding enclosures complete.*

effects, in order to produce an estimate of $A_{\rm PV}$ at a specific kinematic "point". Any correction due to this averaging is accounted by a multiplicative factor $R_v \sim 1$.

2.4.1 Precision of the Asymmetry Measurement

The ultimate limit for statistical precision of a scattering asymmetry measurement is the counting statistics, while any practical experiment must minimize other sources of random noise in order to approach this limit. It is most convenient to consider the statistical power of the measurement using the "pair width", that is, the precision for a single measurement made with a pair of integration periods at the helicity-reversal frequency. Ultimately, this pair width, divided by the square root of the number of pairs, provides the statistical uncertainty estimate for the measured asymmetry. Equation 6 can then be used to translate this to the uncertainty on $A_{\rm PV}$.

Table 2 summarizes the largest expected contributors of statistical noise. The time basis for this estimate is the 1920 Hz helicity reversal rate[1] Assuming a 20 μs transition time, this suggests an integration period of 500μs for each helicity state and 1 msec for each complementary pair. Counting statistics for this integration period, at the estimated rates and including the expected 10% background fraction, leads to a precision of 82.4 ppm for each pair.

There are a number of sources of random noise which will increase the pair width and correspondingly reduce the statistical power of the measurement, as shown in Tab. 2. The most significant source of noise in the estimated noise budget is due to density fluctuations in the LH2 target. There is no practical way to measure the rapid variations in target density, which can arise through deformation of a vaporized layer near the target windows, or through density variations or nucleation of voids within the flowing cryogen. There has been significant operational experience with a high power cryotarget during the Qweak measurement,

[1]This specific frequency is divisible by the 60 Hz line frequency. In general, when this document reference "2 kHz" it is referring to helicity changes at 1920 Hz and pairs at 960 Hz.

Table 2: *Summary of projected contributions to the pulse pair asymmetry random noise width.*

Parameter	Random Noise (65 μA)
Statistical width (0.5 ms)	$\sim$ **82 ppm**
Target Density Fluctuation	30 ppm
Beam Intensity Resolution	10 ppm
Beam Position Noise	7 ppm
Detector Resolution (25%)	21 ppm (3.1%)
Electronics noise	10 ppm
Measured Width (σ_{pair})	**91 ppm**

for which a clear frequency dependence of the target density fluctuation was observed, and with the density fluctuation noise limited to lower frequencies. While Qweak used a 1 kHz helicity flip rate to reduce target density fluctuation noise, an empirical fit of test data taken during Qweak suggests that suppression of noise is more robust at even higher frequencies. The estimates for this noise have been further supported using Computational Fluid Dynamics studies in the MOLLER target design.

The intensity of the beam varies rapidly over the time scale of the measurement windows, so the beam intensity requires constant monitoring and real-time correction. MOLLER expects to operate the beam intensity monitors at a precision of 10 ppm for the integration of 1 ms pairs. The beam trajectory parameters averaged over the integration window, *e.g.* position or angle differences and energy asymmetry between pair windows, will also contribute to random noise. After correction, the dominant noise contributions from beam trajectory differences are due to the calibration precision for the correction coefficients rather than the intrinsic monitor resolution. These contributions are estimated in Sect. 3.2.4.

Because the integrated detector signal is taken to be proportional to the incident flux, the variations in the signal size for each incident particle contribute to the random noise above particle counting statistics. The detector resolution $\sigma_{\rm res}$, measured as the root-mean-square variance of the response to a single electron divided by the average response, contributes the random noise above counting statistics as

$$\sigma_{\rm total} = \sigma_{\rm count}\sqrt{1+\sigma_{\rm res}^2}. \tag{7}$$

With the expected detector resolution of 25%, this will contribute a relative 3% increase in the pair width.

In addition to the electron-by-electron signal variations, integrating electronics are sensitive to variations in the electronic baseline. For the low-noise electronics to be used for MOLLER, this contribution will be small.

2.4.2 Control of Systematic Uncertainties

The projected leading systematic uncertainties for the experimental apparatus design are listed in Tab. 3. This table lists contributions larger than 0.1%; other sources of systematic uncertainty have been considered but are negligible at this level. Each individual uncertainty is no larger than 0.5% and in quadrature combination the total is about half of the projected statistical uncertainty. The methods used to estimate and control these leading sources of systematic uncertainty are described below.

Following the practice of most previous parity-violation measurements, MOLLER will use a "blinded" analysis, in which the analysis software will add an offset asymmetry when unpacking the data. With careful design and application, the application of this offset prevents any comparison to the Standard Model expectation but does not obscure any experimental or apparatus cross-checks. The blinding offset will

remain hidden from the collaboration until the analysis of a blinded data set is completed. There is no risk of corruption of the raw data, which is stored without modification.

Beam Properties The detected scattering rate asymmetry is sensitive to changes in the intensity, trajectory, or energy of the polarized beam. As represented in Eq. 4, correction for variation in the beam properties is required to control experimental random noise. In addition, the finite precision of these corrections can also be a potential source of systematic error due to an average helicity-correlated difference in the beam being misinterpreted as a scattering rate asymmetry. The MOLLER goal is to keep the uncertainty due to beam parameter corrections to be less than 0.2 ppb, both by minimizing the size of the average beam asymmetries and by making precise corrections.

The control of helicity-correlated beam asymmetries has been refined over the history of parity-violation measurements, and recent experiments at Jefferson Lab have demonstrated a level of control consistent with achieving the MOLLER goals. The first step is configuration of the laser optics of the polarized source to reduce the initial polarization-dependent variations in beam properties, while care is taken in implementing the electron beam optics to avoid enhancing the effect of variations in the beam. Active feedback is used to reduce the average beam intensity asymmetry, and if needed a similar system will be available to minimize beam trajectory differences as well. MOLLER will also utilize three methods for reversing the beam helicity which are independent of the primary helicity control, which will provide additional cancellation for remaining beam asymmetries.

The corrections for beam trajectory and energy require a precise calibration of the correction coefficients in Eq. 4. Linear regression analysis of the dependence of measured asymmetries on beam properties is a powerful diagnostic tool, but distortions due to finite resolution are a crucial limit on the applicability of such techniques. An independent calibration system driving modulation of the beam trajectory and energy is employed and, in particular, an analysis combining regression inputs with constraints from the modulation calibration has demonstrated the level of precision required for MOLLER [30].

The systems used for beam monitoring, control of helicity-correlated beam asymmetries, and calibration of correction coefficients are described in Sect. 3.

Transverse Polarization The orientation of beam polarization requires precise control during the MOLLER measurement. A transverse component of beam polarization would create an azimuthal modulation in the scattering rate asymmetry due to the beam-normal single-spin analyzing power A_T, which is about 400 times larger than the parity-violating analyzing power. While this should be expected to cancel over the experimental acceptance, practical variations in the acceptance would introduce unacceptable systematic uncertainty without tight limits on the degree of transverse polarization.

For this reason, MOLLER will measure the transverse polarization component using the detected azimuthal variation. As described in Sect. 7.2, a small component of transverse polarization will produce an easily identifiable pattern of azimuthally dependent asymmetries over the detector segmentation. This results in a measurement of spin orientation with a precision of about 1° in a few hours, which can be zeroed by spin manipulation in the low energy injector. In combination, this control on the transverse polarization and the intrinsic cancellation of the variation over the experimental acceptance will sufficiently control this possible source of systematic uncertainty.

Kinematic Normalization An uncertainty is applied to the asymmetry result corresponding to the uncertainty in averaging over the finite experimental acceptance, including radiative effects in the target. The alignment precision of the primary acceptance collimator relative to other beam line components provides a starting estimate of this uncertainty. Studies with very low beam current and thin solid targets will charac-

terize the spectrometer optics and, through comparison with simulation, cross-check the expected scattered flux distribution, as discussed in Sect. 8.3.

Backgrounds A fraction of the electrons scattered from nuclei in the target form an irreducible background, indistinguishable from the Møller signal in the region where the detector response is integrated. The radial and azimuthal segmentation of the MOLLER detector provides a map over varied ratios of background signals and asymmetries. A deconvolution analysis over this distribution will separately determine the asymmetric background corrections for the Møller A_{PV} measurement as described in Sect. 7. This analysis will be supplemented by comparison to tracking studies of the distribution of scattered electrons. Pion detector results will also bound possible contributions from other inelastic channels, including hyperon decay.

Other backgrounds can be created from stray electrons or photons striking elements in the spectrometer or in the exhaust beamline and then scattering into the main detector. The MOLLER apparatus is designed to reduce these backgrounds through the use of lintels, shielding elements, and collimators in the spectrometer. Tracking runs taken with very low current, and high current studies with the blocking detector, will help to characterize this background.

The use of ferromagnetic materials is carefully vetted in the experimental design. A biased, step-wise simulation was used to estimate very low probability scattering events for potentially magnetic material, and estimates of the potential magnitude of spin polarization in the ambient field were used to derive a conservative upper limit on a double-spin scattering asymmetry for events producing a signal in the main detector. Components with an estimated upper limit for such an asymmetry within an order-of-magnitude of the experimental systematic uncertainty goals were either changed to non-magnetic materials, or redesigned to reduce the rescattered flux reaching the detector.

Detector Linearity The proportionality of PMT response to light level will be characterized in bench tests under operating conditions, and is specified to achieve $< 0.5\%$ measured to a precision of 0.1%, as described in Sect. 6.4.3. This will be cross-checked during the run with beam current monitors, especially in calibration studies that induce large beam current intensity asymmetries.

2.4.3 Run Phases

Previous experience with high precision measurements has shown the importance of pacing the data collection campaign. In particular, an engineering run with ample room for commissioning and calibration and followed by a significant pause before data collection restarts, is a high priority. Gaps between run phases provide time for changing hardware to fix problems uncovered during calibration phases, which as a practical matter has proven necessary in previous experimental efforts. They also provide an opportunity for the collaboration to complete a more detailed analysis of collected data, improve calibration procedures and refine run planning. Finally, the separations provide a natural break point for reblinding the data, allowing initial publications of early data sets to proceed while data collection and analysis continues on the later phases. Notably, both E158 and Qweak followed a similar strategy, with significant hardware and electronics modifications between run phases, and analysis results completed during experimental pauses used to improve run planning and calibration plans during later phases.

Planning for the MOLLER experiment has targeted three phases, summarized in Tab. 4. The first run would be planned to approximately match the precision of the E158 apparatus while providing a thorough characterization of the MOLLER apparatus. Two subsequent phases would each sequentially approximately double the statistical power. This organization provides an opportunity to improve the performance of each system to progressively higher precision and to reach the ultimate performance goal for the majority of data taking in the final run.

Table 3: *Summary of projected fractional statistical and systematic errors on A_{PV} for the MOLLER experiment.*

Error Source	Fractional Error (%)	
	Run 1	Ultimate
Statistical	**11.4**	**2.1**
Absolute Norm. of the Kinematic Factor	3	0.5
Beam (second moment)	2	0.4
Beam polarization	1	0.4
$e + p(+\gamma) \rightarrow e + X(+\gamma)$	2	0.4
Beam (position, angle, energy)	2	0.4
Beam (intensity)	1	0.3
$e + p(+\gamma) \rightarrow e + p(+\gamma)$	0.6	0.3
$\gamma^{(*)} + p \rightarrow (\pi, \mu, K) + X$	1.5	0.3
$e + Al(+\gamma) \rightarrow e + Al(+\gamma)$	0.3	0.15
Transverse polarization	2	0.2
Neutral background (soft photons, neutrons)	0.5	0.1
Linearity	0.1	0.1
Total systematic	**5.5**	**1.1**

Table 4: *Summary of notional run phases, with production and calibration estimates used for collaboration planning, to achieve the ultimate precision goals of the MOLLER experiment.*

Run	1 kHz	PAC Days	Stat Error		Efficiency	Calendar Weeks	
Period	Width	(prod)	$\sigma(A_{meas})$	$\sigma(A_{\rm PV})$		(prod)	(calib)
I	101	14	2.96 ppm	11.4%	40%	5	6
II	96	95	1.08 ppm	4.2%	50%	27	3
III	91	235	0.65 ppm	2.5%	60%	56	4
Total		344	0.55	2.1		88	13

The ultimate statistical power of the experiment is estimated from the projected pair width for the individual asymmetry measurements. An allowance for unexpected contributions to random noise is included in the experimental planning, with the expectation that any unexpected noise will be improved after the early experimental phases to reach the ultimate statistical performance goal. Similarly, the path to the ultimate systematic uncertainty will require a progressive refinement of calibrations and cross-checks. Estimates for the systematic uncertainty goals for the engineering run as listed in Tab. 3. Calibration studies, improved statistics and larger data set for cross-checks from production data, and time for improved analysis will all be part of the progression to achieving the ultimate systematic uncertainty goals listed in the last column of Tab. 3.

3 Polarized Beam, Monitoring, and Control

CEBAF at Jefferson Lab routinely operates with > 100 μA electron beam currents and high beam polarization ($> 85\%$) for a variety of nuclear physics studies, with various requirements on beam conditions, in four experimental halls [33]. While the specific requirements on the electron beam for MOLLER are similar in nature to those of previous parity-violation measurements operated at Jefferson Lab, the increased experimental precision goal results in more restrictive allowances for the stability of the beam under rapid helicity reversal and control of the beam polarization. These requirements, and the technology to be used at Jefferson Lab that will achieve them, are described below.

3.1 The CEBAF Polarized Electron Source

The polarized electron beam is generated using photoemission due to circularly-polarized light on a doped gallium arsenide photocathode. The polarization of incident laser light selects the polarization of the electron beam, and the rapid flip of electron beam helicity is performed with a reversal of the incident laser polarization. The laser polarization is created with an electro-optic Pockels cell, so that reversing the applied voltage flips the sense of polarization.The voltage applied to the Pockels cell is the only change in the electron beam generation or transport that is correlated to beam helicity. The photocathode quantum efficiency has an analyzing power for linear polarized light, but is the same for right- and left-handed circular polarization [34].

The photocathode response is symmetric for circularly polarized laser light, and electron beam transport is unaffected by the electron polarization. Therefore, any helicity-correlated asymmetry in the electron beam must be directly related to the voltage applied to the Pockels cell or the polarization-sensitive transport of the laser light to the photocathode.

There is significant operational experience in using the polarized electron source for parity-violation experiments at Jefferson Lab [34]. With this experience, a detailed understanding of the sources of Helicity-Correlated-Beam-Asymmetries (HCBA) has emerged and led to a sophisticated protocol for systematically reducing or eliminating these effects in the laser optics of the polarized source [35–37].

3.1.1 Injector Upgrade

While the photocathode technology is a key component for generating the polarized electron beam, it is the Pockels cell that generates the robust and rapid polarization reversal which is so critical to a precision asymmetry measurement. The Pockels cell at Jefferson Lab has been upgraded from a KD*P (potassium dideuterium phosphate) cell to an RTP (rubidium titanyl phosphate) Pockels cell which will enable the fast flip rates required for MOLLER [37].

An upgrade is ongoing for several key components of the injector, with Phase 1 completed in October 2020 - May 2021, and the final Phase 2 planned for the next long accelerator shutdown in 2023. An upgraded electron gun will be installed which will double the standoff voltage to provide a 200 keV accelerating potential. The higher electric field has been shown to increase the lifetime of the activated photocathode [38], which will allow for a more stable source configuration for MOLLER. In addition, the higher energy in the early injector will improve beam transport. The reduction in space charge effects in the beam will eliminate the need for an RF pre-buncher at its former location and it has been relocated as of Phase 1. In previous operation, it was a complicating element in the early injector. In conjunction with the gun update, the 1/4 cryounit accelerating cavity will be replaced. This is the first RF accelerating element and integrates RF capture and acceleration to 10 MeV. The new cavity will reduce the significant x/y “skew” coupling relative to the existing cavity. This coupling has been a major impediment to reliably achieving a match to design

optics through the injector. Spin manipulating elements based on crossed $\vec{E} \times \vec{B}$ fields ("Wien rotators") are to be upgraded for higher fields to match the new gun voltage and more uniform optical elements [39].

All of these upgrades will benefit MOLLER [40]. The RTP Pockels cell will enable fast flipping between polarization states, the higher gun voltage should better transmit the beam through apertures in the injector with less clipping, and the Wien rotator upgrade along with the removal of the pre-buncher will lead to much more efficient operation of the injector spin flip. The improved transmission and reduced skew coupling will improve the match to design optics, and so improve the benefits to HCBA suppression from adiabatic damping. The anticipated improvements in the polarized source (such as the higher photogun voltage and upgraded 1/4 cryounit) are expected to help achieve a match to the optimized beam optics design. In addition, new diagnostic and analysis tools will improve the matching procedure throughout the accelerator. These accelerator improvements will provide a significant margin of safety for achieving the polarized beam requirements for MOLLER.

3.2 Beam Requirements for MOLLER

MOLLER is an extension of a series of high precision parity-violation experiments which typically operate at small scattering angles and measure cross-section asymmetries that are extremely small. One challenge of these experiments is that changes in the beam properties (intensity, position, profile) will change the detected scattered flux. If the changes in the beam are correlated with the electron helicity, the result can mimic the tiny parity-violating asymmetries. While changes are typically measured and corrections are applied, there is a finite precision associated with these corrections, which can be a potential source for systematic error or a false asymmetry. Helicity-correlated beam asymmetries (HCBA) are therefore a potential systematic error, and a very high level of control of HCBA is required for the precision measurement contemplated here.

There are requirements beyond the specified run-averaged beam asymmetries. In order to achieve the necessary statistical precision, it is necessary to complete individual measurements of the scattering asymmetry very rapidly, so each measurement can occur without a significant change in the apparatus (for example, a change in the target density). In addition, a high level of beam stability is needed during each measurement, so that an imperfect correction for a beam parameter does not introduce significant additional noise.

To first order, the measured asymmetry must be corrected for variations in beam parameters which include intensity, position, energy, or spot-size. The correction can be written as:

$$A_{\rm cor} = A_{\rm det} - A_Q + \alpha_E A_E + \sum \alpha_i \Delta x_i \tag{8}$$

where $A_{\rm det}$ is the asymmetry in the detected flux, A_Q is the beam charge asymmetry, A_E is the helicity correlated energy asymmetry, Δx_i are the helicity correlated position differences, and α_i are the calibration constants, which can be measured through cross correlations and linear regression, or using the beam modulation calibration, in data analysis.

In addition to first-order effects, certain second-order effects can be helicity-correlated and thus lead to systematic shifts. One common manifestation of such an effect would be a helicity-correlated difference in the beam spot-size. There is no technology for directly measuring spot size variation at the requisite level and therefore no correction will be made. However, an upper limit on the helicity-correlated spot-size asymmetry will be demonstrated to limit the uncertainty contribution from it.

The beam performance required for MOLLER to achieve its scientific goals is shown in Tab. 5. A comparison of the requirements for helicity-correlated beam asymmetries (HCBA) during MOLLER and those observed in previous experiments are summarized in Table6. The previous parity experiments include the HAPPEX-II [29] (3 GeV in 2005), Qweak [12] (1 GeV in 2010-2012), PREX-2 [30] (1 GeV in 2019),

and CREX (2 GeV in 2020) experiments [31]. It is expected that the MOLLER goals are achievable given the plans for the new Pockels cell, expected improved matching optics, and slow-reversals.

Beam Property	Defining Equation	Required 960Hz pair random fluctuations	Cumulative Helicity Correlation (full data set)
Intensity	$A_q \equiv \frac{I_0 - I_1}{I_0 + I_1}$	< 1000 ppm	< 10 ppb
Energy	$A_E \equiv \frac{E_0 - E_1}{(E_0 + E_1)} = \frac{\Delta E}{2E}$	< 110 ppm	< 1.4 ppb
Position	$D_x = \Delta x \equiv x_0 - x_1$	$< 50 \times 10^{-6}$ m	$< 0.6 \times 10^{-9}$ m
Angle	$\Delta\theta \equiv \theta_0 - \theta_1$	$< 10 \times 10^{-6}$ radian	$< 0.12 \times 10^{-9}$ radian
Spot-size	$\Delta\sigma/\sigma \equiv \frac{\sigma_0 - \sigma_1}{\frac{1}{2}(\sigma_0 + \sigma_1)}$	-	$< 10^{-5}$

Table 5: *Parity quality beam performance goals for MOLLER.*

	HAPPEX-II [29] (achieved)	$Q_{\rm weak}$ [12] (achieved)	PREX-2 (achieved)	CREX (achieved)	MOLLER (required)
Intensity asymmetry	400 ppb	30 ppb	25 ppb	-88 ppb	10 ppb
Energy asymmetry	0.1 ppb	0.4 ppb	0.8 ± 1 ppb	0.1 ± 1.0ppb	< 1.4 ppb
position differences	1.7 nm	4.4 nm	2.2 ± 4 nm	-5.2 ± 3.6nm	0.6 nm
angle differences	0.2 nrad	0.1 nrad	$< 0.6 \pm 0.6$ nrad	-0.26 ± 0.16nrad	0.12 nrad
size asymmetry (quoted)	–	$< 10^{-4}$	$< 3 \times 10^{-5}$	$< 3 \times 10^{-5}$	$< 10^{-5}$

Table 6: MOLLER beam asymmetry requirements compared to the approximate magnitude of run-averaged asymmetries achieved in previous experiments. The values for position and angle differences are modified from those reported by the experiments in accordance with definitions used as indicated in the table. The quoted $Q_{\rm weak}$ results are from run 2. The uncertainties quoted for PREX-2 and CREX represent a "radius of convergence" of random beam jitter, showing that the trajectory differences are consistent with convergence of random noise with zero systematic offset. The spot size asymmetry estimate for PREX-2 is shown without factoring in slow reversal cancellations.

3.2.1 Rapid Helicity Flip

As described in Sect. 2.2, the MOLLER measurement is optimized for rapid, differential measurements of scattered flux over periods with opposing beam polarization. In particular, time "windows" will be generated in the electron bunch train at a frequency of 1.92 kHz, with the sign of the beam's longitudinal polarization in each window assigned from a set pattern of 64 windows (a "multiplet") optimized to eliminate 60 Hz noise. A pseudo-random sequence will be used to select the sign of the first window in the 64-window pattern, to eliminate possible systematic effects from coherent pick-up of fixed-frequency noise.

MOLLER is designed around a high helicity flip rate, which will preserve the statistical power of its high counting statistics by reducing the effects of baseline electronic noise as well as the density fluctuations in the liquid hydrogen target. With the design flip rate of 1.92 kHz, the integration window for each period of stable helicity is only 520 microseconds long. The helicity flip must be robust, completed significantly before the next integration period begins, and closely matched between the transitions to the two polarization states. In order to maintain a high duty factor, MOLLER aims to keep the "settle" time between integration periods to approximately 10-20 microseconds. The RTP Pockels cell has been demonstrated to be capable of successfully switching in this time frame.

At present, the RTP Pockels cell is capable of achieving a stable transition in $\sim$ 11 μs, with virtually none of the ringing that is observed with KD*P (see Fig. 5). The first operational prototype RTP cell has been pulsed continuously since its installation in CEBAF in January 2019, and the quality of the transition has shown no signs of degradation as of 2022. Helicity control boards have been developed to support the required production of 64 window multiplets at 1920Hz, with backward compatibility to previous helicity control schemes.

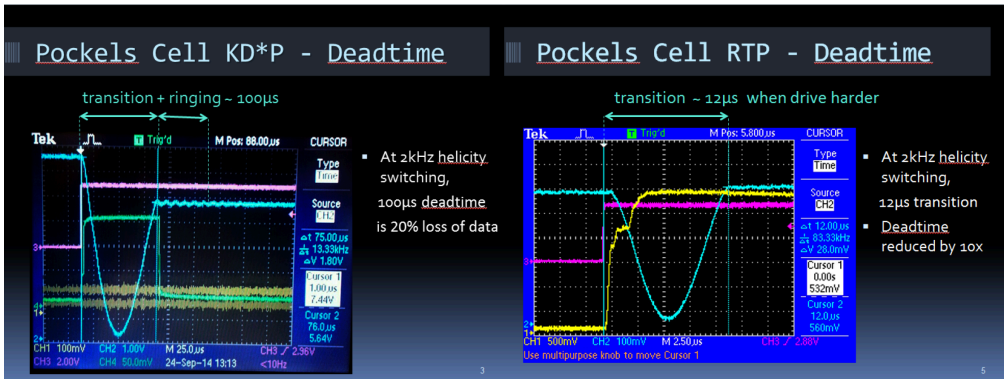

Figure 5: *Transition Time: These measurements were performed by driving the Pockels Cells near quarter-wave voltage and examining the transmission through an analyzer oriented along the birefringence axis. KD*P cell optomechanical ringing has a* $\sim$ $10\mu s$ *period. Left: blue trace is transmission through KD*P cell like that formerly used at CEBAF, pink trace is helicity trigger, green trace is the LED pulse detected by a photodiode. Right: blue trace is transmission through RTP cell newly installed at CEBAF, pink trace is the helicity trigger, yellow trace is the LED pulse detected by a photodiode.*

3.2.2 Intensity Asymmetry

The beam charge asymmetry A_Q arises primarily due to small, opposite linear polarization components in the mostly-circular laser polarization state in the polarized source. These interact with analyzing power in beam transport, or with the analyzing power of the photocathode itself, to create an intensity asymmetry between polarization states in the electron beam. In addition, the electron beam intensity asymmetry can create differential space-charge effects while transiting the low-energy injector, resulting in small amounts of beam loss that can affect other properties of the electron beam such as position differences. For these reasons, A_Q is closely monitored and controlled using feedback.

The correction for A_Q relies on the responses of both the detectors and beam current monitors. The relative non-linearity between these systems is typically controlled at the 0.5% level. Given the goal of 0.1 ppb contributed error from intensity corrections, this implies that the grand average A_I must be smaller than 10 ppb. This level of control requires active feedback to the intensity asymmetry, which is a standard technique for parity-violation experiments [34]. MOLLER will use feedback techniques for both intensity and position differences that will promote faster convergence of statistical noise in the HCBA, as well as greatly reducing any systematic asymmetry.

For previous measurements, as listed in Tab. 6, the intensity asymmetry was controlled well within required limits of those experiments. Intensity jitter has not been found to be a limiting factor. The limits for control of the intensity asymmetry will be determined by feedback efficiency and data set selection. For example, CREX had a larger intensity asymmetry in Tab. 6 compared with Q_{weak} due to a specific choice, motivated by the improvement in statistical precision, to include data for which intensity feedback was not

active. For MOLLER, with a greater focus on this parameter, it is expected that current technology will be able to meet the MOLLER intensity asymmetry requirement. Similarly, it will be required that the feedback integration period matches that of production data collection. In previous runs, off-line analyses which included additional data relative to on-line analysis cuts showed biased A_Q values during recovery from every beam trip, resulting in marginally larger average A_Q values for the data set.

The beam for each experimental hall in simultaneous operation is produced by a separate laser, using the same polarization control optics and illuminating the same spot on the photocathode. During MOLLER, in addition to the measurement and control of A_Q for the MOLLER (Hall A) beam, the net beam asymmetry off the photo-cathode will monitored and controlled. This will prevent asymmetric effects from the photo-cathode or in beam transport induced by large asymmetries in the other beams. Intensity control on each laser system will be used to control the helicity-asymmetry on each beam independently.

3.2.3 Position and Angle Differences

Beam Property	Assumed Sensitivity	Accuracy of Correction	Required 1 kHz random fluctuations	Required cumulative helicity-correlation	Systematic contribution
Intensity	1 ppb / ppb	$\sim$1%	$<$ 1000 ppm	$<$ 10 ppb	$\sim$ 0.1 ppb
Energy	-0.7 ppb / ppb	$\sim$5%	$<$ 110 ppm	$<$ 1.4 ppb	$\sim$ 0.05 ppb
Position	1.7 ppb / nm	$\sim$5%	$<$ 50 μm	$<$ 0.6 nm	$\sim$ 0.05 ppb
Angle	8.5 ppb / nrad	$\sim$5%	$<$ 10 μrad	$<$ 0.12 nrad	$\sim$ 0.05 ppb
Spot Size	0.012 ppb / ppm	-	-	$<$ 10 ppm	$\sim$ 0.1 ppb

Table 7: *MOLLER goals for corrections for helicity correlated electron beam asymmetries and beam noise. The position and angle sensitivities in this table are lowered compared with the single segment sensitivity estimate, gaining a factor of 10 in suppression in sensitivity by averaging over azimuthal segments.*

Averaged over the entire data collection period, the beam trajectory must remain unchanged on average with respect to the sign of the electron beam polarization at the sub-nanometer level in order to keep beam-related false asymmetry corrections at the 1 ppb level. The beam requirements on the cumulative average position and angle differences shown in Tab. 7 are arrived at by considering the sensitivities of A_{PV} to each beam parameter, the precision with which each sensitivity can reasonably be expected to be measured, and the resulting contribution to a beam-related false asymmetry. Beam position and angle differences must remain at the sub-nm and sub-nrad level. Due to the limited precision of control mechanisms, these parameters have typically been the most significant challenge for meeting beam requirements for parity-violation measurements at Jefferson Lab.

Monte Carlo simulation was used to calculate the sensitivity of the apparatus to beam motion and to energy asymmetry. The results are consistent with simple estimates based on the design acceptance implied by the primary acceptance collimator (Collimator 2) and Møller differential cross-section. The detected Møller flux in one azimuthal segment will change by approximately 17.0 ppb for a 1 nm shift in the beam centroid, 85 ppb/nanoradian for beam angle, and -1.4 ppb/ppb for an energy asymmetry. The detector for the MOLLER experiment has seven segments and a high degree of azimuthal symmetry. The effect of this symmetry is conservatively estimated to be a factor of 10 reduction in sensitivity to beam trajectory. A reasonable goal for any measurement of a small asymmetry is to keep the cumulative correction due to random or helicity-correlated beam motion, averaged over the entire data set, to be no larger than the grand statistical error. Consistent with previous experience, these corrections will be made with a precision of better than 5%. The corresponding goals for HCBA and resulting systematic uncertainty expectations are summarized in Tab. 7.

Table 6 shows results sampled from the significant operational experience in using the polarized electron source for parity-violation experiments at Jefferson Lab. The control on beam parameter differences results from careful configuration of the polarized source, electron beam transport that takes advantage of adiabatic damping of trajectory differences (see Sect. 3.2.7), and slow helicity reversals (see Sect. 3.2.8). This experience, along with an improved understanding of the sources of HCBA in the polarized source laser optics [37] have led to a sophisticated protocol for systematically reducing or eliminating these effects.

The HAPPEX-II experiment made use of an early implementation of this protocol [35,36] to achieve run-averaged helicity-correlated position differences, measured in the experimental hall, which were consistent with zero systematic offset within the statistical convergence of random beam jitter. Further refinements of the configuration technique [41] let to a configuration of the laser optics of the polarized source that provided position differences in the injector that were smaller than those during HAPPEX-II by about a factor of two. While Q_{weak} did not take advantage of adiabatic damping, it utilized a slow feedback technique to meet its goals for control of beam position differences [42].

PREX-2 utilized the new RTP Pockels cell system, which allows the use of electric field gradients to counteract crystal non-uniformities, to optimize the beam trajectory differences [37]. This is illustrated in Fig. 6, which shows position differences measured at various beam position monitors through the injector during the source optimization studies. This tight control of position differences at the low-energy front-end of the machine represents the best control yet achieved at JLab. As with HAPPEX-II, the beam parameter difference measured in the hall during PREX-2 were consistent with zero within the expected convergence of beam noise.

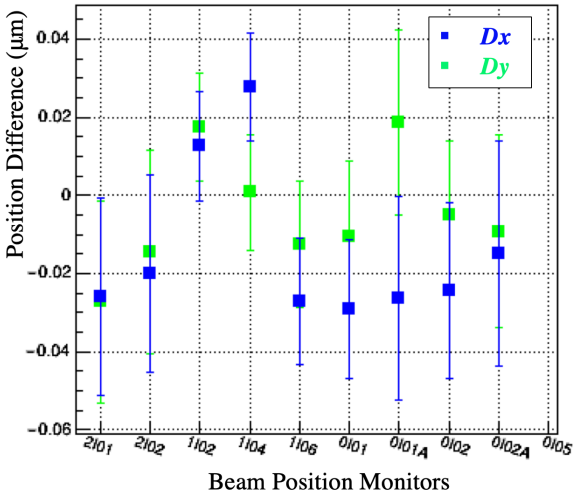

Figure 6: *Position differences in nanometers (vertical axis) measured at various beam position monitors in the injector (horizontal axis) during beam studies leading up to source configuration for the PREX-2 experiment in 2019.*

To achieve the required beam asymmetries, MOLLER aims to use the RTP Pockels cell to minimize beam position differences in the injector at the 20nm level. In addition, consistent with past experience, it is expected that cancellations via slow reversals will further suppress the remaining trajectory differences by a factor of 10. The collaboration also aims for a factor of 100 for suppression of position differences from adiabatic damping. Additionally, MOLLER will use feedback techniques on position differences that will promote faster convergence of statistical noise in the HCBA, as well as greatly reducing any systematic

asymmetry. Taken together, this estimated performance provides a margin of more than a factor of 10 for achieving the trajectory and energy HCBA requirements for MOLLER.

3.2.4 Beam jitter

The small run-averaged requirements on the beam asymmetries arise from the stringent goal for the accuracy of beam corrections. The high precision demand is achieved by integrating measured beam asymmetries over long periods of time. However, the precision is statistically limited by noise (or "jitter") in the intensity or trajectory of the beam, which obscures the true systematic asymmetry generated at the polarized source. Of importance for the precision of the experiment is imposing limits on the statistical noise in beam asymmetries, through optical configuration and fast feedback techniques, or by employing feedback to cause beam asymmetries to converge faster.

The expected precision of the calibration of corrections for beam parameters imposes requirements on the random noise (jitter) that can be tolerated. The additional random noise contribution after correcting for beam jitter should be no larger than 10% of the counting statistics width for a single azimuthal element of the detector and no larger than 7ppm for the combined detector elements [2]. These beam jitter goals are shown in Tab. 8. These jitter requirements will be achieved assuming that the beam jitter properties are similar for the 12 GeV upgraded machine as for 6 GeV operations [3]. To keep the energy noise low, as measured by the beam position monitor located in the most dispersive portion of the MOLLER beamline, the Hall A fast feedback system for position and energy lock on target will be employed, as was done during PREX-2 and CREX.

If noise in a beam parameter is large, then the statistical convergence of beam noise is likely to lead to an average asymmetry that is outside of specification, even if there is no true helicity-correlated systematic difference in the production of the beam. In this case, feedback on the measured beam asymmetry is required to drive the convergence faster than statistical convergence. It is expected that MOLLER will use feedback techniques for both intensity and position differences that will promote faster convergence of statistical noise in the HCBA, as well as greatly reducing any systematic asymmetry as described in Sec 3.3.1.

Beam Property	Assumed Sensitivity	Accuracy of Correction	Required 1 kHz noise	1kHz Noise contribution	HCBA Goal	Uncertainty $RMS/\sqrt{N}$
Intensity	1 ppb / ppb	$\sim$1%	$<$ 1000 ppm	$<$ 10 ppm	$<$ 10 ppb	$\sim$ 5.8 ppb
Energy	-0.7 ppb / ppb	$\sim$5%	$<$ 110 ppm	4 ppm	$<$ 1.4 ppb	$\sim$ 0.6 ppb
Position	1.7 ppb / nm	$\sim$5%	$<$ 50 μm	4 ppm	$<$ 0.6 nm	$\sim$ 0.3nm
Angle	8.5 ppb / nrad	$\sim$ 5%	$<$ 10 μ rad	4 ppm	$<$ 0.12 nrad	$\sim$ 0.06nrad

Table 8: *MOLLER goals for electron beam noise. The position and angle sensitivities in this table are lowered compared with the single segment sensitivity estimate, gaining a factor of 10 in suppression in sensitivity by averaging over azimuthal segments. 344 PAC days are assumed in calculating $RMS/\sqrt{N}$ uncertainty.*

[2] The MOLLER goal is to keep beam-related corrections for each individual measurement to be no larger than the statistical uncertainty for that measurement. For the MOLLER 1.92 kHz flip rate, then complementary pairs are measured at 0.96 kHz, with a precision of about 90 ppm. A goal that greatly facilitates a number of diagnostic techniques is to further require that the beam-related corrections for each of the detector's segments are no larger than twice the statistical width of that individual segment, a width that will be around 200 ppm. As this goal does not take advantage of the azimuthal cancellation for position and angle sensitivities, it specifies a more strict requirement for beam trajectory noise than consideration of the grand averaged uncertainty.

[3] Some recent initial experience with 11 GeV beam in Hall A suggests that the beam jitter properties for 15 Hz window pairs are similar to the 6 GeV machine.

3.2.5 Spot-Size Asymmetry

The systematic error contribution from helicity-dependent variations in the beam spot size is expected to be bounded at the 0.1 ppb level. We have simulated the effect of a helicity-correlated difference in the beam spot-size, usually defined as the Gaussian width of the beam distribution σ, for the proposed spectrometer/collimator geometry. The sensitivity of the physics asymmetry to spot size asymmetry $\Delta\sigma/\sigma$ has been found to be at the level of (12 ppm)$\times\Delta\sigma/\sigma$, thereby determining the goal for spot-size asymmetry as 10^{-5} in order to bound the systematic error contribution to the desired 0.1 ppb. There is no existing technology for directly measuring electron beam spot size variation at this level. An upper limit on the helicity-correlated spot-size asymmetry will be demonstrated at the required 10^{-5} level via bounds from direct measurements on the laser beam, quantification of vacuum window and photo-cathode non-uniformity effects, the application and assessment of injector spin slow-reversals, and the addition of stochastic noise from synchrotron radiation [43].

The possible helicity-correlated spot-size asymmetry will be bounded on the laser beam, with a safety margin to account for reasonable models of photo-cathode non-uniformity, to be $< 10^{-4}$. The spin manipulation slow reversals would precisely reverse this effect, so a conservative order-of-magnitude suppression is expected to reach a bound of $< 10^{-5}$. Measurements from the configuration of the polarized source with the RTP cell for the PREX-2 experiment have already achieved this limit. This approach will be used again to achieve the required spot-size asymmetries for the MOLLER experiment ($< 5 \times 10^{-5}$). Since PREX-2 and CREX ran, the JLab vacuum window at the gun has been replaced with a window with improved uniformity. The window has been characterized under vacuum and its effect on the spot size asymmetry has been determined to be negligible at $< 2 \times 10^{-6}$ level when rough aligned to within 10° of the photocathode analyzing axis [4].

The slow-reversals (Sect. 3.2.8) are also an important component of this suppression, especially the injector spin manipulation and g - 2 reversals which will leave the configuration of the source laser optics untouched. The slow-reversals provide additional suppression beyond this, giving a safety margin. The symmetry of the vertical Wien flip and degree of suppression,performed prior to PREX-2 and CREX and illustrated in Fig. 8, demonstrated a high degree of symmetry between the spin states and excellent suppression.

Beyond the bound that will be achieved on the laser spot size asymmetry, there is an additional suppression of this effect for the MOLLER experiment due to the injection of stochastic noise through synchrotron radiation. This noise increases the normalized emittance of the beam but does so in a manner that is independent of the helicity-correlated asymmetries from the polarized source. The emittance in the hall at 11 GeV has been measured to be a factor of 10 times larger than the emittance measured before significant synchrotron emission.

This can be modeled as an addition of a width σ_s from synchrotron radiation to the original beam spot size in the injector σ_I :

$$\sigma = \sqrt{\sigma_I^2 + \sigma_s^2} \tag{9}$$

$$\delta\sigma = \sqrt{(\sigma_I + \delta\sigma_I)^2 + \sigma_s^2} - \sqrt{(\sigma_I - \delta\sigma_I)^2 + \sigma_s^2} \tag{10}$$

Because a helicity-correlated change in the spot-size has an effect that scales with the beam size, it is the spot-size asymmetry that matters. The spot size asymmetry in the hall compares to that in the injector as:

[4] With no alignment at all, the worst case vacuum window contribution to spot size asymmetry is $< 6 \times 10^{-6}$. With fine alignment of the vacuum window within $1\,\mathrm{deg}$ of the photocathode analyzing axis as was performed during HAPPEX, PREX-2 and CREX, the vacuum window contribution to spot size asymmetry is $< 6 \times 10^{-7}$

$$A_\sigma = \frac{\delta\sigma}{\sigma} = \left(\frac{\sigma_I}{\sigma_s}\right)^2 \frac{\delta\sigma_I}{\sigma_I} \tag{11}$$

The advantage of emittance growth through synchrotron emission is that the additional width is incoherent with the initial spot size asymmetry. For example, the raster on the experimental target does not similarly reduce A_σ, because it only transports the asymmetric spot side-to-side. By contrast, the incoherent synchrotron emission expands the emittance, reducing the impact of the different spot sizes in the initial state.

3.2.6 Asymmetric beam halo

The $Q_{\rm weak}$ experiment saw a false asymmetry that was ascribed to a helicity-correlated change in the beam distribution on target. This is often referred to as a "halo" effect. This false asymmetry was seen in three separate detector systems: the main detectors, large angle monitors near the primary beam, and bare PMTs placed out of the signal region but near the main detectors to test for ambient backgrounds. The ratio between the false asymmetry observed in each detector system was fairly constant throughout the run. While the consistency between the detector systems allowed for sufficient correction for the $Q_{\rm weak}$ result, the characteristics of the beam that led to this effect were never precisely determined. There was no clear evidence to tie this effect to a specific technical definition of "halo". Thus, there is not currently a halo requirement specified for MOLLER.

The MOLLER spectrometer by design, removes any "single bounce" path from the target or primary beam collimator to the Møller detectors, which should reduce sensitivity to similar beam effects. Similarly, the downstream beampipe and spectrometer components are well shielded from line of sight to the target by tight beam and acceptance collimation, and so the small amount of rescattering from other components will not be highly sensitive to halo. In addition, the high level of detector segmentation, with a wide range of signal rates over the azimuthal and radial distribution, would assist in diagnosing and monitoring any effect that does become manifest. While it is not yet possible to rule out a source of asymmetric halo for MOLLER, the experiment is designed to limit sensitivity while providing improved diagnostics. The experiment will have similar detectors as the $Q_{\rm weak}$ experiment (large angle monitors and diffuse beam monitors) to monitor for such effects. These are described further in Section 9.3

3.2.7 Adiabatic Damping

The impact of helicity-correlated spatial variation in the beam, both position differences and spot size asymmetries, can be greatly reduced in the accelerated beam impinging on the target due to the process of adiabatic damping. A simple consequence of relativistic mechanics is that the available transverse phase space for a beam that has been adiabatically accelerated to a momentum p from a momentum p_0 is reduced by a factor of $\sqrt{p/p_0}$. For example, HAPPEX-II ran with a 3 GeV beam energy, which should correspond to a reduction in beam motion relative to the 100 keV source by a factor of ~ 95, compared to motion of the 100 keV injector beam.

While the damping of transverse motion is a simple consequence of the relativistic boost, an optics tune that deviates from design can produce significant correlations in phase space which can magnify helicity-correlated differences in the beam trajectory. Getting close to the theoretical limit requires detailed diagnostics and careful configuration of the beam optics to maintain a match with the design parameters. The best performance from the HAPPEX-II experiment suggested that helicity-correlated variations were suppressed by factors up to ~ 30 (compared to the theoretical maximum of 95), while results from PREX-2 and CREX were near a factor of 10 (compared to the 50x or 80x, respectively).

While it is not expected that the benefits of this effect will be fully realized, it is expected that the level of adiabatic damping will be routinely quantified and kept at a moderate level approaching two orders of magnitude (compared to the maximum of 150x). The collaboration typically works closely with accelerator physicists to produce the best results and maintain them over the duration of data collection. The level of suppression from adiabatic damping within the injector can be efficiently and routinely measured using the RTP cell's ability to generate large position differences at the source. When used in conjunction with the helicity magnets, the level of adiabatic damping between the injector and experimental Hall can also be assessed routinely, as was done during the PREX-2 and CREX experiments.

3.2.8 Slow reversals

It will be necessary to use a "slow reversal" of beam helicity to further cancel systematic errors to the 0.1 ppb level, achieving the parameters listed in Tab. 5, as well as reducing sensitivity from sources such as residual electronics crosstalk and higher-order effects such as potential helicity-dependent variations in the beam spot size. There will be several "slow reversals" for the asymmetry measurement. These change the polarization state in the hall relative to the recorded helicity and relative to the voltage applied to the Pockels cell. Three methods will be used: an insertable half-wave plate in the laser optics of the polarized source, spin manipulation with the Wien filter and solenoids in the electron beamline in the low-energy region of the injector, and a small change in the beam energy which changes the g - 2 spin precession between the injector and the experimental hall by a half-integer rotation. The quoted goals for the run-averaged HCBA are assumed to be averaged over data sets using the slow-reversals, which will further suppress any systematic asymmetries generated in the polarized source.

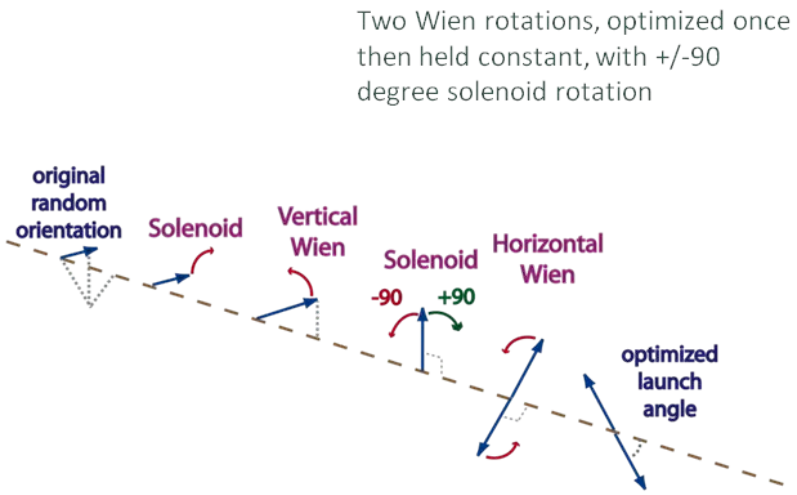

Figure 7: *Schematic of the concept of the "Double-Wien" filter, which allows a full "slow" flip of the electron beam polarization with minimal disruption to the front end electron beam trajectory. The flip is accomplished by adjusting the second solenoid, without changing the settings of the two Wien rotators.*

Insertable Half-Wave Plate Reversal: A half-wave plate can be remotely moved into or out of the laser path, to reverse the sign of laser polarization relative to the voltage applied to the Pockels cell. It is expected that IHWP reversals will occur during MOLLER on the time scale of about a day, depending on beam efficiency. This type of slow-reversal is effective for canceling false asymmetries which are unaffected

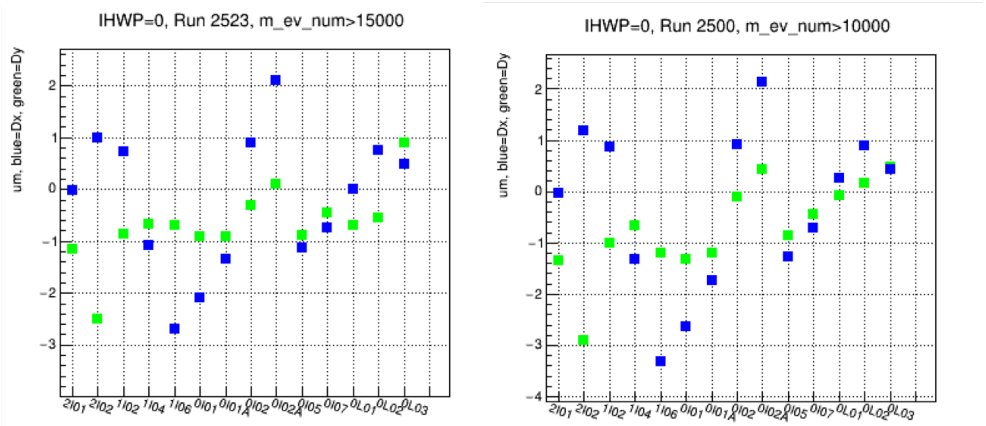

Figure 8: *Measurements through the injector of large position differences induced for this calibration by RTP setpoints. Left and right panels compare the "FlipLeft" and "FlipRight" configurations of the double-Wien rotator during configuration studies for PREX-2. The excellent comparison demonstrates that the beam trajectory remains the same even under this* 180° *spin precession.*

by the IHWP insertion, i.e. which do not change sign while the physics asymmetry does change sign. Two specific models for such asymmetries are any false asymmetry related to electronic signals, such as pickup from the helicity logic or Pockels cell high voltage, or Pockels cell induced steering or focusing of the laser beam [37]. Commonly, the more significant sources of HCBAs, however, are explicitly related to helicity-dependent residual linear polarization. Most of these effects will change sign with the insertion of the half-wave plate just at the physics asymmetry does, and hence are not canceled using this reversal technique. For this reason, other methods of slow-helicity reversal will also be required during MOLLER.

g-2 Reversal: At 11 GeV, the total number of $g-2$ spin rotations will be large, on the order of 120π. It will be possible to change the orientation of spin polarization at the experimental target, while maintaining very similar beam optics properties, by changing the energy of the accelerator by about 100 MeV. This interval is small enough to not require invasive reconfiguration of the experiment: backgrounds, spectrometer optics, etc. will remain very similar. This type of reversal is expected to be very effective in that all sources of HCBAs will be reversed under this operation. However, since this method is disruptive to other halls, MOLLER expects to only employ a $g-2$ reversal a few times over the duration of the entire run.

Wien Reversal: A similarly effective slow reversal that can be used much more often than the $g-2$ reversal is the so-called "Wien" reversal, created using spin manipulation in the injector. Rotation in the injector provides a method for a suitably precise "helicity flip" which does not interfere with the beam profile or mechanisms which might lead to a spot size asymmetry or other helicity-correlated beam asymmetries. The Wien rotators in the low-energy CEBAF injector use spin precession in crossed $\vec{E} \times \vec{B}$ fields to align the electron polarization into the horizontal plane, and then to set the in-plane launch angle to optimize longitudinal polarization at the experimental target. In principle, it is possible to apply a half-cycle spin rotation using a single Wien rotator, however, in practice this is complicated by large differences in the focusing effects of the Wien at the different setpoints. For this reason, additional spin manipulation hardware has been added to the CEBAF injector to provide more dynamic range. The double-Wien system in the injector will be used to provide this helicity flip, as well as make the regular small corrections to the spin launch angle to preserve a minimized transverse polarization for the MOLLER measurement. The "Double-Wien" rotator (shown schematically in Fig. 7) uses a second Wien rotator and a solenoid to provide a full 180° spin precession through the injector. This system was commissioned prior to the original PREX run in 2010, and it was used routinely during the Q_{weak}, PREX-2, and CREX experiments. The operation of

reversing the Vertical Wien in Fig. 7) during PREX-2 produced a slow spin flip with negligible changes to the trajectory in the injector, as demonstrated in Fig. 8. MOLLER intends to use this reversal weekly. With the upgrade to a 200 keV electron gun voltage, the Wien rotators also required an upgrade to maintain the required dynamic range. New Wien elements have been tested and will be installed in Phase II of the injector upgrade.

It is expected that cancellations in HCBAs via employing these 3 methods of slow reversals will further suppress position differences and spot size asymmetries by a factor of 10 during MOLLER. The degree of slow reversal cancellations as characterized by the symmetry of the slow reversals will be measured using the RTP Pockels cell or the Helicity Magnets, which are each capable of generating large position differences at the source or in the injector that will subsequently be measured and tracked throughout the injector and experimental hall. MOLLER expects to perform periodic dedicated (potentially efficiently automated) measurements of beam transport, which will demonstrate the effectiveness of each type of reversal, characterize beam optics for adiabatic damping, and update the correction slopes for feedback on position differences.

3.3 Beam Control

3.3.1 Feedback

MOLLER expects to perform feedback upon the measured intensity asymmetries and position differences and promote faster convergence of statistical noise in the HCBA, as well as greatly reducing any systematic asymmetry. Direct feedback on the measured beam asymmetry drives the convergence faster than statistical convergence. This technique has been employed for control of charge asymmetry for every high-precision parity-violating electron scattering measurement.

The beam charge asymmetry, A_Q, is controlled using active feedback in which small changes to the voltage setpoints for the source Pockels cell are used to minimize the charge asymmetry in the hall. MOLLER will also require feedback mechanisms to control the helicity-correlated charge asymmetry of the Hall B and Hall D lasers (measured before the slit) and the Hall C laser. This will be accomplished using the so-called IA (Intensity Asymmetry) systems in the polarized source. These setpoints will require periodic updates to maintain low asymmetries on the low-current Halls B and C, while automated feedback on the Hall C A_Q measured in the experimental hall will be possible. This technique has been applied in previous high precision parity runs such as PREX-2 and Q_{weak}.

For position difference control, there are both optical (RTP Pockels cell) and electrical (helicity magnets) devices in the low-energy portion of the injector which can change the electron beam trajectory. Active feedback using either mechanism is possible. The RTP Pockels system was tested for automated feedback during the configuration of the PREX-2 experiment and the helicity magnet system was used for feedback during Q_{weak}. Both systems will be available for use during MOLLER. The dynamic range and independence for position and angle of the helicity magnets will be best suited for feedback on measurements in the experimental hall, while the RTP will be best suited to periodic updates using dedicated measurements of the Hall A beam alone in the injector.

In addition to performing active feedback upon measured beam asymmetries, MOLLER will also employ the standard Hall A fast-feedback system to reduce beam fluctuations and noise at high frequencies. This system is not coherent with helicity and is optimized for reducing noise in power-line harmonics. This noise control is particularly important for the beam energy monitor, a beam position monitor located in the dispersive portion of the Hall A beamline.

3.3.2 Beam Modulation System

To obtain the small uncertainties in beam corrections required for MOLLER, it is not only important to minimize HCBAs, but it is also equally important to minimize the uncertainty in the sensitivities which

relate beam parameters to measured asymmetry. These sensitivities, denoted by the α_i in Eq. 8, and the uncertainty with which they are measured, determine the precision with which beam corrections can be made. In previous parity experiments, these beam sensitivities have been precisely measured using the beam modulation system.

The beam modulation system's purpose is to measure the response of the main detectors to variations in beam position, angle, and energy. Air core steering coils in the Hall A beamline will be used to modulate beam position and angle, and an energy cavity in the linac is used to modulate energy.

The successful use of the beam modulation system requires that the modulation magnets can span the position/angle phase space of the beam, which is an important constraint on the beamline optics design. It is also necessary to "pause" position lock and energy lock during these modulation periods. This calibration cycle will be run every few minutes during data taking, with a total duty cycle between 5-15%. This system has been employed for all recent high precision measurements, most recently PREX-2 and $Q_{\rm weak}$.

3.3.3 Transverse Beam Polarization Control

MOLLER is highly sensitive to components of transverse polarization as described in detail in Sect. 7.2. The plan to control the degree of transverse polarization P_T consists of an initial setup with an accuracy of 1° followed by regular daily corrections for both vertical and horizontal transverse polarization. These polarization components will be continually monitored in the experimental hall by measuring the transverse scattering asymmetry with an accuracy of well below 1° within a few hours. A "manual" feedback loop will be used to make small tweaks to the launch angle ($< 1^\circ$) of the electron beam polarization with the injector Wien rotator. These corrections for drifts are envisioned to occur daily during regular running, or in a shorter time scale every few hours after any significant linac energy rebalancing. We expect the use of this feedback technique will suppress the transverse polarization well below the initial setup accuracy.

3.4 Beam Monitoring

The physics goal of the MOLLER experiment requires precise measurement and control of the electron beam properties. The systems in this category are needed to properly measure and correct for helicity-correlated beam properties and to characterize beam properties (such as beam halo) that could lead to potentially irreducible backgrounds from scattered beam interacting downstream of the target.

The scattered flux is integrated over the duration ($\sim 520\mu s$) of each helicity window. Eq. 8 shows how one then extracts a signal proportional to the raw cross-section asymmetry by removing correlations of the scattered flux with beam properties. Uncertainties are introduced in this correction procedure due to the precision limits of measuring the beam properties and of determining the correlation coefficients of the scattered flux with beam properties. In this section, we describe the requirements to ensure that these uncertainty contributions to our random noise width (Tab. 8) and systematic errors (Tab. 7) can be achieved.

3.4.1 Position and Intensity Monitoring Requirements

The so-called "standard" HCBA have traditionally been quoted as the zeroth and first moment of the asymmetry in the beam intensity profile in the experimental hall. These are measured by RF monitors, typically using cavity monitors for intensity and strip-line monitors for position. Using these monitors, the relative [5] beam intensity changes will be measured with a resolution of $\lesssim 10$ ppm for 960 Hz window-pairs. The relative beam position changes will be measured with a resolution of $\lesssim 3$ μm for 960 Hz window-pairs at

[5] To perform the correction procedure, relative changes (not absolute values) of the beam properties between adjacent helicity windows ("window-pairs") need to be measured with specified precision ("resolution").

two locations separated by ~ 10 m (to determine projected position and angle at the target) and at a point of high (> 3 m) dispersion (to determine the beam energy).

3.4.2 Beam Position Monitor Resolution

The most stringent requirement on beam position monitor resolution comes from requiring that the additional random noise contribution from beam jitter (after correction for it) be no larger than 10% of the counting statistics width for a single azimuthal element of the detector. This leads to a more stringent requirement than applying the same criterion to the average over all detectors. This is important for two reasons. It allows for high precision comparison among selected combinations of the azimuthal detector elements to study the behavior of the linear regression corrections. It also ensures the precision necessary to measure the azimuthal dependence of the raw detector asymmetries for the "manual" feedback loop to control transverse polarization described in Section 7.2. Applying this criterion leads to the requirement stated above on the beam position monitor measurement resolution: 3 μm for 960 Hz window-pairs.

The standard beam position monitors at JLab are referred to as thin wire "stripline" monitors [44, 45], which consist of four thin wires operating in a quarter-wavelength antenna mode. The $Q_{\rm weak}$ experiment has measured the beam position monitor resolution for 960 Hz quartets for these types of monitors. The study [46] was done versus beam current and the results are shown in Fig. 9. For MOLLER beam currents, typical resolutions of ~ 1.3 μm are found. Taking the conservative assumption that the monitor noise is dominated by white noise[6], the scaling from quartets to pairs and the scaling from 480 Hz pairs to 960 Hz pairs can be estimated as two factors of $\sqrt{2}$. This results in an estimated 2.6 μm resolution for 960 Hz pairs for MOLLER, which achieves the MOLLER goal of 3 μm. It is also planned that redundant beam position measurements with a similar resolution will be performed with radio frequency microwave cavity monitors operating in the TM_{110} mode at 1497 MHz that are installed in the Hall A beamline. These have been used during parity-violation experiments running in Hall A, during which performance comparable to stripline monitors has been demonstrated.

3.4.3 Beam Charge Monitor Resolution

The MOLLER requirement is 10 ppm resolution for relative beam intensity measurements for 960 Hz window-pairs, in order to keep this contribution to the random noise small compared to the counting statistics contribution. As described below, the existing beam current monitor (BCM) instrumentation is close but not fully sufficient to meet this goal. The best values achieved to date are reported, and progress toward improving the instrumentation is described.

The best BCM resolution achieved during an experiment was for the $Q_{\rm weak}$measurement, which used BCMs consisting of the standard JLab hardware of resonant microwave cavities operating in the TM_{010} mode. The best results were obtained with all-digital receiver electronics designed at JLab [47]. The random noise in the beam charge measurement was determined by forming the "double-difference", which is the difference between the helicity-correlated charge asymmetry for two BCMs. The RMS of this distribution determines the uncorrelated random noise of the charge measurement, referred to as the resolution. A typical value of this RMS during regular $Q_{\rm weak}$ running at a beam current of 180 μA was ~ 62 ppm.

To facilitate improvements, dedicated bench tests with these digital receivers were done with a $Q_{\rm weak}$ data acquisition test stand, with the beam signal replaced with a radio-frequency source signal. A more detailed description of these studies is in [48], but here we discuss the main conclusions. A study versus

[6] Operational experience with the stripline BPMs during the PREX-II experiment at $70\mu A$, similar to Qweak, with 240Hz octets (an equivalent of 30Hz) showed resolutions for different BPMs of > 0.5 μm. Scaling by $\sqrt{f}$ would have implied at that Qweak would have seen $> \sqrt{8} \times 0.5\mu m = 1.4\mu m$ at 480Hz quartets. But Qweak saw $1.3\mu m$ so the $\sqrt{f}$ scaling is a conservative assumption

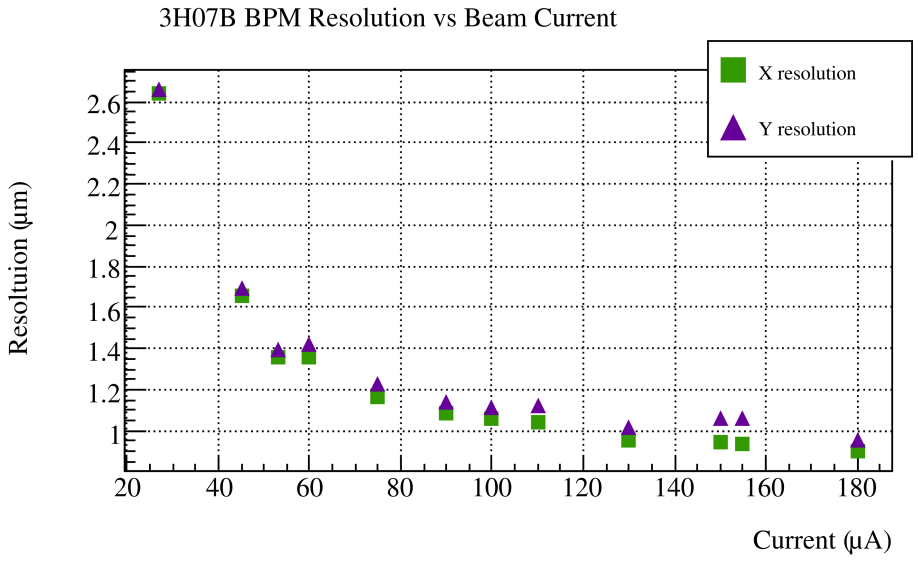

Figure 9: *Measurements of beam position monitor resolution as a function of beam current during the $Q_{\rm weak}$ experiment [46]. See text for further details.*

data-taking frequency is shown in Fig. 10. The observed value at the $Q_{\rm weak}$ 240 Hz quartet frequency of 62 ppm agrees with what $Q_{\rm weak}$ observed with beam. At double that frequency, corresponding to the MOLLER data-taking frequency of 1.92 kHz, a lower value of 42 ppm was observed. That implies a resolution of 42 ppm for 960 Hz window-pairs[7]. As shown below, the MOLLER beamline will be equipped with seven BCMs, so brute force averaging of those seven, making the assumption of uncorrelated noise, would lead to 42 ppm/$\sqrt{7} \sim 16$ ppm, close to the MOLLER goal[8]. However, this limits flexibility in doing systematic studies among the monitors, so ideally the resolution of an individual monitor would be improved further.

The bench studies reported in [48] strongly suggest that the beam current independent noise floor observed for the digital receiver electronics is limited by phase and amplitude noise in the 1.5 GHz local oscillator that is mixed with the incoming signal in the receiver electronics.

An upgraded version of the aforementioned digital receivers has been developed. Among various changes, a different local oscillator was employed. Initial bench tests with these receivers for $Q_{\rm weak}$ running parameters gave a factor of two smaller double-difference, about 32 ppm. That would bring the brute-force averaged result quoted above down below the MOLLER goal of 10 ppm. The signal from the microwave cavity monitors in Hall A is typically split between two independent readout chains. This allows for testing digital receiver modifications with beam, parasitically during other experiments in Hall A or in dedicated beam tests during upcoming running periods.

The LBNL Digital Receiver : An all-digital beam processor is being independently pursued by collaborators at UC Berkeley and Lawrence Berkeley National Lab. This development makes use of a high sampling rate ($\gtrsim$ 3 Gsps) and high dynamic range (14-bit) ADCs that are capable of direct RF sampling, thus elimi-

[7]This conclusion assumes white noise spectrum, so that the $1/\sqrt{2}$ conversion from the double-difference width to resolution cancels with a factor of $\sqrt{2}$ to convert from quartets to pairs.

[8]This BCM noise above the goal would imply a pair width of 91.5 ppm, compared to the goal of 91 ppm discussed in Sect. 2. Additionally, there are ongoing efforts at LBNL to design a single BCM with higher resolution

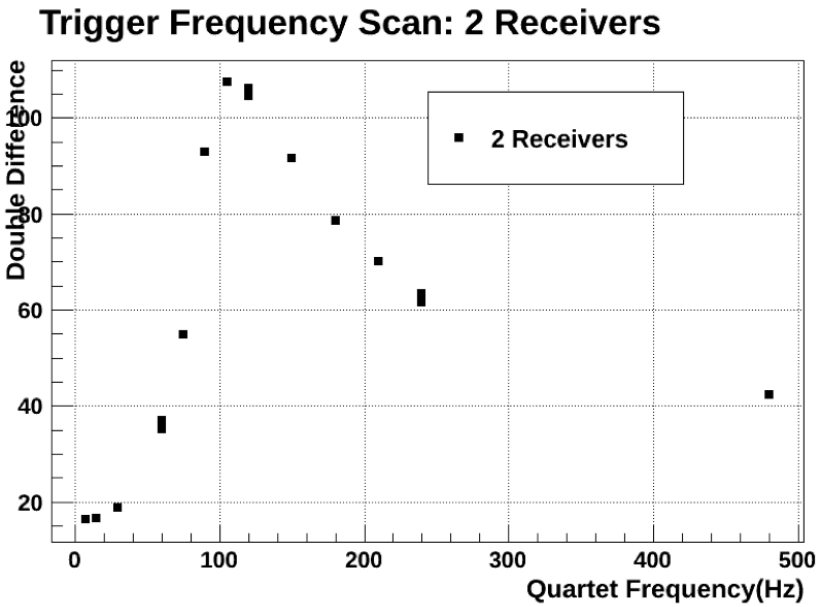

Figure 10: *Bench study of Q_{weak} digital receivers with two receivers and a common RF source to simulate the beam signal. The observed double difference versus quartet frequency is shown.*

nating the need for the local oscillator. Such a direct-sampling RF receiver has been recently developed and tested with Hall A beam during the CREX experiment in 2020.

The results of the direct RF sampling receiver development and beam tests have been reported in [49]. A novel, fully digital microwave processor, based on a commercial 3 Gsps, 14-bit digitizer was developed. Recent advances in digital electronics, both in fast digitizers with high dynamic range and advanced Field-Programmable Gate-Arrays (FPGA) specialized for digital signal processing enable direct signal processing at the JLab 1.5 GHz carrier frequency in the digital domain. The receiver digitizes the cavity signal directly (after appropriate amplification and bandpass filtering), applies a digital filter to the digitized waveform, performs digital down-conversion (DDC) of the waveform, measures the amplitude and phase of the signal for each helicity window, coverts them to charge, and sends the output data to the data acquisition system. In this direct RF sampling scheme, the local oscillator amplitude noise does not contribute to the resolution of the signal processor, and the local oscillator phase noise can be very small. The receiver consists of three main components: an RF front-end that brings the signal to an appropriate amplitude and preliminarily rejects out-of-band signal contributions, noise and interference; an analog-to-digital converter (ADC) system that directly digitizes the RF signal; and an FPGA that processes the data and transmits the pre-processed data to a commodity server for further analysis. A schematic of the signal path from the cavities to the receiver in the setup at Jefferson Lab and a top-view photograph of the receiver with the key components labeled are shown in Fig. 11.

The RF receiver was initially characterized in bench tests by injecting known signals from signal generators. The results for the double-difference of 960 Hz window-pairs are shown in Fig. 12. The resulting double-difference width of 8 ppm is below the goal of 10 ppm. In September 2020, the RF receiver was installed in the Hall A counting house at Jefferson Lab and recorded actual beam-induced RF signals during the CREX experiment. The signals were taken from two TM_{010} mode cavities that were part of beam position monitor (BPM) triplet systems. Results for the double-difference between the two cavity signals as a function of the integration window size are shown in Fig. 12. For the two cavity results, the observed

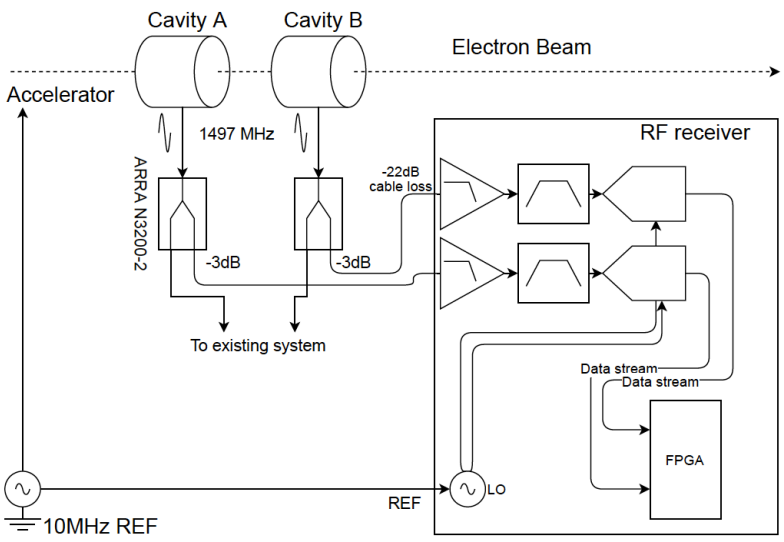

(a) RF Signal Processing Chain Block Schematic

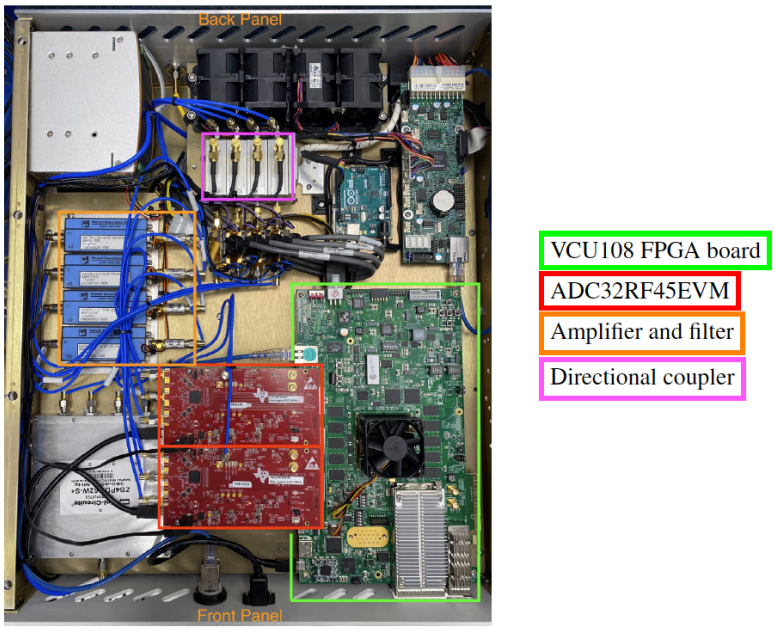

(b) Top View of the Digital Receiver

Figure 11: *The block schematic of the RF signal processing chain from the beam cavity to the receiver is shown in (a). The signal and data flow inside the receiver is also shown. Four identical channels were actually implemented in the built device but only two are shown for clarity. The top view of the digital receiver is shown in (b). The locations of the ADC, FPGA, amplifier/filter, and directional coupler are highlighted.*

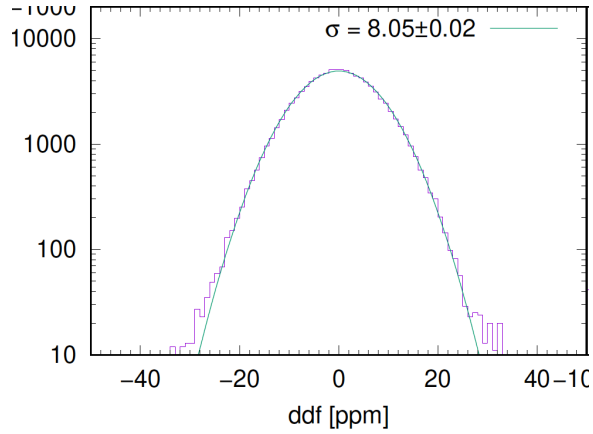

(a) Double-difference in Bench Test

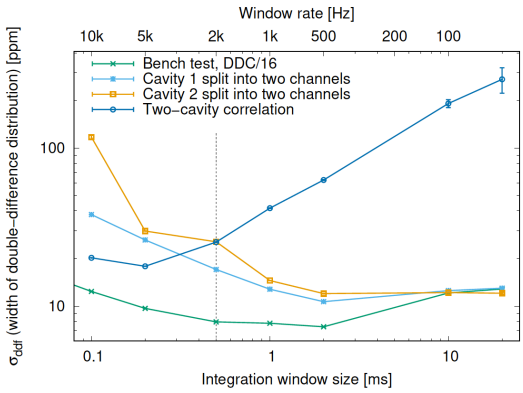

(b) Double-difference in Beam Test

Figure 12: *The double-difference distribution in a bench test is shown in (a). The test was performed with a signal generator output split and connected to two ADC channels via a passive RF power splitter. Results for the double-difference distribution between two microwave cavity monitor outputs in the Jefferson Lab beam versus integration window size are shown in (b).*

double-difference width was 25 ppm for the integration window size corresponding to 960 Hz window pairs. This is higher than the result seen in the bench tests, but the behavior of the double-difference with bandwidth indicates that this additional noise is inconsistent with phase noise in the RF receiver. This additional noise thus appears to be beam-related and not intrinsic to the measurement resolution of the RF receiver. This additional source of noise will be further investigated in subsequent beam measurements at Jefferson Lab.

3.4.4 Monitors During Low Current Running

For the counting mode measurements using the tracking system that are described in Section 8.2, the beam current will be reduced by many orders of magnitude relative to the expected production running current of 65 μA. Beam currents in the range of 1 - 100 nA are anticipated. As described in the MOLLER Beamline section below, the beamline will have two microwave cavity "triplet" boxes. Each of these has two cavity monitors operating in the TM_{110} mode at 1497 MHz to perform beam position measurements in two orthogonal orientations and a third cavity in the TM_{010} for beam charge measurements. These have been demonstrated in Hall A running to reliably provide adequate beam current and position monitoring down to 10 nA. For lower beam currents, the Q_{weak} experiment successfully monitored beam current and position down to a beam current of 100 pA through a combination of periodic superharp scans (with small charged particle detectors for monitoring) and relative position and charge measurements using small angle monitors, further described in Sect. 9.

3.4.5 Beam Halo Monitor

As described in the MOLLER beamline section below, the beamline will be instrumented with a halo target that can be used to characterize any part of the beam profile that extends well beyond the core of the beam. The 1 mm thick aluminum target is mounted on a superharp-type fixture that allows it to be moved vertically in the path of the beam. Small Lucite detectors mounted downstream of the target are used to monitor scattering from the halo target when it is in use. The target will have a rectangular hole to allow for a well-

defined invasive characterization of the halo, and a larger circular hole that could be used if desired during production running to allow for easier detection of any halo that is present. Such a system was used during the $Q_{\rm weak}$ experiment [32], and it was capable of determining the halo fraction to a precision of 2×10^{-8} at 180 μA beam current.

3.4.6 MOLLER Beamline

A reference design for the MOLLER beamline in Hall A has been developed [50] [51] [40]. It largely uses existing instrumentation with modifications to the beam line needed to satisfy the MOLLER requirements. The layout is shown in Fig. 13. Complete details of the design can be found in the tech note, but we summarize some of the highlights here. A major feature of this design is that the six Møller polarimeter magnets are completely degaussed so they act as a beam drift during normal beam transport. The fast raster is thus downstream of the last focusing element. [48]

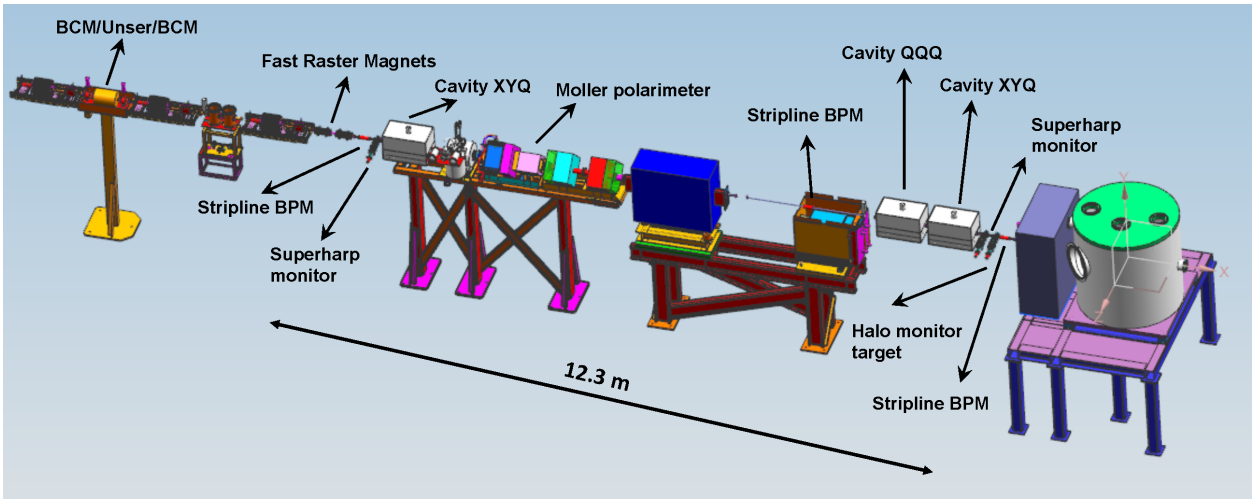

Figure 13: *Reference design of the MOLLER beam line.*

Major elements of this design, from upstream to downstream in Fig. 13 include [48]:

- Quadrupole and corrector magnets, for position lock at both the Møller polarimeter and MOLLER experiment targets
- The existing BCM/Unser/BCM combination, moved ~ 4 m upstream of its current location
- The fast raster, moved ~ 3 m downstream of its current location, with only two of the coils used
- A short 1.6 meter diagnostic girder, with a stripline beam position monitors (BPMs), microwave cavity XYQ box, and a superharp beam profile monitor
- The Møller polarimeter, unmoved from its current location, but with fully degaussed quadrupoles and dipole during production running
- A 4 meter diagnostic girder including a stripline BPM, a microwave cavity XYQ box, a microwave cavity QQQ box (three BCMs), a superharp beam profile monitor, and a superharp drive with a halo hole target in it that can be used to monitor beam halo with simple downstream Lucite based counters (as was done during $Q_{\rm weak}$)
- The MOLLER target.

In terms of the critical instrumentation for measuring MOLLER beam properties, this design has redundant position and angle measurements with stripline and microwave cavity beam position monitors (BPMs) separated by > 10 m to ensure good angular resolution. It also has a total of seven BCMs, with two upstream of the fast raster and five downstream. The OptiMX code was used to determine the beam optical properties of this configuration [50] [51] [40]. Figure 14 shows the beam size in X and Y along the beamline. The intrinsic spot size sigma at the MOLLER target is ~ 150 μm in both dimensions. The largest spot size sigma is ~ 340 μm, and it occurs in a region with a 22 mm ID beam pipe. Figure 15 shows the raster response, with the desired half-size of 2.5 cm at the MOLLER target. Finally, Fig. 16 shows that the phase advance between the beam modulation coils and the beam position monitors is adequate ($> \pi/6$) to ensure that the full phase space of position and angle motions can be probed [48].

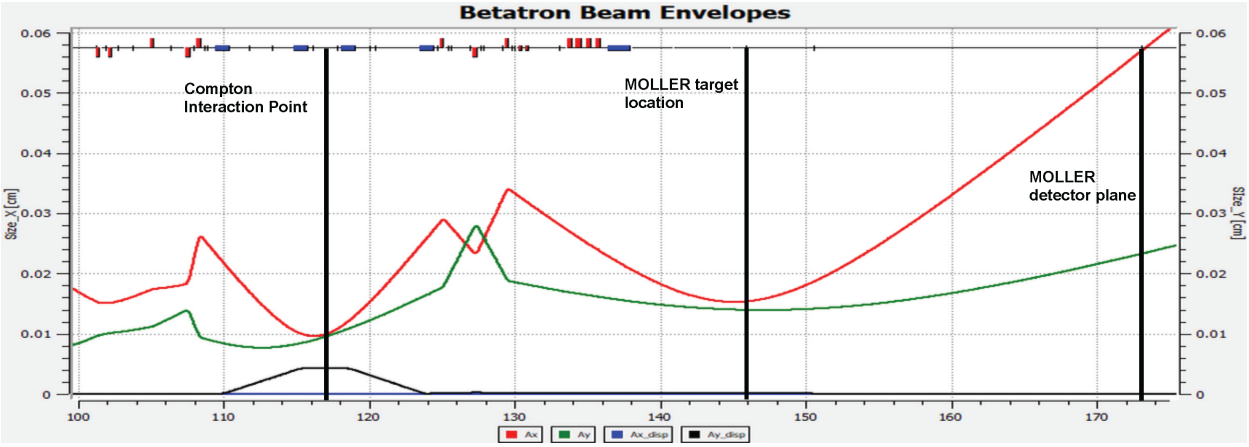

Figure 14: *Reference design betatron envelopes. The red trace is X and the green trace is Y. The x axis is the location along the beamline in meters. The location of the MOLLER target and detector plane are indicated by vertical lines.*

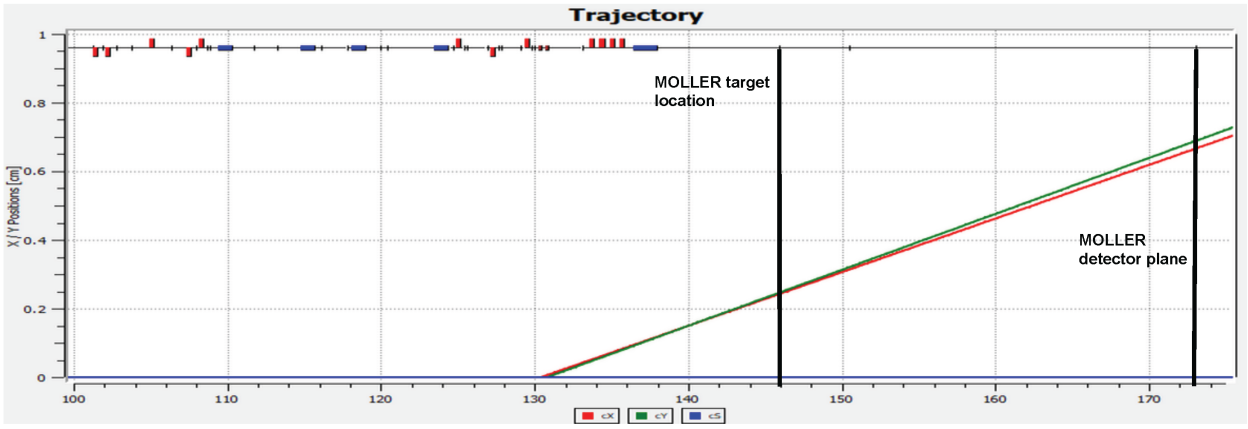

Figure 15: *Reference design raster response. The x axis is the location along the beamline in meters. The y axis is the half-size of the rastered beam. The location of the MOLLER target and detector plane are indicated by vertical lines.*

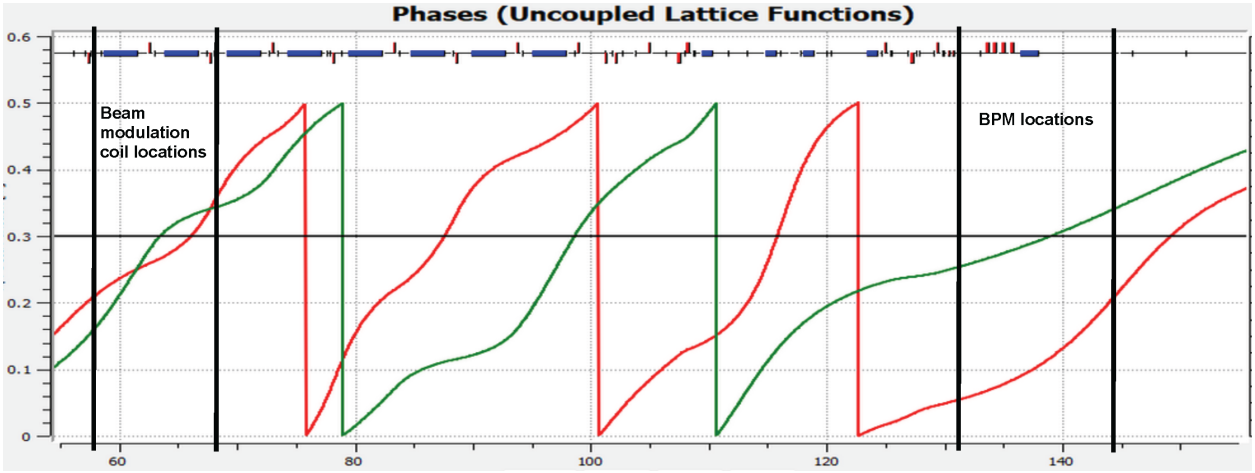

Figure 16: *Reference design phase advance. The units of the left axis are 1.0 = 2π. The two vertical lines on the left represent the location of air core correctors in the beam modulation system, with an XY pair at each location. The two vertical lines at the right show the locations of beam position monitors. The red trace is X and the green trace is Y. The phase advance between the modulation coils and the beam position monitors for both X and Y is adequate ($> \pi/6$) to ensure that the full phase space of position and angle motions can be probed.*

4 Target System

4.1 Definitions

Definitions and Acronyms used in this chapter.

AHJ Authority Having Jurisdiction
AISC American Institute of Steel Construction
ASD Allowable Stress Design
ASME American Society of Mechanical Engineers
AWS American Welding Society
BPVC ASME Boiler and Pressure Vessel Code
CEBAF Continuous Electron Beam Accelerator Facility
CFD Computational Fluid Dynamics
COR Code of Record
EDM Extensible Display Manager
EPICS Experimental Physics and Industrial Control System
ESR II End Station Refrigerator 2
FSD Fast Shut Down
JT-Valve Joule-Thompson Valve: control valve which employs the Joule Thomson effect on compressed gas by throttling its flow expansion.
LEL Lower explosive limit
LFL Lower flammability limit
LH2 Liquid Hydrogen
LRFD Load and Resistance Factor Design
NFPA National Fire Protection Association
ODH Oxygen Deficiency Hazard
PLC Programmable Logic Controller
PSS JLAB Pressure Safety Supplement to ESH
VME Versa Module Europe

4.1.1 Coordinate system

The coordinate system used in Hall A is a right-handed coordinate system with the positive Z axis along the electron beam axis and the Y axis vertically up, putting the positive X axis to beam left looking at the beam dump. The zero point is located on the beam axis at the center of Hall A, directly above the HRS pivot. The center of the MOLLER hydrogen target is located 450 cm upstream at (0,0,-450). The accelerator coordinate system is LEFT-HANDED with positive X towards beam right, in the direction of the CEBAF arc bends. The center of Hall A is at (x,y,z) = (-3295.843, 10002.200, -39303.108) in Accelerator coordinates. The center of the MOLLER target is at (x,y,z) = (-3569.786, 10002.200, -38946.099) in Accelerator coordinates. Note that beamline elements may be referenced in some documents to a beam trajectory coordinate "S." The center of Hall A (the "pivot") is at S=15055.1 cm and the MOLLER target center at S=14605.1 cm.

4.2 Target System Overview

In this chapter we describe the design choices for the target system, which includes the target vacuum chamber with everything inside, on top and underneath it, gas service circuits for helium and hydrogen, instrumentation and controls. The target system can naturally be subdivided into six subsystems:

- Vacuum system
- Hydrogen gas service system
- Cryogenic helium service
- Target loop
- Motion system
- Control system

Each of these subsystems is discussed in detail in the following sections. The vacuum, cryostat, and motion systems are shown in Fig. 17.

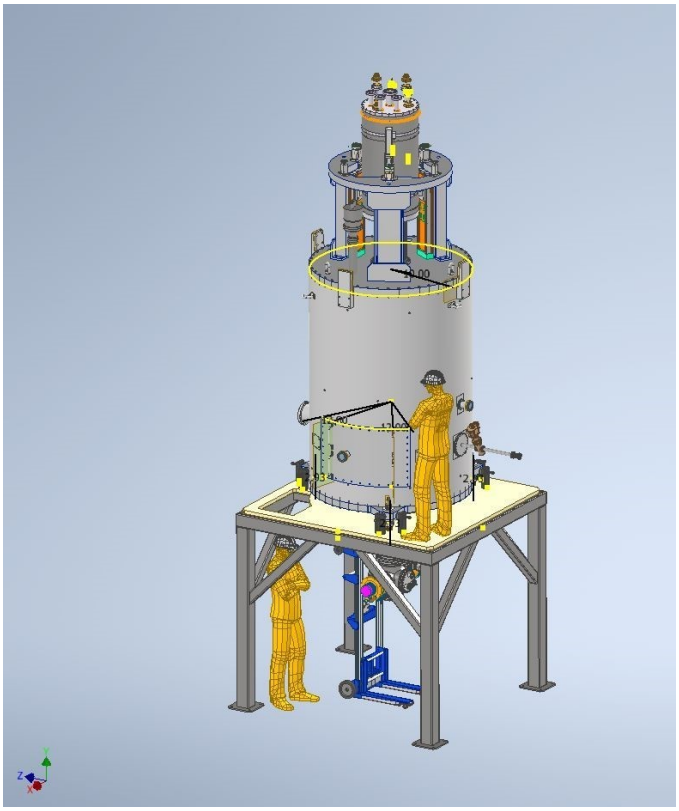

Figure 17: Target vacuum, cryostat, and motion systems. Person shown for scale is 6 ft.

The target chamber vacuum is maintained by a system of vacuum pumps located underneath the chamber. The chamber is supported on the beam line in Hall A by its own stand. The target vacuum chamber hosts inside it the cryogenic target loop. The main components of the target loop are the liquid hydrogen pump, the high power heater, the He-H counterflow heat exchanger and the cell. The target loop is supported inside the target chamber by a vertical motion mechanism with most of its components sitting on top of the target chamber outside the vacuum space. The target loop is serviced with helium and hydrogen gases via separate closed gas circuits. The target system is equipped with instrumentation for monitoring it. The target controls are done with both hardware and software tools.

4.3 Physics requirements

In this section we describe the physics requirements driving the mechanical design of the target components. Hydrogen is the ideal source of target electrons for two reasons. First, it provides the greatest electron target

thickness for the least radiation length. Secondly, the irreducible backgrounds are confined to radiative electron-proton elastic and inelastic scattering, which are relatively well-understood. Scattering off other nuclei would include radiative elastic scattering ($\propto Z^2$), breakup channels and scattering off neutrons, which would introduce significant systematic errors due to unknown and potentially large electroweak couplings. In this respect, liquid hydrogen (LH2) provides the cleanest background and the thickest nuclear target material. In terms of thickness, for example, liquid water at room temperature provides a hydrogen thickness 50% more than LH2 does (one m^3 of water contains 111 kg of hydrogen, while LH2 contains about 72 kg at 20 K), but water also provides a sizeable and unavoidable thickness of oxygen target.

In order to achieve the proposed rate, a target cell at least 8.5 g/cm^2 thickness will be needed. A 125 cm long target cell operated with LH2 at 20 K and 35 psia will provide the required scattering rate. The target cell thickness is estimated to be 8.9 g/cm^2. The nominal target design parameters are provided in Tab. 9. The target cell has been designed to satisfy the requirements for acceptance of the scattered particles. The supports of the target cell and the vacuum chamber have been designed to satisfy the tolerance for cell alignment on the Hall A beam line.

Table 9: *MOLLER LH2 target and beam nominal parameters.*

Target Parameters		Beam Design Parameters	
cell length	125 cm	I, E	70 μA, 11 GeV
cell thickness	8.9 g/cm^2	max raster size	5 mm x 5 mm
cell acceptance (ϕ, θ)	2π, 12 mrad	beam spot	≥ 100 μm
p, T	35 psia, 20 K	helicity flip rate	1920 Hz
Al windows in beam	< 0.25 mm	cell alignment tolerance	$\pm$0.5 mm
LH_2 pump rate	<25 l/s		
target power	**4.5** kW	beam power	**3.1** kW
ρ fluctuations <30 ppm		Luminosity loss <1 %	

To achieve the proposed uncertainty on the measured parity-violating asymmetry the systematic effects from the target have been mitigated with extensive CFD simulations in designing the target cell. Based on steady-state CFD simulations we estimate that the current design of the target cell will have a luminosity loss of less than 1% at 70 μA with a beam rastered on the target cell over a square area of side 5 mm. Based on transient CFD simulations of the target cell we estimate that the target noise on the time scale of the electron beam helicity reversal frequency of 1920 Hz will be less than 30 ppm. The time dependent target noise is required to contribute less than 5% to the parity-violating asymmetry width. To mitigate the target noise LH2 will be recirculated at high flow in a closed loop and operated in constant heat load. To realize this, the target loop will integrate, aside from the target cell, a high flow LH2 pump, a He-H heat exchanger (to extract the beam heating from LH2), and a high power heater (to compensate for beam current fluctuations when operating the target in constant heat load).

To satisfy the requirements for beam alignment, backgrounds and optical studies for the MOLLER apparatus, a solid targets ladder will be attached to the bottom of the LH2 target cell and thermally linked to it. A vertical lifter will provide a single-axis motion mechanism that will position each required target on the beam line during beam operations. The vertical lifter will also provide a “no target in beam” position for accelerator beam tuning. The design for each target subsystem will be detailed in the following sections.

4.4 Target vacuum system

In this section we describe the design of the target vacuum system. The target vacuum system includes the target vacuum chamber, the cryostat, the vacuum pumping system and instrumentation. The target chamber,

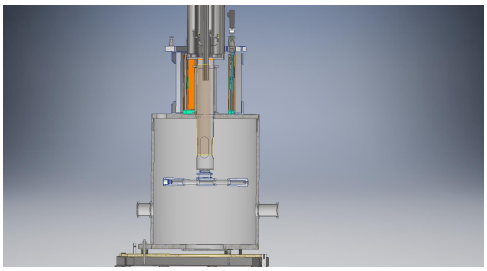

Figure 18: *CAD model of the cross-section through the Moller target vacuum chamber on its stand. The chamber will accommodate the 125 cm long target cell, the target loop and the optics targets.*

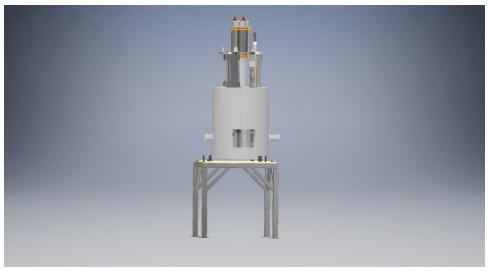

Figure 19: *CAD model of the target assembly on the beam line. The target loop will be remotely movable in the vertical direction with a range of motion of about 45 cm by the target motion mechanism.*

called the vacuum or scattering chamber, will be supported by its own stand on the beam line and will be located 4.5 m upstream from the Hall A pivot. The chamber will be fabricated from forged Al-2219 alloy with a total volume in excess of 6 m^3, a diameter of 1.75 m and a wall thickness of 44.45 mm and will provide the insulating vacuum for the cryogenic system. The vacuum load is expected to be 22.5 tons. The chamber itself will be fabricated with no welds, which will substantially reduce the risk of leaks. The chamber will have beam line ports to connect with the upstream beam pipe and downstream with the beam pipe that goes through the spectrometer. The vacuum space of the target chamber will be separated from the vacuum space of the spectrometer by a beam line Al window. A gate valve is installed just upstream from the target chamber on the beam line. The purpose of this gate valve is to separate the upstream beam pipe vacuum space from the target chamber in case of a vacuum breach in the target chamber or vice versa to protect the target chamber vacuum from a vacuum breach in the upstream beam pipe. The target system space on the beam line in Hall A is defined between the upstream gate valve and the downstream target chamber exit window in the beam line.

The target chamber exit window must be thin in order to minimize backgrounds. A central window will allow the disrupted beam to pass through a 15 mm diameter window that will be 250 micron thick. This will be surrounded by a 75mm annulus, forming a window for the scattered flux with thickness 640 micron. While the static atmospheric load on this window will be small, it must be able to hold off pressure if there is a failure condition on the target or spectrometer side. The primary design challenge is to handle the cyclic thermal stress load due to the frequent expected beam trips. For this reason, the thin window will be slightly ”dished” to alleviate the thermal stress of changing beam conditions.

The beam line ports of the target chamber will have Conflat flanges with metallic seals, which will mitigate the risks of leaks caused by radiation damage. All the other seals on the chamber will be made with radiation hard O-rings. The target chamber has a side access port for alignment, installation and service. The vacuum in the target chamber will be maintained by two turbo-molecular vacuum pumps, see Fig. 21, each with a capacity of 1000 l/s. The turbo-pumps will be backed by a hydrogen-proof mechanical pump which will exhaust into the dedicated hydrogen vent for the target. The pressure in the target chamber will be monitored with cold cathode gauges rated for 10^9 Rad. At room temperature the operating pressure in the target chamber will be below 5 μTorr, capping the convective heat losses of the target loop during cool down and LH2 operations to less than 200 W.

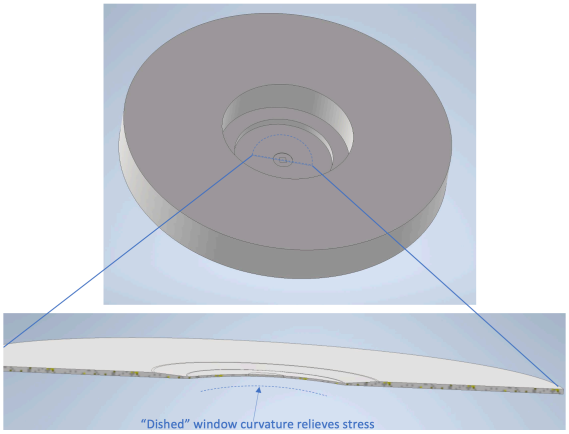

Figure 20: *The target chamber beam line exit vacuum window.*

The BPVC VIII D1/D2 will be used as guidance in the design of the target chamber shell and head. A safety factor of at least 2 will be required to resist all loads in combination, including buckling, column, live load and seismic. The mechanical design complies with Section 7.4.1 of the PSS. The chamber support stand, shown in Fig. 19, is designed and will be fabricated in compliance with AISC LRFD, and AWS D1.1. The four legs of the stand will be fixed to the floor. An alignment system, integrated with the stand, for the scattering chamber, similar to that shown in Fig. 50, will be designed for load resistance and rigidity. The motion of the chamber/target when personnel are accessing the target is undetectable with alignment instruments. The alignment jacks specifications are: $\pm$25 mm vertical adjustment (y), $\pm$18 mm in-plane (x and z) , 3° in pitch and roll (spherical washers), 1.13° in yaw, and the ability to handle the chamber load of 3 tons. It will be possible to align the target chamber with the alignment jacks to an accuracy of better than 1 mm in position and 1 mrad for all three angles.

4.5 Hydrogen gas service

In this section we describe the design of the hydrogen gas service system. The components of the hydrogen gas service system are: the supply and return piping, the gas panel, over-pressure protection, exhaust piping and storage vessels. A schematic of the hydrogen gas circuit is shown in Fig. 22. Hydrogen is the primary target material. The target loop will be serviced with hydrogen gas from three storage vessels located outside of Hall A via a gas panel located inside Hall A. The hydrogen gas storage vessels, interconnecting piping, gas panel and target loop will form a closed volume circuit during operations. The three storage vessels, located outside Hall A, with a volume of 6000 gal or 22.7 m^3, will be charged at room temperature to about 65 psia or 4.4 atm hydrogen pressure. During beam operations, the LH2 will be at 35 psia or 2.3 atm, which will be the pressure of the hydrogen circuit. The total hydrogen inventory is expected to be about 8.4 kg. When the target loop is full of LH2 it will contain about 4.4 kg of hydrogen. The hydrogen storage vessels will be situated on a dedicated concrete pad on the north side of the Hall A truck ramp.

The hydrogen gas panel will be located on an elevated platform inside Hall A. The hydrogen gas management that will be done through the panel will include: filling, releasing and purging of the target loop. The gas panel will be instrumented with pressure gauges, including a differential pressure gauge that will monitor the LH2 pump head in the target loop. The gas panel will have a hydrogen bottle connected to it that will be used for pumping and purging of the target loop and interconnecting piping. This hydrogen bottle is not part of the target loop hydrogen inventory. Hall A has a dedicated hydrogen exhaust line installed for its standard hydrogen target system, but it serves a target a tenth of the size of the MOLLER target and it

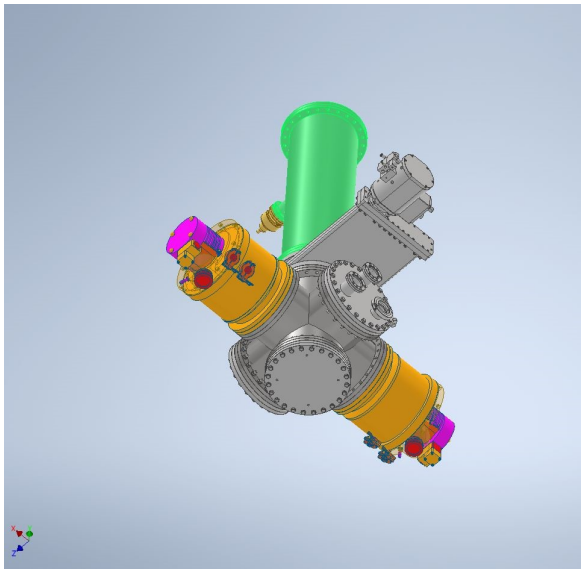

Figure 21: *Twin turbo-pumps connection with the bottom plate of the target chamber. A gate valve will separate the pumps from the chamber space.*

is inadequate to safely service this target system. A new hydrogen exhaust line will be installed to service the MOLLER target system. All the pumping stations that will handle hydrogen gas will exhaust into this line. The hydrogen exhaust line will snake its way from the target chamber in the Hall to the access truck ramp, and along the ramp's roof it will punch through the ramp's outside wall and exhaust to air through a Protecto-Seal 7800 header. The exhaust line will be purged with inert gas and maintained at a positive pressure of 1.5 psig. Figs. 23, 24 show the designed path for the hydrogen exhaust line.

4.6 Cryogenic Helium Gas Service

The purpose of the cryogenic helium gas service is to provide cooling for the liquid hydrogen loop. Gaseous helium is supplied to Hall A from the second-generation end-station refrigerator (ESR II). The capacity of this refrigerator exceeds the expected 4.5 kW heat load from the target (including transfer line losses) by a comfortable margin. The supply temperature and pressure from the ESR II at the Hall A distribution can is 11.7 K and 16 atm. At the same physical location, it is estimated that the return temperature and pressure will be 19 K and 3.8 atm. Under ideal conditions, with 100% efficiency in the heat exchanger, the required mass flow from the ESR II is about 82 g/s. The upstream and downstream boundaries of the cryogenic helium gas service system shall be defined to be at the Hall A distribution can. The distribution can is located on the side of and above the beam line. The major subsystems which make up this system are:

- Helium distribution system
- Flexible transfer lines
- Cryostat located at the top of the target assembly
- Heat exchanger coils (internal flow is He external is H2)

Each of these is discussed in detail in the following sections. Note that the heat exchanger detail is discussed in Sect. 4.7.3. A schematic of the cryogenic He gas service is shown in Fig 25.

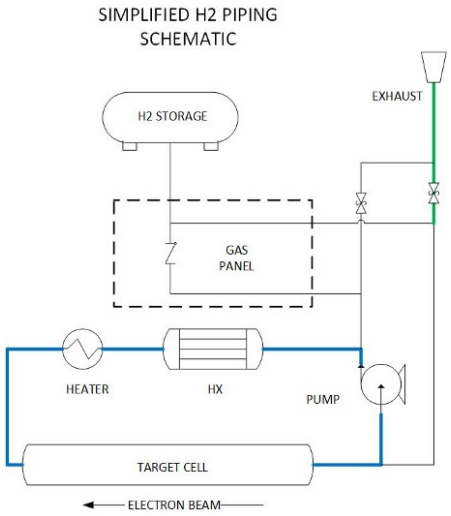

Figure 22: *Hydrogen gas service diagram.*

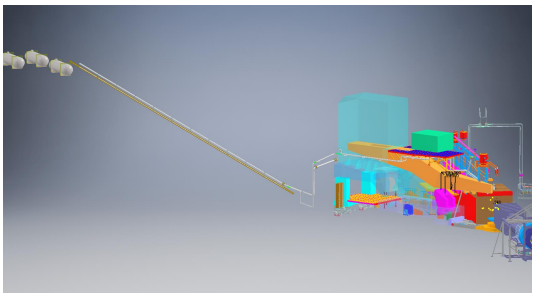

Figure 23: *Hydrogen exhaust line overview.*

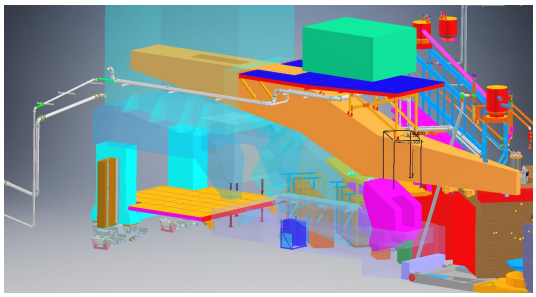

Figure 24: *Hydrogen exhaust lines inside Hall A.*

4.6.1 Helium Distribution System

The existing He distribution system in Hall A is not suitable for MOLLER target operations, thus a new distribution system is required. The system consists of two cans connected by hard piping which connect to the Hall A distribution can on the upstream end and terminate near the top of the target at the end of the infrastructure support frame (blue frame as shown in Fig. 26). Note that short flexible sections are employed to accommodate thermal strains and piping segment misalignment. The full extent of the piping conveying the cold He is insulated by an outer vacuum shield and at least 21 layers of multi-layer insulation (MLI). Additionally, connections to both ends of the subsystem are made through re-entrant bayonets. These insulating measures effectively mitigate heat loads from all three modes of heat transfer. The vacuum shield meets the requirements of the PSS. The He piping meets the requirements of ASME B31.3 (2020), which shall be the COR, and the PSS. The system top level assembly drawing is JLAB drawing A09005-09-02-0100.

4.6.2 Flexible Transfer Lines

Flexible transfer lines (two each) are required to connect the downstream can in the distribution system to the top of the target. The flexibility is chiefly required to allow vertical motion of the target system as discussed in Sect. 4.9.1. The internal He piping is insulated in the same fashion as the He distribution system

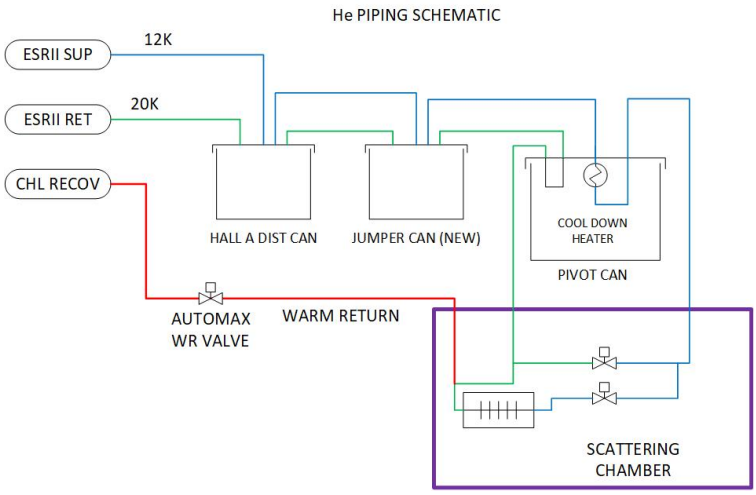

Figure 25: Schematic representation of the Cryogenic Helium Gas Service.

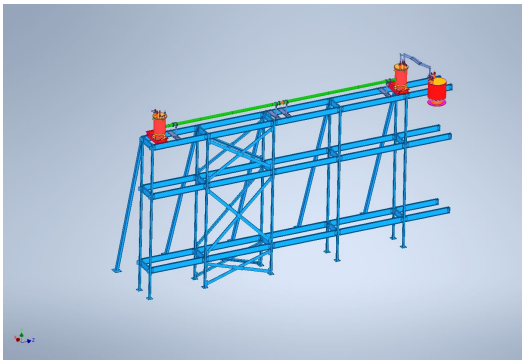

Figure 26: Helium distribution system. The existing Hall A distribution can is shown at the far right. Note the Hall A wall and other infrastructure have been removed for clarity.

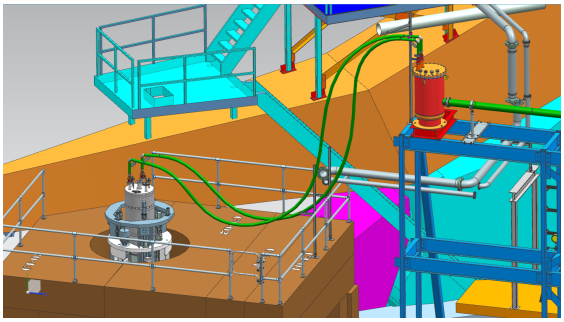

Figure 27: Flexible transfer lines shown connected to the distribution system and to the top of the cryostat.

(see Sect. 4.6.1. The lines are terminated with male bayonets which connect to the distribution system and to the cryostat. The flex lines are shown in Fig. 27. The vacuum shield meets the requirements of the PSS. The He flex piping meets the requirements of ASME B31.3 (2020), which shall be the COR, and the PSS.

4.6.3 Cryostat

The cryostat is attached to the vertical motion system and serves several purposes:

- Connects the cold piping of the flexible transfer lines to the control valves known as JT-Valves.
- Connects the cold hydrogen piping connected to the target loop to the room temperature hydrogen piping service (see Sect. 4.5)
- Connects cold electrical services to room temperature cabling

The two JT-Valves control flow to a bypass circuit and to the helium side of the heat exchanger. The vacuum in the cryostat connects with the scattering chamber vacuum via an edge-welded bellows as discussed in Sect. 4.9.1. The vacuum or outer can of the cryostat meets the requirements of the PSS. The helium piping

meets the requirements of ASME B31.3 (2020), which shall be the COR, and the PSS. The hydrogen piping is discussed in Sect. 4.5. The external view of the cryostat is shown in Fig. 28. A section view is shown in Fig. 29.

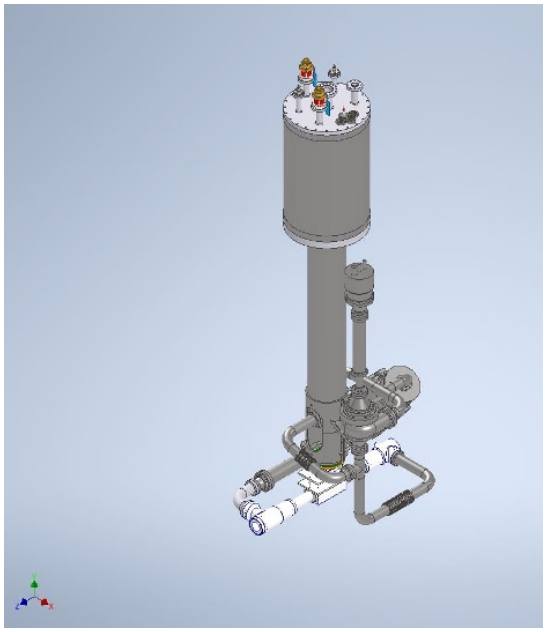

Figure 28: External view of the cryostat, support shaft, and loop. Note that the chamber and the vertical motion system have been suppressed for clarity.

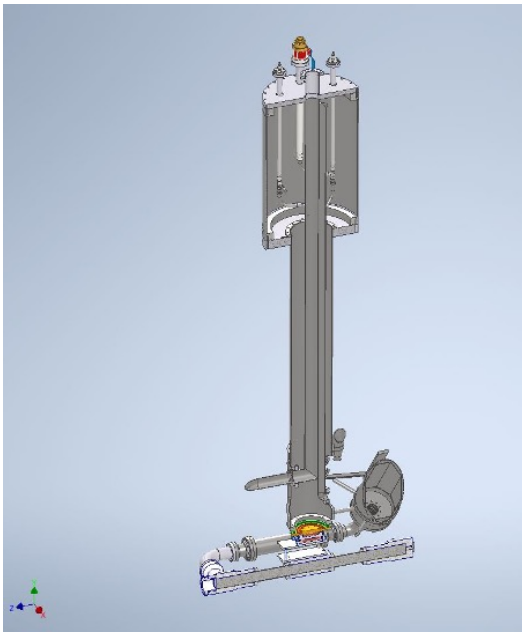

Figure 29: External view of the cryostat, cutaway view. support shaft, and loop. Note that chamber and vertical motion system have been suppressed for clarity.

4.7 Target loop

In this section we describe the cryogenic target loop. The components of the target loop are the target cell, the He-H heat exchanger, the LH2 pump, the high power heater (HPH), interconnecting piping and the solid targets ladder. The design of the target loop is shown in Fig. 30. The design pressure of the target loop is 100 psi.

4.7.1 Target Cell

The main component of the target loop is the target cell in beam, shown in Fig. 31. The cell body will be fabricated from B209 Al7075-T651. The cell is cylindrical with a length in beam from the beam entrance window to the beam exit window of 125 cm and a diameter of 7.6 cm. The flow space inside the cell has a volume of about 7 l. The cell shape accommodates the required acceptance of the MOLLER apparatus: 2π azimuthally and 5-20 mrad in polar angle. The thickness of the LH2 target at the operating thermodynamic point in (p,T) of (35 psia, 20 K) will be $t = \rho l \approx 8.9$ g/cm^2. The only materials in beam during production operations will be the Al windows of the target cell and the LH2. The thickness of the target cell Al windows in beam will be less than 0.07 g/cm^2 or less than 1% of the LH2 thickness. The target cell will have a flow inlet manifold, a mid-section, a flow outlet manifold and two spool pieces connecting the manifolds with the mid-section, as seen in Figs. 31 and 32. The mid-section of the target cell will connect to the 6 degrees of freedom alignment stage that will position the cell on the beam line with an accuracy of 0.25 mm both

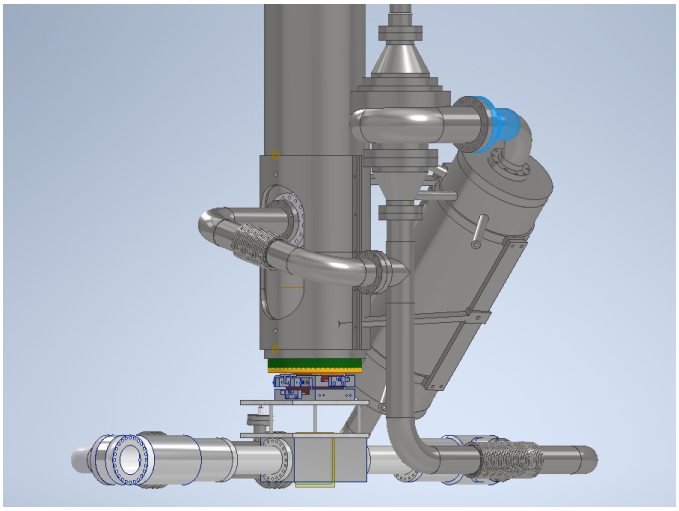

Figure 30: The target loop.

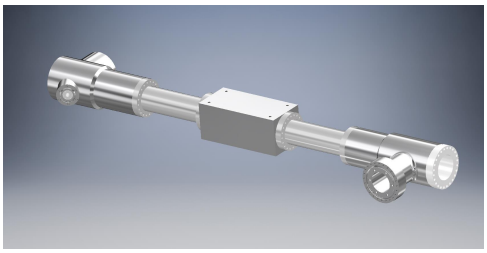

Figure 31: *The target cell.*

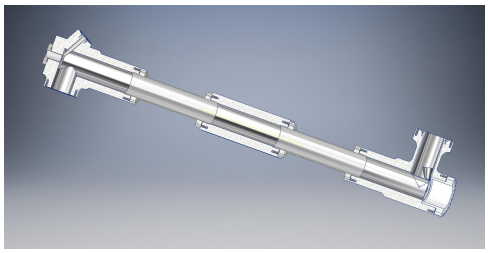

Figure 32: *Section through the target cell.*

vertically and horizontally. There are no welds on the target cell body, all connections are made with Conflat flanges with Al 1100-O gaskets. These gaskets are leak tight to less than 10^{-11} mbar·l/s helium in reverse mode at pressure and at 20 K. All materials in the cell are made of aluminum alloys, all bolts and threaded inserts are made of titanium alloy.

The target cell will have two windows for beam, both made from Al7075. The beam entrance window has a diameter of 20 mm and a thickness of 0.125 mm and will be made on an Al Conflat flange. Jefferson Lab has extensive experience with such beam windows. This particular size window fails in hydro-pressure tests at pressures above 500 psi. The beam exit window will have a diameter of 7.6 cm, a thickness of 0.25 mm with a nipple at the center of it 0.125 mm thick over a diameter of 12 mm. The curvature radius of the beam exit window is expected to be 20 cm. The thinner nipple at the center of the window will mitigate the background in the experiment. The target cell fluid space was designed with CFD to mitigate LH2 systematic effects in the bulk of the fluid and at the cell windows in beam. The CFD design process will be described in Sect. 4.8.

4.7.2 LH2 pump

The LH2 pump will recirculate the liquid around the target loop at a nominal volume rate of 25 l/s or about 1.5 kg/s with a maximum pressure head of 4 psi at 55 Hz shaft rotation. This volume rate will ensure a high turbulence inside the target cell, mitigating target density noise. If the pump stops turning with the beam on at 70 μA it would take the beam heating about 5 s to bring LH2 to saturation and about 60 s to boil off to vapor the LH2 in the whole volume of the target cell. The design pressure of the pump is 100 psi.

Figure 33: The LH2 pump volute and impeller.

The MOLLER LH2 pump is based on the Q_{weak} LH2 pump. We will reuse the Q_{weak} pump impeller and pump case or volute, both shown in Fig. 33. The impeller was made by Turbonetics and the case by Garrett Motion, both from Al alloys. The pump case was modified to have a Conflat flange and seal. The pump impeller was balanced by the manufacturer up to 10,000 rpm or 166 Hz. The motor driving the pump will be located outside the target chamber, thermally decoupling it from the cold mass of the target loop. The Q_{weak} LH2 pump motor was thermally in contact with the target loop and needed about 700 W of cooling power to operate. The MOLLER LH2 pump motor will operate in air and connect with the pump impeller via about 1 m long shaft with proper bearings. The motor shaft will operate at 20 K at the impeller connection and at 300 K at the motor rotor connection.

4.7.3 Heat exchanger

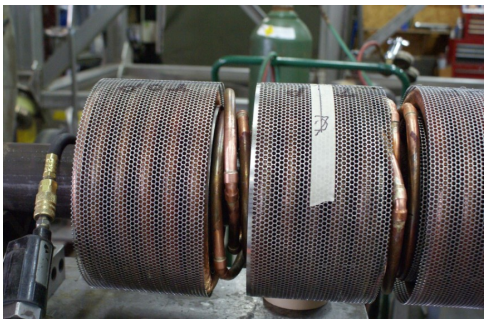

Figure 34: *The He-H heat exchanger at the factory.*

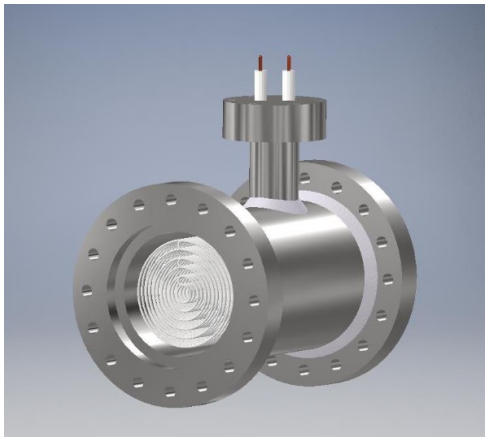

Figure 35: *The high power heater.*

We plan to reuse the Q_{weak} target heat exchanger (HX). The cooling capacity of the HX is at least 5 kW, more than enough for the MOLLER target. The shell of the HX has an ASME stamp. A picture of the finned tubing coils of the HX is shown in Fig. 34 while at the manufacturer. The cold helium gas will be supplied by ESR II at 16 atm, 11.7 K with a maximum flow of 84 g/s. The return of the gas will be at 19 K and

2.5 atm. The pressure loss from the ESR II cold box to the target is estimated to be about 1 atm one way, leaving about 14 atm of pressure loss over the target JT valve and HX plumbing.

4.7.4 High power heater and loop piping

A heater element immersed into the LH2 is required to operate the target loop in constant heat mode. The heater is part of the target loop and its design is shown in Fig. 35. This high power heater (HPH) has two primary functions: to stabilize the LH2 temperature with beam on target and to replace the heat equivalent to beam heat load with beam off. The temperature stabilization is done with a PID feedback loop which aims to keep one of the temperature sensors immersed in LH2 constant. It is expected that the maximum heater power needed will be 3.1 kW, the maximum heating power of the electron beam into the LH2 cell. A heater designed to operate at 4 kW with no boiling would satisfy the operational requirement for it.

The HPH will be made from 16 Ga Kapton insulated NiCr wire with an electrical resistance of 12.5 Ω. The HPH will be operated by a dc power supply at 250 V and 20 A with a maximum power of 5 kW. The heater wiring will be held by a G10 frame inside a stainless steel cylindrical spool piece with diameter 7.8 cm and it will be electrically isolated from the target loop piping. The HPH model was simulated with

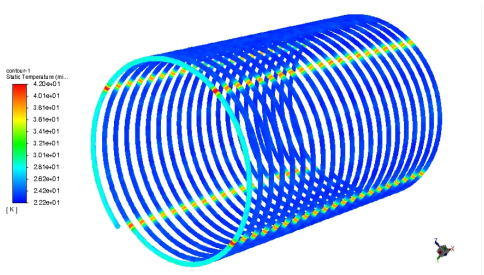

Figure 36: *HPH coil 5 temperature profile for 4 kW of heater power. The maximum temperature is registered in locations where the heater wire goes through the G10 holding frame.*

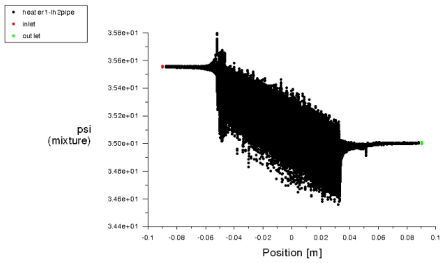

Figure 37: *LH2 pressure loss across the HPH. The vertical axis units are psi, the horizontal axis is the displacement along the heater flow direction.*

CFD to assess its design requirement. The LH2 was assumed to be at 20 K, 35 psia at the inlet to the heater with a flow of 1.5 kg/s. A two-phase mixture CFD model was used in the simulations. The heating was sourced uniformly in the volume of the heater wires integrating to 4 kW. The temperature profile on the wire surface of coil 5 is shown in Fig. 36. The maximum temperature in the heater wire was predicted to be 42 K. The location of the maximum temperature in the heater wire is inside the G10 frame that holds the coils. The maximum LH2 density loss inside the heater geometry is predicted to be 5.5% at 4 kW, which is below the 6.7% LH2 density loss required to reach saturation. There are no boiling spots inside the HPH at 4 kW with a nominal LH2 flow of 1.5 kg/s. The LH2 pressure loss over the HPH pipe is predicted to be 0.55 psi at 1.5 kg/s. The pressure loss profile is shown in Fig. 37.

4.7.5 Solid targets

Solid targets will be available for ancillary, background and optics studies. Two solid frames, which are thermally connected with the LH2 target cell, will each hold 3 solid targets in a vertical ladder. The frames will be located along the beam line at the location of the beam entrance and beam exit Al windows of the LH2 cell. One of the 3 solid targets in each ladder will be a foil with a hole which will be used for beam centering studies of each end of the LH2 target cell on the beam line. The bottoms of the two ladders will

be connected by a tray containing thin foil targets for optical studies of the MOLLER apparatus, as seen in Fig. 38.

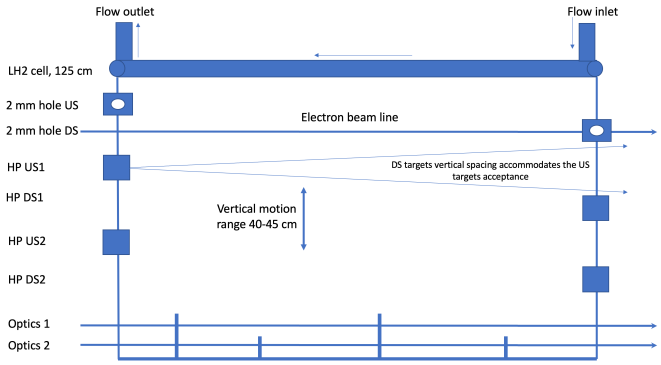

Figure 38: Sketch of the solid targets ladder with the optics foils tray.

4.8 Cell design with CFD

In this section we describe the use of CFD in the design of the flow space of the target cell. Before CFD became feasible to use in the design of high power LH2 target cells, target design was done based on experience by establishing a set of global parameters that was believed to satisfy the requirements for performance. Most of the time the target performance could only be established during operations of the target, at which point any design changes would be futile. The advent of CFD offered for the first time an insight into local processes inside a target cell and the possibility to predict the performance of a specific geometry of the cell. Designing a cell with CFD became a process of refining the geometry of a cell until it satisfies a set of performance parameters. The first high power target designed with CFD at Jefferson Lab was the 2.5 kW Q_{weak} target. CFD simulations predicted a LH2 density loss of 0.8% at the nominal running point for Q_{weak}. The luminosity loss, caused by the beam heating the LH2 target, measured by Q_{weak} at the nominal running point was 0.8%. The Q_{weak} target satisfied all its design requirements validating the use of CFD in designing high power targets.

The focus of the CFD design of the target cell was to mitigate the luminosity loss caused by the LH2 density reduction at the nominal running point and to minimize the target noise on the time scale of the beam helicity reversal frequency. The CFD design goals, listed in Tab. 9, are a luminosity loss of less than 1% and LH2 density fluctuations of less than 30 ppm at 70 μA beam current with a beam square raster area on the target with side 5 mm, at 1.5 kg/s LH2 flow in the target loop and a helicity reversal frequency of 1920 Hz. Steady-state CFD simulations were developed to predict the luminosity loss of the target cell and time-dependent simulations were developed to predict the LH2 noise at the beam helicity reversal frequency. The CFD simulations were developed and carried out on the HPC (high performance computing) resources available at Jefferson Lab. Most of the steady-state simulations were done on 128 CPUs, while most of the time-dependent simulations were done on 512 CPUs. The software engine used was Fluent, part of ANSYS, Inc.

4.8.1 Steady-state CFD simulations

The luminosity loss is a time-independent effect caused by the fact that the target material is a fluid and the density of a fluid depends on temperature and pressure. When the beam is on target, at 70 μA, it deposits about 3.1 kW of power, locally heating the LH2, hence reducing its density. If all the LH2 flow of 1.5 kg/s passes through the beam area the minimum expected LH2 density loss would be 0.4%.

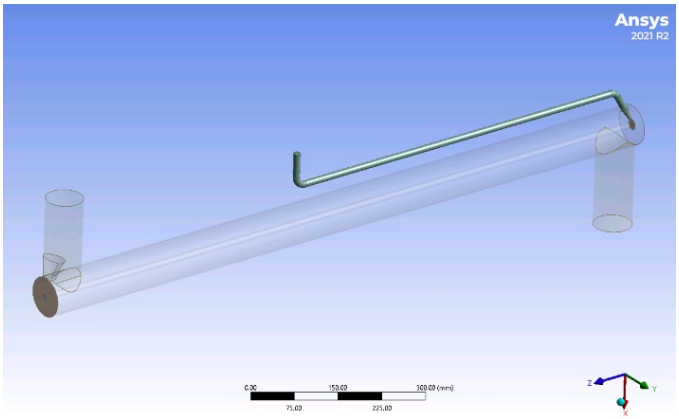

Figure 39: *Cell 21 geometry. There is a nozzle jetting LH2 at the beam area on the beam entrance window of the cell. The inlet manifold to the cell, which is next to the beam exit window of the cell, has an internal flow diverter that produces a jet aimed at the beam exit window of the cell. The inlet manifold also has an aperture that accelerates the flow as it enters the cell. The nozzle and the flow diverter are mitigating heating on the windows as seen in Tab. 10*

Table 10: *CFD comparison between cell designs 01 and 21.*

Cell	P	Δp	v_{BV}	T_{BV}	$T_{max,in}$	$T_{max,out}$	$\Delta\rho/\rho$	$(\Delta\rho/\rho)_{max}$
	W	psi	m/s	K	K	K	%	%
01	3360	0.34	3.4	20.78	67	90	1.3	6.9
21	3396	1.6	6.2	20.52	32	41	0.85	6.3

The cell design process started with a geometry similar to the E-158 target cell used at SLAC and progressively molded into the geometry in Fig. 39. There were 21 intermediate cell geometries that were assessed with CFD, cell-21 being our production cell, shown engineered in Figs. 31 and 32. A set of conservative values were considered for the CFD simulations parameters, such as 3350 W of beam power, though 3100 W is the expected one, a square beam raster area of side 4 mm, though the nominal value is 5 mm, and a LH2 mass flow of 1.5 kg/s, though the LH2 pump maximum designed capacity is 1.8 kg/s. Table 10 shows the CFD comparison between cell designs 01 and 21, where P is the total beam power deposited in the cell, LH2 and Al windows, Δp is the LH2 pressure loss between cell inlet and cell outlet, v_{BV} and T_{BV} are the flow velocity and temperature respectively in the beam volume in the cell, $T_{max,in}$ and $T_{max,out}$ are the maximum temperatures in the cell windows on the beam, for beam entrance and beam exit respectively, and $\Delta\rho/\rho$ and $(\Delta\rho/\rho)_{max}$ are the LH2 density loss in the beam volume in the cell and its maximum value in %. Cell 01 is 30% over the requirement for less than 1% LH2 density loss. This cell design has a boiling spot in the LH2 bulk and the average maximum temperatures in the cell windows indicate LH2 boiling in these regions too, the dominant cause of LH2 density fluctuations. The beam power deposited into LH2 varies in the CFD simulations between cells 01 and 21, as seen in Tab. 10. This variation is caused by the fact that the simulations are done on spatially-discretized volumes and the script that sources the beam power can grab a slightly different volume between two models with different mesh resolutions in the same region. The difference in this case is about 1%, which has a negligible effect on the simulation results. Cell 01 has an open geometry with two 90° turns for the flow at the inlet and outlet to the cell. The LH2 pressure loss over this geometry at a mass rate of 1.5 kg/s is 0.34 psi. On top of the two 90° turns for

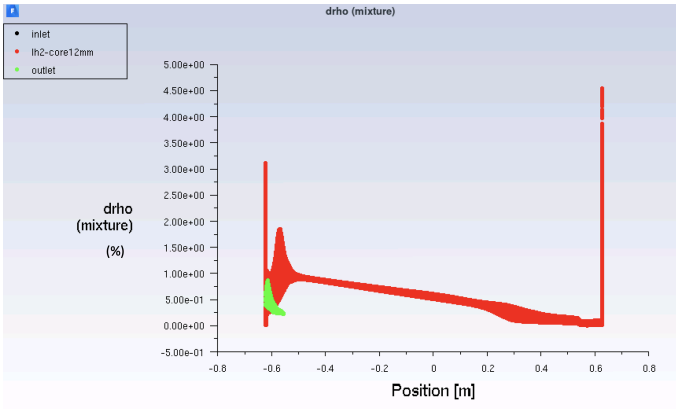

Figure 40: *Cell 21 LH2 density loss profile along the beam line inside a virtual tube of 12 mm diameter. The maximum LH2 density loss in the bulk is less than 5%. A 12 mm diameter cylindrical region centered on the cell's axis was meshed with a higher resolution than the rest of the geometry to better capture fine details of rastered beam heating of LH2.*

the flow, cell 21 has a flow diverter in the flow inlet manifold and an aperture at the entrance to the cell. These features increase the pressure loss of LH2 over this cell at 1.5 kg/s to 1.6 psi. These features are also responsible for increasing the average flow velocity in the beam volume from 3.4 m/s in cell 01 to 6.2 m/s in cell 21. A faster flowing liquid through the beam volume reduces the effects of beam heating in the bulk of LH2. The flow diverter in the cell inlet manifold and the nozzle aimed at the beam entrance window are directly responsible for reducing the average maximum temperature in the beam line windows of the cell by a factor of more than 2 for both windows, as seen in Figs. 41 and 42, mitigating boiling at the windows.

The average LH2 density loss in beam volume in cell 21 is predicted to be 0.85%. The profile of local LH2 density loss along the beam line in cell 21 is shown in Fig. 40. At every horizontal position the vertical spread shows the variation of LH2 density loss inside the 12 mm diameter cylindrical region centered on the beam axis. To reach saturation at 35 psia the LH2 density has to decrease about 6.8%. There are no boiling spots in the bulk of LH2 for cell 21 as the maximum LH2 density loss in the bulk of the cell is less than 5%. Nucleate LH2 boiling may be possible at the cell beam line windows as the average maximum LH2 density loss in the cell is predicted to be 6.3% with occasional excursions.

The maximum temperatures in the beam line windows are shown in Figs. 41 and 42 for cells 02 and 21 respectively. Cell 02 is an improved design on cell 01 in that it eliminated the boiling spot in the bulk of LH2. A temperature difference between the window and the bulk LH2 of less than 20 K usually correlates with nucleate LH2 boiling at the window, while a temperature difference larger than 40–50 K correlates with bubble LH2 boiling at the window. LH2 boils at both windows of cell 02, bubble boiling is very probable next to the beam entrance window and intermediate nucleate to bubbles at the beam exit window. For cell 21 the prediction is that there is no boiling next to the beam entrance window however nucleate boiling is possible next to the beam exit window.

4.8.2 Time-dependent CFD simulations

The electron helicity state period is the time scale on which the parity-violating asymmetry is measured. The variations of LH2 density on this time scale are called density fluctuations. This noise source increases the width of the measured parity-violating asymmetry. An upper bound of 30 ppm on the target density fluctuations enlarges the measured asymmetry width by about 5% at the electron beam helicity reversal frequency.

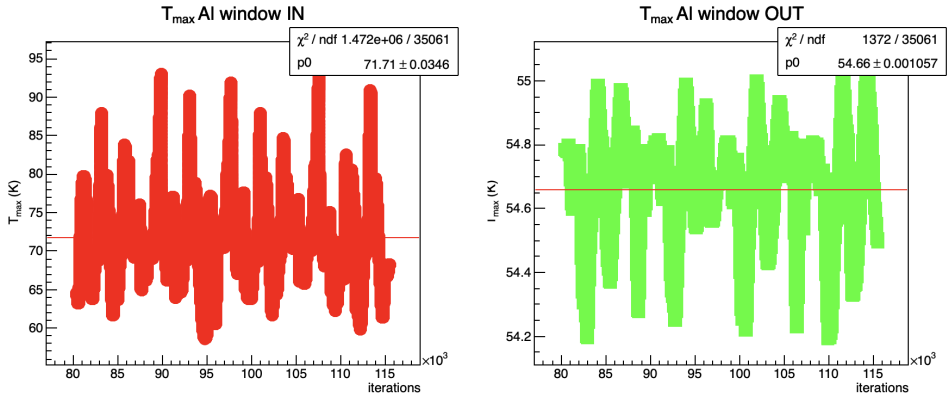

Figure 41: *Maximum temperature in cell 02 Al windows.*

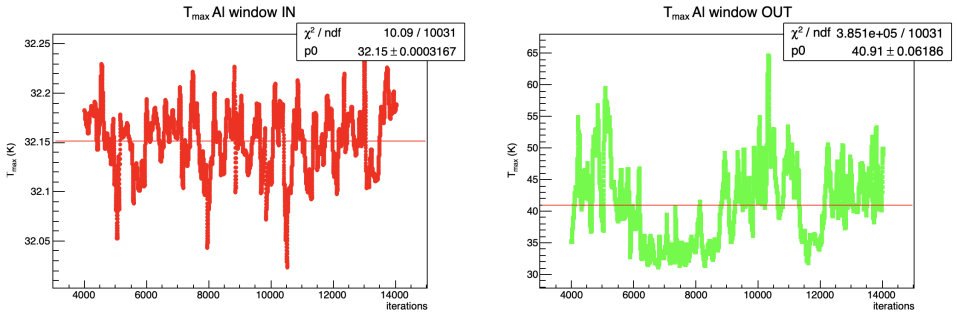

Figure 42: *Maximum temperature in cell 21 Al windows.*

The electron beam delivered by the CEBAF machine into Hall A has a diameter typically about 0.3 mm. To mitigate heating into the target cell Al windows and the bulk of LH2 this beam is rastered by pairs of coils to paint a rectangular area on the target. The raster coils are a race-track design with a pair along the horizontal axis coupled with a pair along the vertical axis. The coils are driven by periodic currents with a triangular shape, with frequencies around 25 kHz. The difference in frequencies between the horizontal coil and the vertical one in the same pair, Δf, defines the period of covering the raster area on the target as illustrated in Figs. 43 and 44, where the raster area painted on the target is considered to be a square with side 4 mm. If the raster frequencies difference is Δf = 960 Hz then the raster coils paint the raster area on target in about 1 ms, as seen in Fig. 44. In the same amount of time, 1 ms, if Δf = 120 Hz, the raster paints 1/8 of the raster area, see Fig. 43. The dwell time for a raster with Δf = 120 Hz is eight times longer than for a raster with Δf = 960 Hz, which strongly correlates with local heating in the bulk of LH2.

When the Q_{weak} target was designed with CFD, about two decades ago, it was expected that time-dependent CFD simulations would capture the LH2 density fluctuations. While this would have been possible in principle it proved to be computationally prohibitive at the time to provide an estimate for LH2 density fluctuations based on CFD simulations. Simulating the whole volume of the Q_{weak} target cell, about 7 liters, with enough spatial and temporal resolutions to capture LH2 density fluctuations would have taken at least one month to acquire 1 second of flow time on, what was at the time, a top of the line 4-CPU workstation. LH2 data for a whole minute of flow time would have been needed to capture medium term flow features, which would have required to run the simulation for about 5 years. This would have been needed to get enough statistics for a single data point of target running conditions.

For the time-dependent simulations covered here it was assumed that the intrinsic beam spot width is 0.32 mm, the beam raster area is a square of side 4 mm, the beam heating was in excess of 3.3 kW, the LH2

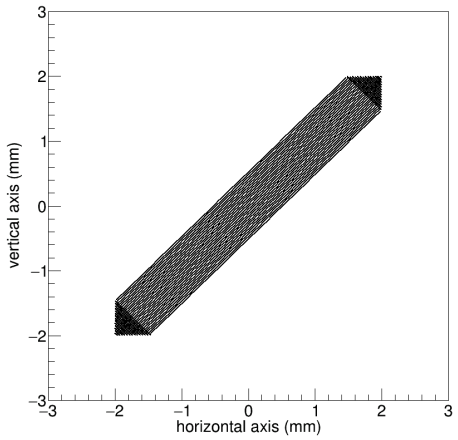

Figure 43: *Area covered on target in 1 ms by the beam raster for Δf = 120 Hz.*

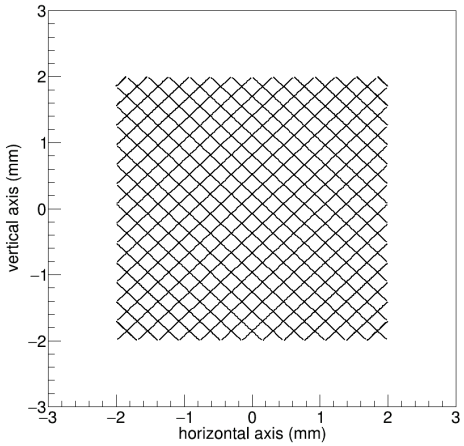

Figure 44: *Area covered on target in 1 ms by the beam raster for Δf = 960 Hz.*

pump flow is 1.5 kg/s, the LH2 at the flow inlet to the cell is at 20 K and 35 psia. The raster frequencies are f_x = 25920 Hz and f_y = 24960 Hz with a difference between them of 960 Hz. The full beam raster motion was implemented in Fluent with user scripts. Material properties for the cell Al windows and target fluid were corrected for temperature dependence. A 2-phase model with evaporation-condensation for the phase transition was provided by Fluent and customized for this simulation. The whole geometry of the cell 21 was included in the simulation, about 6.8 liters. The results presented in what follows are preliminary. The time dependent simulations are actively being carried out at the time of this writing. The production simulations are performed on a homogeneous farm of 512 CPUs, part of the *ifarm* cluster at Jefferson Lab. It takes about 5 days to acquire one second of flow time on this farm, a tremendous improvement on the Q_{weak} target cell conditions, considering also that the spatial resolution of the meshed cell has improved by a factor of 3. The

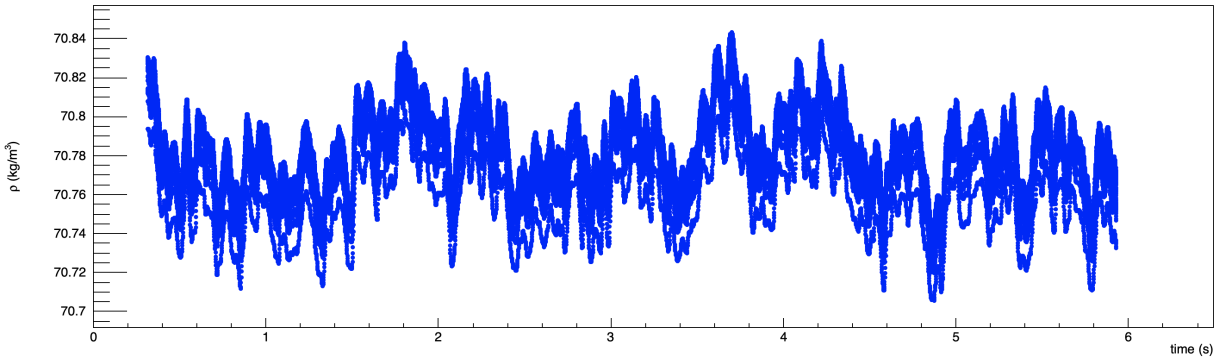

Figure 45: *Cell 21: LH2 density variation in time.*

time step of the CFD simulation was either the period of the raster y drive signal $1/f_y \approx 40$ μs or twice that, 80 μs. Fig. 45 shows the LH2 density variation for the first 6 s of flow time averaged over the cell volume traced by the beam raster during the time step. The CFD simulations produce a train of LH2 density values for each time step. LH2 density over a suitable number of consecutive CFD time steps is averaged to reach the period of the electron helicity reversal. In the case of a frequency reversal of 1920 Hz, the reversal period is about 0.52 ms and the LH2 density over this time period is given by averaging 13 CFD 40 μs

consecutive time steps. The pair and quartet LH2 density asymmetry calculations at 1920 Hz is illustrated in Fig. 46. The procedure described in Fig. 46 can be extended to an arbitrary number of time periods which

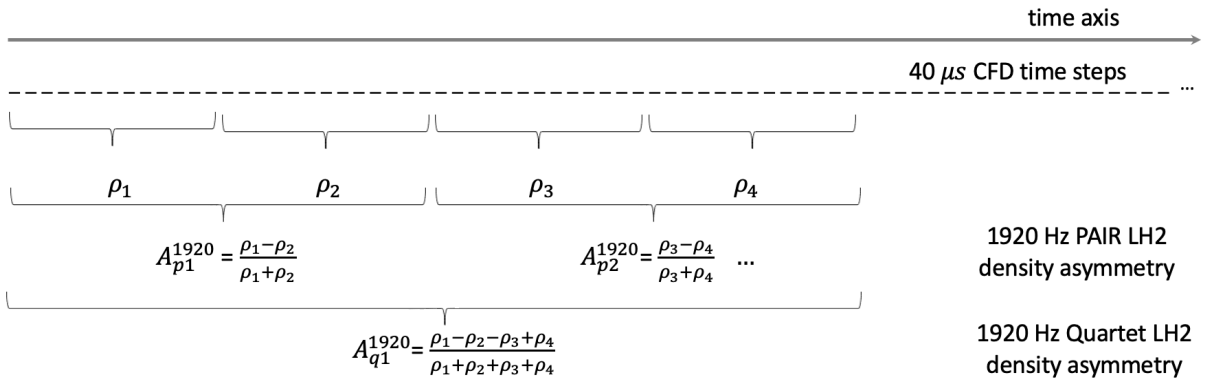

Figure 46: *Cell 21: LH2 density asymmetry formations at 1920 Hz.*

are multiples of 40 μs. The LH2 density noise is extracted from histograms of the LH2 density asymmetry

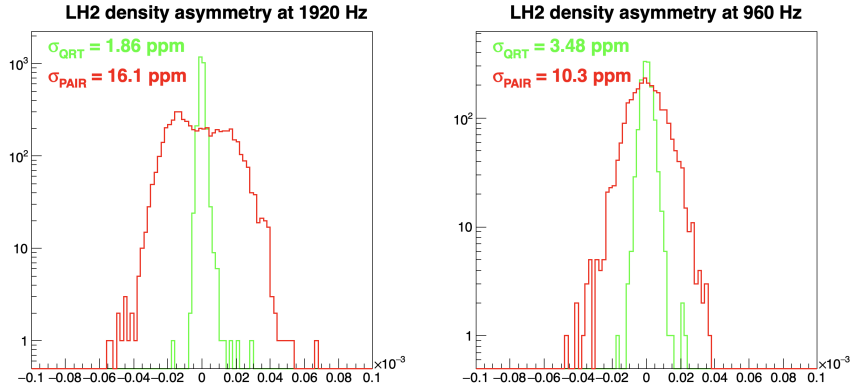

Figure 47: *Cell 21 LH2 density asymmetry comparison between pair and quartet asymmetries at two frequencies: 1920 Hz and 960 Hz.*

data at each helicity reversal frequency and pair/quartet considered. A comparison between 1920 Hz and 960 Hz for both pair and quartet LH2 density asymmetries is shown in Fig. 47. The data extracted from these simulations is preliminary as it covers only about 6 s of flow time while the LH2 flow can have fluctuations and drifts over longer periods of time which may affect the local beam heating in the target cell. The data, so far, predicts that the target noise in quartet asymmetry formations seems to be several times smaller than the noise in pair asymmetry formations at 1920 Hz and 960 Hz. The target noise from pair asymmetry at 1920 Hz is predicted to be larger than at 960 Hz, the red histograms in Fig. 47. This may be caused by the fact that at 1920 Hz in one helicity period of 0.52 s the beam raster with frequencies difference of Δf = 960 Hz covers about half the raster area capturing the LH2 density variations between two halves of the raster area on the target cell in a pair asymmetry. Based on the amount of current CFD time-dependent data, the target noise at 1920 Hz for pair asymmetries is estimated to be around 16 ppm, well below the required noise figure of 30 ppm in these conditions.

4.9 Target motion

The motion system is composed of three subsystems which work in concert to allow absolute positioning of the target to better than 1 mm and relative repositioning of the target to better than 20 μm. These subsystems are:

- Vertical motion system, also known as the target lifter, which operates remotely
- Chamber positioning system
- Cell alignment system

4.9.1 Vertical Motion System

A single axis motion system has been developed to accurately and remotely position the target to better than 0.1 mm absolute and 0.02 mm repeatable in the vertical ("y") direction. The length of travel shall be 18 in (45 cm) with a lifting capacity of 3500 lbf (15.6 kN) with a factor of safety of more than two. Motion is allowed and vacuum is maintained via an edge-welded bellows with an inner diameter of roughly 12 in (30 cm). The vacuum and spring load of the bellows is the dominant load to the lifter system. Motion is guided by three high precision double rail sled assemblies. Each of these sleds is driven by ball screws with gear reduction, chain drive, and AC servo motor. Electromagnetic shaft brakes are installed and must be energized to be released and allow motion. These brakes are capable of holding the full load of the target under vacuum, mitigating possible effects from a motor failure. Motion is controlled via a Koll Morgan BDS-5 AC servo motor PLC. These PLCs have been in operation at JLAB for decades and have proven to be reliable even in high radiation fields. The vertical motion system is shown in Fig. 48.

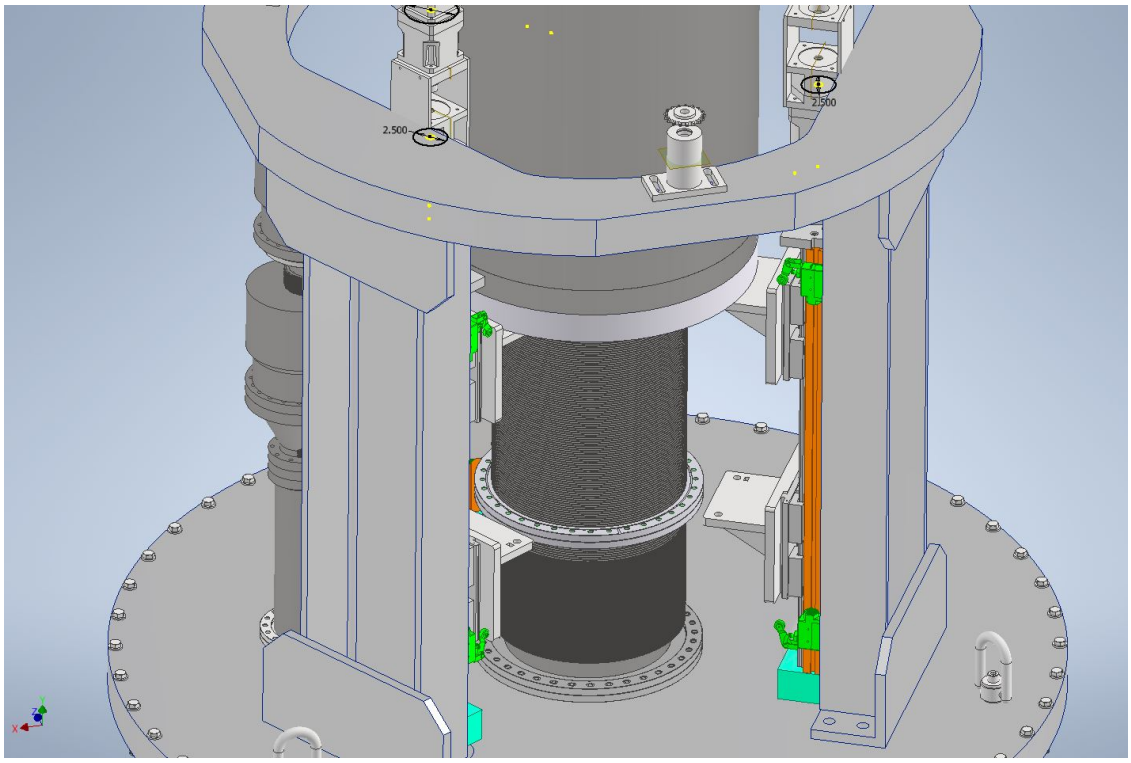

Figure 48: Target vertical motion system upper side view. Bellows flanges are shown in both the fully extended and fully compressed condition.

4.9.2 Cell Alignment System

The final position of the cell is determined during the alignment process. This process is completed using a portable CMM which is tied into the Hall coordinate system via a two step alignment procedure. During the alignment, the cell is positioned vertically (y direction) with the motion system described in Sect. 4.9.1, but all other degrees of freedom (pitch, yaw, roll, x and z) are adjusted using the cell alignment system shown in Fig. 49. This system is only accessible when the scattering chamber is open and covers have been removed. Motion is effected by standard hand tools.

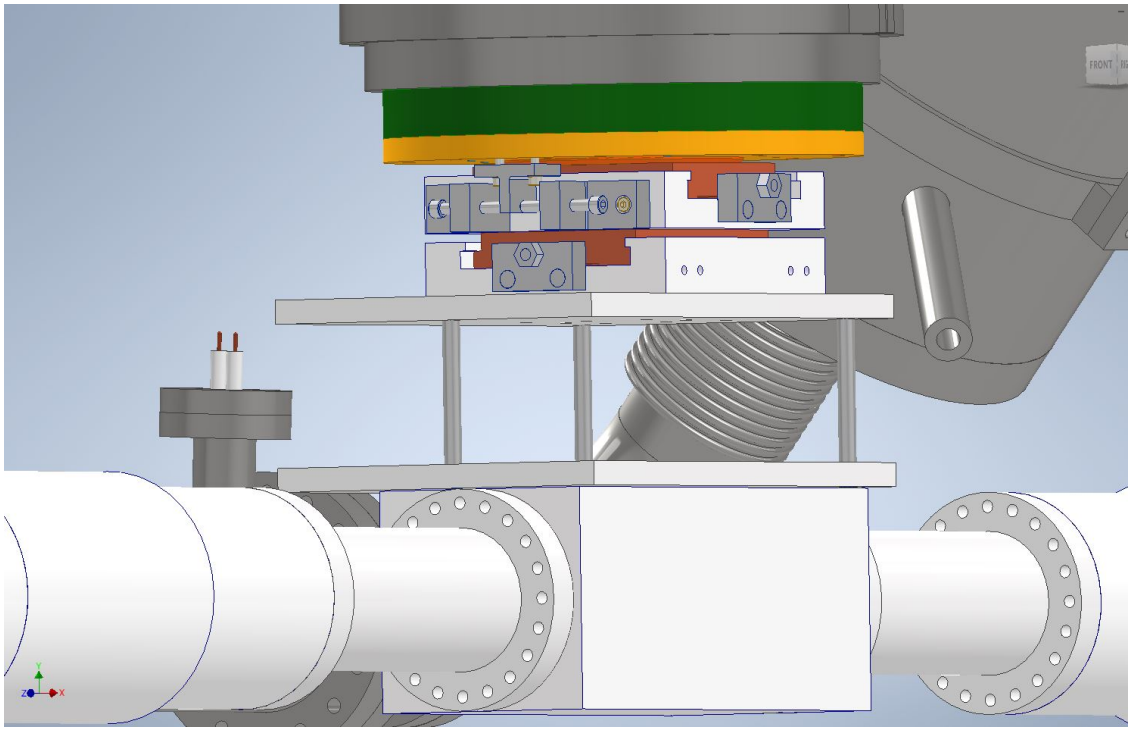

Figure 49: Target cell positioning system, upstream beam left view.

4.9.3 Chamber Positioning System

The chamber positioning system capable of positioning the chamber to better than 1 mm absolute in x, y, and z) under full load. Pitch and roll can also be set to high accuracy with this system. Yaw motion is possible but more difficult. The chamber base is attached to the threaded studs through oversized holes as shown in Fig. 50. The chamber rests on oversized spherical washers. This allows the chamber to be moved up to 12 mm in either x, y and/or z. This alignment system is operated manually via standard hand tools. Magnet-based dial indicators can be used to monitor this motion.

4.10 Safety System

There are a number of hazards associated with the target system. These include electrical, mechanical, pressure components, cryogens/ODH, and most severe is the flammable nature of the hydrogen target fluid. Some pertinent properties of hydrogen are given below.

- LFL/LEL 4% in air at STP
- Auto ignition temperature of 571.1 C

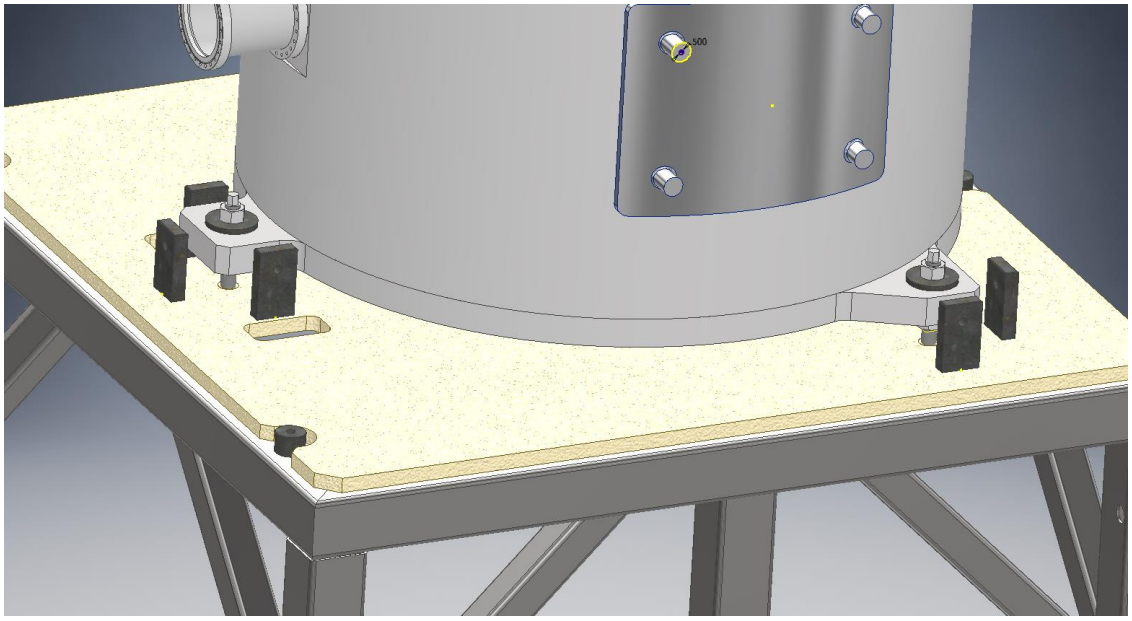

Figure 50: Chamber positioning system. Note only two of three legs are visible.

- Boiling point -253 C at 1 atm
- Melting point -259 C at 1 atm

4.10.1 Electrical

Electrical hazards are present in the vertical motion control subsystem, LH2 pump, the vacuum pumping system, and the heater system. All electrical enclosures shall comply with NFPA 70 and all purchased components shall be UL listed. Components subject to possible hydrogen exposure shall be either intrinsically safe or de-energized during any possible H2 exposure.

The following elements shall be electrically bonded and grounded by physical cable:

- GH2 storage vessels located on concrete pad
  - These vessels shall be bonded and grounded in compliance with NFPA 70
  - Resistance to ground shall be less than 25 Ω.
- Scattering Chamber
  - Scattering chamber shall be grounded with # 4/0 ground wire to a physical ground.
  - Resistance to ground shall be less than 1 Ω.
- GH2 piping system shall be bonded via metallic piping connections.
  - Resistance to ground at any point in the piping system shall be less than 25 Ω
- Gas panel components shall be bonded/grounded via ground wire # 2/0 to physical ground
  - Resistance to ground for any component shall be less than 25 Ω.
- Electronics racks shall be grounded as required in NFPA 70
  - Resistance to ground shall be less than 5 Ω.
- Lightning protection shall be installed on the H2 vent.

4.10.2 ODH Hazards

Oxygen deficiency hazards exist due to the volume of liquid hydrogen and gaseous helium in the target system. These hazards are effectively mitigated due to the large volume of Hall A, buoyancy, and rapid diffusion of He and H2 in air.

4.10.3 Mechanical Hazards

The vertical motion system presents a mechanical hazard. This system is capable of positioning the target at any position over a 18 in (45 cm) continuous range. This load exceeds 3500 lbf (15.6 kN); therefore, the drive system is capable of causing injury. Further, a chain drive mechanism is used to sync all three ball screw assemblies presenting a pinch and catch hazard. These hazards are mitigated by a guard system which can be removed for maintenance.

4.10.4 Fire Protection

The most likely source of ignition is electrical. As described in the Sections below, there are multiply redundant safety systems that switch off any possible ignition source where hydrogen could reasonably be expected for each failure mode. All electrical equipment subject to hydrogen exposure shall either be interlocked to failure monitors and de-energized, or be intrinsically safe. Electrical installations shall comply with appropriate NFPA Codes.

The engineering firm Mason and Hanger was contracted to consult and perform a full fire protection analysis which was approved by a Fire Protection Engineer (employed by Mason and Hanger), the MOLLER target DA, and the JLAB Fire Marshal/AHJ.

4.10.5 Operator Audible Alarms

A dedicated target operator is required when the MOLLER target has condensed liquid hydrogen in the loop. This operator shall be located in the Hall A Counting Room and shall be required to staff the target 24/7. The exception to this is when the target operator (typically an expert) is located within Hall A as is typically the case for cool down and warm up operations. An audible alarm chassis shall be located in the counting room and in the Hall. These alarms shall include the following:

- Vacuum chamber fault (mechanical pressure switch)
- Exhaust line low pressure alarm (less than 1 psig)
- Gas panel low pressure alarm.
- H2 sniffer alarm (active if H2 is detected above threshold 25% of LEL/LFL)

4.10.6 Fast Shut-Down (FSD) System

The FSD system is typically for accelerator machine protection, but in this case, it shall also serve as an additional safety system. Each FSD signal supplied by the target system shall be 24V DC for normal OK condition and 0V DC or disconnected for fault. Table 11 lists the FSD signals required for the MOLLER target system. Each FSD channel shall be separate, and a chassis developed by the Target Group shall clearly indicate the status of each FSD. FSD testing and verification shall be part of the Hot Checkout procedure. See JLAB Drawing TGT-1060-4001-0001 for logic details.

Table 11: Target Fast Shut Down signals

FSD Description	**FSD Fault Condition**
Target Motion	Target motion system enabled
Chamber Exit Window Cooling	Low flow/high temp
Vacuum Pressure Mech/CC	Vacuum >2e-5 torr
Loop Temperatures	Any temp >25K
Gas panel pressure	H2 pressure less than 20 psia
Exhaust line pressure switch	Fault on pressure in exhaust line less than 1 psig.
Hydrogen sniffer/VESDA	Fault on H2 detection in sniffer
Target Ion Chamber	Signal above threshold calibrated at run start.

4.10.7 Hydrogen Detection

A remote sampling hydrogen detection system shall be installed in Hall A and incorporated into the existing fire safety controls, specifically the Very Early Smoke Detection Apparatus (VESDA). The remote sniffer installed in the target shield bunker allows the detection electronics to be located in a lower radiation environment while sampling the air in the high radiation field of the bunker. Should H2 be detected in the sampled air at a concentration higher than 1% the following functions shall be performed:

- Issue FSD to stop the beam
- Remove power to
  - Vacuum cold cathode gauge
  - Heater power supplies
  - Pump motor power
- Close vacuum gate valves isolating the chamber from the beam line and turbo pumps
- Issue audible alarm in counting house

4.11 Target Instrumentation and Controls

Operation of the MOLLER target requires accurate monitoring of many key parameters. This includes temperature and pressure gauges, heater power, pump speed and power, motion system feedback, etc. Target control must be accessible both locally and remotely and further, must be integrated with safety systems. The target instrumentation and control system meets these requirements by integrating commercially available components and custom chassis with an EPICS based distributed I/O allowing remote control of the target system from any location within the Accelerator Control Firewall. Similar systems have been in successful operation for more than two decades. Chassis for the target control system are installed in equipment racks located in the same position as the standard cryogenic target controls rack; this location is upstream and beam right of the target behind a shield wall.

4.11.1 Instrumentation

Multiple types of instrumentation are required for the target system. These are summarized in Tab. 12. This instrumentation provides temperature, pressure, position feedback, power, etc. to the target control system as well as local observation and operation.

Table 12: Target instrumentation

Instrument	**Function**
8 Cernox RTD	Temperatures in loop at (4) key locations
4 Cernox RTD	Temperature in He system on supply/return
4 Platinum RTD	Solid target temperatures
Tachometer	Shaft speed on pump
(2) CC gauge	Chamber vacuum
Convectron gauge	Chamber vacuum
(4) Pressure transducers	H2 gas pressure at key locations on gas panel and in the relief line
Heater power supply	Voltage/Current to heater

4.11.2 Controls

The central hub of the control system is an IOC, or single board computer, installed in a VME crate located in the Hall A labyrinth. It is located in this position to minimize the radiation load on the computer. This practice has been proven to reduce the number of reboots required to essentially zero during a run. The IOC operates a custom EPICS database which is available via network to linux PCs running a user interface software package written in EDM. These PCs must be located behind the Accelerator virtual firewall. The IOC is connected via bus extender to a VME crate located in the target control equipment racks. This crate houses several ADC and DAC cards as well as DIO and serial communication modules. These modules in turn send/receive signals from various special purpose devices. These devices are listed in Tab. 13.

Table 13: Control device summary table

Device	Make/Model	Function
Temperature monitor	Lakeshore 218	Local display and calibration of RTDs
PT readback	JLAB	Local display and conversion for pressure transducers
JT valve controller	JLAB	Local/remote display/ control of JT valve and valve position
Warm return controller	JLAB	Local/remote display control of warm return valve
Tachometer readback	JLAB	Local display and conversion of pump motor tachometer
Heater Power Supply	TDK Lambda/TBD	DC power supply for heater in H2 loop
Motion system PLC	Koll Morgan BDS5	Motion system controller.
Aux Heater Power Supply	TDK Lambda/TBD	DC power supply for auxiliary heater
FSD breakout	JLAB	24V logic conversion for FSD system IOC EPICS database
VME crate		Carrier boards for IPs (ADC,DAC, Serial . . .)
I/O controller	Power PC	Integrating control computer

5 Spectrometer

In this chapter we describe the spectrometer subsystem (see Fig. 51), which includes everything inside the magnet enclosures and beamline (and their supports) in the region downstream of the exit window of the scattering chamber to the end of the hall. This includes the set of warm magnets, the collimators which define the acceptances, the lintels and collars which shield components, including the main detectors, as well as the detector window, beampipe itself, and the bellows. It also includes the necessary water and power supplies, connections, and the required instrumentation. The first section describes an overview of the open spectrometer concept and the physics requirements it must satisfy. The following sections provide details of the design.

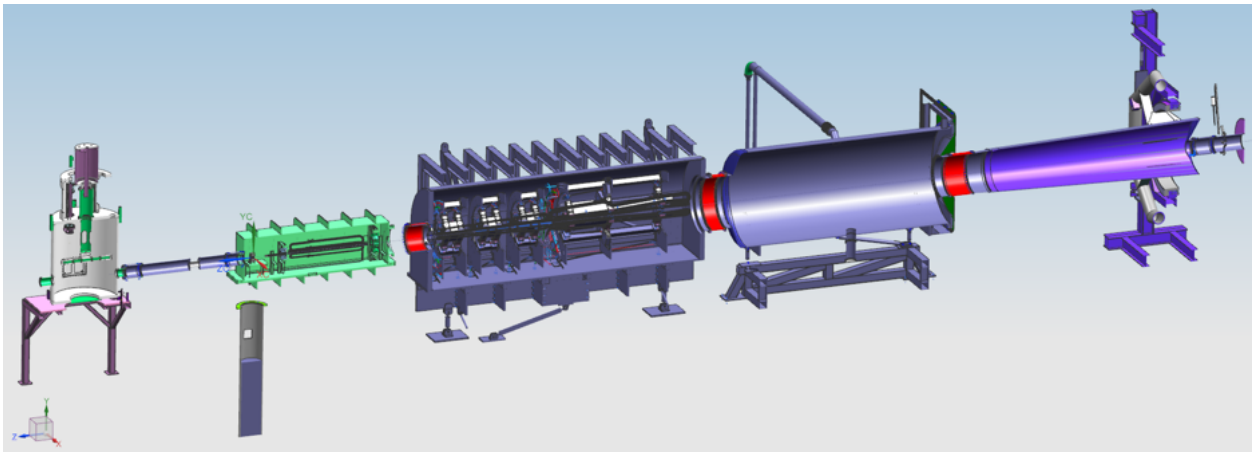

Figure 51: *Spectrometer subsystem and scattering chamber with a centered vertical cut plane. The beam enters from the left side of the page and enters the scattering chamber (not part of the spectrometer subsystem). There are two magnet subsystems, the upstream and downstream magnets and enclosures. Following the downstream enclosure is the drift pipe, then the detector pipe and neckdown pipe for the small angle monitors (SAMs) at the end of the hall.*

5.1 Overview and Physics Requirements

In this subsection we describe the physics requirements and give an overview of the spectrometer system. The spectrometer consists of 5 resistive toroidal magnets (TM0-TM4) with 7-fold symmetry around the beam axis, each with 7 coils (SC0-A through SC0-G for TM0, *etc.*). The upstream (US) magnet and the first 3 subcoils of the downstream (DS) magnet set are essentially racetrack coils, and the fourth subcoil in the downstream magnet has a more complicated shape (see Sect. 5.1.3). The magnets provide the necessary kinematic separation of the scattered electrons and the focal plane distribution for determining the Møller asymmetry to the required precision. The primary collimators define the acceptance for the signal, $5 < \theta_{lab} < 20$ mrad over half the azimuth. They also define the "unscattered beam", up to $5\times$ the multiple scattering angle in the target, which must travel to the beam dump with as few interferences as possible. Other collimators, lintels and collars ensure there is a "2-bounce" system to shield the detector plane from backgrounds. Additional shielding elements are necessary to protect the experimental components, such as the epoxy which surrounds the coils. Two movable collimator-like components, the sieve and blocker, which will be used for systematic studies, are located upstream of the upstream magnet. The larger shield walls and bunkers (not shown in Fig. 51) are not part of the spectrometer subsystem.

5.1.1 Open Spectrometer Concept

The MOLLER spectrometer is an "open", rather than high resolution, spectrometer. It moves the electrons away from the beamline and provides separation of the electrons which scatter via different processes in the target, allowing for the identification of the signal Møller electrons. The Møller electrons have a strong energy angle correlation, shown in Fig. 52, while the electrons that scatter elastically from the target protons have close to the incident beam energy of 11 GeV. The acceptance of the experiment is defined by collimator

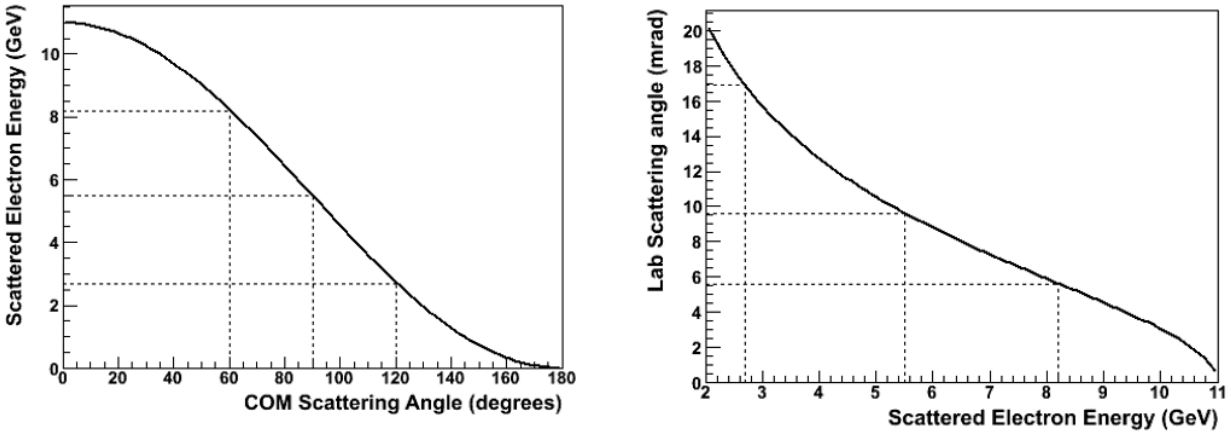

Figure 52: *On the left is a plot of the scattered electron energy in GeV as a function of the center-of-momentum (COM) scattering angle in degrees. The figure on the right shows the lab scattering angle in mrad vs. the scattered electron energy in GeV. The dotted lines show the 90° COM angle and ±30°*

2. The acceptance defining and "cleanup" collimators (collimators 2 and 4, respectively) are circular disks with 7 equally spaced approximately trapezoidal openings, with the coils placed in the shadow of the closed sectors (see Fig. 53). Each of the 7 open and 7 closed sectors are "semi-septants". The closed sectors provide some shielding for the epoxy around the conductor and help to localize the sources of backgrounds. Both the scattering angle θ and azimuthal angle ϕ ranges of the Møller signal are defined by collimator 2, and no other apertures throughout the experiment. This collimator is located upstream of all magnetic elements so that the acceptance does not change with fluctuations in any of the magnetic fields (though the position on the detector plane may).

Møller scattering is identical-particle scattering, so it is possible to achieve full azimuthal acceptance for scattering events, even with half the azimuth blocked (see Fig. 54). Every forward scattered electron has a corresponding backward scattered partner on the opposite side of the beamline in the lab frame. By accepting both the forward and backward scattered electrons on one side of the beamline, all the information about the scattering is collected for the part of the angular range that is symmetric about 90° in the COM frame. The range of lab scattering angles for MOLLER is $5 < \theta_{lab} < 20$ mrad, corresponding to approximately $60^\circ < \theta_{COM} < 120^\circ$, resulting in a large energy range for the scattered Møllers of $2 < E' < 8.5$ GeV. The spectrometer is designed to focus the Møller electrons into a radial peak at the detector plane. While any odd number of coils would work, a configuration with only 5 coils has fields that are not uniform enough to provide the right azimuthal (de-)focusing, and 9 coils don't have enough space to fit all the necessary current at low radius.

The primary processes that make up the irreducible background in the detectors are the elastically and inelastically scattered electrons. The elastic electrons (ep's) predominantly scatter with an energy close to the incident energy of 11 GeV and form a lower radius peak at the detector plane. The ep's can undergo

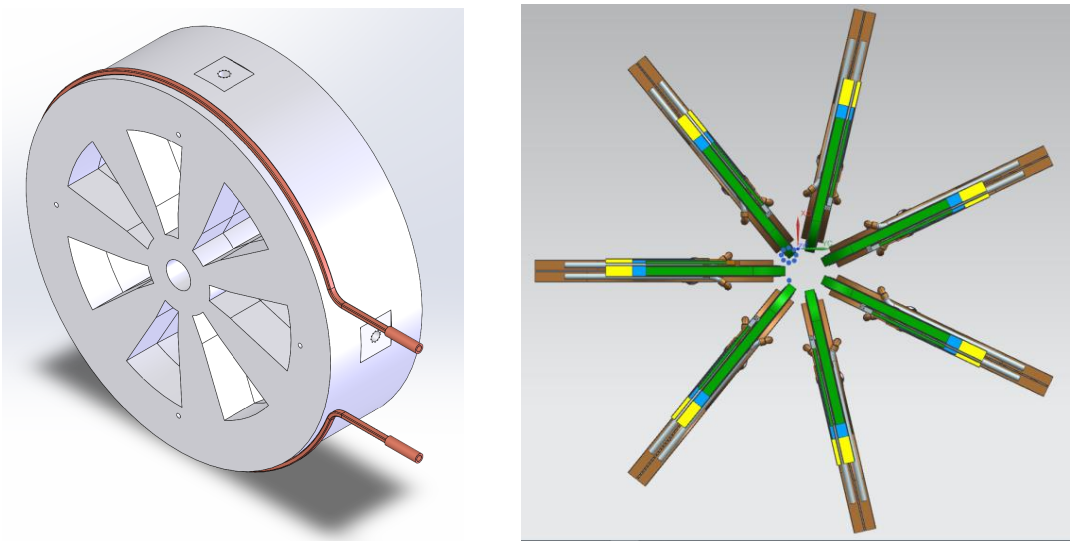

(a) "Cleanup" collimator 4 (b) End view of coils

Figure 53: *The acceptance defining collimator as well as the cleanup collimator 4 (a) have a central bore for the unscattered beam, with 7 symmetrically placed approximately trapezoidal openings which define the angular acceptance for the signal Møller electrons or to block backgrounds, respectively. They are oriented so that the closed sector is to beam left to block the synchrotron radiation created into the bend coming into the hall. The coils (b) seen looking downstream, are oriented so that they are in the shadow behind the blocked sectors of the collimators.*

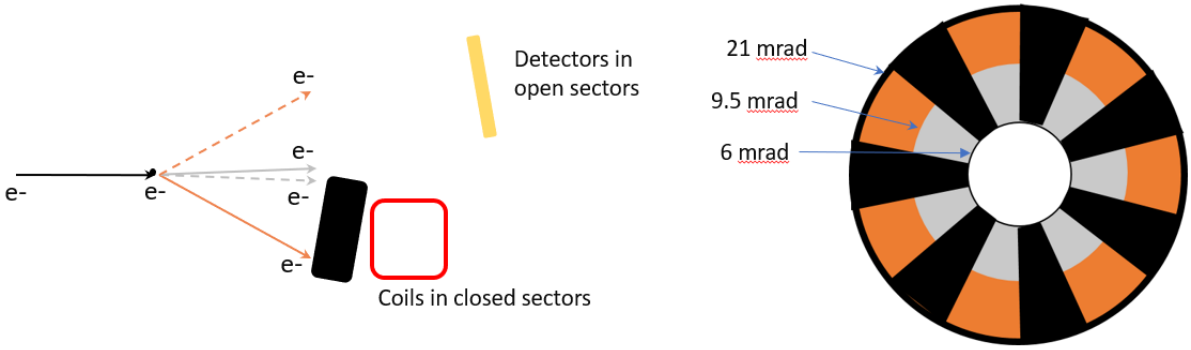

Figure 54: *This figure shows how full azimuthal acceptance can be achieved for the Møller events. On the left is a scattering diagram showing the scattered electrons from two scattering events. The electrons with the dashed lines are from one event, and the straight lines correspond to the other. One electron from each event goes into the closed sector (indicated by the black trapezoids on the right), and one from each event goes into the open sector (the grey and orange regions). The grey color indicates the forward scattered electrons and the orange indicates the backward scattered electrons.*

radiative processes in the target pre- or post-scattering that cause them to lose some energy. This results in a "radiative tail" that is swept out into the Møller peak. This causes a dilution of the Møller asymmetry

which we can deconvolve (see Sect. 7.4) due to the azimuthal segmentation of the detector array (see Sect. 6). Because the electrons which scatter inelastically from the protons in the target (inelastics) have lower energy, they also have a tail that appears in the Møller peak.

Photons are considered a "reducible" background because they feel no effect from the magnetic fields and can be effectively separated from the Møller peak. It is possible to create a "2-bounce" system such that a photon would have to undergo two "bounces" or interactions (with considerably reduced probability) in order to make it from the target to the detectors. Another way to say this is not only is there no line-of-sight from the detectors to the target, but no line-of-sight from the detectors to anything that "sees" the target. In order to achieve this, it is necessary to have a moderate vacuum ($\sim 10^{-2}$ Torr) for as much of the electron's trajectory from target to detectors as possible, otherwise interactions in the air result in bremsstrahlung photons which completely swamp the signal in the detectors.

The collimators form an inner photon envelope (IPE) that gets through the central bore and 7 outer photon envelopes (OPE) which get through the acceptance openings. A system of lintels and collars eliminates potential backgrounds which could come from these envelopes intercepting and scattering from items throughout the experiment. These are strategically placed to keep the weight to a minimum. The lintels, collars and cleanup collimators cannot intercept the Møller envelopes at any point, though they may intercept the ep envelope in places if necessary.

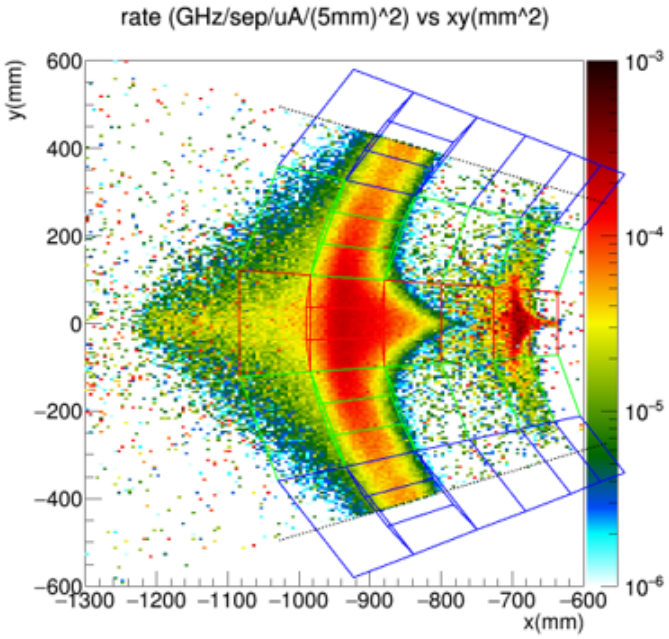

Figure 55: *2D rate-weighted particle distributions in a single septant at a plane located 26.5 m downstream of the target center. In this figure, the beam center (x=0, y=0) is off to the right of the plot. The lines indicate the individual quartz pieces in the detector array concept. The open (red), closed (blue) and transition (green) sectors indicate whether the quartz is wholly within either the open or closed sector, or partially in each (transition). The different particle species peak in the second ring from the center (ep's, Ring 2) and the fifth ring from the center (Møllers, Ring 5). The Møller electrons spread out to cover the full azimuth, and even into the adjacent septants.*

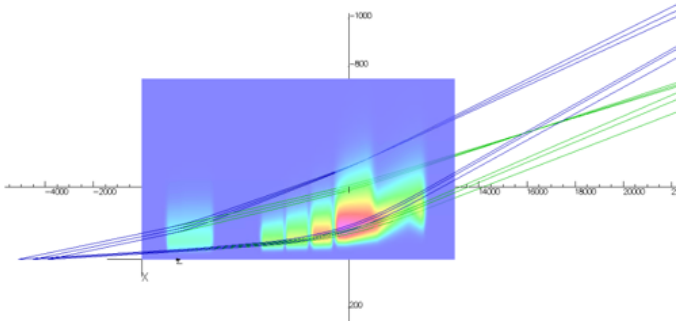

(a) Field at center of open sector with tracks superimposed.

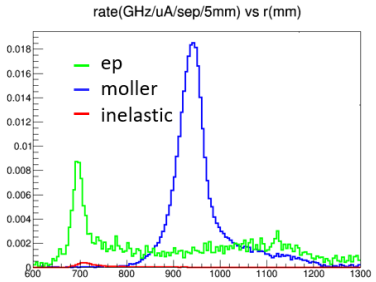

(b) Radial distribution of particles at the detector plane.

Figure 56: *The figure on the left shows a superposition of the relative field magnitude (blue is zero field and red is the highest field) required to produce the desired particle distributions. There are two sets of tracks superimposed on the field plot, one for the Møllers (blue) and one for the ep's (green). Each set has three low angle tracks and three high angle tracks, for particles originating in the middle, upstream and downstream ends of the target. The figure on the right shows the resulting rate-weighted radial distribution of the Møller (blue), ep (green) and inelastic (red) particles at the detector plane.*

5.1.2 Distribution at the Detector Plane

The distribution of the various particle envelopes at the detector plane (see Fig. 55) facilitates the deconvolution of the Møller asymmetry. The collimators define the angular acceptance, and because the different processes have different energy-angle correlations, they form peaks at different radial ranges after being kinematically separated in the magnets. The magnets also affect the azimuthal distribution of the particles. Electrons which pass between the inner legs of the coils as they go downstream are azimuthally focused. If they pass between the outer leg of the coils, they are azimuthally de-focused. The lower energy Møllers are de-focused until they completely fill the azimuth, reducing the rate density on the individual quartz pieces. The higher energy ep's are de-focused to a lesser extent. Most importantly, the inelastics are separated kinematically into different quartz pieces, which is essential for determining the inelastic asymmetry (see Sect. 7.4).

The detector array concept is also shown in Fig. 55 with the particle distributions in a single septant at a plane located 26.5 m downstream of the target center. The Møllers and ep's peak in different radial ranges (Ring 5 and Ring 2, respectively). The segmentation of the detector array allows for different ratios of Møllers to backgrounds in each of the detectors, allowing for the deconvolution of the asymmetries from the various background processes. Accurate modeling of the magnetic fields (conductor locations) is necessary to provide knowledge about the rate distributions, which will be verified using the tracking detectors during dedicated low current running and the monitoring of the detector asymmetry widths during normal running.

5.1.3 Field Distributions

In order to achieve the desired particle distributions at the detector plane, the locations of the conductor were optimized within the available space in the experimental hall. The spectrometer must focus a large range of Møller electron energies and angles. The conductor locations and high current densities are necessary to provide adequate ep/Møller separation at the detector plane. The current distribution is designed so that the field will be greatest for the low angle, high energy Møllers, and smallest for the higher angle, lower energy Møllers (see Fig. 56). The relative field in the figure goes from zero (blue) to the highest magnitude (red). The particle tracks originate in the upstream and downstream ends and the middle of the target, with

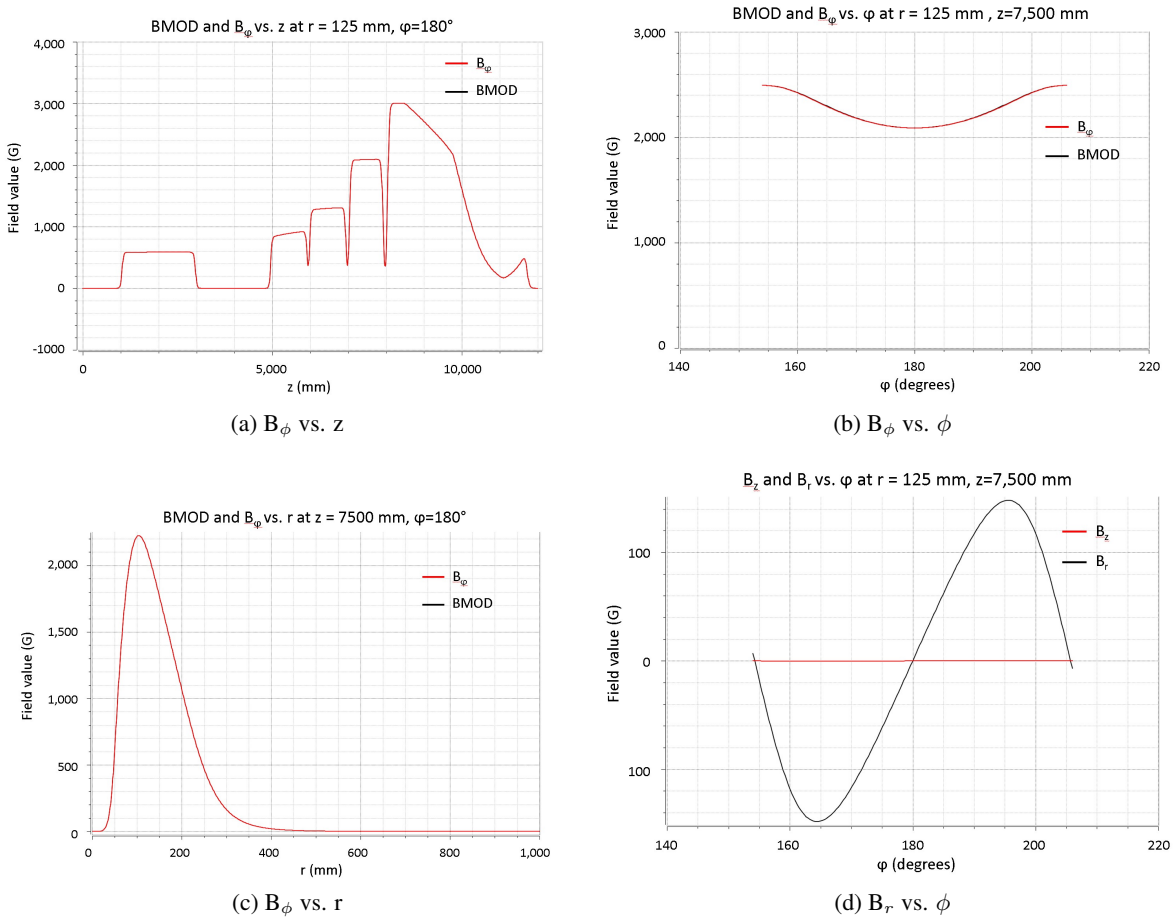

(a) B_ϕ vs. z

(b) B_ϕ vs. ϕ

(c) B_ϕ vs. r

(d) B_r vs. ϕ

Figure 57: *Plots of the radially-focusing component of the field, B_ϕ vs. z (a) (along the beamline) at the center of an open sector and a radius of 125 mm, vs. ϕ (b) (along the azimuth) at a radius of 125 mm at z=7,500 mm (the center of TM3), and vs. r (c) at the center of an open sector in the center of TM3. The fourth plot (d) is of the azimuthally (pre-)focusing component at the center of TM3, at a radius of 125 mm, which is just outside the conductor at the inner leg of the coil.*

the lowest angle ($\approx$ 5 mrad) and the highest angle ($\approx$ 20 mrad) for both the Møller (blue) and ep (green) electrons. The total NI (and hence the $\int B \cdot \ell$) increases as the particles move downstream (as the separation between the Møller and ep electrons increases, see Fig. 57, (a)). The current distribution moves out in radius going downstream to reduce the field experienced by the ep's. This results in the Møller and ep radial peaks shown in the right side of Fig. 56. At a given z location, the field increases as a function of radius, until the radius is larger than the current distribution, and then falls off as approximately $1/r$ (see Fig. 57, (c)), until it reaches the radius of the outer leg of the coil, where it drops off faster as the opposite current cancels the field from the inner leg. The radially focusing component of the magnetic field is the azimuthal component, B_ϕ. The radial distribution of the particles can be reasonably approximated using a series of kicks estimated using an estimate of the angular bend due to each magnet

$$\alpha\,[rad] = \frac{\int B \cdot d\ell\,[Tm]}{3.33E\,[GeV]} \tag{12}$$

as shown in Fig. 58. In practice it is necessary to use the field at the radius the particle will have based on the drift after the previous kick (plots like 57, (c) for each magnet/subcoil). The upstream torus provides

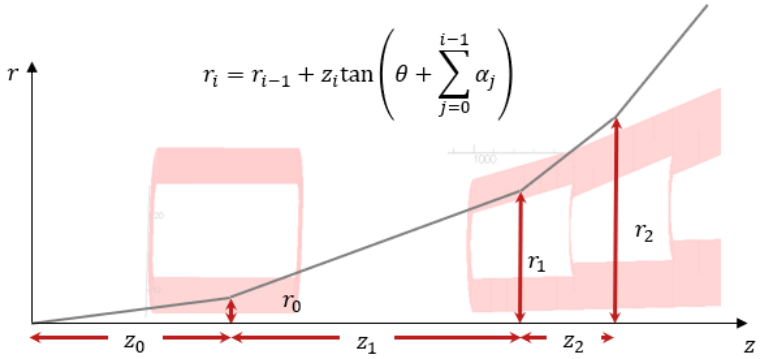

Figure 58: *This figure shows how to approximate the radial focusing of the spectrometer system using a series of radial kicks. The* $\int B \cdot d\ell$ *and z location of the center of the straight sections determines the radial focusing.*

pre-bending before the particles enter the downstream torus. There is a bigger space between the upstream magnet and the set of four downstream magnets in order to allow for the ep's and Møllers to drift apart radially. This makes it easier to "sculpt" the field in the downstream magnet set.

The magnets are far from ideal toroids, which results in some deviation from the ideal fields. The magnitude of B_ϕ "sags" in the center of the azimuth due to the distance from the conductor (see Fig. 57, (b)). At the center of an open sector, the radial component of the field is zero, as expected for an ideal torus, but near the conductor the magnitude of the B_r component increases. The sign of the B_r component changes from one side of the open sector to the other, and depending on whether the location is between the inner or outer legs of the adjacent coils. This is seen in the plot of B_r in Fig. 57,(d), which shows B_r as negative at the left and positive on the right for low radii. At the larger radius, the signs are reversed. Thus the lower angle particles experience some azimuthal pre-focusing in particular in the upstream magnet, because they pass between the inner legs of the coils. Closer to the edge of the azimuthal acceptance (near the coils) the effect is bigger due to the relative magnitude of the radial component of the field. If they pass between the outer legs of the adjacent coils, the electrons experience azimuthal de-focusing. The effect depends on the energy of the particles as well, thus the effect is greatest for the low energy, high angle Møllers. The effect on the inelastic electrons is essential for the determination of the inelastic asymmetry because it separates them into different quartz pieces which roughly correspond to different W bins (see 7.4.1).

Until now we have focused on the particle distributions at the detector plane, but they actually have a complicated trajectory depending on not only their scattered angle θ_{lab} but also the initial azimuthal angle, due to the azimuthal (de-)focusing near the conductor. In order to communicate the various particle "envelopes" defined by these trajectories to the engineers, an object is created from the distributions for each particle type at equally spaced z locations throughout the experiment. The outer envelopes at each z location are chosen automatically by plotting the rate-weighted distribution vs. x for bins in y, and for y in bins of x, and choosing the locations where the rate drops to some fraction of the maximum rate in that bin. Figure 75, in Sect. 5.2.2, shows an example set of particle envelopes at a particular z location within the downstream magnet. They are shown as single particle types (Møller, ep, and inner and outer photon envelopes) in different septants so that they can be distinguished. These envelopes are produced from rate maps produced in the full simulation (including radiative corrections) and are provided to the engineers to be imported into the CAD files. The Møller envelope is the absolute keep-out zone, and the other envelopes are considered

keep-out zones which are possible to be violated *if absolutely necessary*. Another way to visualize this is a side view of a single septant showing the ray traces from various particles (Fig. 59). The coils are shown in the same plane as the collimator openings for comparison.

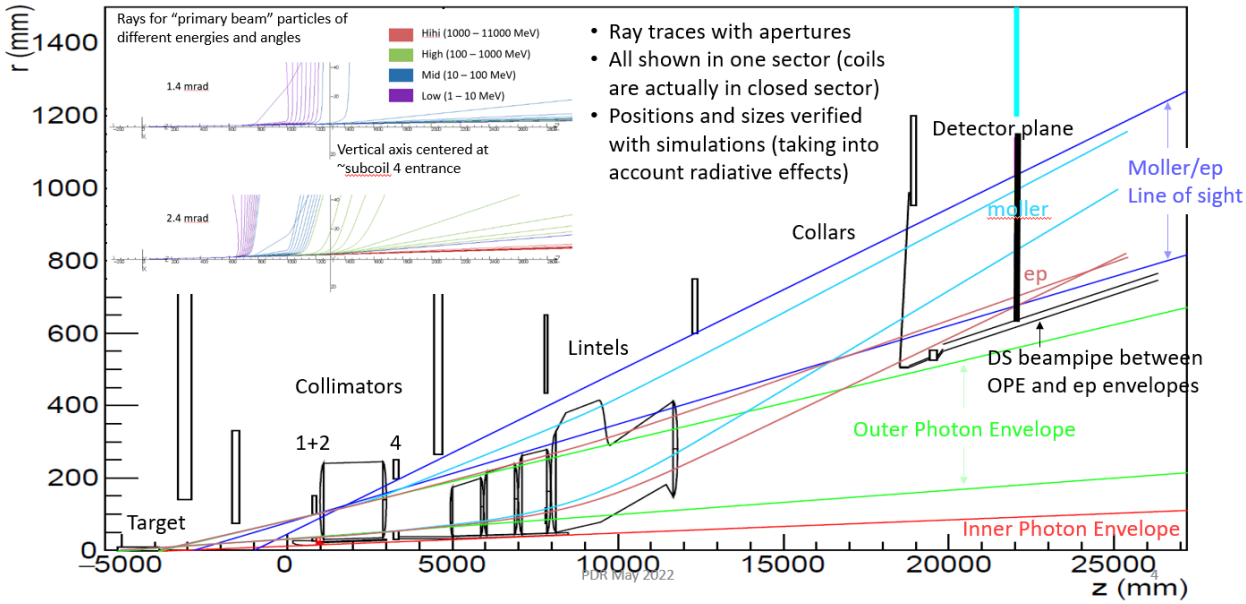

Figure 59: *Conceptual drawing of the various particle ray traces in a single septant, including the inner and outer photon envelopes and the Møller and elastic ep envelopes. The coils are pictured in the same plane as the collimator openings for comparison. As part of the 2-bounce system philosophy, no material should be placed within line-of-sight of the target, which means the conical inner photon envelope as well as the outer photon envelopes. In the upper left is an overlay showing the deflection of the beam by the stray fields along the beamline.*

5.1.4 Tolerances on positions

In order to accurately interpret the Møller scattering parity-violating asymmetry measurement, one must carry out a calibration to evaluate the effective analyzing power of the apparatus, which appears as a normalization factor.

In practice, it is necessary to determine the acceptance function, or the rate-weighted position and asymmetry distributions based on the initial scattering variables. The acceptance-defining collimators are placed upstream of any magnetic elements to eliminate changes in the acceptance due to the absolute scale of the magnetic fields. Special low (beam) current tracking runs will be performed periodically to measure the acceptance. Knowledge of the rates in each of the quartz detectors will be informed by simulation, which requires accurate knowledge of the as-built coils.

Table 14: *Summary of the position tolerances based on the single coil/single offset study.*

Offset	Sensitivity (mm)
z	97
r	3
ϕ	64
roll	6
pitch	45
yaw	97

In order to assign position tolerances for the coils, several considerations were taken into account. First was the determination of the sensitivity of the asymmetry determined with incorrect fields to position and orientation offsets (r, z, ϕ and roll, pitch and yaw) for a single coil in a

single septant. The tightest tolerance comes from offsets in the radial position, while the ability to determine the asymmetry to the required precision is largely insensitive to other types of offsets. Rotation sensitivities are presented as an allowed position offset along that dimension (half-radius for roll, half-length for pitch and yaw). The position tolerance of the coils is set at $\pm$ 1 mm at the inner radius of the coils and $\pm$ 3 mm at the outer radius, with the tighter tolerance at inner radius needed to avoid interference with the signal envelopes. Using the tolerances thus determined, coils were modeled such that they were offset in the worst possible configuration within those tolerances, including distortions of the coils. This conductor configuration was used to check both that the unscattered beam could travel cleanly to the beam dump, and also to design shielding for the coil epoxy to protect it from radiation damage.

Several additional effects have been considered, including temporal stability in the power supplies and fluctuations in the coil temperature. These effects are mitigated by forming asymmetries over short time scales (to avoid helicity correlations) as well as averaging over the length of the experimental run. Based on the effect of variations in the power supply current (linear with field values), the variation over a 24 hour period should be within $\pm$ 500 ppm (at the nominal operating current). The maximum variation of coil temperature from nominal should be no greater than $\pm$ 3 °C over a 24 hour period to ensure that the motion of the coils is within acceptable limits.

5.2 Torus magnet subsystems

In this section we describe the resistive toroidal magnets that satisfy the optics requirements of the MOLLER experiment, as described in Sect. 5.1, as well as the collimation that defines the acceptance, the magnet enclosures and supports. The spectrometer consists of five magnets, each made of resistive, water-cooled copper coils with 7-fold symmetry around the azimuth. The length of the magnets is limited by the available

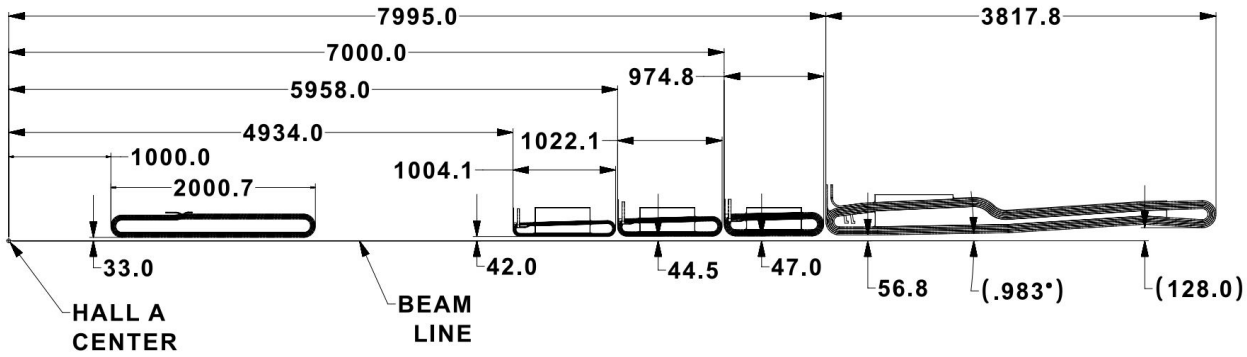

Figure 60: *Side view of coils with the same vertical and horizontal scale. Only a single septant is shown for visibility. The upstream torus is approximately 2 m long and separated from the downstream torus by ≈2 m. The first 3 subcoils of the downstream torus are each approximately 1 m long, and the fourth has an overall length of about 4 m. The upstream and downstream toroids are housed in separate vacuum enclosures.*

space in the experimental hall, and the total NI is limited by the available space in the azimuthal direction (around the beamline) as well as ensuring the ability to power and adequately water-cool the magnets. The upstream (TM0) magnet is separated by a larger distance along the beamline than any of the downstream magnets (TM1-4) from each other (see Fig. 60), and so requires a separate vacuum enclosure, both of which will be described in their respective sections. The conductor (current distribution) and coil construction and supports are described in detail here, and the necessary water and power connections and instrumentation are described.

5.2.1 Upstream Torus

The upstream magnet chamber and enclosed hardware are shown in Fig. 61. All the hardware enclosed in

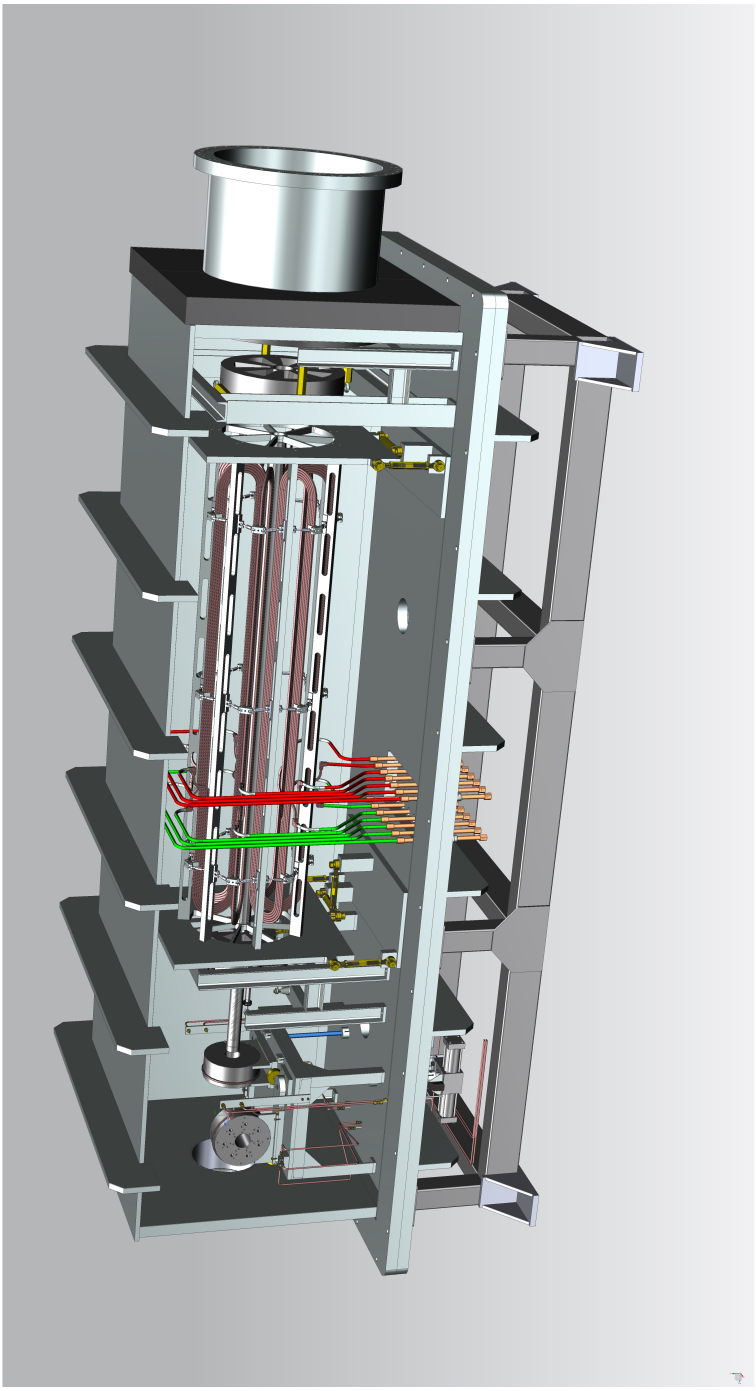

Figure 61: *Isometric view of the upstream enclosure (rotated by 90° to fit on the page) with the enclosure set to transparent. Inside the enclosure from upstream (left in the figure) to downstream are the sieve and blocker, collimator 1+2, support bulkheads in blue, the coils, water and power leads going to the bottom plate, additional bulkheads and then collimator 4 near the downstream end.*

the upstream vacuum chamber is designed with several considerations. The upstream torus is near the target, and so is designed to require no hands-on servicing during the duration of the experiment to meet ALARA goals. The material selection is compatible with the high radiation flux and excludes ferrous materials that could result in backgrounds with large asymmetries. Alignment, including the movable sieve and blocker, does not require checking during the experiment. Because no remote adjustment of individual components is possible, all hardware is designed for low deflections and repeatable movement. No instrumentation is contained inside the vacuum chamber to reduce the risk of degradation and if there are failures, the instruments are far from the highest radiation areas.

The upstream coil package contains seven individual coils that are each a single layer pancake of high conductivity copper with a cross section of 9 by 9 millimeters with a circular hole of 5.7 mm diameter for water cooling. The maximum current density in the coils is approximately 20 A/mm^2, as determined from early design and testing. The maximum ΔT of the cooling water is 30°C and it is expected to have an inlet water temperature of 28°C. All cooling paths through the upstream coil package were designed to allow for flow, power and temperature interlocks to be external to the vacuum chamber. The power connections to each of the seven coils enter the vacuum chamber through a slightly modified MPF ceramic feedthrough that carries water flow and current to each coil. The water is in parallel and the current is in series. A single coil can be fully hydraulically and electrically tested outside the vacuum.

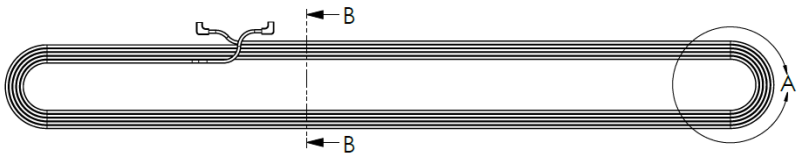

Figure 62: *Upstream coil package, view from the side.*

A single coil of the seven-coil spectrometer is 2 meters long, and is placed 33 mm radius from the beam central axis. The upstream part of the coil is 1 m downstream of the Hall A center and 5.5 m from the center of the hydrogen target. The coil is a conventional air core racetrack with best practices of potting and winding for use in high radiation. It is vacuum impregnated coil with fiberglass tape, half-lapped to provide both turn-to-turn insulation and turn-to-ground insulation that is potted in a cyanate ester resin CTD-403 epoxy. Extensive testing was done to quantify the strength of the epoxy after exposure to radiation doses similar to what will be seen in the MOLLER experiment coils. The CTD-403 is similar to the selected resin for the ITER TF coils in France for similar reasons.

Supports The seven coils are supported on the inner radius by the two-bounce shield. The two-bounce shield is a 72 mm outer diameter tungsten tube with a 54 mm ID bore and its function is to shield two bounce photons from the experiment. It will be gun drilled on the 2 m long inner diameter and conventionally turned and milled on the exterior.

The entire two-bounce shield and 7 coils are supported on a strong back frame that uses a kinematic mounting system similar to systems used extensively in other large nuclear and particle physics installations. A completely brass adjustment strut is used in the upstream support. It is expected the coil package can be adjusted to approximately 200 microns using this alignment system and laser trackers. An entire alignment procedure will be developed in collaboration with the Jefferson Lab alignment group. Downstream of collimator four is more passive lead shielding to limit background to the experiment detectors. This system consists of a circular internal lead ring that has direct line of sight to the background going down the beamline and larger rectangular lead block supported outside the vacuum.

Figure 63: *Brass struts for use in the US torus enclosure.*

Enclosure The Main large vacuum chamber dimensions are shown below. It was designed to be completely non-magnetic by using welded 6061 Aluminum plates. The welding on the exterior will be done by MIG welding with either 4043 or possibly 5356 wire. All vacuum quality internal welds need to be TIG welded. This choice is still being investigated but either wire is stronger than the heat affected regions in the 6061 weldments. The chamber was designed from the deflection parameter and thus the stresses are well within allowable limits. FEA calculations were done to fine tune deflections version plate thicknesses and final FEA versions in ANSYS are being completed.

Collimation and Shielding The upstream torus chamber contains a number of tungsten collimators whose job is to absorb and shape the spray of particles coming off the target upstream. Two of these collimators will be able to move in and out of the beam via remote control in order to conduct diagnostic measurements (see Fig. 64). The remaining collimators will be fixed in a single position for the duration of data collection. The complete list includes the following two movable collimators (for diagnostics) - the blocker and sieve collimators, as well as fixed collimators 1+2, 4, and the "2-bounce shield" which ensures that photons must go through at least 2 bounces to reach the detectors. All of these collimators are specified to be 99.9% pure tungsten, for a total of about 1900 lb of the sintered metal. The addition of small amounts ($<$1%) of lanthanum to aid machining is acceptable. Tungsten-Copper materials might also be used for these components, with the primary disadvantage being the reduction in density and therefore a slight increase in re-scattered background.

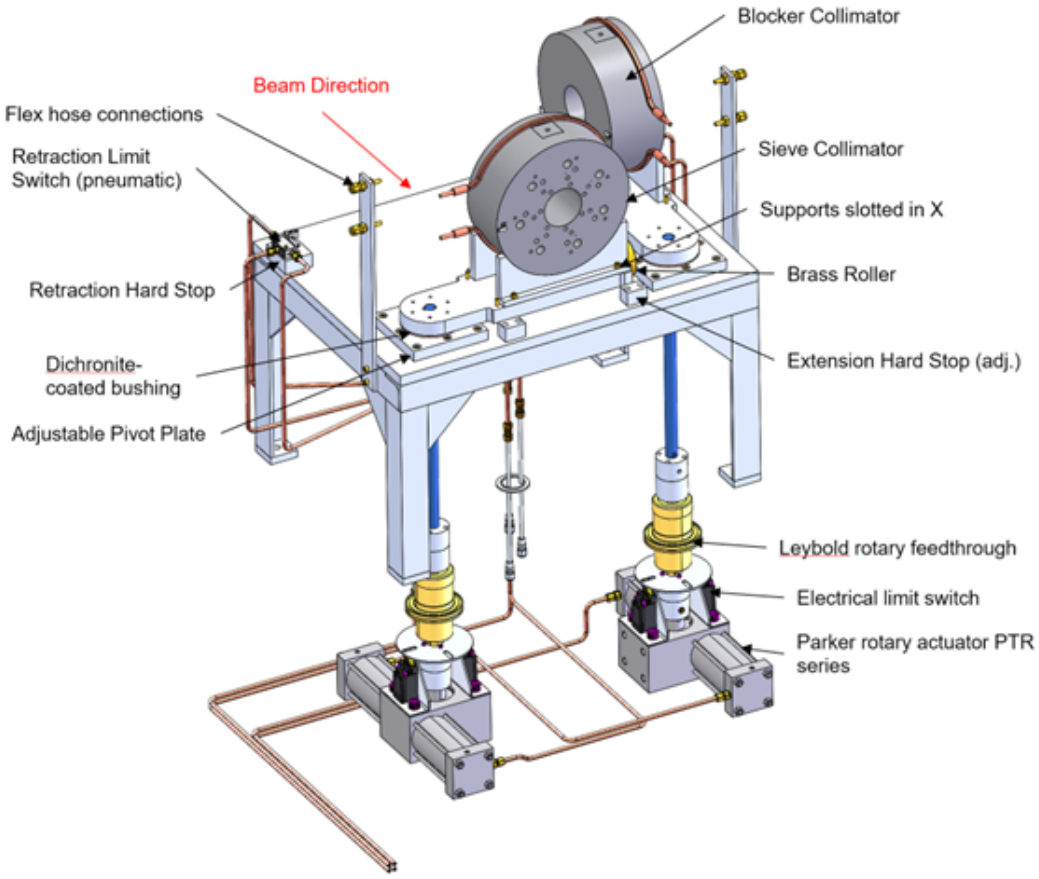

Figure 64: *CAD view of the movable collimator subsystem, from downstream, with major components labeled. The sieve and blocker will block part or all of the acceptance in order to do acceptance and background studies, respectively.*

Movable collimators Two movable collimators will be inserted for periodic diagnostics and calibration. The first of these is an annular tungsten "sieve" collimator which will block the entire acceptance except for a pattern of selected holes in different semi-septants. The sieve will be used in low-beam current measurements of scattering from thin ^{12}C foil targets, for verification of the magnetic optics and the acceptance of the spectrometer system (see Sect. 8). The second of these will be an annular "blocker" collimator which will block the entire acceptance using 100 mm (20 X_0) of tungsten thereby suppressing the Møller and ep electrons by a factor of $> 10^4$. This will be used to study backgrounds in the main integrating detectors not arising from GeV-scale electrons from the main acceptance, and also to enhance the signal seen due to pions for calibration of the pion detector system, see Sect. 9.2.5. The blocker collimator will be operated with the full liquid hydrogen target at the nominal full beam current.

The movable diagnostic collimators are located at the far upstream end of the upstream torus subsystem vacuum chamber. They are mounted to pivoting arms on either side of the beamline (see Fig. 64). Control of the motion will be accomplished with pneumatic rotary actuators, with a capacity of 430 lb-in of torque at 100 psi. The two movable collimators will be hardware-interlocked to each other using pneumatic limit switches, such that they can never interfere with each other. When the left diagnostic collimator is signaled to extend into the beam, the pressure is first routed to the retraction side of the right collimator until it

reaches its retraction limit switch (pneumatic). Once the limit switch is activated, the actuation pressure can then travel to the extension side of the left diagnostic collimator actuator. The process is inverted to extend the right diagnostic collimator.

By employing rotary actuators, they can be placed below the chamber where more space is available, and rotary motion can be easily transferred to the vacuum with an off-the-shelf rotary feedthrough, which itself can be shielded. In addition to the hardware-interlock pneumatic limit switches, electrical limit switches are located on the actuator shaft, outside of the vacuum, to give experiment operators real-time readback of diagnostic collimator extension and retraction.

Cooling of the diagnostic collimators will be accomplished by passing 1 GPM of water through a loop of hollow-core, rectangular copper conductor brazed to the outside of the collimators. Neither diagnostic collimator should see more than 1 kW of heat, resulting in a water temperature rise of at most 6.9 °F.

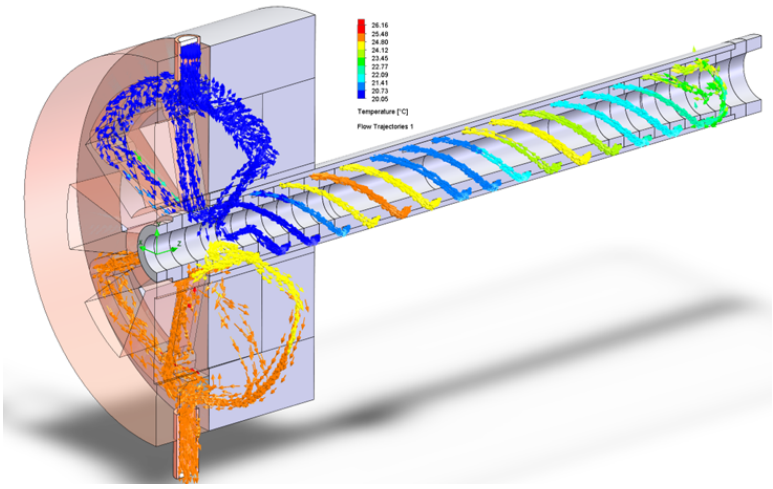

Figure 65: *Collimator 1 and 2 are merged into one item, with integrated water-cooling. A helical water channel moves water from collimator 2 around collimator 1 to its upstream end and back again. Pictured CFD Simulation of collimator 1-2 shows water streamlines colored by temperature. Maximum water temperature is 53.2 °C, maximum tungsten temperature is 147 °C.*

Collimator 1-2 The collimator 1-2 assembly consists of collimator 1, a jacketed, cigar-shaped device about 570 mm long, and a 2-piece disk-shaped collimator 2, with internal cooling passages (see Fig. 65). Water flows into collimator 2 at 4 GPM, travels around the vanes and into the middle, where it passes into collimator 1. The water then flows upstream along 3 helical grooves machined into the core of collimator 1, contained by the jacket. Water turns around about 150 mm from the upstream tip of collimator 1 and returns through another 3 helical grooves to the inner radius of collimator 2, where it completes its circuit out to the cooling plant. During operation, the tip of collimator 1 is expected to get to 147 °C, with the water not exceeding 53 °C.

Fabrication of collimator 1-2 is complex due to the number of brazing operations. There are several water-to-water and water-to-vacuum brazes, the latter of which must be leak-tight. A small amount of water-water leakage can be acceptable, however, the area between the flutes needs to be brazed, as leakage between the core and jacket from supply to return flutes has been calculated to be excessive.

Collimator 4 and the Two-Bounce Shield Collimator 4 is a single piece collimator with a central bore and flared petal openings, similar to collimator 2. It will absorb 1000 W of scattered beam. It can easily be cooled in a manner similar to the diagnostic collimators, with a single 4mm × 6mm hollow-core copper conductor brazed around the outer perimeter, with 1 GPM of water flowing through. The water temperature rise is expected to be 6.9 °F, and the maximum temperature at the center of collimator 4 should not exceed 102 °F (see Fig. 66). The most significant feature of collimator 4 is its mass, approximately 1100 lb.

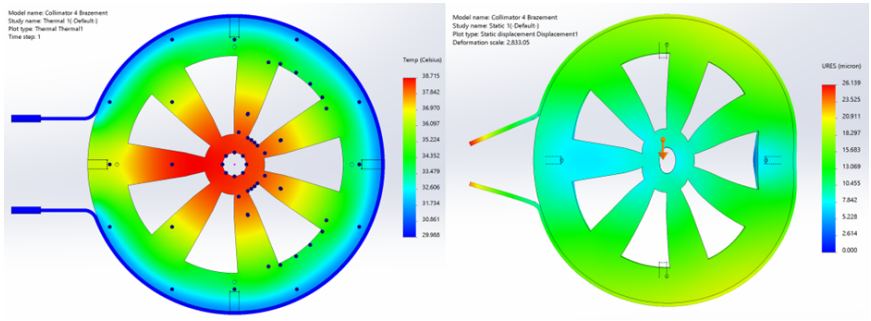

Figure 66: *Collimator 4 simulations showing predicted temperature (left) and deformation (right). Maximum temperature is 38.7°C, and maximum deflection is 26 microns. Deflection is scaled by over 2800x to enhance clarity.*

The two-bounce shield is a long, thin collimator that occupies the space around the beam and within the upstream toroid coils. It is furnished with 7 grooves that the coils will fit into, becoming an intrinsic structural component of the 7-coil toroid. It will be made of several pieces of tungsten brazed to one another. The two-bounce shield will be fixed at its upstream end and allowed to float downstream to allow for thermal expansion. It will absorb about 10 W of power, which will be carried away through conduction to the water-cooled coils.

Collimator Cooling The total collimator heat load is at most 8.5 kW for all collimators. Each collimator will be fed by a separate, parallel circuit split off the primary supply. This will allow independent monitoring of flow and temperature rise for each collimator, and this instrumentation can be placed outside the vacuum and away from the high-radiation area. It is unclear at this point whether temperature sensors will be mounted directly to the collimator tungsten, as the sensors' radiation tolerance is unknown. Each of the collimators will be fed with $\frac{1}{4}''$ copper lines, except for collimator 1-2, which will use $\frac{1}{2}''$ lines. This makes the expected pressure drops across each of the 4 branches approximately equal, between 30.9 and 32.2 psi: very little flow balancing will need to be done. At the time of writing, the planned cooling plant is a welding cooler that exhausts heat directly to air without refrigeration, and has a capacity of 10 GPM at 50 psi.

5.2.2 Downstream Torus

The downstream torus consists of a set of four toroidal magnets placed end-to-end. Each of the magnets has 7 coils placed symmetrically about the beamline. Here we describe in detail the conductor size, shape and stack height as well as the overall shape of the conductors in each downstream magnet (roughly racetracks, except for TM4) including the winding and insulation. The first three magnets' coils are relatively simple racetrack-like coils, with the downstream end having a larger radius than the upstream end so the inner and outer straight sections are not parallel.

[9] Outer r at a different z than the ds end of inner leg due to the negative bend at the outer radius.

Table 15: *Positions of the current at the inner radius part of each of the coils, relative to the hall center. The outer radius of each coil at the upstream and downstream ends is also listed. Note that for the second segment of TM4 (b) the outer radius that is listed is the largest value, at a z somewhat upstream of the end of the inner radius segment.*

Magnet	Central z (mm)	Total NI (mm)	Inner (Outer up, down) r (mm)	Length (mm)	Stack Height (mm)	Tilt angle (degrees)
TM0	1998	5357	33.0 (251, 261)	1778	47.9	0
TM1	5430	8920	42.0 (175, 197)	856	30.1	0
TM2	6463	12200	44.5 (218, 239)	836	43.3	0
TM3	7484	22260	47.0 (266, 276)	748	61.8	0
TM4	9900	33500	56.8 (340, 392)	3567	80.7	–
TMa	8314	33500	56.8 (340, 370)	373	80.7	0.02
TMb	9140	33500	57 (370, 415)[9]	1270	80.7	0.98
TMc	10450	33500	79 (289, 375)	1325	80.7	3.54
TMd	11393	33500	161 (375, 392)	560	80.7	-3.37

The most relevant quantity for the physics result is the location of the straight sections of the coils at the inner radius, and the total current, NI, in that section. Ideally, the 7 coils are positioned symmetrically about the beamline, with a horizontal coil to beam left (looking downstream). The inner radii and stack height can be found in Tab. 15, along with the current in each subcoil, and the width and number of turns for the conductors is shown in Fig. 67. Each of the conductors has a hole to flow LCW to cool the conductors during operation (see Sect. 5.4 for more information about the power and water-cooling).

Everson-Tesla has been chosen as the manufacturer of the downstream coils. A build-to-print design for the magnet coils, based upon extensive electromagnetic (TOSCA) and mechanical (ANSYS) analyses, was provided in the form of 2D drawings and 3D CAD models. As part of the contract, they were required to produce a set of pre-production prototype magnet coils consisting of one of each of the four subcoils (TM1, TM2, TM3 and TM4). The manufacturing process has been observed and the testing process, which includes powering the coils of this pre-production prototype coil set at JLab, has begun for subcoils 3 and 4 (see Fig. 68). JLab has already purchased all the copper conductor, which has been measured to assure that it meets the tolerances for each of the 4 conductor designs. This check will only be on the free end of the conductor and it is incumbent upon the vendor to further check the conductor as part of their fabrication/QA process. The goal of the prototyping is to demonstrate that the coil designs provided can be built as designed, satisfy MOLLER physics requirements, and additionally identify ways of improving quality or consistency and easing the manufacture of the coils.

The coils have braze joints, some of which will carry current but all of the braze joints will be part of the coil cooling water pressure boundary, with the exception of sub-coil 4 where there is a braze plate that connects the left and right pancake coils. The coil vendor is on the Jefferson Lab approved vendors list for welding fabrication. G-10 Glass Epoxy Laminate filler plates are to be potted with the coil. The filler plates are insulated and mounted to the winding table. In order to carry out some of the pressure, water flow and helium leak detection tests, it will be necessary to attach suitable fittings to the coil leads and/or to braze in plugs. Sufficient conductor lengths on each coil for testing allow these to be cut off at the end of testing without compromising the lead length requirements.

CTD-450 is applied to the conductor as a primer, which improves the bonding strength of the potting medium to the coil and its glass-cloth insulation. The conductor is then half-lapped wrapped with glass-cloth insulation and each sub-coil will be wound into the required shape. A ground layer (ground wrap) of

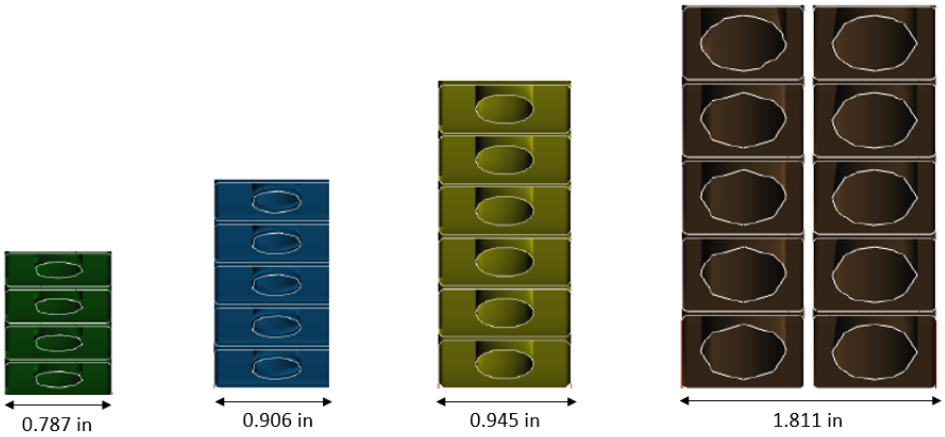

(a) Conductor stacks for each of the downstream subcoils.

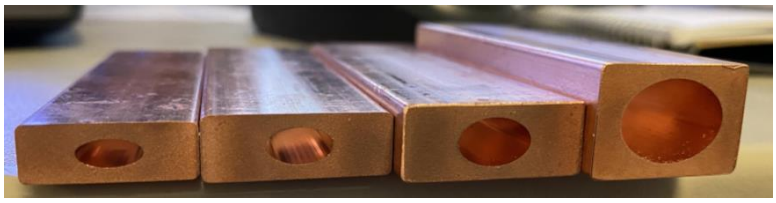

(b) Picture of the 4 sizes of conductor used in the downstream torus.

Figure 67: *The four subcoils in the downstream torus have different size conductors, water cooling holes and number of turns, as shown in the figures above. The first three subcoils are single pancakes of 4, 5, and 6 turns, respectively, and the fourth subcoil is two single pancakes, each with 5 turns.*

half-lapped glass cloth will be applied to each completed TM1, TM2 and TM3 single-pancake coil. TM4 has two pancakes – additional insulation glass cloth will be placed between the two pancakes, before the half-lapped ground layer is applied to the double-pancake coil. The magnet coils are to be wound without splices in individual pancakes. The coils will be vacuum pressure impregnated with CTD-403, a Cyanate Ester resin that has been developed specifically for use in high radiation environments, and has been tested for our particular operation temperatures.

Collimation and shielding The collimators and shielding elements are designed to minimize edge-scattering and improve the signal-to-background ratio at the detector plane. Collimators 1+2 and 4 are described in Sect. 5.2.1. Due to radiative processes in the target, including the electron-proton (ep) scattering radiative tail - there is a swamp of low-energy electrons, some of which make it through the bore of collimator 1 and the collimator 2 openings. The higher angle electrons that make it through the acceptance bend more and can potentially hit vacuum vessels and other elements of the apparatus at larger radius near the detector system. Two collars and a set of lintels are designed to stop these radiative ep-electrons and help to improve the signal-to-background ratio and reduce radiation level inside the experimental hall. The lower angle electrons can make it through the bore of collimator 1 and be bent by the stray field in the bore of the magnets. Collimator 5 and 6a and b (see Fig. 69) block these low-energy beam-like electrons that would otherwise reach the main detectors. The collimators and the clamps they are attached to are shown in their relative positions in Fig. 70. In order to shield the epoxy surrounding the conductors from these low angle electrons, “belly plates” consisting of 3 mm of tungsten are located on the inner side of the coils, with space between them along z to allow for thermal expansion.

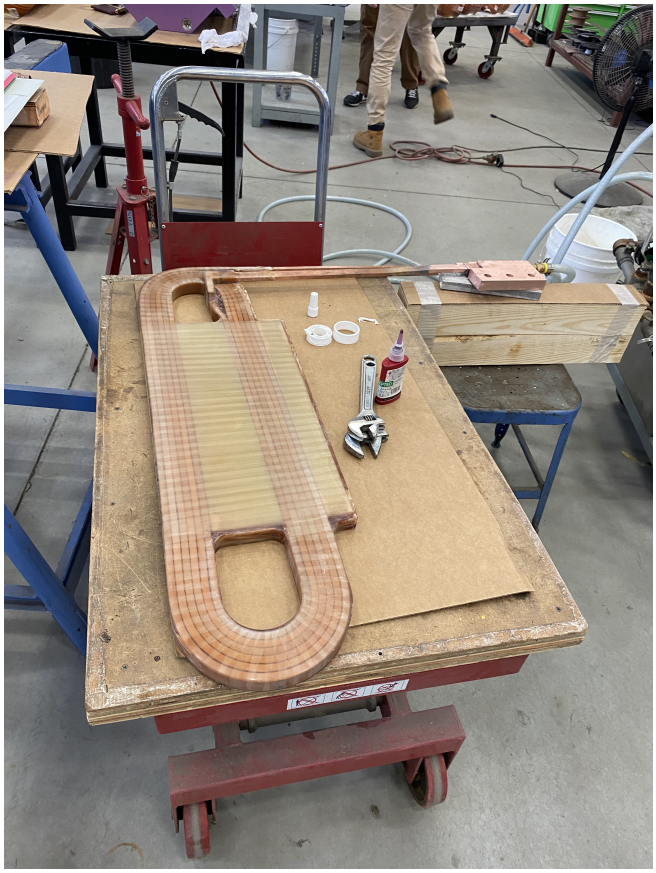

Figure 68: *Picture of the prototype of subcoil 3 during a water test at the manufacturer ETI. The coil is a single pancake with six turns, wrapped in fiberglass tape, (half-lapped) and back-filled with CTD-403 epoxy and cured with the G10 support. The current and water return is routed out at the outer radius of the upstream end so that it doesn't interfere with the particle envelopes.*

Enclosure and supports The DS enclosure (see Fig. 71) is entirely composed of AL 6061 aluminum alloy with all the necessary hardware made of silicon bronze 655 H04. Its main function is to maintain a nominal - 1×10^{-2} Torr vacuum while supporting its internal components. It houses Toroidal Magnets (TM) 1-4, the Photon Scraper and Collar 1. The enclosure has two primary mating components – Top hat and Base plate (see Fig. 71) which are sealed using a $\frac{1}{4}$" peroxide-cured EPDM O-ring. The enclosure is supported by a 7-link alignment system giving a range of motion $\pm$6 mm in all directions. Each link has two stainless steel rod ends and a pin, and an aluminum link body. The top hat is a welded assembly in the form of a mailbox. It has two secondary sealing surfaces that attach to two vacuum bellows. The Photon Scraper is attached to the US end on the Top hat. The base plate is a bolted structure consisting of multiple 2" thick plates. The floor plate of the enclosure is supported by a grid of longitudinal and transverse plates which are fastened to each other via tapped holes. The base plate supports TM 1-4, COLLAR – 1, and the Top hat, a total of approximately 10 Tonnes. The base plate houses vacuum pump-out flanges, TM 1-4 power supply feedthroughs, water cooling feedthroughs, and electrical feedthroughs for I & C. The Base plate is designed to limit the deformation during assembly as well as operation. The peak deflection is less than 0.5 mm after complete assembly. The welded areas have at least a factor of safety of 2 and un-welded regions have at least a safety factor of 5. The coils and collimators are supported by clamps (see Fig. 70) which are

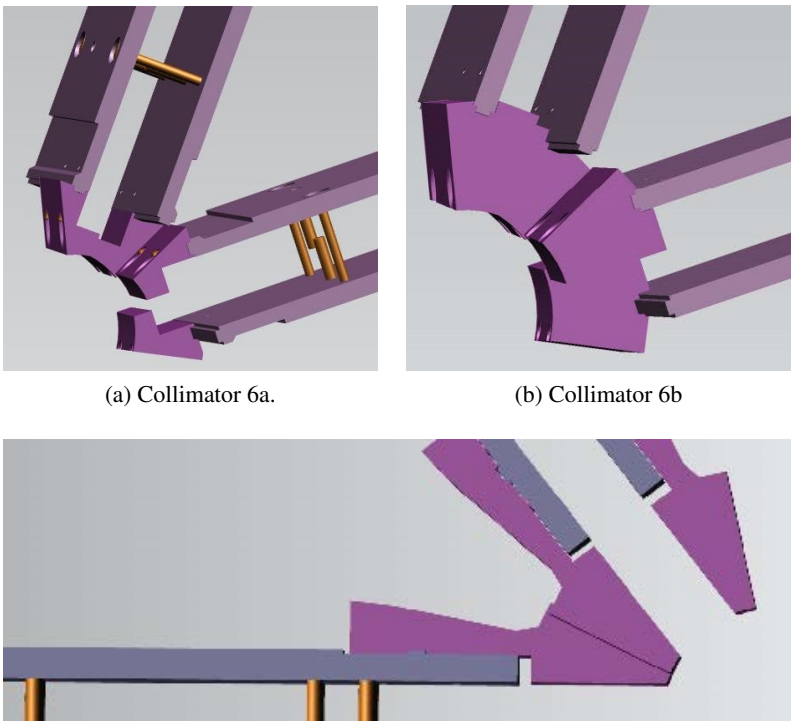

(a) Collimator 6a.

(b) Collimator 6b

(c) Collimator 5

Figure 69: *Collimators 5 (bottom), 6a (top left) and 6b (top right).*

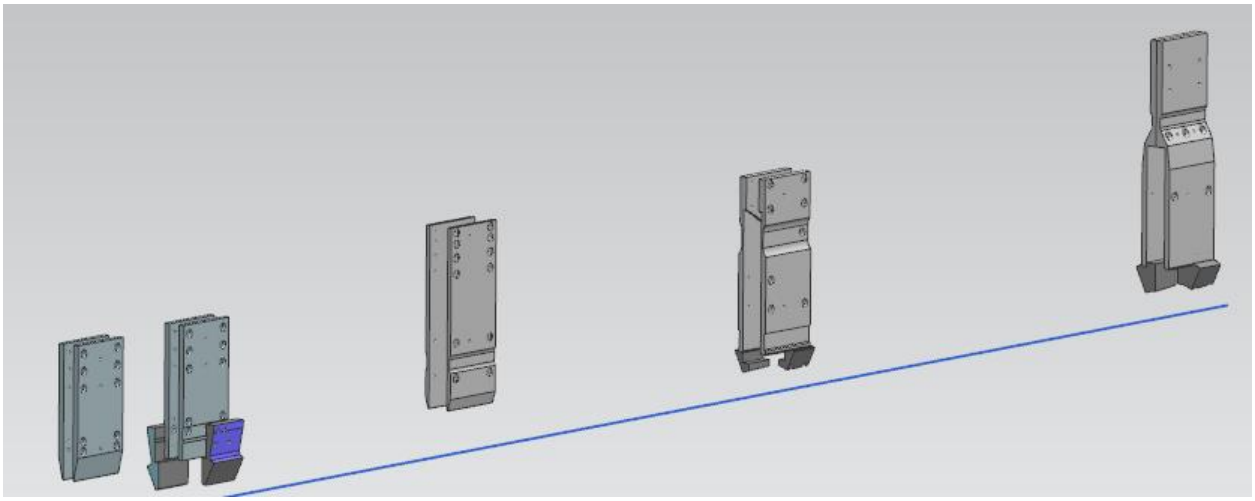

Figure 70: *Overview of clamps and collimators*

bolted to coils and attached to the structure with adjustable links (see Figs. 72 and 73). The clamps have been notched where necessary to maintain clearance with the envelopes (see Fig. 75).

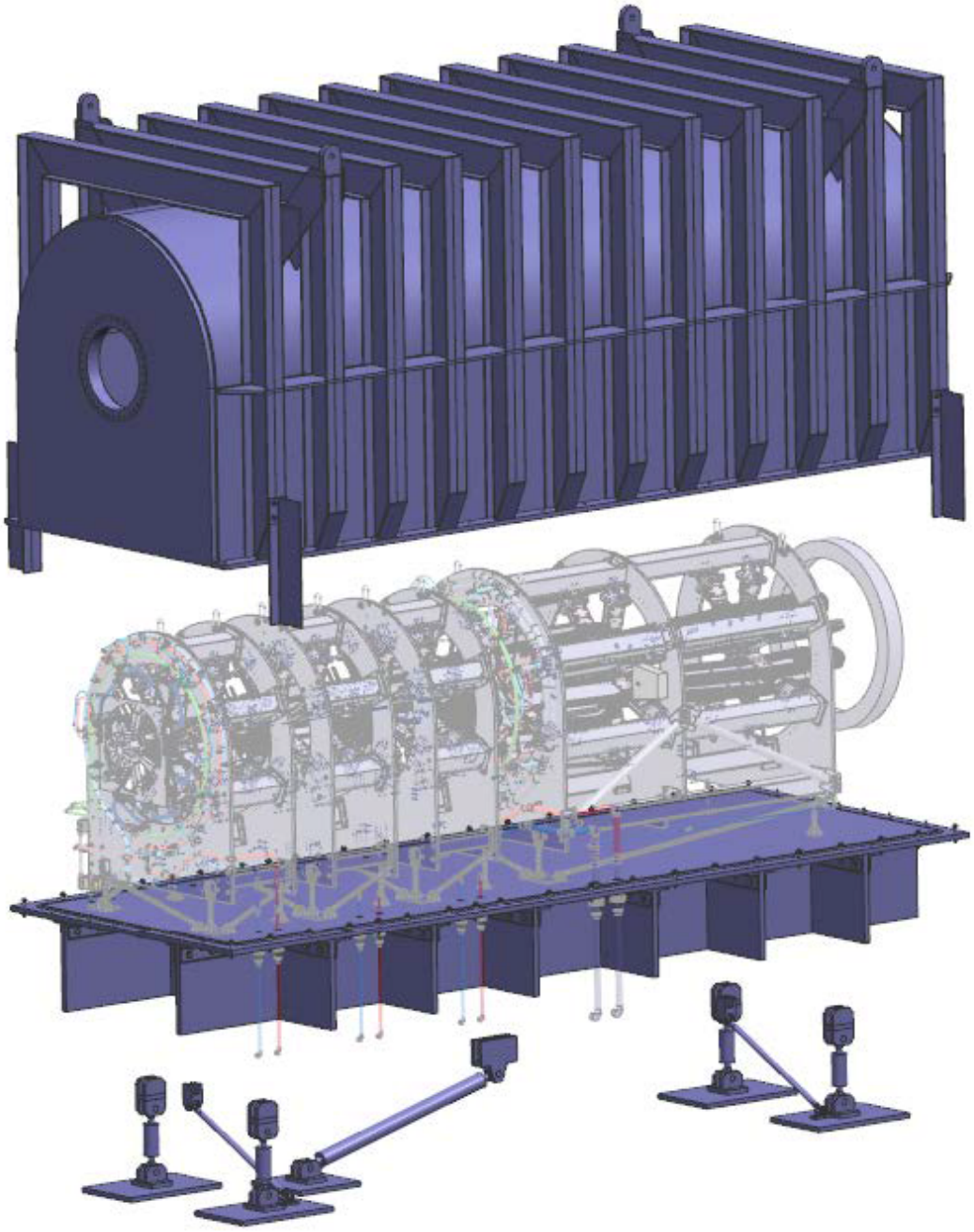

Figure 71: *CAD with the top of the downstream enclosure lifted up.*

5.3 Beampipe, Windows and Bellows

The spectrometer subsystem includes everything downstream of the scattering chamber window through the Hall to the dump entrance excluding the shielding and the detectors and detector stands. All active elements of the spectrometer; magnets, blockers, collimators, lintels etc. are contained in a vacuum system. Major elements of the vacuum system (shown in Fig. 76) are the upstream and downstream enclosures, the drift pipe (see Fig. 77), the detector pipe (see Fig. 79) and beam pipes. Bellows are strategically located between

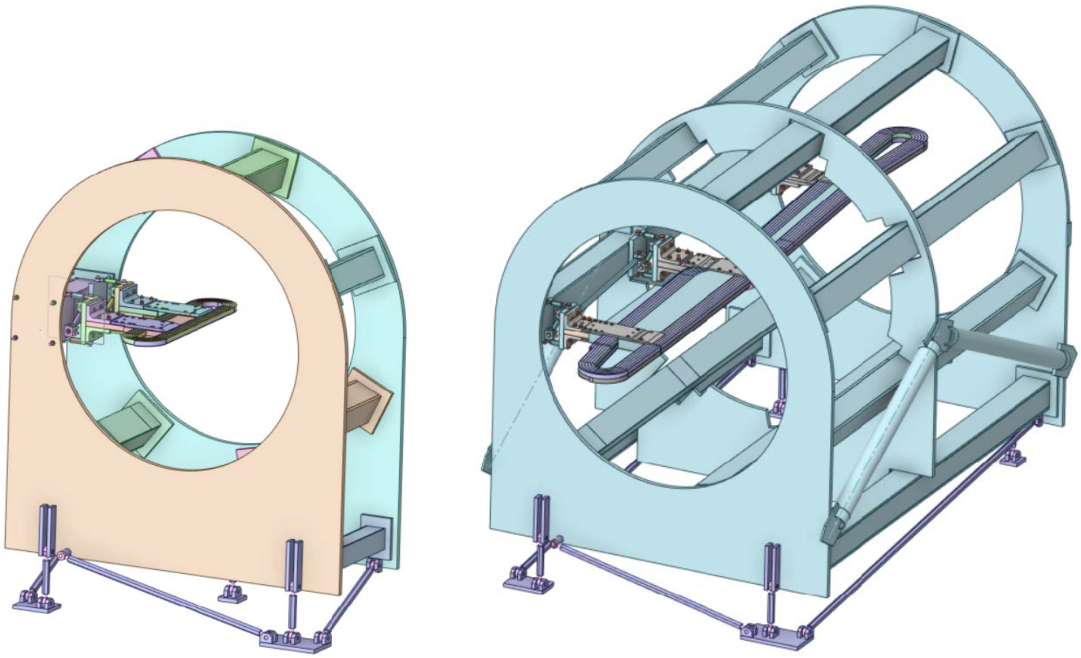

(a) Subcoil 3 supports (b) Subcoil 4 supports

Figure 72: *Supports for the downstream subcoils 3 and 4. The supports for subcoils 1 and 2 are similar to that of subcoil 3.*

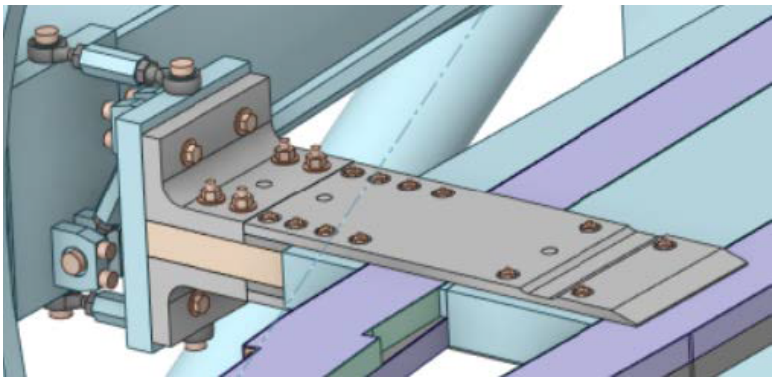

Figure 73: *Close-up view of a coil clamp, showing the G10 plate (light blue) in the center of the coil (purple). The clamp is bolted to the G10 filler plate, and connected to the support structure with adjustable links (shown toward the left of the picture).*

all the major elements in the vacuum system, as well as between the upstream enclosure, the target scattering chamber, and the detector pipe and the dump entrance. The main purpose of the bellows is to allow proper alignment of all components, they also allow for thermal expansion and contraction of the large vessels and pipes due to temperature changes and any imperfection in fabrication. Upstream of the upstream enclosure, there is a pipe connecting the scattering chamber to the upstream enclosure, with a bellows near the upstream enclosure. There is also a special section of pipe for collar 0 that is connected with flanges upstream of the bellows. Details of the locations and sizes of the components are summarized in Tab. 16.

At the end of the detector pipe there is a diameter change, a “neckdown”, requiring a window followed

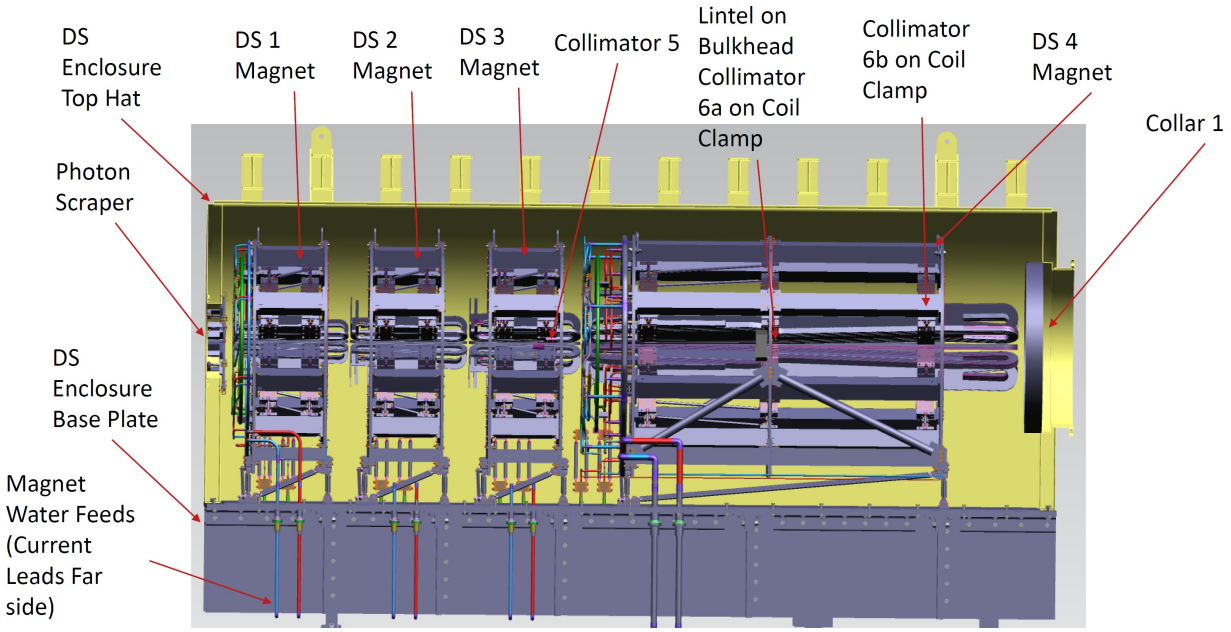

Figure 74: *Downstream torus enclosure, including the magnets, support bulkheads, collimators, lintels and passthroughs for water and power feeds.*

Table 16: *Summary of the various vacuum elements in the beamline with their nominal positions, inner diameters, thickness and material.*

Name	Upstream end (mm)	Inner diameter (mm)	Thickness (mm)	Material
Bellows 1	3432.18	304.8	28.58 (flange)	Stainless steel
12” pipe	2974.98	292.1	6.35	Al 6061-T6
Collar 0	1329.23	152.4	12.7 (containment)	Al 6061-T6 + lead
Bellows 2	856.44	304.8	28.58 (flange)	Stainless steel
US enclosure	400.00	NA	50.8 (front plate)	Al 6061-T6
Bellows 3	-4090.14	660.04	15.24 (flange)	Stainless steel
DS enclosure	-4699.89	NA	25.4 (shell)	Al 6061-T6
Bellows 4	-12284.34	1371.6	15.24 (flange)	Stainless steel
Drift pipe	-12772.76	2495.55	22.23	Al 6061-T6
Detector window	-18452.35	NA	0.94 mm to 1.55 mm to 3.175 mm	Al 5083-H116
Bellows 5	-18755.56	1043.43	15.24 (flange)	Inconel 625
Detector pipe	-19377.86	1352.89 (Max)	6.35 and 19.05	Al 6061-T6
Pion donut	-24567.10	NA	6.35 (side plate)	Lead
Neckdown window	-25200.71	NA	6.35	Al 6061-T6
Bellows 7	-25375.13	406.4	28.45 (flange)	Inconel 625
SAM detector pipe	-25933.93	393.7	6.35	Al 6061-T6

by the “neckdown” pipe. The purpose of this is to allow high energy particles to be tracked by downstream linear scanners. The final section of the spectrometer vacuum system is the SAM pipe. It supports and

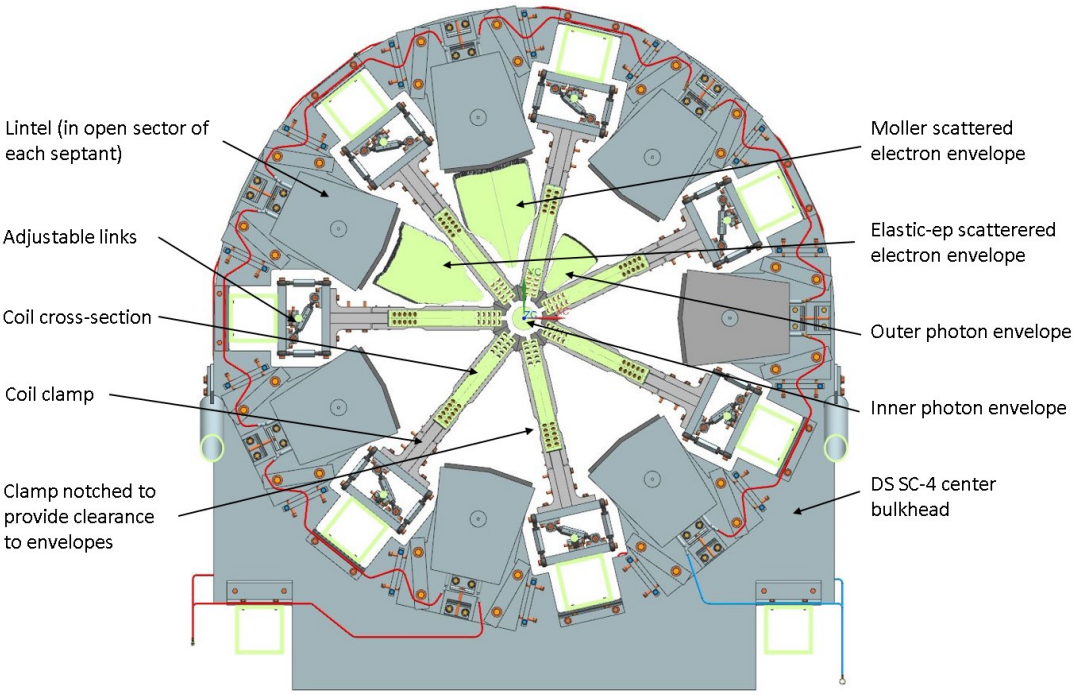

Figure 75: *Cross-sections of the envelopes for different particle types at a single z location along the beamline within the downstream magnet. Only one envelope (Møller, ep, or inner and outer photon) is shown per open sector in order to be able to differentiate them. Envelopes of the various particle types are produced as objects that can be built into the CAD models, defining the keep-out zones for the engineering designs.*

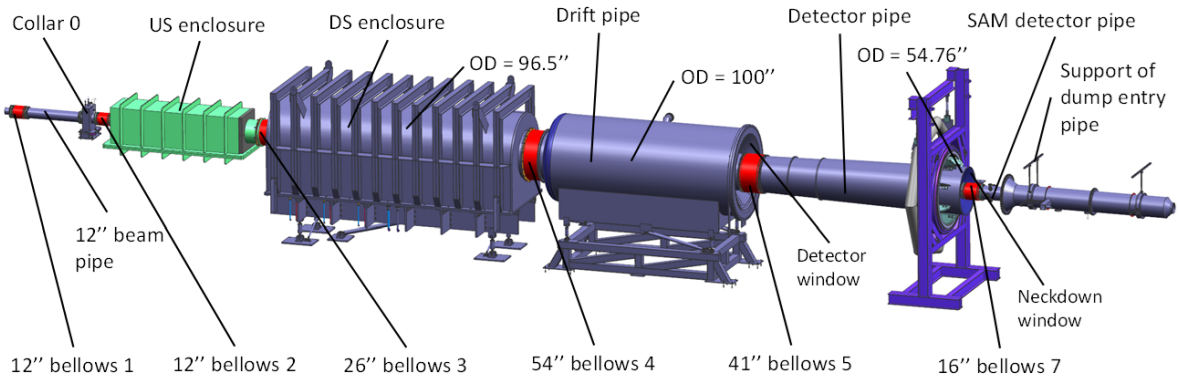

Figure 76: *Diagram showing the outer radius of the various beamline elements. After the scattering chamber at the left (not shown) there is a beampipe, the upstream magnet enclosure, the downstream magnet enclosure, and the drift and detector pipes (with connecting pipes between). Then there is the pipe that goes to the end of the hall or the dump pipe.*

contains small angle monitors (SAM detectors) which are connected with flanges. Bellows 1-3 (and their flanges) can be made of stainless steel. The bellows and flanges 4-7 are made of non-ferrous materials (Inconel 625) to avoid scattered backgrounds with high asymmetries incident on the detectors. The upstream

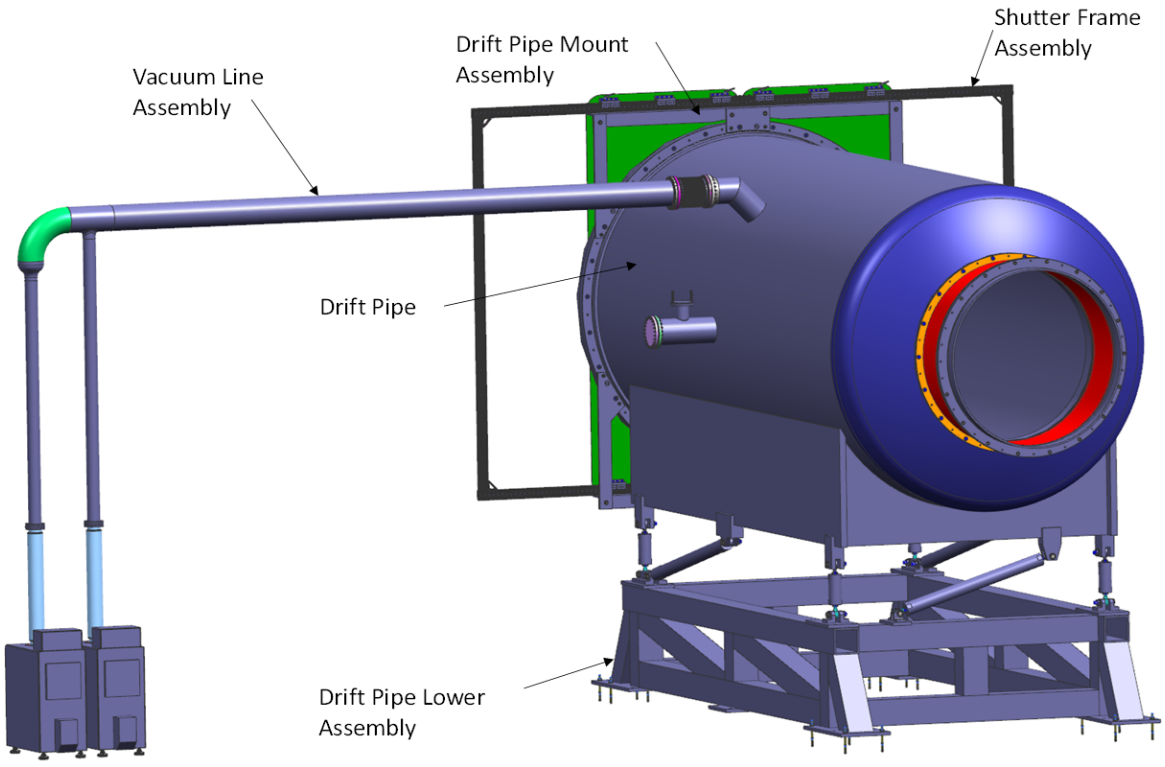

Figure 77: *Drift pipe*

and downstream enclosures and their supports are described in more detail in Sections 5.2.1 and 5.2.2. The various lintels, collars and collimators within those enclosures are described there as well.

The upstream beampipe is supported by collar 0, which has a support system and alignment system. There are several collars and lintels that appear outside of the enclosures, including collar 0 upstream of the upstream torus and several lintels in the drift pipe or just downstream of it. These lintels are supported by the bulkhead in the middle of TM4. Table 16 illustrates the nominal positions of various elements in the beamline. The positions were located at the upstream end of the elements; they are not at the center of the elements. Fig. 76 shows the relative locations of various beamline elements including 6 bellows.

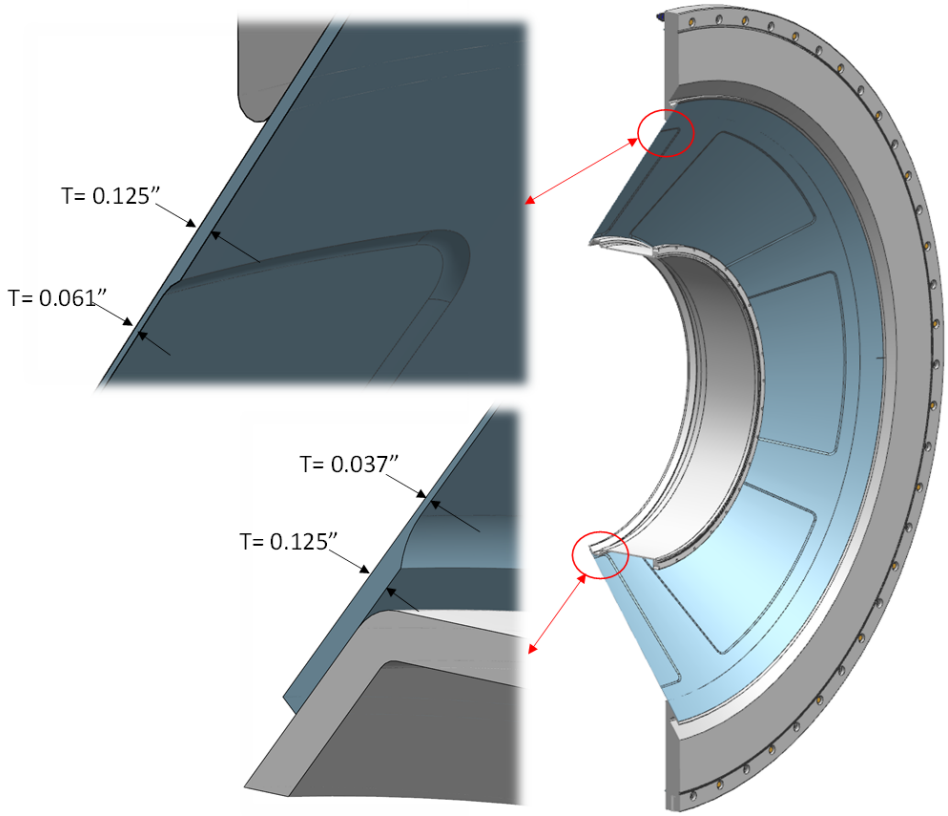

Figure 78: *View of the detector window and flange.*

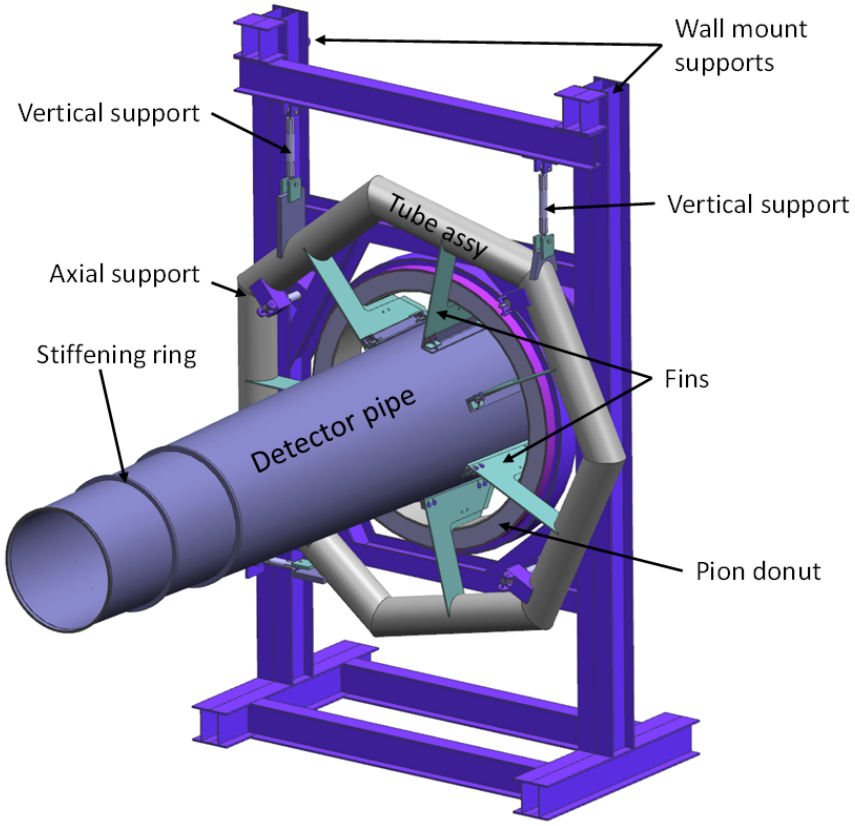

Figure 79: *CAD view of the detector pipe and the pion donut support stand near the end of the hall. The upstream end of the detector pipe connects to the inner radius of the detector window via bellows 5. The neckdown window is at the downstream end, connected to the SAM detector pipe via bellows 7.*

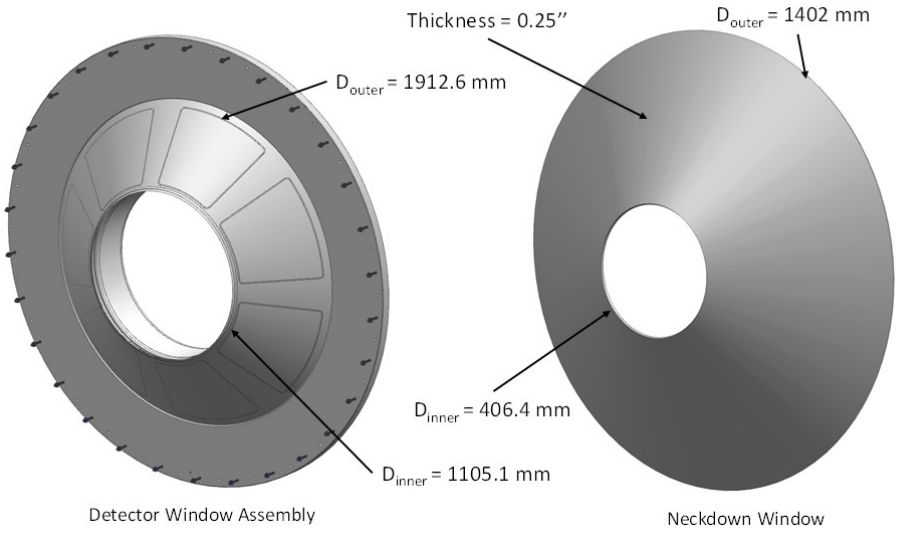

Figure 80: *The two large windows at the end of the drift pipe and at the neckdown near the end of the hall.*

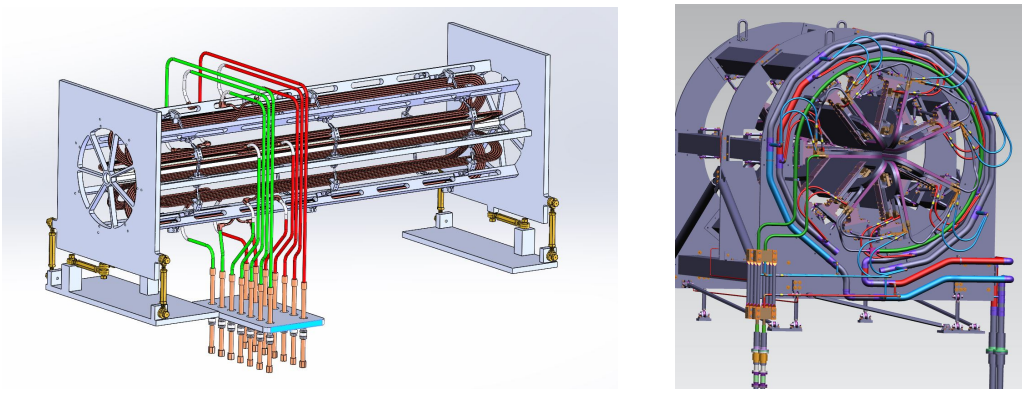

(a) Upstream (b) End view of coils

Figure 81: *Upstream water returns thru bottom plate of enclosure, and water and power leads for one of the downstream torus magnets.*

5.4 Power, water cooling and vacuum services

In this section we describe the overall power and water-cooling systems, including the power supplies and hall low-conductivity water (LCW) supply. The torus magnet consists of 5 sets of 7-fold coil symmetry, that is, 5 assemblies of 7 toroidal coils. Each of the 5 assemblies has 7 independent coil masses (CM) all electrically connected in series, and LCW process connected in parallel (individual pancakes) for all 7 coils. The interfaces to the vacuum within the enclosures will be described.

5.4.1 Power supplies and bus

The magnet configurations presented are required to operate in either polarity – i.e. clockwise or anticlockwise field direction for all coil systems TM0-TM4. Individual magnets are energized with independent magnet power supplies (MPS). The nominal MPS characteristics are detailed in Tab. 17. The magnet coils are powered by MPS through - flexible jumper leads (both magnet and MPS end), water-cooled leads (WCL) in air.

Table 17: *Nominal power supply operating (op) characteristics. Output current (I_{out}) stability to be better than listed values over 24 hours at the operating current. LCW flow is based on estimates.*

Power Supply	Nominal I_{op} (DC Amps)	I_{out} Stability (mA rms)	Normal V_{op} (DC Volts)	LCW flow (gpm)
US torus	1075	500	77.5	5
DSTorus 1	2230	1000	40	7
DSTorus 2	2440	1000	42	7
DSTorus 3	3372[10]	1500	57	10
DSTorus 4	3350	1500	224	20

[10]New nominal (previously was 3235A)

5.4.2 Cooling system

There are three different cooling systems for the spectrometer equipment. Some items will get direct LCW from the JLab Hall LCW system which is located in Building 92. These include the Magnet Power supplies and the spectrometer vacuum pumps. The MOLLER Magnet Water Cooler will also use Hall LCW as the heat sink to reject heat from the magnet coils and is described in more detail below. The LCW temperature and supply pressure to Hall A is nominally $\approx$81°F and 235 psig but the supply pressure and temperature does vary in time. The main variance is in the pressure due to load changes in other Experimental Halls. The LCW pressure will be regulated down to lower pressures as required for each different load.

A separate closed loop system which rejects heat to air will absorb high levels of power by stopping electrons and other particles such as Collar 0, Collimator 1 and 2, the blocker/sieve and Collimator 4. In previous runs, a 4kW Welding Chiller has been used. These are self-contained units and typically reject the heat to the air via a heat exchanger and fan. The total load power load includes the contributions from Tab. 18.

Table 18: *Power deposition in collimator and shielding elements for the spectrometer.*

Item	Nominal Power (W)
Collar 0	275
Blocker	1400
Sieve	19 W (at 1 μA)
Collimator 1	4700
Collimator 2	950
Collimator 4	60
US enc. Pb ring (inner)	30 W
US enc. Pb ring (outer)	20 W

The advantage of using a small, closed loop system is that the amount of highly irradiated water will be reduced and not spread around the main LCW system. The Spectrometer Magnets will have their own cooling system. This system specifically called the MOLLER Magnet Water Cooler MMWC, is a build to Spec item. The specification is [52]. System parameters are listed in Tab. 19. Heat absorbed by the

Table 19: *System design values (SDV) the full MMWC system design parameter which allows for pressure drop of full piping, valves, flow transmitters etc.*

Operating Point	SDV Max	SDV Min
Pump Flow (GPM)	168	106
Differential Pressure (PSID)	132	52
ft	305	120
Cooling Power (kW)	1200	630
Maximum LCW conductivity (micro-siemens/cm)	0.5	NA
Supply Temperature (°F)	83	79
Nominal Supply Temperature (°F)	81	NA
Maximum Hall LCW flow (GPM)	250	NA
Maximum Power into Hall LCW (kW)	1500	NA
Hall LCW Supply Temperature °F	83	80

MMWC is rejected to the Hall LCW just as it is from the Magnet Power Supplies. The detailed piping and

instrumentation diagram (P&ID) is A090005-15-00-0106. To transport and control the water flow to and from the magnet coils, two more P&ID are used. The first is the A09005-15-00-0111 the water distribution panel and the others are the individual Magnet P&ID's A090005-15-00-0101 to 0104 for TM 1 through TM4. The MMWC rejects the resistive heat load from the 5 magnets along with a few other minor loads. These include beam heating of Collimators 5, 6a, 6b, coil belly plates, Collar 1 and the Lintels as well as conduction heating from coils to their support systems. One of the key requirements of this system is to keep the magnets at constant temperature independent of operating current and other parameters such as the Hall LCW temperature or pressure instabilities. The system has been specified to run the magnets from 90% to 110% of the nominal current and keep the temperature constant. This is done by adjusting the flow to each magnet independently based on its temperature. The primary input variable will be the outlet temperature, but other parameters are also available such as the average of each coil outlet temperature and the magnet inlet temperature. The MMWC will have a built in 200kW chiller that uses vapor compression to potentially lower and stabilize the supply temperature to the magnet coils.

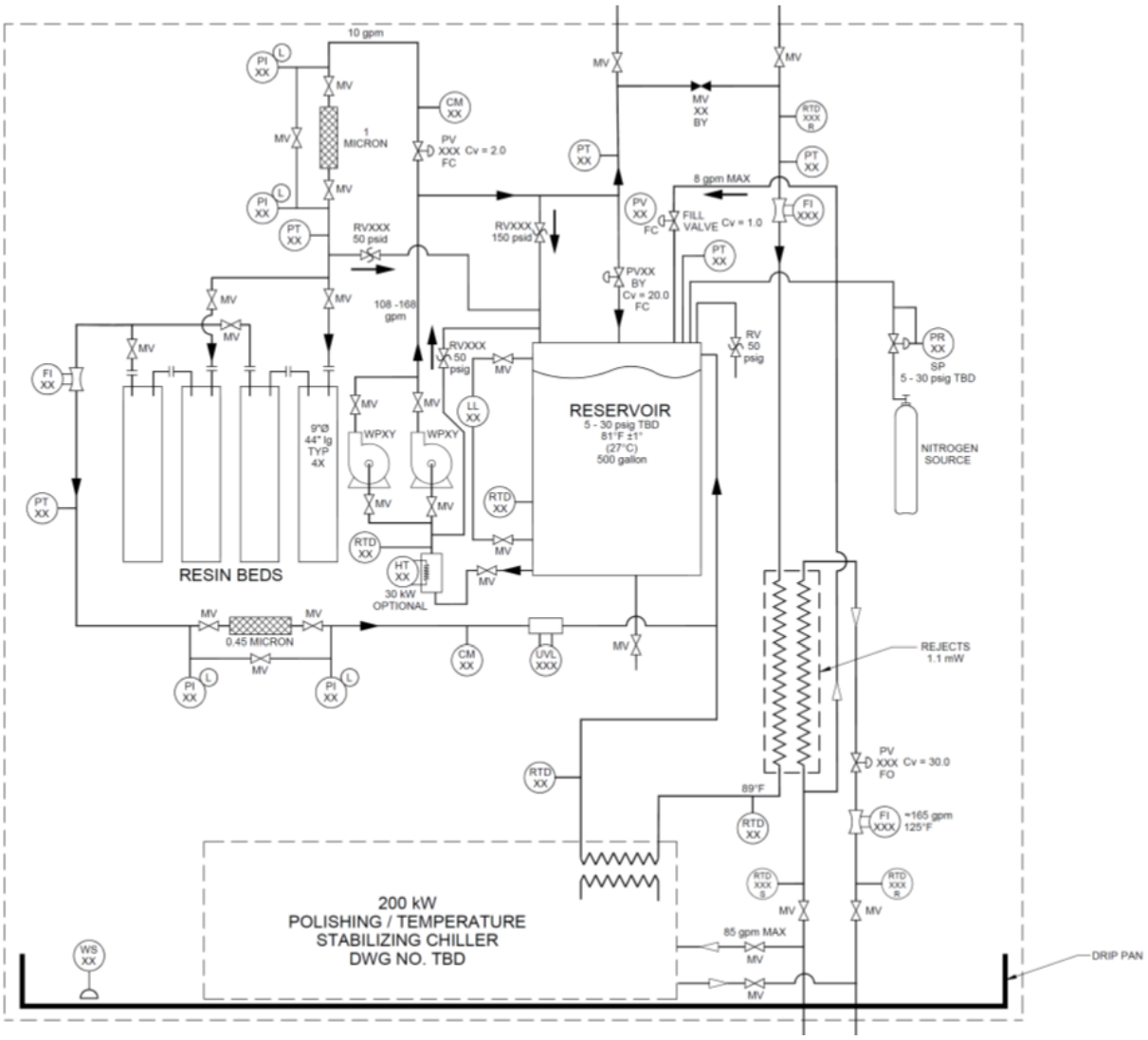

Figure 82: *Chiller diagram*

5.4.3 Vacuum System

The vacuum requirements for MOLLER are not particularly demanding, but the system is very large and contains lots of hardware that will outgas for long periods of time. Simulations were done which show vacuum levels below 0.1 Torr are sufficient for the physics program. The design requirement was chosen to be 0.01 Torr. All vacuum vessels are required to have a leak rate of 10E-7 Torr/Liter/sec or better when checked with a Helium Mass Spectrometer leak detector. The vacuum system will have two identical Edwards iH1000 pumps (pump curves are shown in Fig. 83). With outgassing and a 25 ft, 8" ID suction line

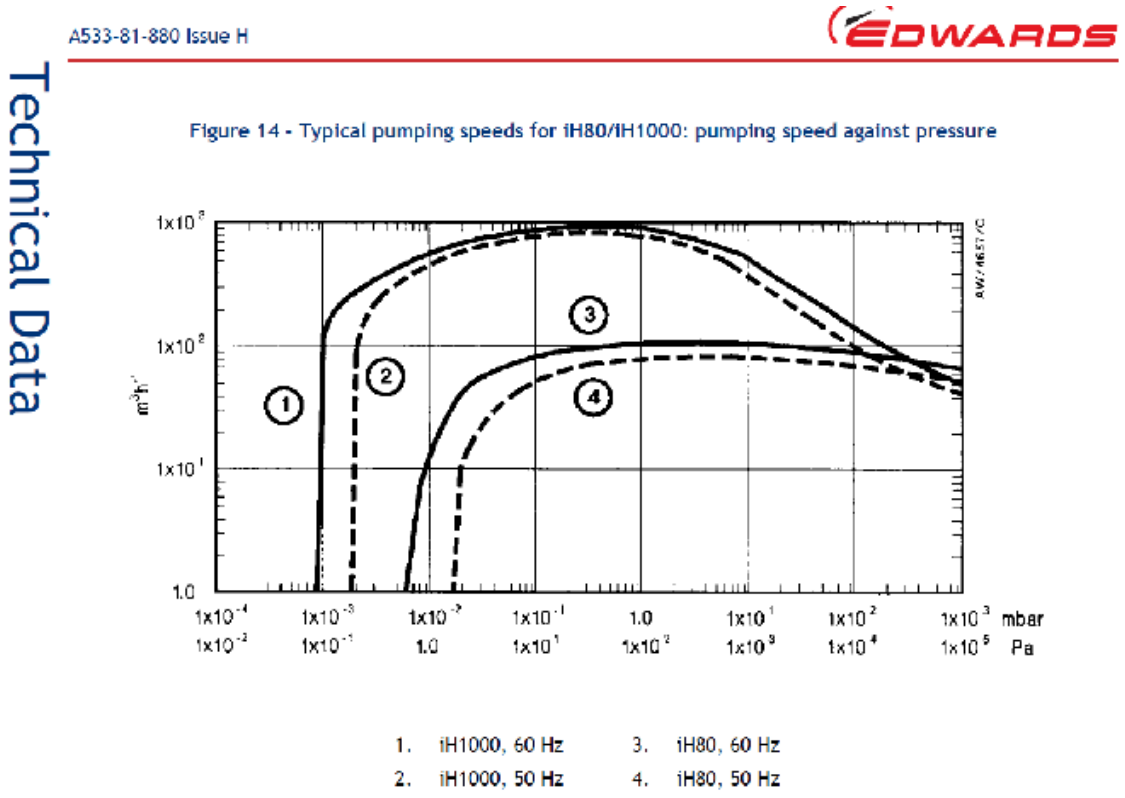

Figure 83: *Pumping speed for the iH1000 operating at 60 Hz (curve 1).*

the pumpdown time to 0.01 Torr will be approximately 5 hours and the ultimate pressure (using only one pump) with constant outgassing of 0.47 Torr Liter/sec is 0.004 Torr.

5.5 Instrumentation

Process and Instrumentation Diagram (P&ID) The typical P&ID for individual magnet coil configuration will consist of the type of instruments and sensing required to monitor the magnet performance during operation. This primarily consists of multiple voltage taps, measurement of inlet and outlet LCW temperature to individual pancakes, pressure in the supply and return header, along with flow monitoring for each individual magnet (TM1-4, a total of 4). A typical example P&ID from TM4 is shown in Fig. 85

In summary, the following parameters are monitored and can be used to control- (a) Voltages across individual coil/pancake, WCL, flex jumper leads, MPS, (b) Pressure – inlet and outlet LCW supply and return header, (c) Temperature – outlet temp of the LCW/coil in every coil, and (d) Flow in every DS-magnet.

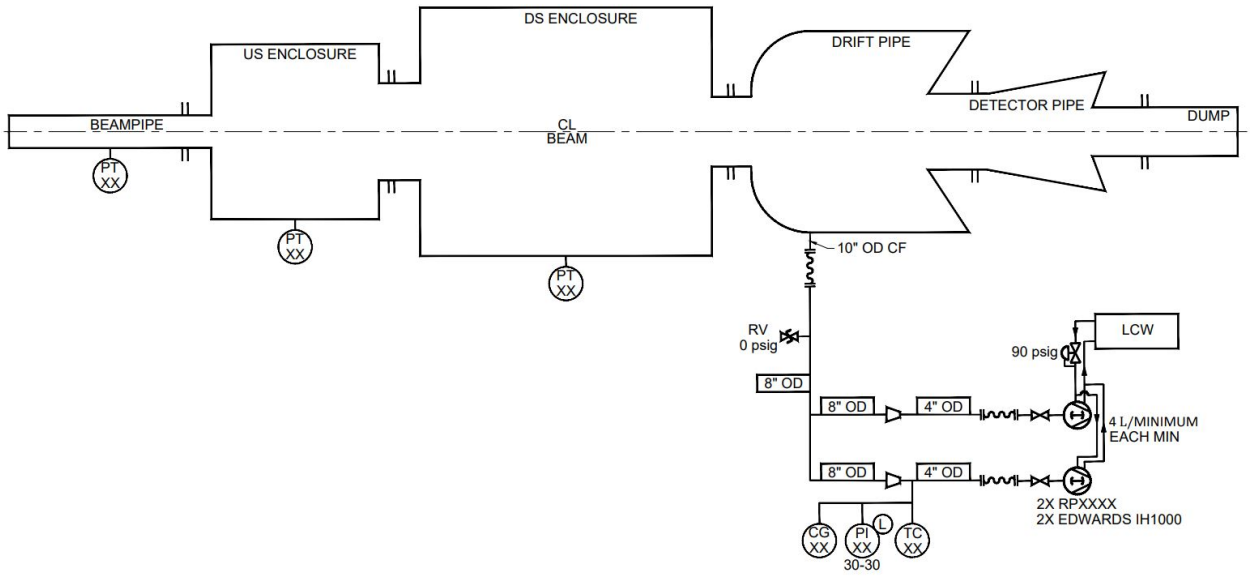

Figure 84: *Overview of the vacuum volume of the spectrometer system.*

Instrumentation and control layout Typical layout configuration for the torus magnet system I&C is represented in Fig 86.

This includes a total of 5 MPS, closed loop water chiller, magnet instrumentation, pumping system, others. Primary Control is provided through Ethernet Interface, direct interlock capability having 5 or 24 VDC (e.g. voltage, temperature, field, flow, etc.), sensors planned to be used are Klixon (temperature dependent switch), thermistors, RTD, voltage taps, flowmeters, digital (IN and OUT), Analog (IN and OUT). Typical layout of the magnet control and monitoring is shown in Fig. 87.

Magnet safety and interlocks The magnet protection system comprises primary and secondary protection sub-systems. Parallel path voltage taps from multiple locations feed both these sub-systems. Voltage taps feeding the primary protection sub-system are hardwired directly from the magnet. The secondary protection sub-system is also fed from the same voltage tap locations along with the outlet temperature of each coil. The information is acquired by a data acquisition system using a National Instruments cRIO device and then routed to a PLC to provide backup for the hard-wired primary sub-system. The other process parameters are also monitored and shall be used to control the magnet system. The magnet diagnostic system (MDS) includes the control and the data acquisition sub-system. The MDS shall also display the status of the magnets during normal operation.

Magnet Control System (MCS) The combined functions of the magnet protection system and magnet control system (MCS) ensure that each magnet is protected under any fault conditions (voltage, LCW flow, current lead & coil temperature, vacuum, pressure). A fault on any section that has been monitored by the magnet protection system and MCS automatically operates the power supply to discharge the magnet. The selection of devices to include in the MCS was driven largely identified by the failure mode and effect analysis (FMEA) process.

The torus magnet interlock architecture event from hardwired protection is registered in the Sequence of Events (SOE) monitor and transferred to the PLC and EPICS for real-time display and archiving.

The magnet power and LCW control are implemented in an Allen Bradley Control-Logix Controller

with Rockwell Automation software to program the PLC and enable viewing of the status in real-time. Functions such as magnet interlocks act locally and independently of remote interfaces. Sensor instrumentation is routed into the PLC (FPGA/RT application) using the MSELV/other chassis. Configuration, monitoring, operator interface, alarm handler and archiving system for each magnet system is provided by the Experimental Physics Instrumentation & Control System (EPICS).

5.6 Quality Assurance and Measurement

Mechanical and electrical inspections and tests shall be performed on each sub-coil before and after the coils are vacuum pressure impregnated.

1. **Dimensional, Damage and Defect Inspection**
   A careful visual and quantitative dimensional inspection shall be made to verify conformance to drawing and specification requirements and to identify any defects.

2. **DC Resistance**
   The DC resistance of each sub-coil at a known temperature shall be measured and recorded, with an accuracy of +/- of 1%, following the application of the glass cloth ground wall insulation.

3. **Induced Voltage/Impulse Test**
   An induced voltage test (also known as surge test) to be carried out for locating any shorted turns shall be employed to test each circuit both before and after the vacuum pressure impregnation process. An alternative to the induced voltage test might be a 4-wire voltage drop measurement through the coil under test where the voltage drop per turn would be of the order of several millivolts.

4. **Pneumatic Pressure Test and Helium Leak Test**
   After brazing on the custom fitting to the coil lead, a pneumatic pressure test shall be performed on the coil using dry air or nitrogen according to B31.3 Paragraph 345.5. The design pressure of the coil is 215 PSI, and the test pressure is 286 PSIG. The test pressure shall be maintained for at least 15min. After the pressure test, the coil shall be leak-tested using a Helium Mass Spectrometer Leak Detector. The measured leak rate (after allowing for any helium background levels) should be no higher than 1.0×10^{-9} mbar·l/sec when subjected to 1 atmosphere of helium (reverse leak test).

5. **Flow Test**
   The coolant circuits shall be tested for flow and pressure drop and shall be subjected to a hydrostatic pressure test. Flow test inlet pressure shall be at a minimum of 50 PSI. Coil-to-coil variations for identical circuits shall not exceed 5% and shall be within 10% of the expected flow when corrected for line pressure.

6. **DC Hi-POT Test**
   Following the induced voltage/impulse tests, establish an intimate Ground Plane and DC Hi-pot on each circuit at 1.5 kV for one minute along with the DC leakage current at the beginning of the test, at 30 and at 60 seconds.

7. **Low power and thermal cycle testing at JLab**
   Coils will be run at current > 500 A with LCW and evaluate the coil temperature rise with restricted flow of LCW. The prototype coil will be exposed to a thermal cycle with the temperature varied between 25-65 °C to see any sign of coil fatigue and delamination.

In addition to the above-mentioned quality-control measures, the field of the assembled subcoils will be measured in the test lab using a custom device (see Fig. 88). This device was used to successfully map the

field of the Hall B torus (6-fold symmetry, peak field 3.58 T) This device was used successfully to determine offsets of individual coils in the Hall B torus, allowing for the creation of an accurate simulated field map to be used in the analysis of particle tracks [53].

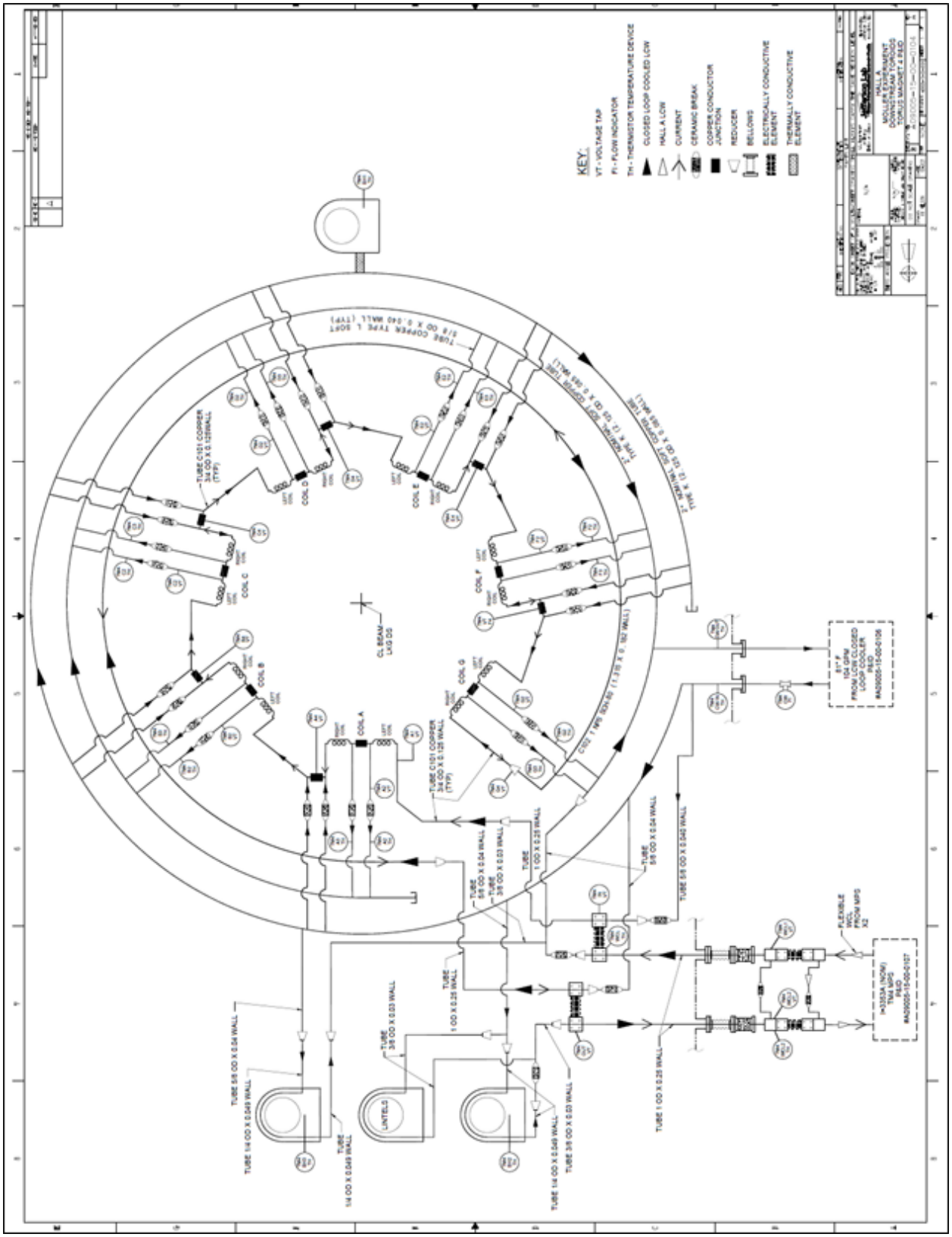

Figure 85: *P&ID.(Reference – JLAB drawing A09005-15-00-0104).*

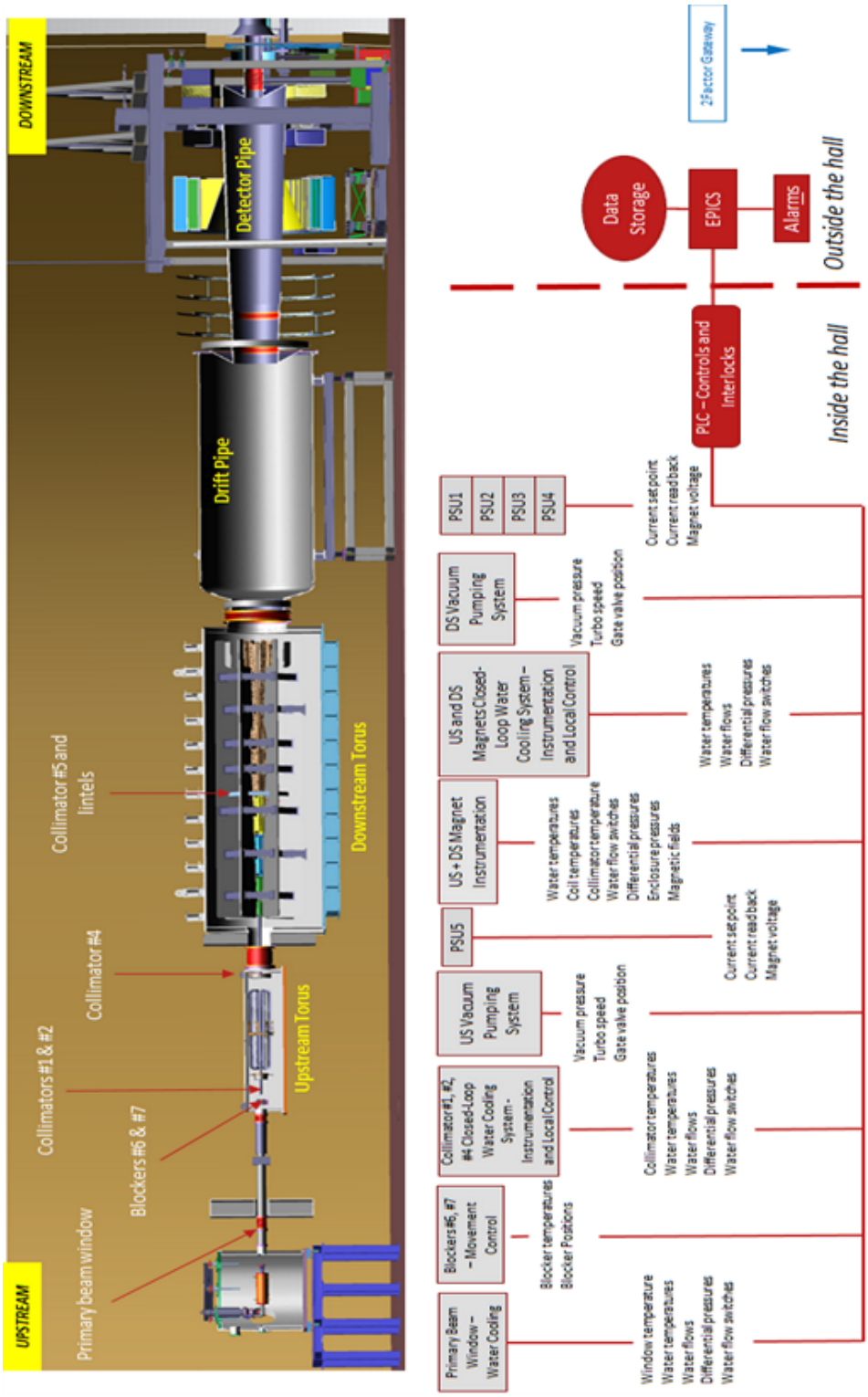

Figure 86: *Overview of instrumentation and control systems for the magnets.*

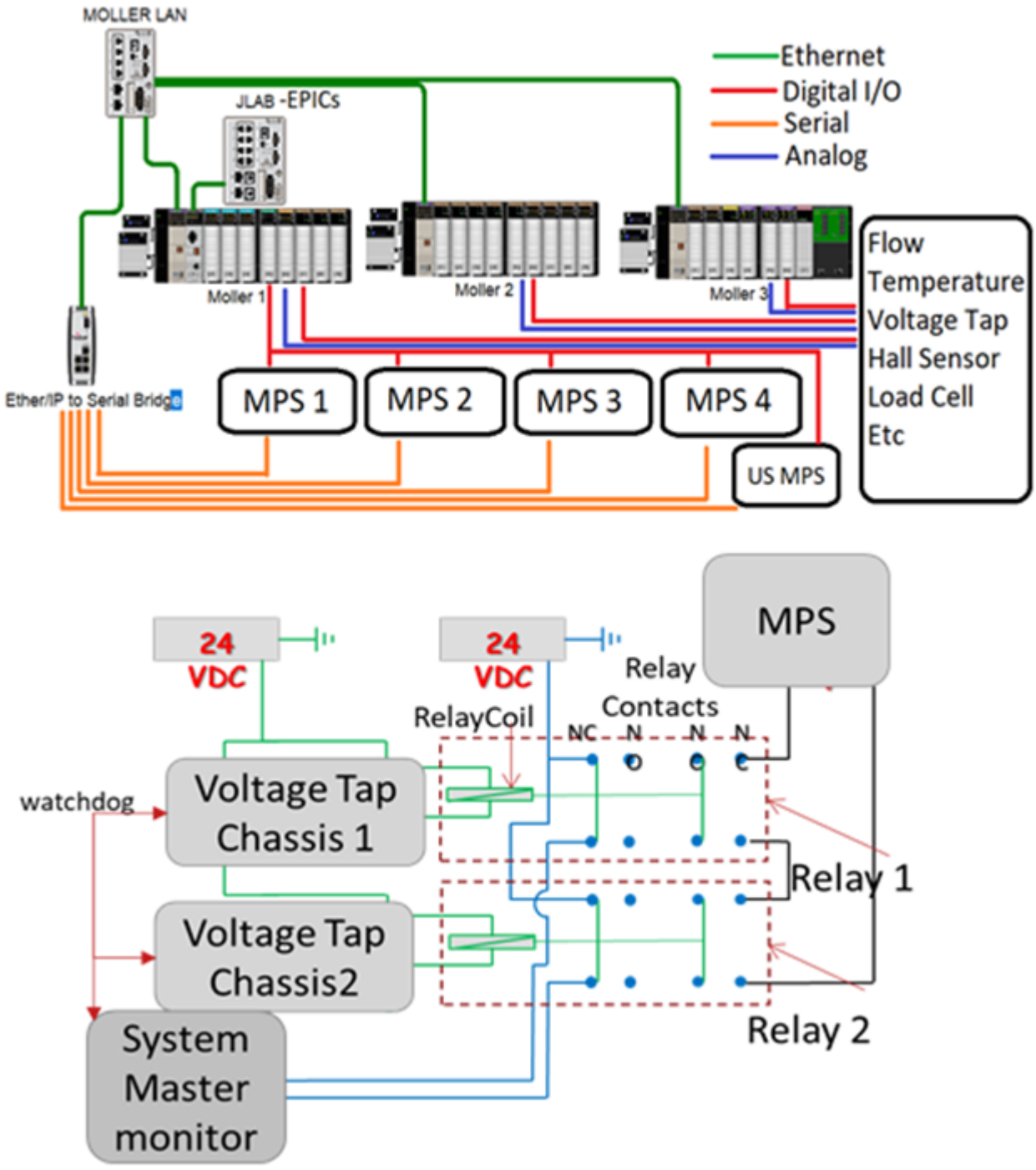

Figure 87: *Magnet control and monitoring system diagram.*

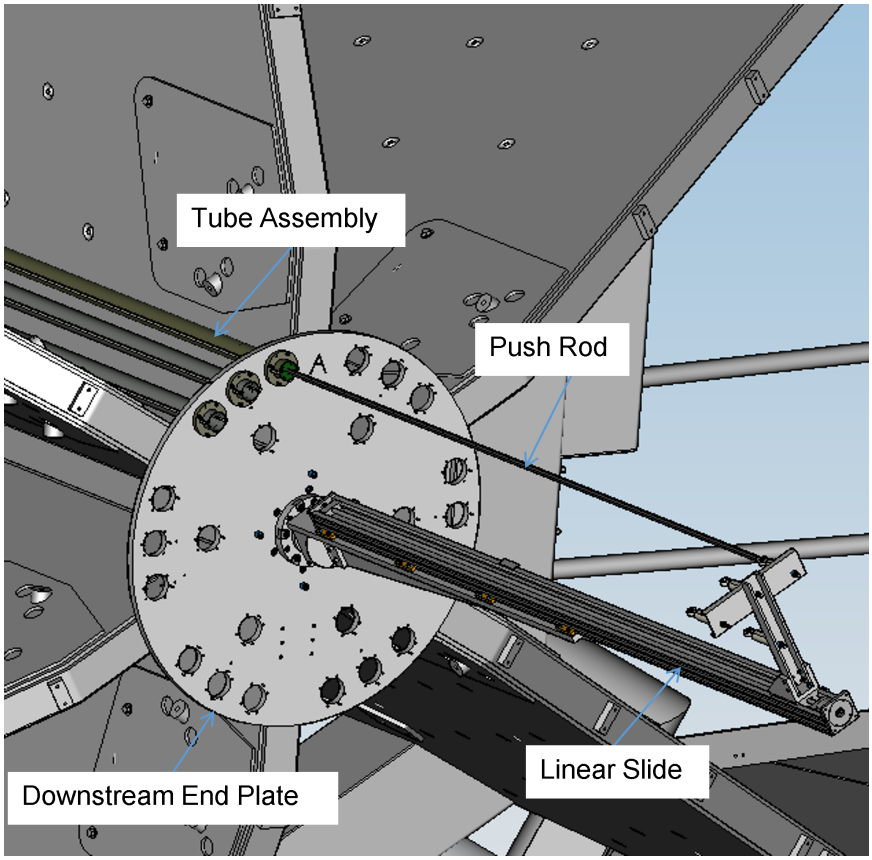

Figure 88: *This is a diagram of the field measurement system used to successfully measure the field of the Hall B torus.*

6 Main Integrating Detectors

6.1 Operational Principle and Requirements

As described in sections 5.1.3 and 2, the spectrometers produce a profile of scattered electrons, shown in Figs. 55 and 56. The purpose of the main integrating detectors is to measure the flux of scattered electrons over this profile, within each helicity window. The asymmetries that form the main observables of the experiment are formed from these flux integrated measurements.

The profile is separated into 6 rings, five of which are further separated into 28 detector elements around the azimuth, while the Møller ring (Ring 5 in Fig. 55) is separated into 84 detector elements. A CAD illustration of the entire detector array, including the shower max detector (chapter 9) is shown in Fig. 89.

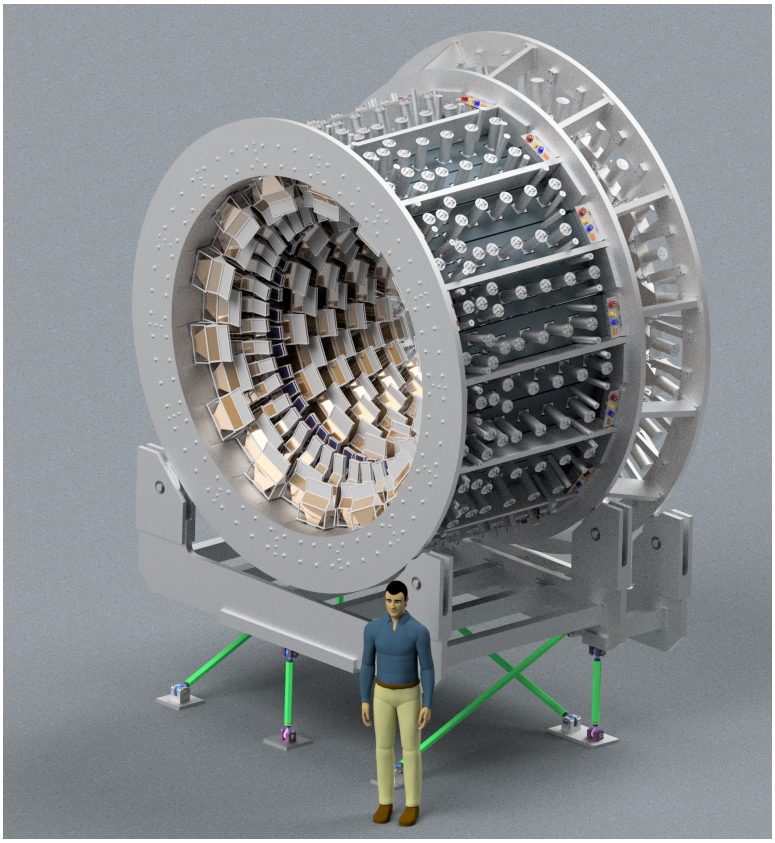

Figure 89: CAD illustration of the entire main integrating detector array, including the 224 thin quartz detectors (front barrel) and the shower max detectors (back barrel flare). The latter are described in a separate chapter.

The small size of the Møller asymmetry (Ring 5) and the goal precision require very high statistics, meaning very high event rates in the detectors. The average electron rate over all detectors is only about $50\ \mathrm{kHz/mm^2}$, but the peak electron rate for MOLLER can reach $1\ \mathrm{MHz/mm^2}$ in certain regions of the integrating detectors. The latter requires either a very high detector segmentation or a continuous integration of many overlapping pulses. Modern solid state pixel detectors, such as those used as vertex detectors in collider experiments, can have a spatial resolution as small as $\sim 4 \times 10^{-4}\ \mathrm{mm^2}$, so that, in this regard, pulse counting may be possible. However, given the needed accuracy of the proposed experiments, background susceptibility, linearity, noise behavior, and radiation hardness are major issues. Beyond that, even if all of

these issues have been addressed, the implementation of this technology for such a large surface area detector is cost prohibitive. For these reasons, MOLLER has adopted radiation hard, highly linear, and relatively large active area ($O(100\ \mathrm{cm}^2)$) fused silica (quartz) Čerenkov detectors. The total rate in the highest rate detector tiles is on the order of one to several GHz. At these rates the counting of individual pulses is no longer possible, requiring integration mode operation, in which individual pulses overlap to such a degree, that they produce a continuous current at the detector cathode (therefore this is also sometimes referred to as current mode detection, as opposed to pulse mode). An additional ring of shower max, quartz-tungsten sandwich detectors is located behind the Møller ring to make another measurement of the primary signal that is less susceptible to soft backgrounds, but will have less statistical resolution. Together with the 6 rings described above, this system is referred to as the main integrating detectors. The shower max detector is described in chapter 9. Here we only describe the function and design of the 224 main or "thin" integrating detectors.

Although the purpose of the main detectors is to operate in integration mode, for tracking and diagnostic purposes, they also have to function in standard event counting mode. The requirements for the detector array, for both modes, are described here.

6.1.1 Integration mode requirements

The asymmetry to be measured by each of the main integrating detectors is defined by

$$A = \frac{I_k^+ - I_k^-}{I_k^+ + I_k^-} \ , \tag{13}$$

which is here expressed in terms of the average cathode current $I_k = R\langle n_{pe}\rangle e^- \ [C/s]$, with $R\ [s^{-1}]$ being the rate of electrons scattered into the detector and $\langle n_{pe}\rangle$ being the mean number of cathode photo-electrons per detector electron event.

As discussed in more detail below, the precision with which the measurement can be made depends not only on the number of detected electrons (counting statistics), but also requires a reasonably high detector light yield and correspondingly high number of photo-electrons (high with respect to background as well as with respect to additional noise sources). Therefore, the primary concern for the detector design is the maximization of light yield, and the simultaneous minimization of additional noise (what we call excess noise above counting statistics), which is always present in an integration mode detector.

For a successful measurement, the integrating detectors have to satisfy a number of performance requirements that dictate the overall design, including the detector geometry, the choice of detector technology, materials, and readout technique. Each requirement is briefly discussed below and the corresponding design solutions are discussed in the following sections.

1. **Maximize Signal yield:** To ensure that the target precision of the experiment can be reached, the detectors must maximize the detected signal yield, which means that they have to cover the full azimuth of the Møller peak region. This also means that the detector must be able to handle the high Møller event rate, which is approximately 134 GHz for that ring. This places requirements on the detector active material as well as the readout electronics and mode (integration mode).

2. **Background suppression:** In integration mode experiments, the rejection of backgrounds based on particle ID or electronic discrimination is not possible. Therefore, the experiment itself has to be designed to minimize the background in the detector region (Sect. 7.3.1 and the detectors have to be designed/chosen such that the sensitivity to the remaining background is minimized (this section) or can be determined by measurement using separate detectors (Sect. 9). This places constraints on the detector type and material, position, geometry, shielding (Sect. 12), and readout electronics (this section and Sect. 10).

3. **Helicity-correlated systematic effects:** Helicity-correlated changes produce false asymmetries. The detectors must be designed to help suppress helicity-correlated systematic effects as much as possible. These include possible detector signal correlation to changes in the beam current, energy, position, and angle on target (chapter 14). Helicity-correlated changes, for the most part, place constraints on the detector geometry, through symmetry requirements, coverage of the scattered profile, and position accuracy (Sect. 6.6) but also on the electronics.

4. **Drifts in the detector signal:** The detector signal contains systematic drifts, both fast and slow. Non-random drifts in the detector signal can be the result of beam drifts, changes in temperature, long time-scale degradation of the detector parts, as well as electronics drifts. Almost all of these can be controlled to some degree - for example by operating the PMTs at a reasonable HV bias, in a reasonably stable temperature environment, and removed from or shielded from direct radiation exposure - but the primary way to deal with possible false asymmetries due to drifts and unwanted noise above counting statistics, is to perform each asymmetry measurement on a time scale that is short compared to the timescale of the drifts. This is achieved by running the experiment with a fast helicity reversal rate (Sect. 3). The faster the helicity reversal rate, the more the signal variation with respect to time is well approximated as constant on the time scale of an asymmetry calculation. Variations that are faster than the helicity reversal rate are dealt with and used to advantage in the electronics chain, as discussed here (Sect. 6.3) and in Sect. 10. The choice of helicity reversal rate influences or determines almost every detail of the detector electronics design.

5. **Excess noise (above counting statistics):** Integration mode measurements never achieve counting statistics precision, but the goal must be to suppress excess noise above counting statistics as much as possible. Low light yield, poor photo-electron conversion and amplification, and poor electronics design can increase excess noise, either lowering the overall measurement precision or requiring longer running times to achieve the goal precision. The entire detector design, including the geometry, choice of materials, and the front-end electronics, affects the excess noise behavior of the detector. We define excess noise as a combination of three factors: $\alpha^2 = \alpha^2_{DR} + \alpha^2_{PMT} + \alpha^2_E$ incorporates noise components stemming from the finite detector resolution (RD), PMT gain noise (PMT), and electronics noise (E) [54]. With this definition the statistical error on the measured asymmetry becomes

$$\delta A = \frac{\sqrt{1+\alpha^2}}{\sqrt{N}}. \tag{14}$$

6. **Detector (non-)linearity:** For the purpose of this measurement, a non-linearity in the detector is defined as a change in the size of the measured asymmetry as a function of absolute signal amplitude (or offset), rather than only on the difference in the signal for different helicity states. An asymmetry from non-linearity is a multiplicative effect, meaning that it scales the real physics asymmetry. As a result, it is important to establish that the non-linearity is zero or measure it at the needed level of precision.

7. **Radiation hardness and shielding:** Due to the very high rate in the detector region, the Ring-5 detector elements can expect to see doses of up to $\sim$45 Mrad/5x5 mm^2 (Sect. 12 in their active region over the lifetime of the experiment. And although the elastic e-p overall rate is lower than the Møller rate, it is concentrated over a much smaller area producing up to $\sim$120 Mrad/5x5 mm^2 (Sect. 12 dose on the Ring-2 detector active region. This means that the detector active material must be radiation hard enough (i.e. high purity quartz), to limit transmission loss. The other detector elements, such as photosensitive devices and electronics are somewhat removed from direct shine of the scattered

electron envelope, but must still be appropriately shielded to reduce radiation damage as much as possible. All materials used in the detector construction and mounting must be radiation hard enough to maintain the structural and functional integrity of the detector system over the duration of the experiment.

8. **Positioning and stability:** The detector mounting structure must provide stable and reproducible positioning, with positioning accuracy at the millimeter level. The structure must provide access to all of the vital parts of the detector and allow replacement if need be.

6.2 Detector Segmentation and Tiling

As discussed above and in Sect. 5, the main detector active region is separated into 28 azimuthal segments and 6 radial regions, called rings (Figs. 55 and 56). Each segment contains 8 detector modules (3 for Ring 5). Figure 90 shows a front view (in beam direction) of the main detector array, with the azimuthal and radial segmentation shown by the rectangular grey outlines for each active area detector tile. The radial and azimuthal positioning and tile size arrangement is shown in Fig. 90.

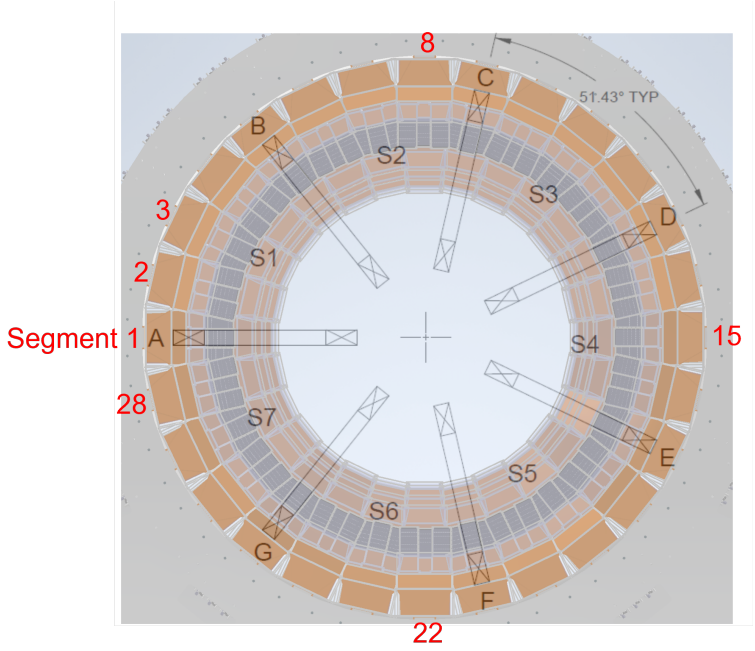

Figure 90: Front view (beam into page) of the main detector array. The 28 azimuthal segments are numbered (red) 1 (beam left) through 28. The spectrometer coils are labeled A through G and the septant regions (see Sect. 5) are labeled S1 through S7. The segments are arranged such that segment 1 is oriented in the same direction as spectrometer coil A. It is evident that the detector tiles overlap slightly at the lower edge of each tile. Ring 5 appears darker than the other rings.

6.2.1 Tile size requirements

The size of each detector tile is based on detailed simulations of event rate, type, and associated asymmetries and a deconvolution analysis and the corresponding best precision extraction of the Møller asymmetry in

Ring 5 (see Sect. 7.3.1). To maximize statistics, the tiles must cover the entire azimuth and radial region of the event profile.

Rather than making the active area of each tile trapezoidal, which is expensive to manufacture to the required specifications, it was decided to make them rectangular and take the tile edge at the outer radius to drive the width of each tile. This way, the array still covers the full azimuth, but at the expense of having tile overlap at the inner radial edge. This was taken into account in the deconvolution and will be straightforward to take into account in the analysis.

6.2.2 Positioning along z

To reduce the radiation dose to the PMT and front-end electronics (preamplifiers), these have to be located at larger radius, away from the direct shine of the envelope of the primary scattered electronics and further shielded against diffuse or back-scattered background. This means that the modules need a light guide to connect the active volume (quartz) and the PMT (See Sect. 6.3 for details). Therefore, to allow sufficient room for the hardware and access for assembly and maintenance, the quartz tiles have to be located at different positions along the beam (the z-axis). This is, of course, also necessary, because the active volumes slightly overlap, but the physical size of the detector modules requires more space than what is dictated by the module overlap.

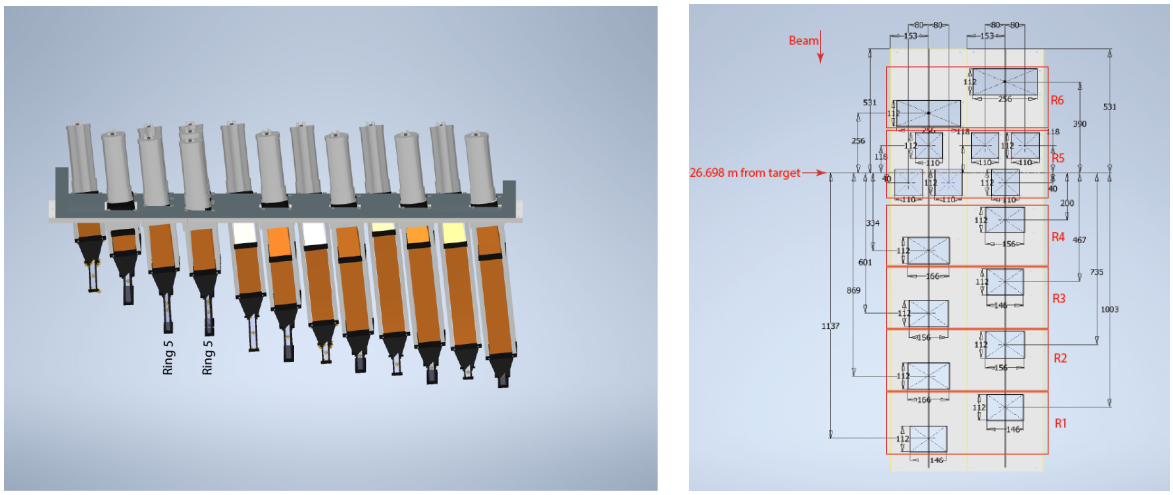

Figure 91: Left: CAD illustration of two adjacent front-flush and back-flush detector segments, illustrating the detector module positioning in the beam direction (z-axis), with the beam traveling from left to right in the figure. Right: Front-flush and back-flush segment plates with module openings, illustrating the arrangement of the staggered detector elements.

Figure 91 shows two adjacent segments, illustrating the displacement of the ring modules along the beam axis (z-axis). One of the segments has the detector modules shifted downstream (the direction to the right in the figure) with respect to the other so that there are two detectors per detector ring visible, each defining a separate detector plane in the overall detector structure. The midpoint between the two Ring 5 planes is located $22.198\ m$ downstream of the hall center (or $26.698\ m$ from the target center). We call the segments with the detector modules arranged more upstream the ”front-flush” segments while the segments with the detector modules shifted downstream are called the ”back-flush” segments.

As a result of the detector module placement along the beam and the envelope of the scattered electrons as a function of event type, the radial position of different ring quartz tiles will be different, requiring

longer modules toward the downstream end of the array. The back-flush and front-flush quartz tiles within the same ring will also be slightly different. This is visible in Fig. 90. The corresponding position and azimuthal size were carefully calculated and adjusted. Figure 92 shows the positioning and orientation of the detector modules with respect to the segment plates and the beam direction. The quartz tiles are rotated with respect to the vertical (y-axis) by $\theta = 3^\circ$, so that the tile front is normal to the mean momentum direction of the scattered electron profile in the detector plane. The light guides are rotated with respect to the quartz by an additional $\alpha = 3^\circ$, giving the entire module a 6° rotation with respect to the vertical axis. The additional rotation of the light guide with respect to the quartz tile is the result of an optimization that reduces background amplitude from events moving through the light guides [55].

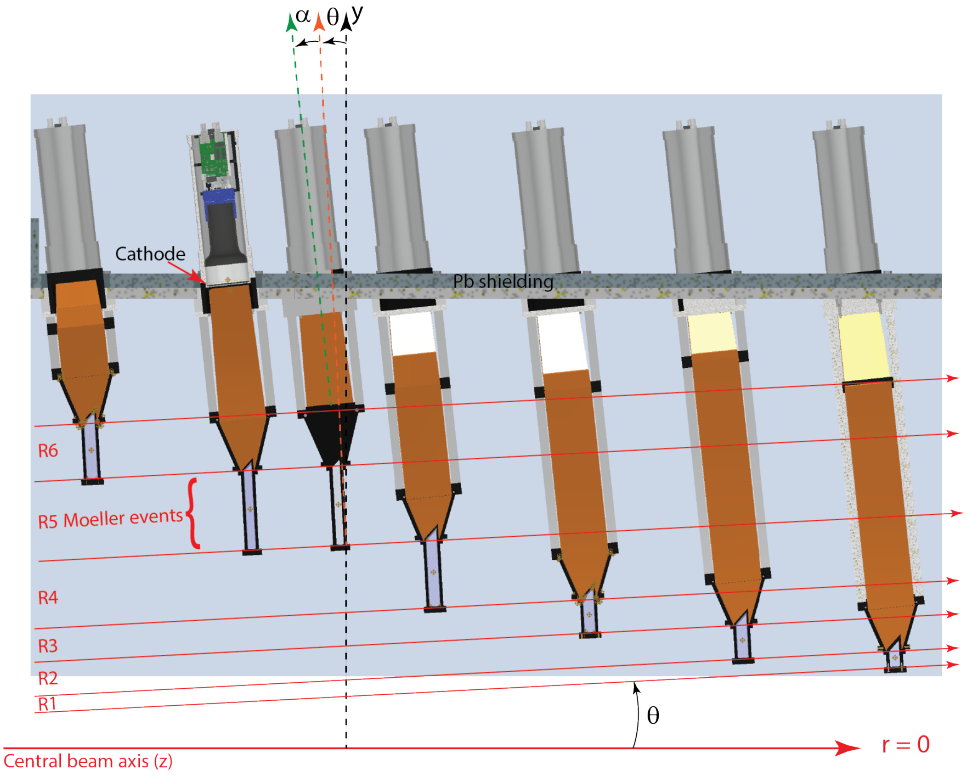

Figure 92: Arrangement of the detector modules in the front-flush segment plate. The length of each module is consistent with the tile location, covering the assigned radial region of the scattered profile, and the location of the PMT photocathode, which is surrounded by Pb in the segment plate assembly. The quartz tile is rotated by the mean polar angle ($\theta = 3^\circ$) of the steered electrons and the light guide is rotated by an additional angle ($\alpha = 3^\circ$) to reduce light guide background [55].

6.3 Module Design

Figure 93 shows an illustration of the Ring 5 module. Each module consists of a fused silica tile (here referred to as quartz), an air-core light guide, a PMT, and front-end electronics. The latter consists of the PMT voltage divider and two preamplifiers, one for single event counting mode and one for integration mode. The overall criteria for the module design include the maximization of signal yield and statistical resolution, as measured by the number of photo-electrons at the PMT cathode, the minimization of backgrounds and excess noise, relative signal stability over time, and detector linearity.

Each module design is somewhat different, due to the various module lengths and quartz tile sizes. The shape of the light guide and its orientation with respect to the quartz tile and the PMT have been carefully adjusted, based on light yield simulations and verified with beam tests of prototype modules, as described in subsequent sections below. The various parts are assembled and held together by a mounting structure that balances position precision, stability, and rigidity with a minimization of high Z material in

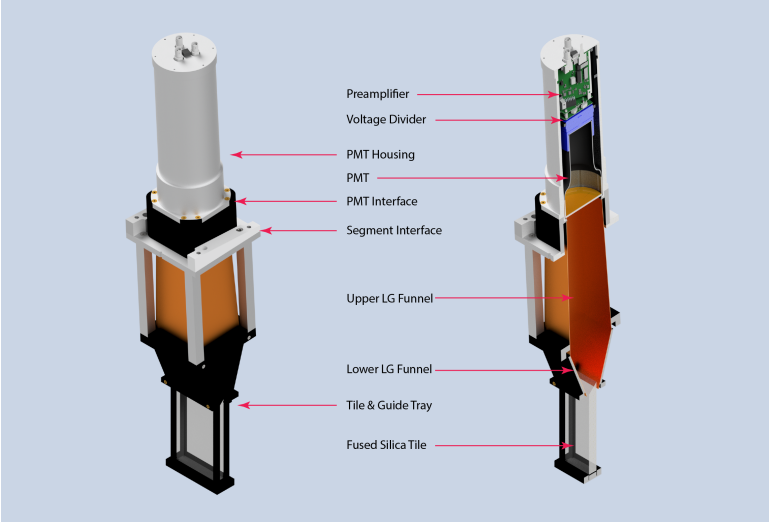

Figure 93: Annotated CAD model of the Ring 5 module. The left picture is shown with a cut-away, to show the internal structure of the module. In the left model, all items in black are currently proposed to be 3D printed, while all grey pieces would be made from aluminum.

Figure 94: Photos of the partially assembled Ring 5 prototype in May 2022, prior to beam tests. In the photo on the left, the quartz tile and lower guide cone tray is covered by part of the light seal bag that will surround the module up to the segment interface. Here the segment interface plate was 3D printed, as were most of the other pieces, but in the final construction these will be made from aluminum. The PMT housing is still detached (seen in the background on the right). It will be made from aluminum to aid in electromagnetic shielding of the PMT and electronics.

the detector region, which minimizes the amount of multiple scattering and showering and the cross-talk between detector elements. The module mounting structure, with the interface between the PMT housing, the light guide, and the quartz also has do be designed to allow air flushing of the light guide region and moderate cooling of the electronics.

Figure 94 shows photos of the Ring 5 prototype that was built for the May 2022 beam tests. For the beam test prototypes all parts were made from 3D printed plastics with the exception of the longer support rods, which were standard aluminum rounds. The final modules will have certain parts made from aluminum, as indicated and described in Fig. 93.

6.3.1 Fused Silica Tile Design

The active volume of the detector module consists of rectangular tiles of quartz, in which light is generated by charged particles traversing the material via the Cherenkov process. The tiles are highly polished, with a high degree of parallelism and perpendicularity of the sides with respect to each other, so that the generated photons are totally internally reflected until they reach the exit, which is a single edge/surface on the tile that has a 45 degree angle with respect to the surface of particle incidence. Figure 95 shows a photo of a 1 cm thick prototype Ring 5 tile (left) and a single electron event simulation (right) that illustrates how the Cherenkov light is normally incident at the 45 degree surface and exits the quartz into the light guide region. For safety reasons, and to prevent chipping, manufacturers prefer to add bevels to the tiles. The quartz tile has been simulated with and without bevels to determine the effect of the bevels as a function of bevel size. Up to a 0.5 mm bevel size, the losses are relatively minor at less than 5% of the overall yield. Table 20 lists the nominal manufacturing specifications for the quartz tiles.

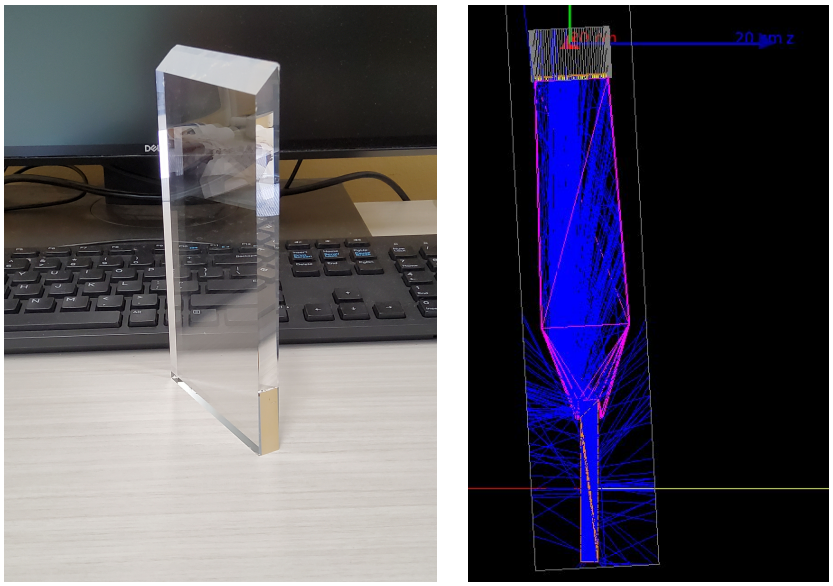

Figure 95: Left: A 1 cm thick fused silica tile with the Ring 5 prototype active area ($84 \times 140\text{mm}^2$) . The 45 degree cut that allows the Cherenkov photons to exit is visible. Right: A simulation image of a single electron event (red) incident from the left, on the quartz. The light is totally internally reflected until it reaches the 45 degree cut at the top of the quartz tile, where it exists into the light guide region. The angle of the lower light guide cone upstream surface (left side in the figure), is carefully adjusted, with respect to the quartz and the PMT, to allow most of the photons that exit the quartz to be reflected only once, and then shine directly onto the PMT cathode (yellow in the figure).

Table 20: *Nominal manufacturing specifications for the fused silica tiles.*

Material	Spectrosil 2000, radiation hard (H_2 doped)
Polish	20 Å or better, no gray
Dimensional precision	± 0.1 mm
45 degree cut precision	0.5 degrees
Primary surfaces parallelism	0.05 degrees
Perpendicularity (edges)	0.5 degrees
Bevels	0.5 mm

As mentioned above, the quartz tile lateral dimensions are set by the overall scattering profile, the need to resolve the different event types, and their deconvolution in the final analysis. The thickness for each tile was determined from light yield and excess noise simulations, in conjunction with the properties of the light guide geometry (see below). For Rings 5, 6, and 1, prototypes were tested with beam, to verify the simulation results. Beam test results are briefly presented below. The simulations incorporated all optical properties of the fused silica, light guide, and PMT window and cathode materials. Figure 96 (left) shows the theoretically expected number of Cherenkov photons generated per unit length and wavelength and the simulated number of photons at the tile exit (the 45 degree cut). The manufacturer specified quantum efficiency of the PMT that has been used for the prototype tests is overlaid for comparison. The right-hand figure shows the reflectivity of a standard light guide material for various angles (measured with respect to the reflective surface).

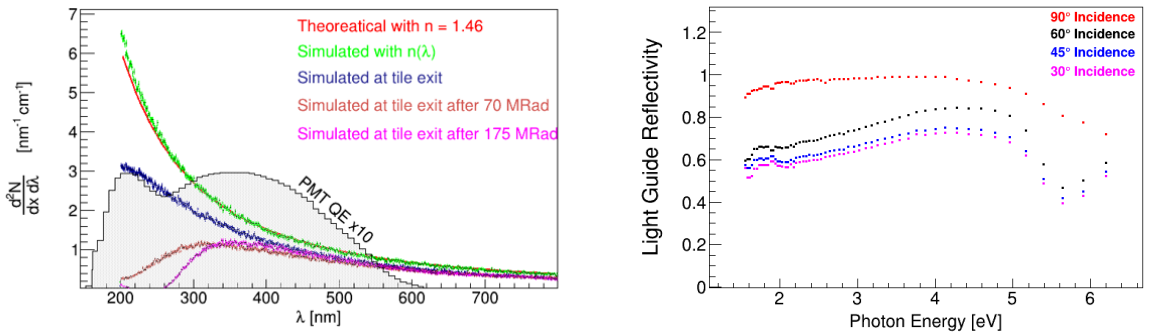

Figure 96: Left: Distribution of Cherenkov photon creation as a function of wavelength. Shown are the theoretical and simulated number of photon creation (red and green) and the number of photons emitted from the quartz tile at the 45 degree cut (see text), taking into account absorption and other losses. Also shown are the emitted photon numbers after radiation exposure of the quartz. The quantum efficiency of the PMT used in prototype development is also shown (gray) - here the vertical axis should be read as a probability). Right: Measured reflectance of the light guide material that was used in prototypes and for simulations (Anomet Miro Silver). The angles are given with respect to the reflective surface.

Generally speaking, thicker quartz means more photons and therefore a stronger signal. However, thicker quartz also produces more shower activity, which increases the photo-electron number fluctuations and therefore the overall signal RMS (a contribution to excess noise, above counting statistics). For Ring 5 the final excess noise factor should be kept below 6%, (ideally at or below 4%). From the point of view of quartz thickness (There are multiple factors that determine the excess noise level. See further discussion below), this can be achieved for tiles with 15 to 17 mm thickness. For the other rings we will use 20 mm thick quartz and accept 10% excess noise. The tiles for Rings 6, 4, 3, 2, and 1 need to be thicker, because

the light guide geometry is different (longer and/or more complicated) and reduces the overall number of photo-electrons.

6.3.2 Light guide design

The light guide design has to maximize the light yield at the photocathode and suppress background from events in the guide as much as possible. To achieve this, the guide is designed such that the number of reflections for photons coming from the quartz is minimized, while the number of reflections for Cherenkov photons created by events in the light guide is maximized. The latter is achieved primarily by the detailed guide design (see below) and the angle of the guide with respect to the vertical (see Fig. 92). Furthermore, the guide volume will be flushed with dry air, to minimize background event light yield in general, including from scintillation. Flushing the guides also prevents degradation of the reflective surfaces over time (see below for more details).

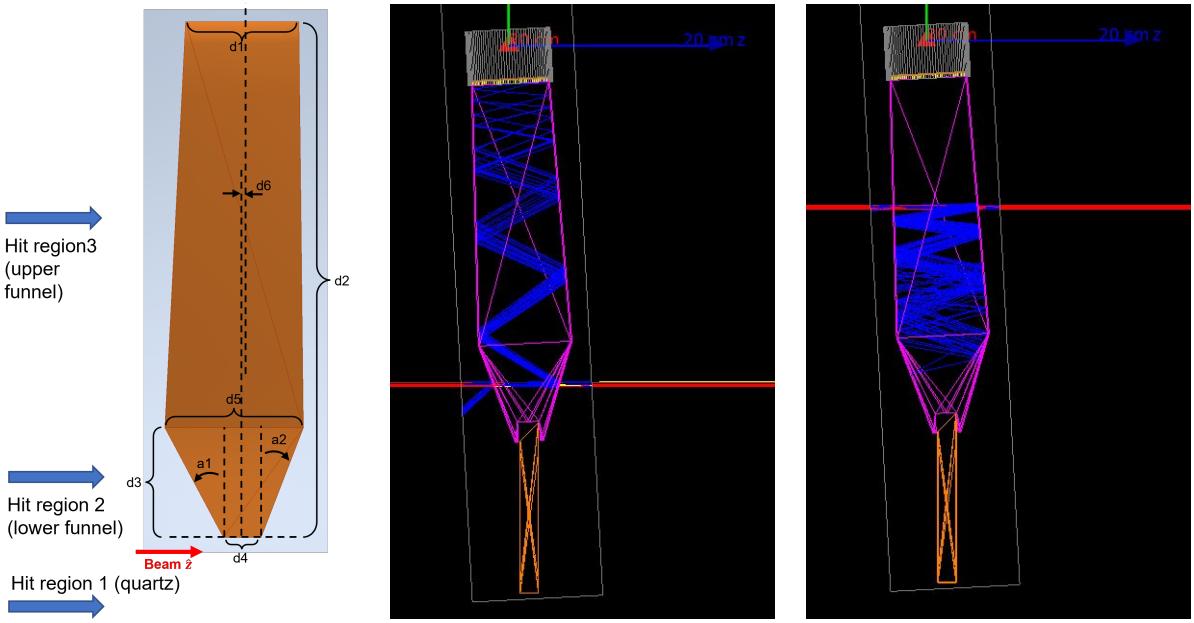

Figure 97: Left: Light guide design parameters for the two main regions of the Ring 5 design (see text). Right: The light guide has to be designed to maximize light yield from the quartz, but also to minimize light yield from events traversing the guide itself, which can be achieved by having many reflections and directing the light away from the PMT, as much as possible.

Ring 5 guide design: The design for Ring 5 is somewhat different from the light guide design for the other rings, owing to that fact that the Ring 5 quartz width is significantly smaller than for the other rings. Figure 97 (left) shows the design parameters for the Ring 5 light guide. Dimensions d_1 and d_4 are fixed by the PMT and quartz size respectively and dimension d_2 is fixed by the quartz and PMT radial positions. The main variables used to adjust the light yield performance of the module are then dimensions d_3 and d_6 and angles a_1 and a_2. Dimension d_5 is driven. The optimum light guide geometry was determined by simulating the light yield output for many different combinations of the free parameters (d_3, d_6, a_1, and a_2). The simulation code implemented all of the relevant optical quantities, such the reflectivity of the light

guide materials (see Fig. 96 (right) and Fig. 156), the absorption length of the fused silica and the reflectivity of the PMT window.

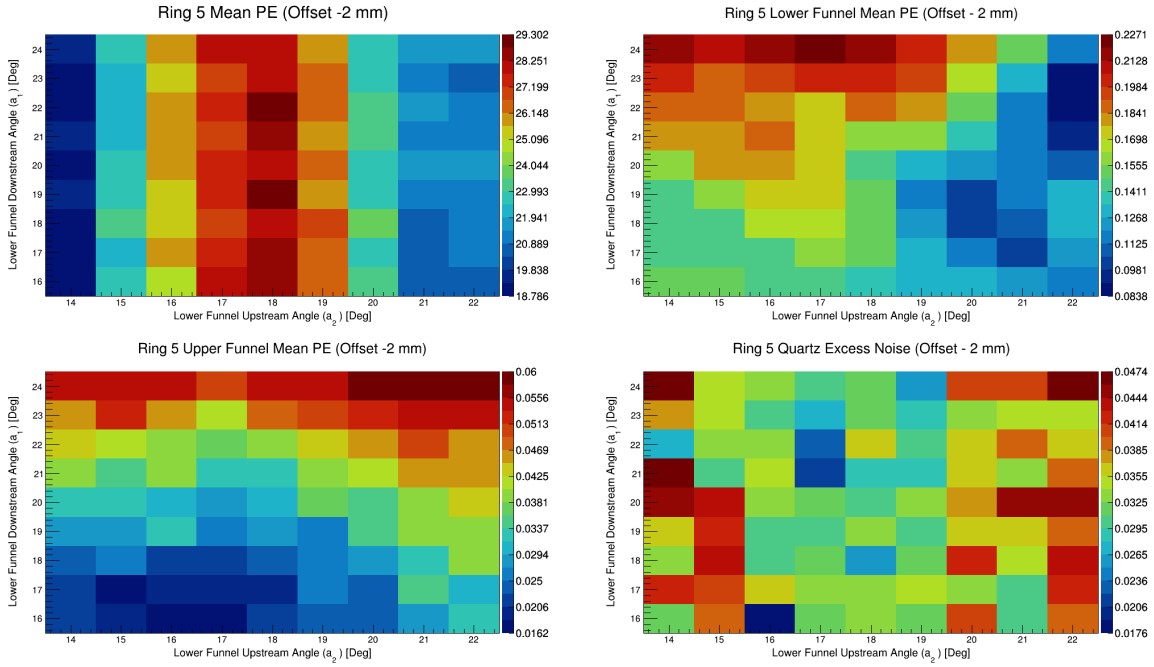

Figure 98: Shown here is an example of the Ring 5 light yield simulation results for a 15 mm thick quartz tile, as a function of the upstream and downstream angles. The axis labels reference Fig. 97 (left), with an offset $d_6 = -2$ mm, the shift between the quartz tile center and the PMT center along the beam, fixed for this set. The upper left plot shows the mean number of cathode photoelectrons for electron events in the quartz. The upper right and the lower left plots show the same quantity for hit regions 2 and 3 respectively (see Fig. 97). The lower right plot shows the excess noise for these configurations, which here refers to the statistical detector resolution.

Figure 98 shows example simulation results for a range of reasonable upstream and downstream lower funnel angles (a_1, a_2) at a fixed z-direction (beam) offset between the PMT and the quartz ($d_6 = -2$ mm - the negative sign meaning an upstream shift of the PMT with respect to the quartz tile). The length of the lower funnel length (d_3) was held fixed at a length that allowed the capture of all photons exiting the quartz tile. The upper left plot in Fig. 98 shows that the signal strength from the quartz is pretty much independent of the downstream angle (a_2), as expected. At the same time, the light yield from the light guide depends somewhat on that angle. For this reason, we may completely omit any reflective material for the lower funnel downstream surface, which would remove the Cherenkov signal from the lower funnel entirely. The lower right plot in Fig. 98 shows the excess noise due to the detector statistical resolution $\alpha^2_{RD} = \sigma^2_{n_{pe}}/\langle n_{pe}\rangle^2$ (see Eq. 14 and the text below Eq. 13 - electronic noise contributions are discussed below).

It is apparent from the results in Fig 98, that good results are obtained for light yield and excess noise, for the lower funnel angles with $a_1 = 18^\circ$ and $a_2 = 19^\circ$. Additional results obtained with different offsets showed that $d_6 = -2$ mm produced the best overall results for Ring 5. This was the geometry chosen for the prototype that was tested with beam in May 2022, at the MAMI facility in Mainz, Germany. Figure 99 shows beam data (left) and simulation data (right) of this prototype and the two agree reasonably well, at round $\langle n_{pe}\rangle \simeq 25$. The statistical resolution excess noise factor for this design is about 3.5%, which is better than our ideal design goal.

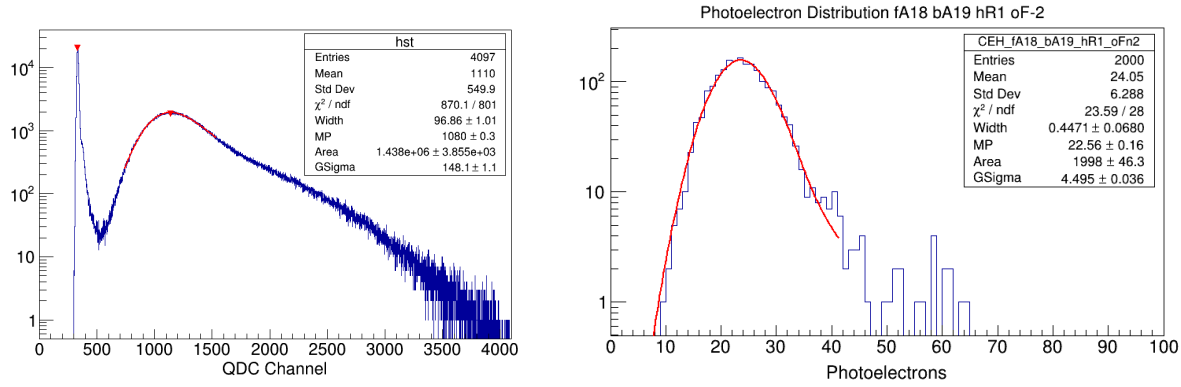

Figure 99: Left: Measured QDC spectrum from the prototype test performed in May 2022. The number of photoelectrons can be extracted from the fit parameters as $\langle n_{pe} \rangle \simeq 25$. Right: Simulated number of photoelectrons $\langle n_{pe} \rangle \simeq 23 - 25$, depending on whether one uses the fit most probable value or the mean of the histogram. In either case, the simulations agree well with the beam data.

Ring 1-4, and 6 Design The design process for the other rings follows the same principles as that for Ring 5. However, due to the larger width of the tiles, the photoelectron yield has a stronger dependence on the azimuthal width of the light guide. A single funnel, extending from the lower funnel toward the PMT, as is the case for Ring 5 created a strong variation of the light yield when one looks at electron events on the center of the quartz versus the edges. Given that the scattering angle (and therefore the hit location on the tile) depends on the kinematics and the asymmetry depends on the electron energy, this light yield variation across the face of the detector tile could produce a bias in the asymmetry. While this would likely be a small effect, it should nonetheless be reduced as much as possible, as it could be complicated to correct for in the analysis. This effect is strongly reduced by introducing a straight section in the guide, between the lower funnel and the upper funnel. Figure 100 shows how the corresponding design for Ring 4, but all the other remaining rings have this section.

As indicated in Fig. 100, the design parameters are again the upstream and downstream angles of the lower funnel (a_1 and a_2) and the linear dimensions d_1 through d_7. Dimensions d_1 and d_6 are constrained by the quartz tile dimension, while d_2 and d_7 are constrained by the size of the PMT. The overall length of the guide is again constrained by the location of the tile and the PMT, as for Ring 5. So for these rings, the variable design parameters are then again the two angles and linear dimensions $d_4 - d_5$. As mentioned above, all of the quartz tiles for these modules are 20 mm thick. That and the much larger width of the tiles require significantly more bulky light guides that the one for Ring 5. They are also all a fair bit longer (with the exception of Ring 6) than the Ring 5 light guide. As a result, the light yield can be expected to be smaller, requiring thicker quartz tiles.

Light guide material The choice of the light guide material has a large effect on the photo-electron yield and the yield stability over time, as a function of radiation exposure. Figure 96 in Sect. 6.3.2 shows the reflectivity as a function of wavelength and angle of incidence for the material mostly used in beam tests so far, Miro-Silver, produced by Anomet [56]. Figure 156 in Sect. 9.1.3 shows additional examples of reflectivity measurements on various materials. The highest light yields were achieved with anolux UVS, which produced up to 37 photo-electrons for a Ring 5 prototype, compared to about 25 photo-electrons for Miro-Silver. However, most of the additional light yield is coming from the UV and deep UV region and the UVS material is known to lose most of its reflectivity in that range, due to radiation damage.

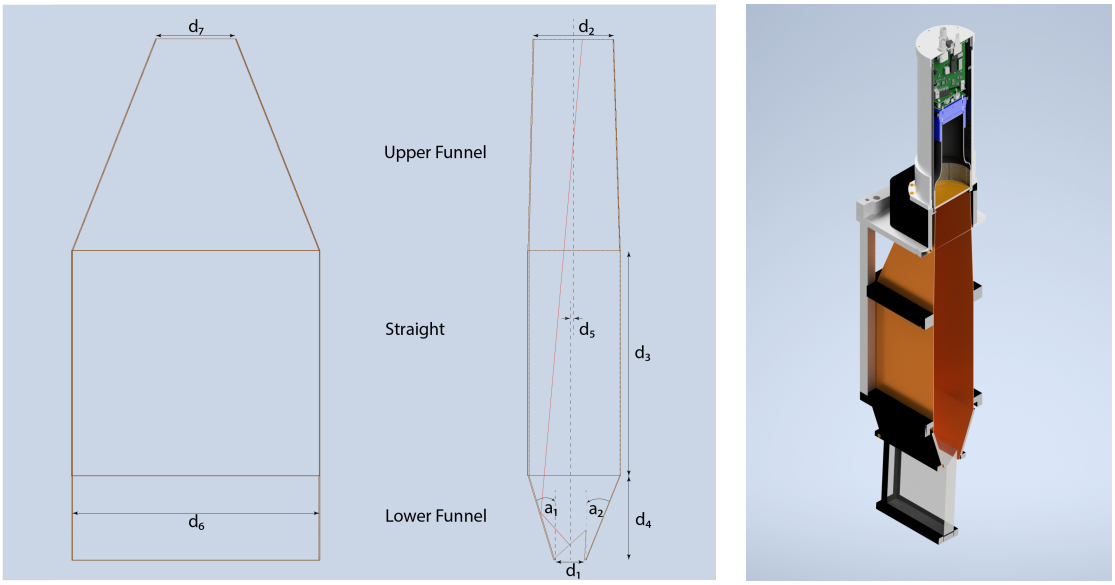

Figure 100: Right: Ring 4 light guide geometry. Left: Ring 4 detector module. Rings 1, 2, and 3 have the same structure, but are longer.

6.3.3 PMT housing

The PMT housing is a four-part design which implements several features for accessibility, security, and signal noise reduction. This housing consists of an aluminum outer tube (or sleeve), aluminum lid, and an internal 3D-printed two-piece tube which fastens to the rest of the detector module via the light guide to PMT (LGPMT) interface as shown in Fig. 101. The aluminum sleeve and lid act as a Faraday cage to shield the detected signal against background noise in Hall A. There is exposed metal around the HV connection on the top PCB disk of the PMT base which will sit in contact with the lid to ground the aluminum sleeve and lid to the PMT HV. The choice to use a combination of the aluminum sleeve with a 3D-printed PMT housing, rather than a housing made entirely with aluminum, was made for several reasons. The thin-walled aluminum sleeve will reduce the weight of the housing, compared to a thicker-walled aluminum tube required to implement the various design features of the 3D-printed parts, and remove the cost of machining those features. Furthermore, the 3D-printed parts are structured to allow air flushing through the housing (discussed further in Sect. 6.5) via internal air channels which cannot be machined.

A vital consideration in the detector housing design is light tightness. A thin O-ring is compressed within a dovetail groove between the two 3D-printed housing parts to light tighten this interface as shown in Fig. 102. There are three flanges located around both tube pieces at the interface plane. There are brass inserts which are heat set into the plastic of each flange on the bottom tube piece. When joined together, the two pieces are fastened by inserting a screw through the top flanges and threading into the brass inserts in the bottom flanges. By fastening with these screws, the O-ring will be compressed, preventing external light from reaching the PMT.

Figure 102 also displays the angled ledge design in the top section of the tube which secures the PMT and attached front-end electronics in place. This ledge sits around the lip of the PMT base socket (blue in the CAD rendered image) to keep the PMT in place, flush against the LGPMT interface, regardless of the detector module orientation. This design feature will also keep the electronics secure inside the 3D-printed housing when inverted without requiring the lid to be fastened, allowing better access inside the housing. The ledge is angled with large openings to allow smooth air flushing through the housing. To protect the

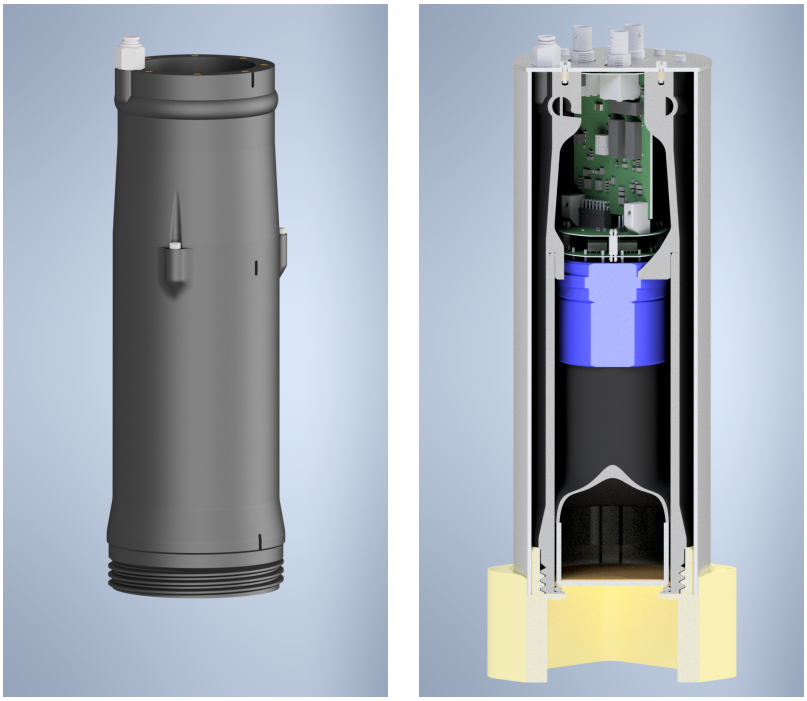

Figure 101: CAD renders of the PMT housing design showing external (left) and internal (right) features. On the right, the 3D-printed housing containing the PMT and front-end electronics is threaded into the 3D-printed LGPMT interface (yellow) with the aluminum outer tube and lid secured. The sliced view also shows the air flushing channels visible in the top 3D-printed piece.

front glass of the PMT from the 3D-printed material in this snug fit, there is an O-ring that sits between the PMT and the bottom lip of the housing tube.

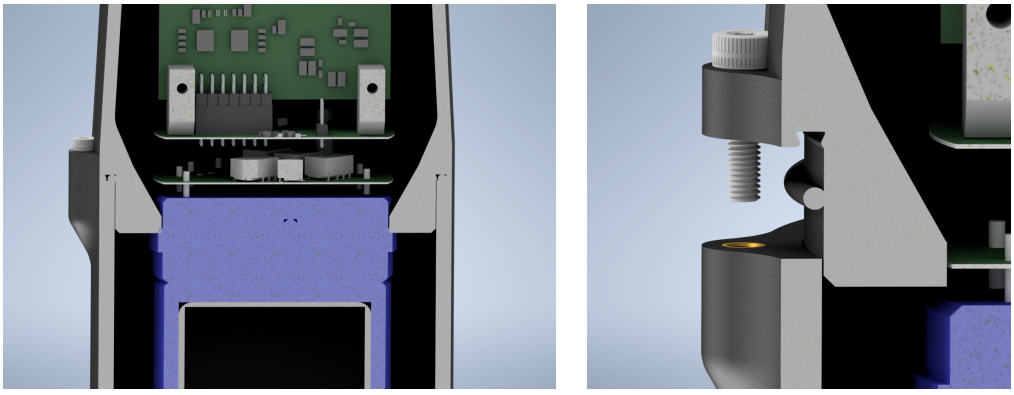

Figure 102: CAD rendered images showing the interfacing between the two tube sections and internal electronics. On the right, the parts are separated to show the dovetail groove for the O-ring in the top section and the brass insert in the bottom section for fastening.

Coarse threads are located around the bottom outside diameter of the 3D-printed PMT housing (see Fig. 103) and inside the LGPMT interface, such that the PMT can easily be fastened to the rest of the de-

tector module. The size of threading was designed to ensure clean 3D-printed threads and to decrease the likelihood of stripping over time. The interface has a leading section to help align the tube and interface threads. This threading is a key feature which allows the easy removal of the tube – holding the PMT and front-end electronics – as needed throughout the experiment. Should the electronics not function as expected, either in calibration or production running, a spare housing and electronics can be replaced instantly to prevent long downtimes. The malfunctioning electronics can then be carried away in the housing and worked on outside of Hall A.

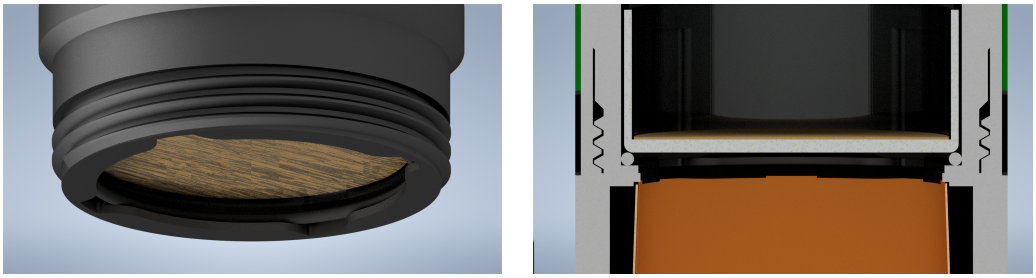

Figure 103: CAD rendered images of the threaded interfacing between PMT housing and LGPMT interface. The left image is a closeup of the threads located at the bottom of the 3D-printed tube. The right image is a slice through the housing to show the alignment of threading and the PMT position with respect to the protective O-ring and light guide (orange).

Inside the PMT housing, along the bottom, there are four grooves allowing the flushed air to exit the enclosure. The air will flow into the light guide via four corner channels cut out of the LGPMT interface, as shown in Fig. 104 and simulated in Sect. 6.5. The grooves are extended just past the widest part of the PMT to allow airflow around the PMT. By 3D-printing the threading between the housing tube and LGPMT interface, the end of the threads is positioned such that the channels are aligned between these two parts. As a further check, there are markers which face the same direction when the two parts are fully threaded, also visible in Fig. 104.

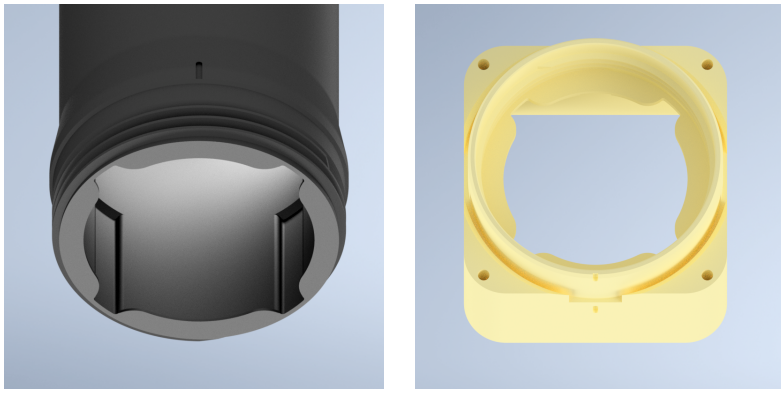

Figure 104: CAD rendered images showing the channels for air to flush from the PMT housing tube (left) through the LGPMT interface (right) into the light guides. Note the additional indented markers in both pieces and the designed thread stop to ensure proper alignment of channels.

6.4 Signal processing and front-end electronics

As mentioned above, the main detector has two signal streams, integration mode for production running, and single event mode, for tracking and diagnostics (e.g. monitoring of photo-electron yield during the course of the experiment). This requires the implementation of two separate signal handling streams and the associated electronics has to satisfy different criteria. Due the number of detectors and the corresponding non-feasibility of physically switching PMT bases to switch between the two modes, the PMT base has to support both modes, which we call low gain and high gain modes respectively. This switching has to happen remotely. The nature of the amplification is also different between the two streams, as is the digitization. The latter is described in Sect. 10.3.1 and Sect. 10.5. Here we describe the signal handling up the output of the preamplifiers. Figure 105 shows an overview schematic of the front-end signal chain for the integrating detectors.

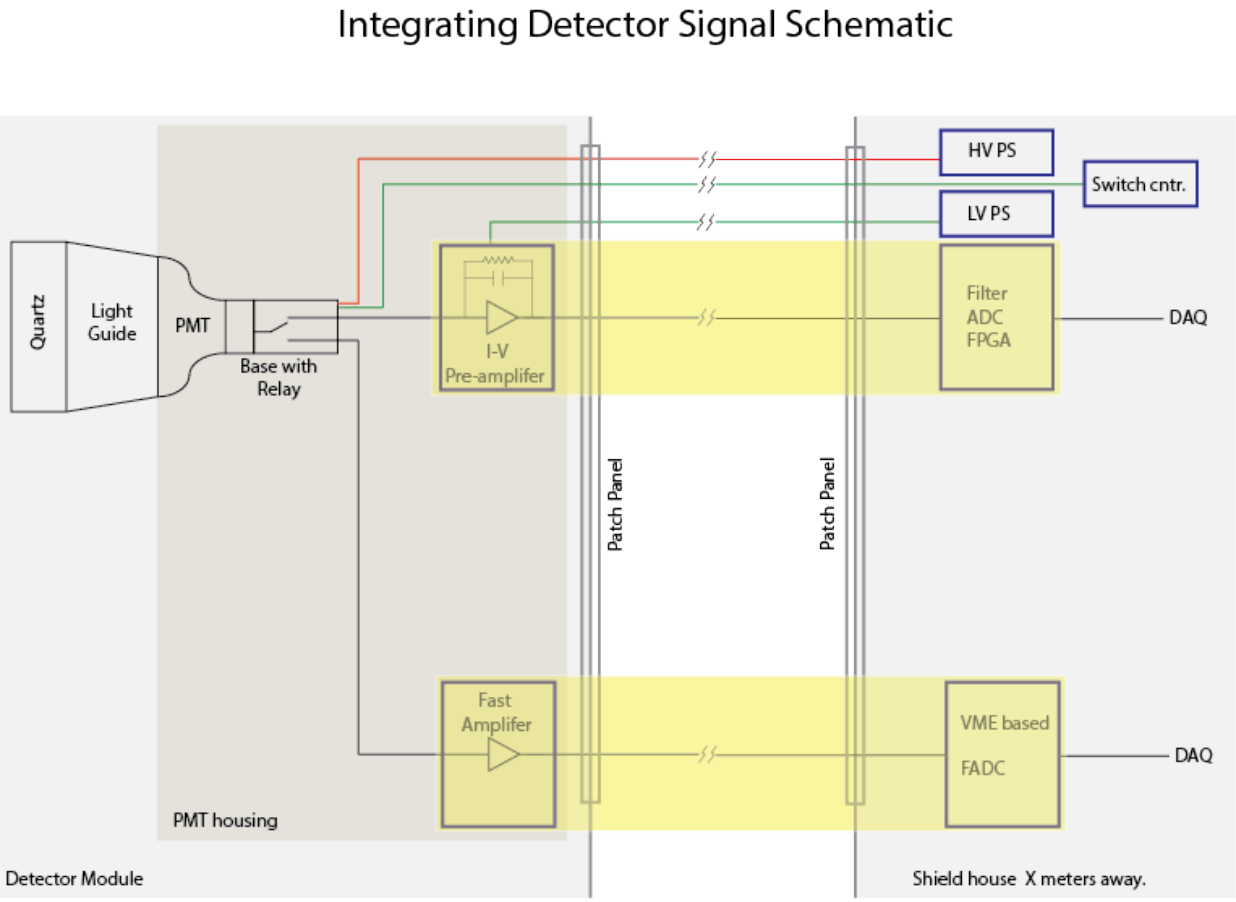

Figure 105: The signal schematic for the integrating detectors

6.4.1 PMT choice

The high rate integrating detectors produce cathode currents between 10 and 25 nA, depending on the actual rate and the number of photoelectrons per event. The cathode and anode current limits are specified by the PMT manufacturer and the maximum anode current sets the maximum gain that can be applied, given a certain cathode current. The PMT that is currently under evaluation for MOLLER is the 9305QKB PMT by ET Enterprises. It has a maximum anode current of 100 μA and one usually wants to stay well below that,

to ensure longevity and relatively long-term gain stability of the PMT. The manufacturer of the 9305QKB does not specify a maximum number of Coulombs that can be drawn from the anode, but other sources [57] give a definition of PMT *end-of-life* when the anode sensitivity has dropped by a factor 2, which typically happens somewhere between 300 and 1000 Coulombs [57].

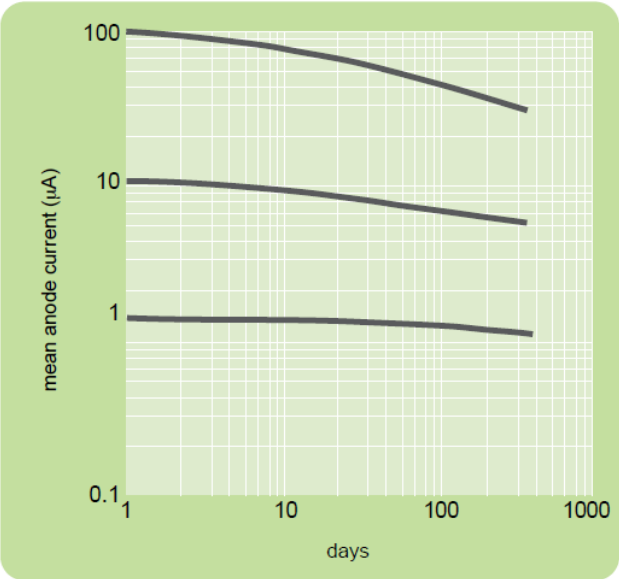

Figure 106: Plot of anode current stability under continuous illumination and constant bias voltage, taken over one year. The higher the anode current, the more pronounced is the gain drop over time. The figure was taken from [58].

Figure 106 shows the long-term gain stability, measured by ET Enterprises (not necessarily with the 9305QKB PMT) for a few different anode currents [58]. The figure shows that, for a starting gain that produces a continuous anode current of 10 μA at the beginning, the PMT will be at its nominal *end-of-life* state after a little less than a year of running. This is roughly consistent with 300 Coulombs of charge drawn over the year. MOLLER will run for 344 full days (or 8256 hours) and P2 will run for 10000 hours or about 416 full days. In current mode, the reduced gain can be countered by increasing the overall bias voltage over time, but, as will be discussed below, we want to start off with a relatively high bias voltage and low number of stages to begin with and the PMT maximum voltage ratings limit the possibility for increasing the bias voltage later on. For these reasons, it is prudent to keep the anode current at or below 10 μA, which means that the total PMT gain should be no more than around 1000, depending on the exact detector rate and photoelectron efficiency. Meanwhile , [54] discusses that large dynode gain and a high photoelectron efficiency reduce excess noise. The list below summarizes the various, partially competing constraints.

1. Optimize the detector resolution, which implies maximizing n_{pe}, as long as this is not achieved while introducing shower noise or other non-Poissonian (non-cathode related) noise sources.

2. Maximize the inter-dynode gain (δ) for, at least, the first and second stages.

3. Maintain a gain that is low enough to keep the anode current at or below 10 μA.

4. Maintain reasonably linear operating conditions, which means keeping the inter-dynode and dynode to anode voltage reasonably high.

The MOLLER candidate PMT has high gain SbCs dynodes for which the gain at the nth dynode satisfies the following relation [59, 60]

$$\delta_{dn} = 0.172 \left(V_{dn-1,dn}\right)^{0.72} \ . \tag{15}$$

Where $V_{n-1,n}$ is the voltage drop between the nth dynode and the one before. So choosing a large inter-dynode voltage increases the dynode gain, which decreases the noise. Having a large gain at the first dynode is critical, to reduce the noise. We also know that a low cathode to first dynode voltage (and a low or unstable voltage between the last dynode and the anode) leads to increased non-linear PMT behavior. At the same time, however, we are limited in how high we can make it and still keep the overall gain low enough. So for integration mode running, we want to use relatively few dynodes with relatively high gain. For the candidate 9305QKB PMT, the maximum cathode to first dynode voltage is $V_{k,d1} = 450$ V and the maximum inter-dynode voltage is $V_{dn-1,dn} = 300$ V. If all of the inter-dynode voltages are the same $(V_{d,d})$, then the total gain for an n stage voltage divider is [59]

$$G = aV_{k,d1}^{b}\left(aV_{d,d}^{b}\right)^{(n-1)} \ . \tag{16}$$

Where $a = 0.172$ and $b = 0.72$, for the SbCs dynode. We can write the total bias voltage as $V_{PMT} = mv + nv$ (an n-stage PMT has $n + 1$ voltage divisions), where $V_{k,d1} = mv$ and $V_{d,d} = v$. With that

$$G = a\left(\frac{mV}{m+n}\right)^{b}\left(a\left(\frac{V_{PMT}}{m+n}\right)^{b}\right)^{(n-1)} = a^{n}m^{b}\left(\frac{V_{PMT}}{m+n}\right)^{nb} \ . \tag{17}$$

Calculating $\partial G/\partial m = 0$, one finds that G is maximized when $m = n/(n-1)$, for a fixed bias voltage V_{PMT}.

6.4.2 PMT voltage divider

The Møller detectors will be operated in both low beam current counting mode for kinematics and background studies and high beam current integrating mode for asymmetry measurement. This requires the PMT attached to each detector can be operated in either high gain mode or low gain mode, accordingly. The PMT gain should be switched remotely between two operating modes. In order to reduce the possibility of radiation damage, we considered using a passive, resistive voltage divider and miniature mechanical reed relays as switches. Fig. 107 shows the schematic design.

The voltage on each stage of the divider was optimized so that the PMT could be operated safely at large cathode and dynode currents and the PMT non-linearity could be minimized. The low gain current mode has an optimized operating voltage of 800 V with a PMT gain of ∼500. Only the first 3 stages of the PMT dynodes are used in low gain mode, and the rest dynodes and anode are all tied together by the normal-close relay contacts. The first dynode voltage is regulated by Zener diodes to 280 V to ensure an effective and stable photo-electron collection. The anode is biased to ground potential by a 10 kΩ load/safety resistor. The high gain pulse mode has an optimized operating voltage of 1.2 kV with a PMT gain of $\sim 10^7$. The first stage is regulated at 280 V using the same Zener diodes. All other stages are utilized and each stage has the same voltage drop. The voltage divider is in current mode by default. The two operating modes can be switched back and forth by energizing and de-energizing the reed relays. Cylindrical, thin film resistors (surface mount, MELF0207 package, 1 W) were selected as the voltage divider resistors. They are chosen for their large surface area which has good heat dissipation capability.

The current return paths of high voltage, current mode signal, pulse mode signal and relay circuit are referred to as GND, I_GND, P_GND and C_GND, respectively. I_GND and P_GND are only tied to GND in their corresponding operating mode; they are isolated with each other to avoid possible ground loops while maintaining common AC grounding to reduce interference noises. C_GND is pulled down to GND potential by a 10 kΩ resistor and grounded by a capacitor.

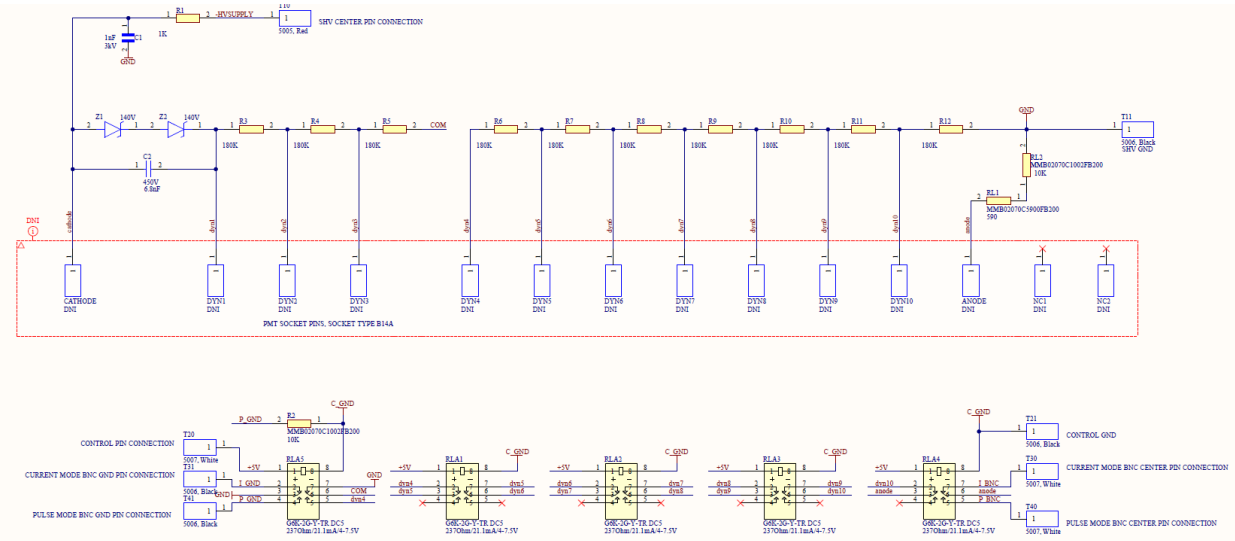

Figure 107: PMT voltage divider schematic diagram.

6.4.3 PMT (non-)linearity

The detector non-linearity is minimized prior to the experiment by characterizing its pmt non-linearity on the bench, and is monitored throughout the experiment by comparison with BCM measurements of beam current fluctuations and routine beam current scans.

The detector linearity requirement for MOLLER integrating detectors is to achieve a PMT non-linearity $\leq 0.5\% \pm 0.1\%$. A bench-top calibration system with multiple light sources and optical filters is used to quantify PMT non-linearity under specific running conditions. That is, the specific PMT cathode currents for the various ring and azimuthal semi-septant detectors. This system was developed and successfully used for PREX-II and CREX PMTs and has been adapted to handle MOLLER PMTs. It allows one to identify combinations of PMT HV and preamplifier gain setting that provide the needed level on non-linearity for a given cathode current.

In these studies, we vary the pre-amp and PMT gain settings while subjecting the PMT photo cathode to the various anticipated detector light levels using a set of LEDs. The input voltage range of the ADC constrains the possible PMT and pre-amp gain combinations. As an example, results from these studies for PREX-II and CREX are presented in Fig. 108. The PMT settings used for these experiments along with their non-linearities are given in Tab. 21.

Experiment	Cathode current (nA)	Detector	Pre-amp Setting (MΩ)	HV (V)	Non-linearity (%)
PREX-II	10	RHRS	0.21	-685	-0.208±0.389
PREX-II	10	LHRS	0.21	-615	0.100±0.056
CREX	0.15	RHRS	2.00	-910	0.298±0.103
CREX	0.15	LHRS	2.00	-905	0.228±0.165

Table 21: *PMT non-linearity results for PREX-II and CREX main detectors. PMTs are 2" Hamamatsu R7723Q with custom voltage divider for improved linearity.*

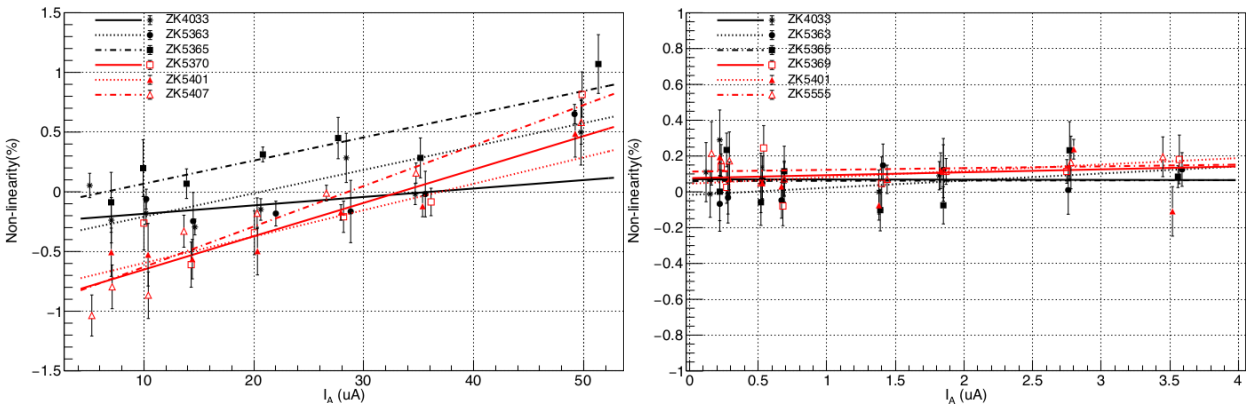

Figure 108: *Sample PMT non-linearity data from PREX-II (left) and CREX (right). Non-linearity is plotted against PMT anode current for various PMTs (serial number in the legend) at 10 nA and 0.15 nA cathode currents for PREX-II and CREX, respectively. The points are the measured non-linearities and lines are straight-line fits through the data for each PMT.*

6.4.4 Preamplifier

The primary considerations for the Møller trans-impedance preamplifier design are gain, bandwidth, noise performance and radiation hardness. The preamplifier needs to have a fully differential output to minimize common mode noises and match the integrating ADC's input. We choose to use two amplification stages in the preamplifier. The first stage is an I-to-V converter and the second stage is a cable driver with a fixed $\times 10$ voltage gain.

The fully differential amplifier LMH5401 is chosen in the first stage for its ultra wideband and low noise properties, as well as its potential of withstanding harsh radiation environments. Figure 109 shows the schematic of the first stage preamplifier. The preamplifier needs a minimum 150 kHz bandwidth to follow the helicity reversal signal which has a 10 μS settling time. Taking into account the component value variations, we have set a signal bandwidth of a minimum of 250 kHz as the design target. There is a wide range of gain requirements for detectors in different sectors and rings. To meet the gain requirements, we use a set of micro DIP switches to select the preamplifier gain between 0.1 and 1.0 MΩ, as seen in Fig. 109. The fully differential amplifier LMH5401 works in single-ended input mode. A small multi-turns potentiometer is used to match the input impedance and make small adjustments to the output common mode voltage.

The second cable driver stage requires exceptional signal fidelity. It must have the ability to sustain signals in a cable over a long distance ($\sim$150 – 200 m) between detectors and the digital integrator. Two ultra-low distortion wideband Op Amp, LMH6702, are used to form a fully differential amplifier, as seen in Fig. 110, by utilizing their wide dynamic range and radiation hardness. An optional offset control circuit (not shown in the figure) can be used to adjust output differential bias voltage. An RC filter at the output limits the bandwidth and reduces the higher frequency noises. It also eliminates possible oscillation due to driving long cables. The output connector and cable are BNC Twinax and RG-108, respectively, which match the integrator input. For suppressing common mode noises, the entire signal chain is fully differential. The simulated bandwidth of this design has an upper bound of $\sim$ 2 MHz, and can be varied by optimizing component values. The bandwidth decreases significantly with increased input and load cable length.

A preamplifier for pulse mode operation is integrated into the housing of the PMT base. It is a fast pulse amplifier with a $\times 5$ gain for pulses with a typical width of less than 100 ns. Fig. 111 shows the schematic design which includes a Silicon Monolithic Microwave Integrated Circuit (MMIC) wideband

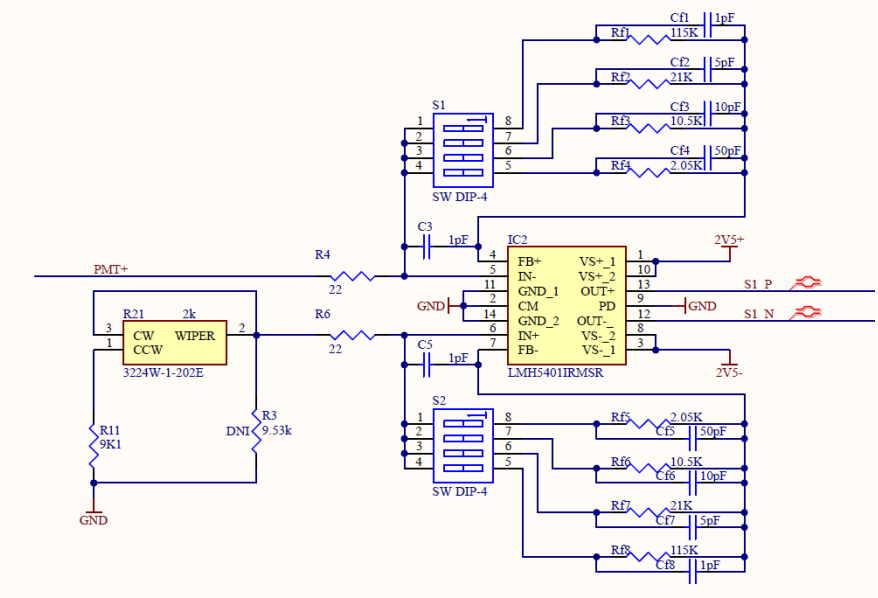

Figure 109: Schematic of the current mode preamplifier input stage.

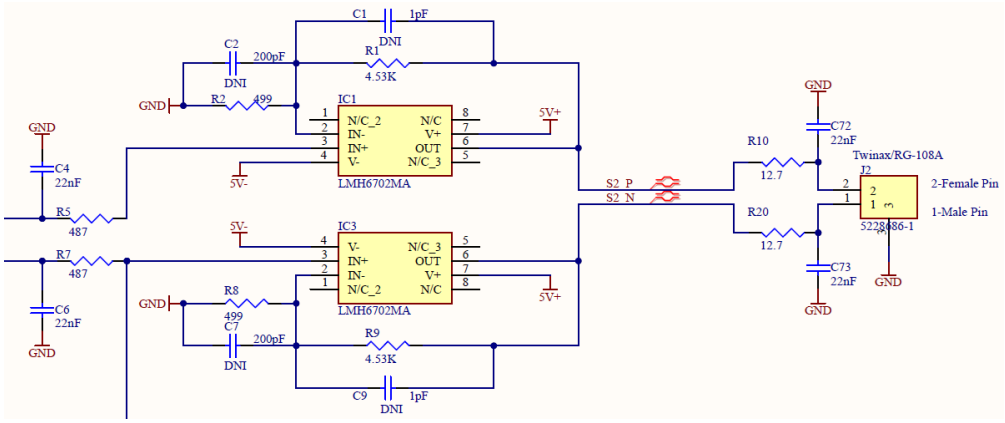

Figure 110: Schematic of the current mode preamplifier cable driver stage.

amplifier BGA2869. It is in a 6-pin SOT363 plastic SMD package with an internal matching circuit. This largely simplified the design. The preamplifier can be completely bypassed by a jumper.

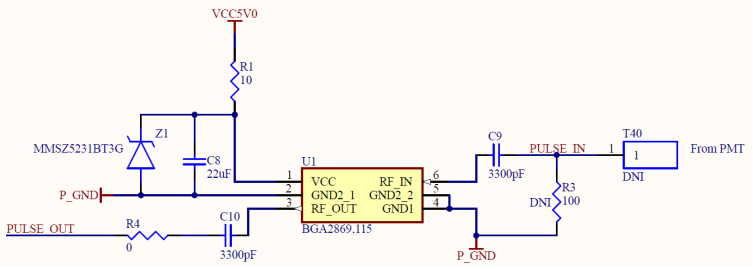

Figure 111: Schematic of the pulse mode preamplifier.

To avoid ground loops, isolated DC-DC converters are used to provide power for the voltage divider,

current mode amplifier and pulse mode amplifier. We have selected a type of DC-DC converters that have proven stability and radiation hardness. Because they are switching-type power supplies, we have carefully designed the filtering and decoupling circuit to minimize power supply interference, ripples and switching noise.

In order to reduce the number of cables and connectors, we implemented a specific design that combined 3 cables, including the current mode power supply cable, pulse mode power supply cable and the mode switching control cable, into a single LEMO cable. When an external +6V power supply is applied, the PMT voltage divider works in low gain mode and the current mode preamplifier is powered on. When reversing the power supply polarity, the voltage divider is switched to high gain mode and the pulse mode preamplifier is in turn powered on. Figure 112 shows a section of the power supply schematic. The PMT base circuit is protected by a PTC resettable fuse. The power consumption is about 2.5 W.

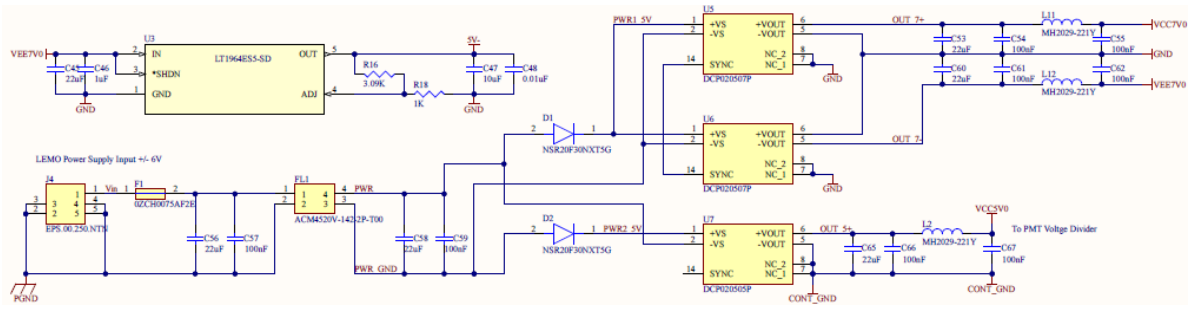

Figure 112: PMT base power supply

From the schematic design, 4 printed circuit board (PCB) layouts were implemented. These PCBs can be arranged and assembled together, and fitted into a 2 inch diameter housing. A picture of an assembled PMT base prototype is shown in Fig. 113. From left to right, there are a PMT socket (the light blue cylindrical part), a voltage divider, a pulse mode preamplifier, a current mode preamplifier and an end-cap which provides a mounting position for connectors as well as acts as a shielding panel and grounding plane. The connection between the pulse mode preamplifier and the current mode preamplifier is via a header connector and two Nylon mounting blocks. The current mode preamplifier board can be easily detached in case a replacement is needed.

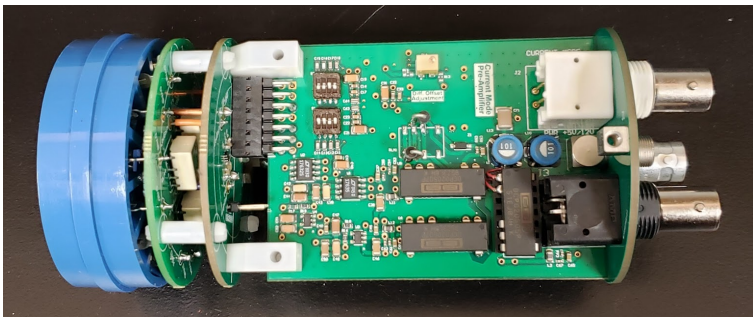

Figure 113: Prototype of the PMT base with a voltage divider and preamplifier.

This latest prototype is an optimized outcome of three design iterations. In each of the previous designs, we had the corresponding prototypes tested on a bench as well as with detectors in beam. The prototype performances and any newer requirements were evaluated, then some modifications and improvements were implemented in the following iteration of the design.

A wide range of bench tests are being carried out using the latest prototype assembly. For a typical

low gain, current mode operation, the gain of the preamplifier was set at 200 kΩ with a 250 kHz signal bandwidth and 400 kHz equivalent noise bandwidth. The boards under test were shielded in cylindrical Aluminium housing. The output signal was measured by a digital oscilloscope. We found the prototype was functioning well under various test conditions. Figure 114 shows a picture of an oscilloscope screen with preamplifier's baseline signal (i.e., the noise floor without input signal) being measured. The width of the light yellow band represents the noise amplitude of the single-ended time domain baseline signal, which has an RMS value of ∼1 mV and a peak-to-peak value of 4 mV. The red trace is an FFT of the baseline signal which reflects the noise amplitudes in the frequency domain.

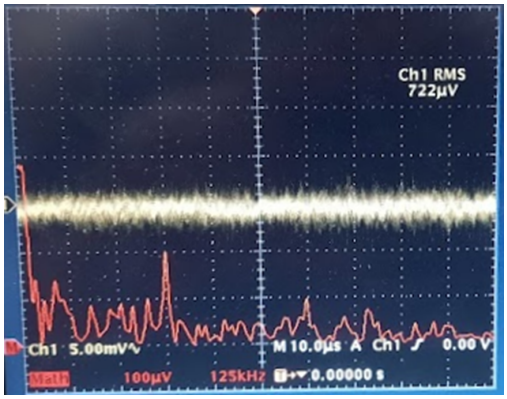

Figure 114: Screen shot of baseline noise measurement of the preamplifier prototype.

The pulse mode preamplifier has also been tested on a bench. Fig. 115 shows an oscilloscope screen shot of a typical cosmic ray pulse captured at the preamplifier output. In this test, the PMT and preamplifier were operated at high gain pulse mode with a high voltage setting at 1200 V.

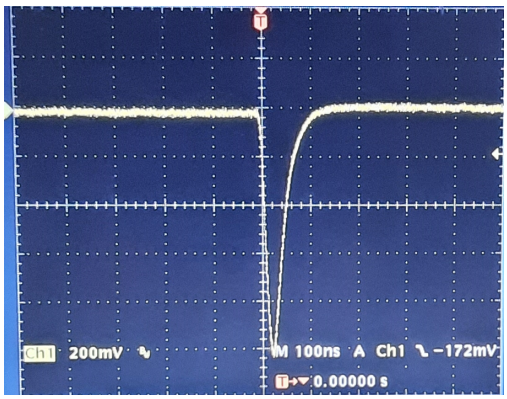

Figure 115: Screen shot of cosmic ray signal measured with the high gain voltage divider pulse mode of the preamplifier prototype.

Currently, more prototype bench tests are being conducted and the design is being finalized. More PMT base prototypes are also being manufactured in preparation for a planned, full electronics chain beam test.

6.5 Cooling and air flushing

There are several reasons for flushing the detector modules with dry air. The most important reason would be to mitigate the observed effect of progressively worse depositions on the light guide reflective surfaces as a result of ionization of air, from the beam electrons, reducing the light yield over time. This effect

has been shown to be much reduced, if not completely removed, by flushing the guides with dry air. A second reason is the reduction of possible background from events moving through the light guide [55]. Additionally, while the power dissipation of the front-end electronics is relatively low, the PMT enclosure together with the light tightening of the module as a whole, does not allow for ready exchange of heat with the environment and the PMT housing has been observed to get warm during prototype operation.

6.5.1 PMT base cooling

The top section of the 3D-printed PMT housing, shown in Fig. 101 of Sect. 6.3.3, includes the design of internal air cooling channels. The incoming air is split into two channels, highlighted in Fig. 116, each ending in nozzles facing the heat generating components on both sides of the current mode preamplifier PCB. The inlet uses a 1/4" push-to-connect fitting with a 1/8" NPT thread, and is directly screwed into the top of the housing. A hexagonal cutout has been added to the lid to accommodate the inlet fitting.

Preliminary airflow cooling tests have been conducted with promising results. When measuring the surface temperature of one of the DC-DC converters, a temperature drop of 10-15 °C was observed. However, this test used an older PMT base with three DC-DC converters. A new design with a single converter is being evaluated for radiation hardness and cooling.

Simulations were conducted in COMSOL 6.1 with the new design to visualise the airflow within the PMT base housing, with the results of these shown in Figs. 117 and 118. The inlet in this simulation uses a volumetric flow rate value of 3933 $\mathrm{cm}^3/\mathrm{min}$.

The simulations indicate the possibility of improving the airflow to cover all the heat-generating components, particularly the op-amps on the back side (Fig. 118). The interfacing of the top section with respect to other parts may be considered final. Some aspects of the internal geometry, such as the positions and angles of the channels and nozzles, may undergo slight modifications to improve airflow, print quality, and to reduce the amount of 3D-printed material used for the housing.

6.5.2 Light guide air flushing

To visualise the airflow and humidity within the light guides, multi-physics simulations (coupling turbulent flow and moisture transport in air), were conducted in COMSOL 6.1. The time-dependent simulation begins with the relative humidity (rH) in the light guide volume at 100%. At the inlets, dry air at 0% rH is pumped in at the same flow rate as the PMT base inlet (3933 $\mathrm{cm}^3/\mathrm{min}$). Figure 119 shows the results for the simulation with the Ring 6 light guide's air volume. The plot in Fig. 119 shows the maximum rH at any point in the light guide volumes plotted against time. For Ring 6, it takes 327 s for the maximum rH to drop below 1%, whereas for Ring 5, it takes 86 s.

The Ring 6 light guide was chosen for this simulation due to its width, which results in slower air mixing compared to the other rings. On the other hand, the Ring 5 light guide is the narrowest. Simulations of light guide air volumes will be completed for all the rings, followed by bench tests for validation.

6.6 Mounting Structure

As described in Sect. 6.2.2, the main "thin" integrating detector array is made up of 6 rings with radial and azimuthal segmentation driven by physics requirements described in Sect. 7. Later in Sect. 9.1, the auxiliary "Shower-max" detector is described, which will make a complementary measurement of the main Møller asymmetry. In this subsection, we lay out the engineering design of the mechanical structure that houses the main detector and shower-max detector assemblies while satisfying the physics requirements for positioning accuracy and ease of installation and maintenance. An overview CAD illustration of the design is shown in Fig. 89 of Sect. 6.1.

The mounting structure design must incorporate the following broad criteria:

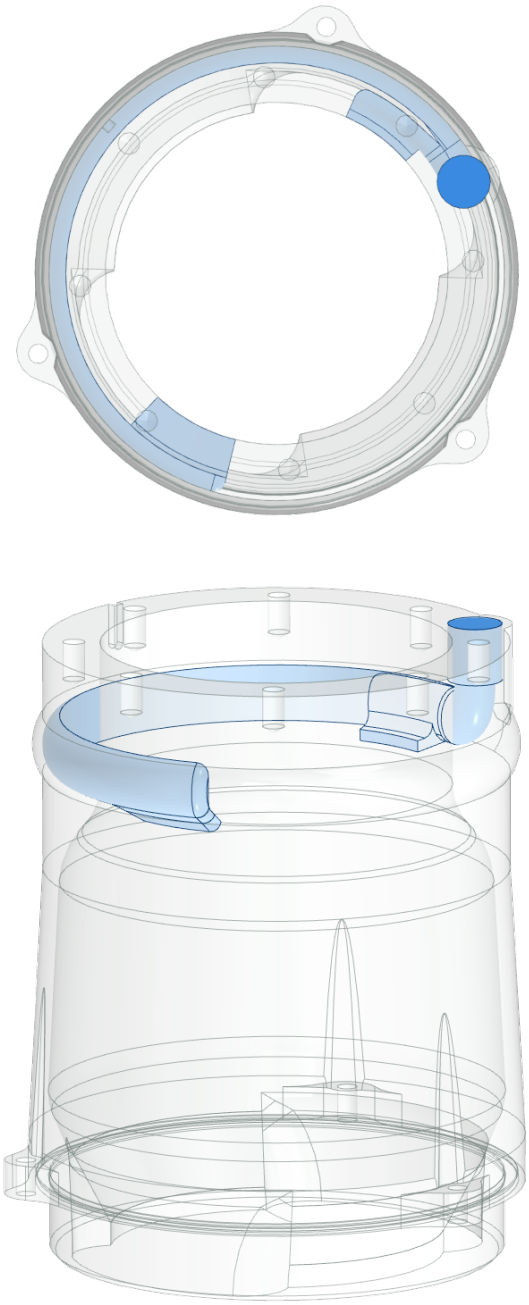

Figure 116: PMT housing top section shown with the internal airflow channels highlighted in blue. The split in the air channel is visible in the top view (top) immediately following the inlet.

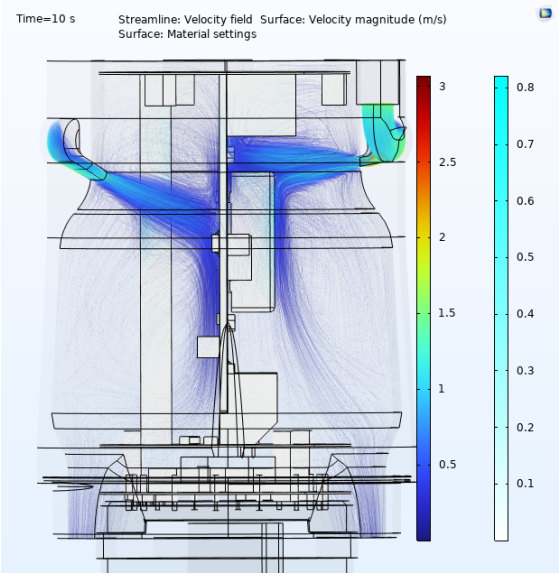

Figure 117: PMT housing airflow simulation results with streamlines showing air exiting the nozzles and flowing directly onto the heat-generating components on the PCB. This side view shows both nozzles.

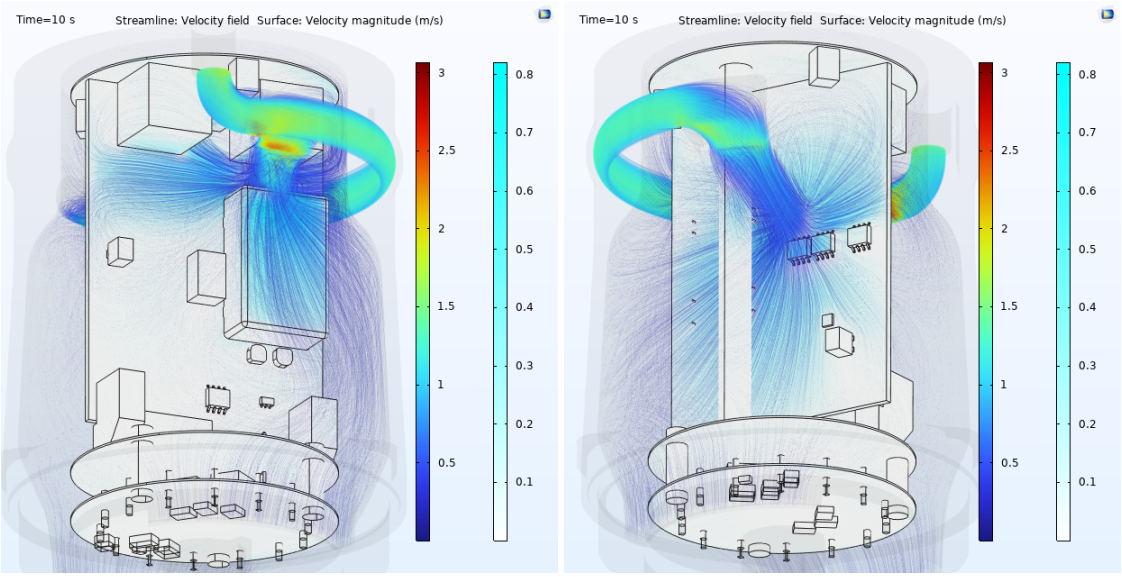

Figure 118: PMT housing airflow simulation results with streamlines showing air exiting the nozzles and flowing directly onto the heat-generating components on the PCB. Front view with DC-DC converter (left), and back view with op-amps (right).

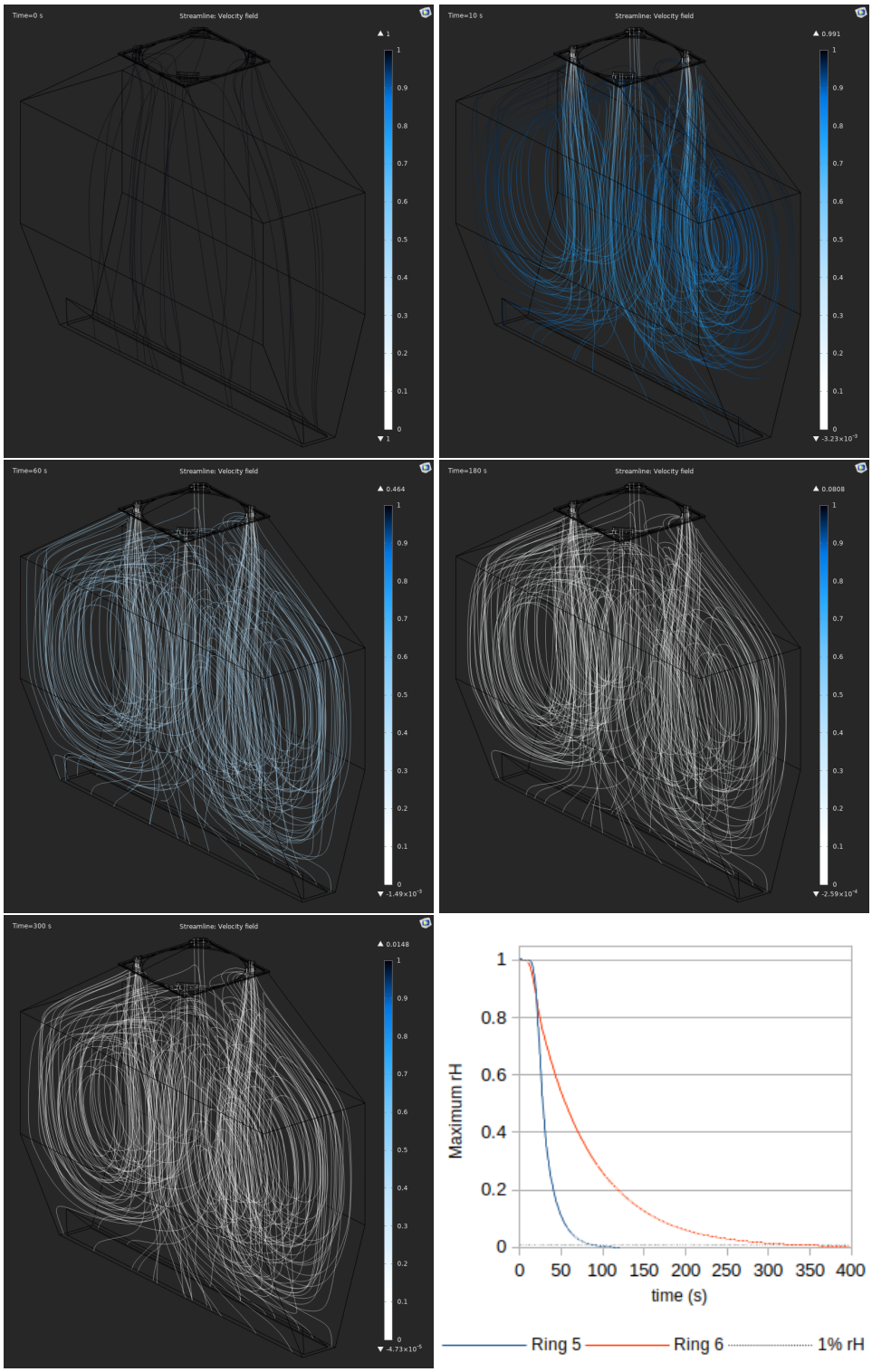

Figure 119: Ring 6 light guide airflow and humidity simulation results showing the stable airflow pattern (streamlines) and relative humidity (streamline colour) within the Ring 6 light guide at 0 s, 10 s, 60 s, 180 s, and 300s. The plot in the bottom right shows the maximum rH at any position within the Ring 5 and Ring 6 light guides vs time. Note that the Ring 5 simulation was performed with an older design and will be updated.

- The quartz tiles must be located in 3-D space to within ± 1 mm of the intended location in the conceptual design while the PMTs that integrates the scattered flux response is shielded from significant radiation
- The detector lightguide assemblies that locate the quartz and attach to the PMTs must not add significantly to the material budget intercepted by the scattered flux
- The assembly must include sufficient shielding in the region of the PMTs and pre-amplifiers and module subassemblies must be capable of being installed safely and efficiently
- The PMT and preamplifier subassemblies must be accessible for maintenance after installation and appropriate conduits leading to cable bundles must be incorporated.
- All materials used in the mounting structure must be sufficiently radiation hard.

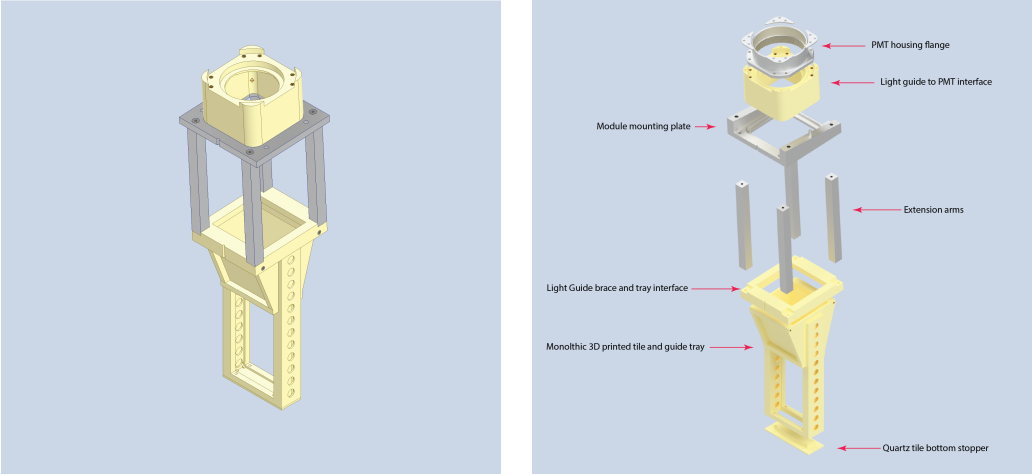

Figure 120: *CAD renderings of the Ring 5 main detector module structure prototype, assembled (left) and exploded, with annotated detail (right).*

6.6.1 Module structure - alignment and positional precision

The individual module structure around the fused silica tiles and the light guide must be both, as low Z as possible, as well as rigid. It must hold the tiles and light guides in position while minimizing stresses on either. The surface contact area between the fused silica tiles and the mounting structure must be minimized as much as possible, while precisely holding the tiles in place at all possible rotational orientations around the beam line. The structure must define the angles between the light guide and the fused silica tile to ensure accuracy during assembly and flatness of the orientation of the primary reflector. The photon exit surface, with the 45° cut (see Fig. 95), cannot be blocked by material, except for very small sections at the corners serving as touch points to hold the tiles in place. The mounting structure must ensure that the positional accuracy of the tiles is maintained under gravity and other stresses (see FEA analysis below).

Figure 120 shows the module structure for Ring 5. The Ring 4 module structure is shown in Fig. 121. The structure for the other long rings (1,2, and 3) is identical to that for Ring 4, except that the middle section, holding the light guide, is longer, corresponding to the different lengths of the guides (see Fig. 92). Figure 121 also shows the Ring 6 structure, which is somewhat different from the other rings, owing to its very wide and short geometry. The Ring 5 structure is different from all the other rings, because it is relatively more narrow and the ring is more crowded, requiring special care in the structure design. Parts

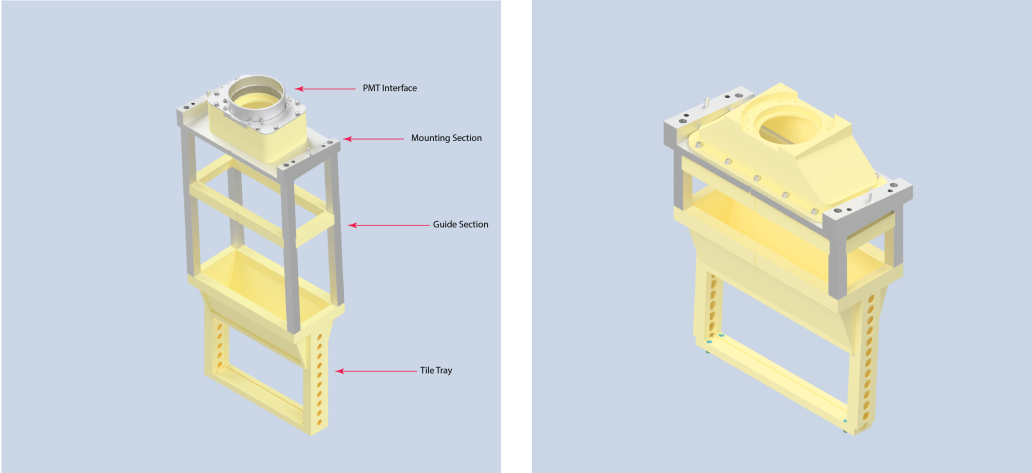

Figure 121: *CAD renderings of the main detector module structure prototype. Shown are the other two examples of the variations in the structure for Ring 4 (left) and Ring 6 (right).*

shown in gray are designed to be made from Aluminum, while parts shown in yellow are designed to be made from a suitably chosen 3D printed plastic.

For all rings, the module structure can be divided into three main sections:

1. The *tray section*, holding the quartz tile and the primary reflectors of the light guide and defining the interface between the two.
2. The *guide section*, holding light guide and defining angles of its lower and upper funnels.
3. The *mounting section*, holding holding the module in the detector array.
4. The *PMT interface section*, defining the interface between the light guide and the PMT.

Tray Section: Figure 122 shows a detail cutaway of the monolithic, 3D printed *tray section* that defines the quartz tile position and the angular relation between the primary reflector of the light guide and the 45 degree cut exit of the quartz tile. The figure also shows the standoffs used to hold the quartz in place while minimizing the contact area between the quartz and the mounting structure. The angles were optimized in simulations and verified in beam tests with prototype detectors. For test purposes, the trays have been constructed in various forms, including from individual, bolted parts and in monolithic form, as shown here. The aim is always to optimize with respect to material budget, accuracy, and rigidity. The trays depicted in Fig. 122 have hollow side arms for the quartz tray, with holes for additional removal of material. Produced parts of the trays for Rings 1, 2, and 5 are shown in Fig. 123. The white colored tray for Ring 2 is made from nylon-12, produced by selective laser sintering (SLS) while the black parts are made from C-fiber infused nylon, with regular 3D printing. Radiation hardness of these materials has been partially addressed, as discussed in Sect. 6.7 and more will be done in a December beam test.

Guide section: Various figures in this chapter, including Fig. 92 and in more detail Fig. 100 illustrate the orientation and geometry of the various ring light guides. The *guide sections* must ensure that the guides can be held in place at the correct orientation and surface angles, while minimizing the material budget around them. Figure 92 shows that primary electrons and shower particles from event regions in upstream

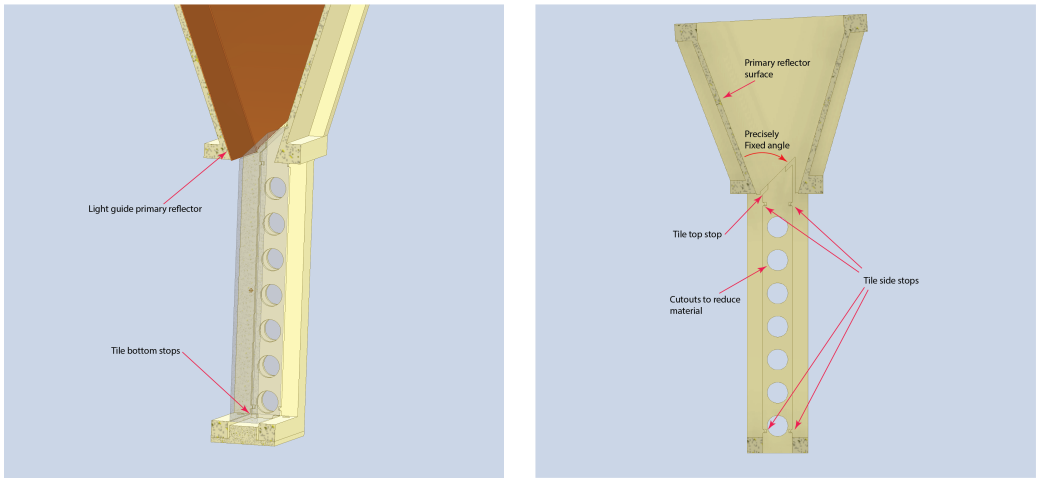

Figure 122: *Cutaway view of the lower part of the quartz-light-guide tray, showing the quartz tile mounting concept and the location of the primary mirror with respect to the quartz tile.*

rings will traverse the light guide sections of downstream rings. To minimize this ”crosstalk” and reduce the possibility of additional background, there should not be a solid, continuous housing around the light guides. The guide geometry and the orientation/angles of the guide surfaces is therefore defined only by the *braces* shown in Fig 120 (right) and Fig. 121 (left). The *extension arms* are chosen to be thick enough to support the modules within the array, locating the quartz tiles to within the desired accuracy.

Mounting section: The modules must be mounted at the correct angles to the segment plates, as illustrated in Fig. 92. The mounting plate incorporates this angle precisely, via the machined wedge sections. It also includes two locating pins that will position the modules precisely on each of the 28 segment plates, in z (beam direction) and in the azimuth.

PMT interface section: Section 6.3.3 describes the PMT housing and the purpose of this (primarily 3D printed) section is to locate the PMT housing, and therefore the PMT itself, precisely with respect to the light guide. Figure 101 shows a cutaway of the tube within which the PMT is positioned. The overall construction of the modules includes a location shift along the beam direction, with respect to the quartz location, that optimizes the position of the locus of the detector light yield on the cathode. This shift is incorporated in the design of the interface section. The design of this section, in combination with the design of the PMT tube, also allows for relatively easy removal and exchange of the PMT, should this be necessary after the array is constructed.

6.6.2 Design of the overall structure

As described at the beginning of the chapter, the detector array will consist of 28 azimuthal segments with 8 detector modules each. The segment plates are mounted on two (upstream and downstream) annular plates, as shown in Fig. 89. To shield the PMT cathodes lead plates are incorporated in each segment plate, surrounding the PMT cathode region, such that a lead barrel of 2.5 cm thickness encircles the entire detector array. A side view of one of the segments is shown in Fig. 91 in Sect. 6.2.2, where the shielding can be discerned as the grey volume between the light guides (orange) and the PMT housings.

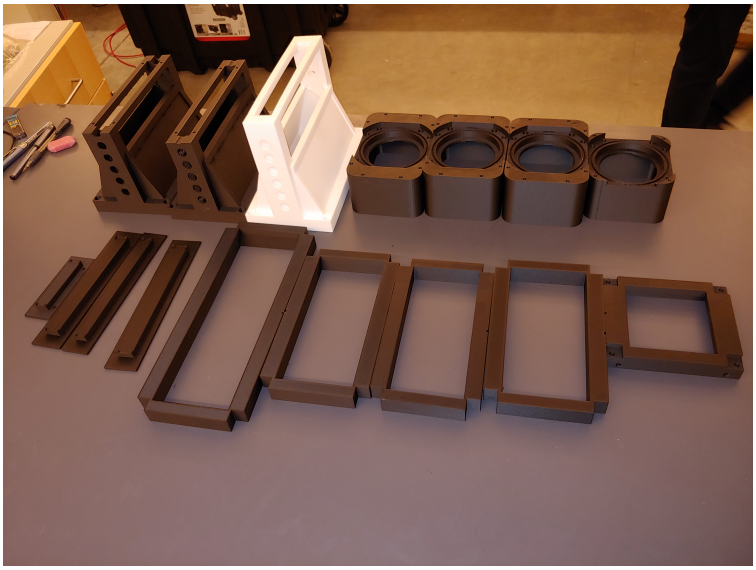

Figure 123: *3D printed parts of the detector modules for Rings 1, 2, and 5. The white tray part consists of SLS (selective laser sintering) printed nylon-12 parts, while the black pieces are Onyx (carbon fiber filled nylon) 3D printed parts.*

6.6.3 Structural analysis and positional precision

An FEA analysis of an individual segment is shown in Fig. 124. The 8 modules in the segment are each custom-designed to ensure that the light guide geometry maximizes light collection from specific tiles (see Sect. 6.3). The "exoskeleton" around each lightguide is made up of machined aluminum and 3-D printed nylon, optimized for ease of assembly and accurate tile positioning with a minimum of stress on the tiles.

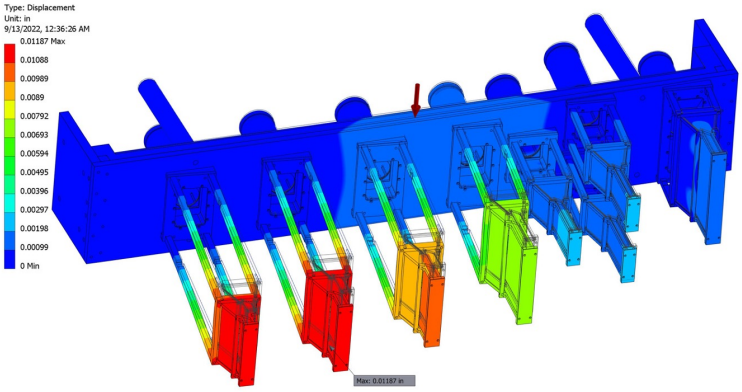

Figure 124: *FEA of a single segment is shown. The largest deflections are for the segments that are positioned horizontally (sag of tiles) and vertically (sag of segment base plate)*

Since each fully assembled segment weighs nearly 500 lbs, dominated by the lead shield mass, the safest and easiest solution for installation was determined to be to load each segment by lowering vertically with an overhead crane and have the entire holding structure be rotatable. Fig. 125a shows the FEA result for the full holding structure and six strut support, fulfilling the requirement that each quartz be placed within

± 0.5 mm. Figure 125b shows the drive mechanism that has been designed to ensure smooth full azimuthal rotation of the entire structure with the capability to handle a one-segment imbalance horizontally.

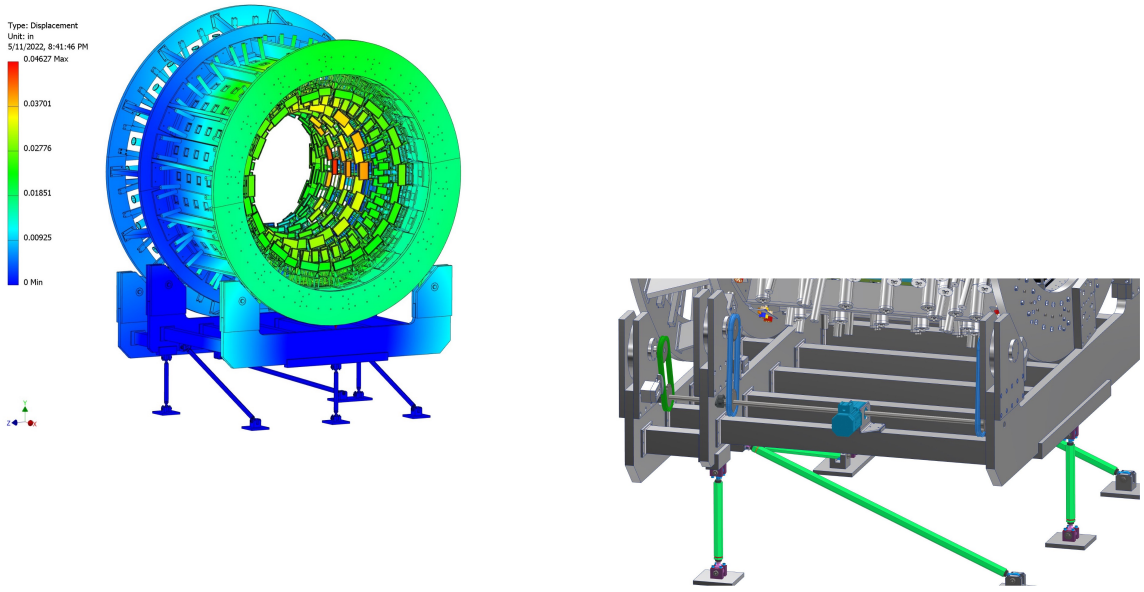

(a) Full Structure FEA (b) Drive Mechanism Concept

Figure 125: *FEA of the full main detector and showermax holding structure and the drive mechanism*

6.6.4 Assembly process

Figure 126 depicts the proposed installation sequence. After the first segment is loaded by lowering with a crane from above and secured, the structure would be rotated by 180°. Two modules would then be loaded before carrying out another 180° rotation. This ensures that the largest horizontal imbalance during the full installation sequence will be at most one segment. In the next cycle, after another 180° rotation, two more modules will be loaded, and so on.

6.6.5 Alignment process

A detailed alignment plan is being developed in collaboration with JLab's survey/alignment group. The specifications are to have the centers of the three primary rings that make up the outer frame of the holding structure to be within 1 mm of the beam axis. It should be noted that the fabrication of the holding structure assembly has sufficient redundancy in the conceptual design to ensure that the 3 main rings are concentric at a level that ensures that the drive mechanisms stay in contact with all 3 wheels at any azimuthal orientation. Appropriate "monuments" specified by the survey group will be placed on the holding structure to aid the process. A rough alignment will be carried out once the holding structure is installed in place. Once all modules are loaded a fine alignment will be carried out to achieve the aforementioned specifications for placement of the ring centers.

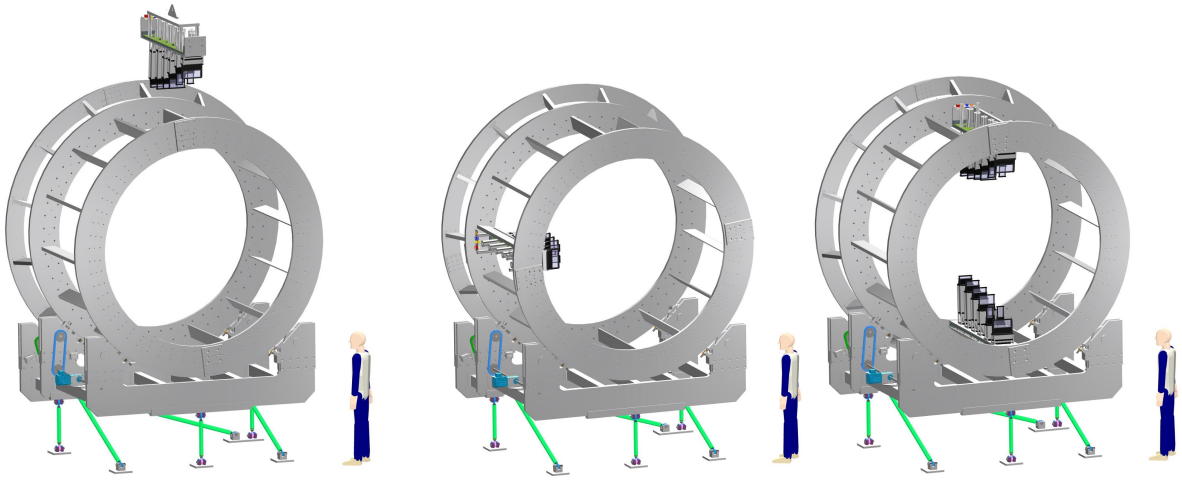

(a) First section loading (b) First section swinging down (c) Second section loading

Figure 126: *The planned loading sequence is depicted such that there will be at most one segment imbalance during the rotation during installation.*

6.6.6 Cabling infrastructure and organization

Each detector segment contains 8 individual detectors, each with the same set of cabling requirements: 2 signal outputs, 1 high voltage input, and 1 low voltage input. Each segment has a patch panel installed at one end where all cables from the 8 detectors are routed. The patch panel provides feed-through connectors for each output signal cable and high density receptacles for high voltage and low voltage inputs. Table 22 lists the cables and connectors needed for the Main detectors and segment patch panels.

Cable purpose	Cable type	Patch panel connector
Integrate mode signal	RG-108 Twinax (78 Ω)	8 BNC Twinax
Event mode signal	RG-58 Coax (50 Ω)	8 BNC Coax
PMT high voltage	RG-58 Coax (50 Ω)	GB 915/1E PTFE (8 conductor)
Amplifier power/switch	18 AWG (low voltage)	D105 Z062-130 (8 conductor)

Table 22: *List of cables needed for each detector module. There are 8 cables of each type routed through the segment patch panel. The high and low voltage high density connectors are from GES and Fischer, respectively.*

Figure 127 shows how signal, power and gas cabling will be routed to patch panels, at the upstream and downstream ends of alternate segments. The alternating pattern results from space considerations due to the z-staggering of detectors in adjacent segments. The patch panels organize all the main detector cables and connections to the upstream and downstream ends of the barrel allowing human access in between for PMT servicing.

6.7 Radiation effects and mitigation strategy

6.7.1 Quartz Radiators

Due to the high rate of intercepted particles, the main detector radiators will experience radiation damage in the form of light transmission loss in the UV region. The Open semi-septant detector radiators in Rings 2 and

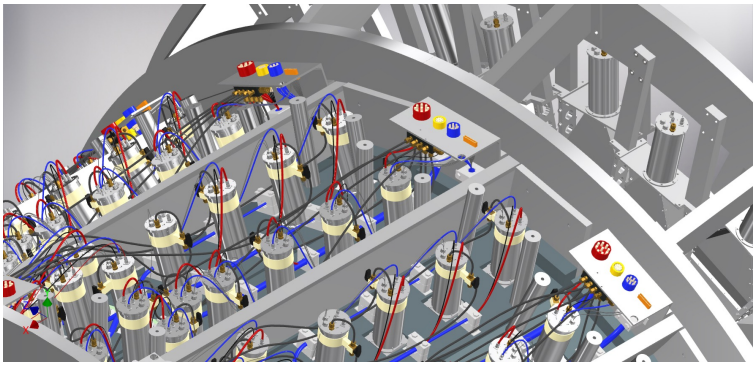

Figure 127: *Main detector segment internal cabling concept. Red color cables and connectors are for PMT high voltage, yellow are coax (event mode) signals, blue are twinax (integrate mode) signals, and orange are low voltage for PMT amplifier power/control.*

5 experience the highest rate densities and therefore radiation dose and optical damage. From simulation, the total peak dose in these detectors over the experiment lifetime is anticipated to be ∼120 Mrad/5x5 mm^2 for Ring 2 and ∼45 Mrad/5x5 mm^2 for Ring 5 (note this is for the center Ring 5 detectors in the Open semi-septants). In order to quantify radiation damage as well as determine a suitable radiator material, we tested 5 different candidate high purity fused silica (quartz) samples from 3 different vendors. Samples tested include Corning 7980 UV Homogeneity grade F, Corning 7980 ArF-Excimer, Heraeus Spectrosil 2000, Heraeus Spectrosil 2000 doped with H_2, and O'Hara SK-1300.

We irradiated the samples to various levels of dose and performed relative light transmission measurements between 200 - 800 nm to quantify damage (see [61] for details). These studies inform our expectations for the optical performance of our detectors over the course of the experiment and allow us to develop strategies to mitigate the effects of radiation damage. Results from the best performing quartz sample type are given in Fig. 128 along with a summary plot of total integrated light intensity loss for all samples versus dose; all of the losses occur in the UV region. Note that the decrease in absorption above ∼5.6 eV (below 220 nm) is not necessarily real as the optical components of the light transmission apparatus and spectrophotometer breakdown below 220 nm. For the 45 Mrad/5x5 mm^2 lifetime peak dose level expected in Ring 5, the total light loss per cm is approximately 2% for the Heraeus doped sample. For 120 Mrad, the total loss is about 6% per cm. The results for the other sample types are all worse than this.

Sample	Total Intensity Loss [%] at dose level				
	5 Mrad	14 Mrad	33 Mrad	65 Mrad	134 Mrad
Heraeus-standard	1.55 ± 0.02	3.81 ± 0.02	11.04 ± 0.02	16.32 ± 0.02	19.84 ± 0.02
Corning ArF-Ex	2.00 ± 0.02	2.69 ± 0.01	4.65 ± 0.01	7.92 ± 0.01	15.29 ± 0.01
O'Hara SK-1300	2.24 ± 0.02	4.98 ± 0.01	7.61 ± 0.01	11.26 ± 0.01	13.05 ± 0.01
Corning UV-HGF	1.44 ± 0.03	2.15 ± 0.01	3.90 ± 0.02	6.84 ± 0.04	12.73 ± 0.01
Heraeus-doped	0.74 ±0.02	0.96 ±0.01	1.64 ±0.02	3.02 ± 0.02	6.37 ± 0.01

Table 23: *Total light intensity loss per cm integrated over* $220 - 400$ *nm wavelengths for each cumulative dose level. There are no detectable losses for* $\lambda > 400$ *nm for all samples at these doses.*

Prior to radiation damage, the spectrum of Cherenkov light generating photoelectrons peaks near 260 nm (∼4.8 eV). This is within the region of light loss and thus over the course of data taking, the detector yields will decrease according to the accumulated dose in their radiators. This slow drift could eventually

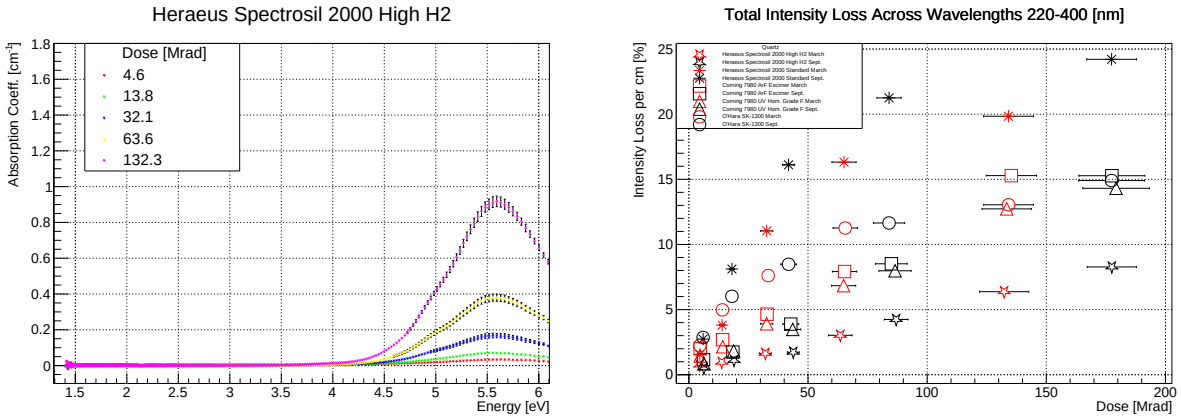

Figure 128: *(left) Plot showing the relative change in light absorption for the Heraeus Spectrosil 2000 sample with H_2 doping (best performing sample type). The data is plotted as a function of photon energy with different colors representing the various dose levels. (right) Summary plot giving the total intensity loss versus dose for all samples. The different symbols represent a particular sample type while the red and black colors are from separate measurements on different days.*

result in too low a detector yield and require mitigation strategies to correct. There are two main strategies: include replacement detector modules and/or perform a rotation of the main detector barrel. For the latter, the design of the main detector support structure allows for a rotation of the detector rings about the beamline by $2pi/14$. This would swap Open and Closed semi-septant detectors, and if performed strategically, could help more uniformly distribute the radiation damage effects prolonging the potential need for using replacement modules in Ring 2 and 5 Open semi-septants.

6.7.2 Mounting structure and 3D-printed parts

Radiation effects on plastic detector chassis materials and PMT electronics have been studied. We have assessed the radiation hardness of candidate 3D-printed plastics for use as specialized, low-density structural detector parts. We have measured the tensile strength of various printer materials before and after receiving doses up to 20 - 30 Mrad/5x5 mm^2. We print ASTM D638 type-I dogbone standard geometry samples and use a United Tension machine to perform the break measurements. Samples are irradiated at the Idaho Accelerator Center using the same beam setup as used for quartz studies. Results show that printer filaments with higher print temperatures, such as ABS and nylon, are more radiation resistant than lower temperature filaments such as PLA. The pre-irradiated elastic modulus and yield strength measurements for a few 3D-printed plastics and carbon-fiber embedded nylon are given in Tab. 24. Note that tensile strength measurements and radiation tests are also being carried out for dogbone samples printed along orthogonal axis relative to these prints. These measurements inform the engineering CAD for accurate FEAs of structures using 3D-printed parts. Tensile strength results for irradiated samples are given in Tab. 25. Tough PLA has high stiffness, but is weakened by radiation. Nylon has the greatest yield strength, but lowest stiffness. Carbon-fiber nylon has greatest stiffness and will be radiation tested in near future. Sample force-displacement curves for baseline and irradiated ABS and tough PLA are given in Fig. 129.

	0 Mrad (baseline)	
Material	Modulus [ksi]	Yield [ksi]
ABS	390 ± 20	4.7 ± 0.2
tough PLA	430 ± 20	4.8 ± 0.2
Nylon	250 ± 30	6.1 ± 0.2
C-fiber Nylon	520 ± 50	5.6 ± 0.3

Table 24: *Measured tensile strength of 3D-printed plastic dogbone samples prior to any irradiation.*

	1 Mrad		5 Mrad		20 Mrad	
Material	Modulus [ksi]	Yield [ksi]	Modulus [ksi]	Yield [ksi]	Modulus [ksi]	Yield [ksi]
ABS	390 ± 30	4.7 ± 0.2	380 ± 20	4.7 ± 0.2	370 ± 30	4.7 ± 0.2
toughPLA	480 ± 20	5.1 ± 0.2	460 ± 30	4.3 ± 0.1	480 ± 30	1.2 ± 0.1
Nylon	380 ± 30	5.0 ± 0.2	230 ± 70	6.2 ± 0.3	220 ± 60	6.1 ± 0.1

Table 25: *Effects of radiation on the tensile strength of 3D-printed plastics. Doses are per 5x5 mm^2. We note an enhancement in stiffness after 1 Mrad for toughPLA and Nylon–this surprising result is being retested. ABS is the least affected by radiation overall, and toughPLA is the most affected as it clearly loses yield strength as dose level increases.*

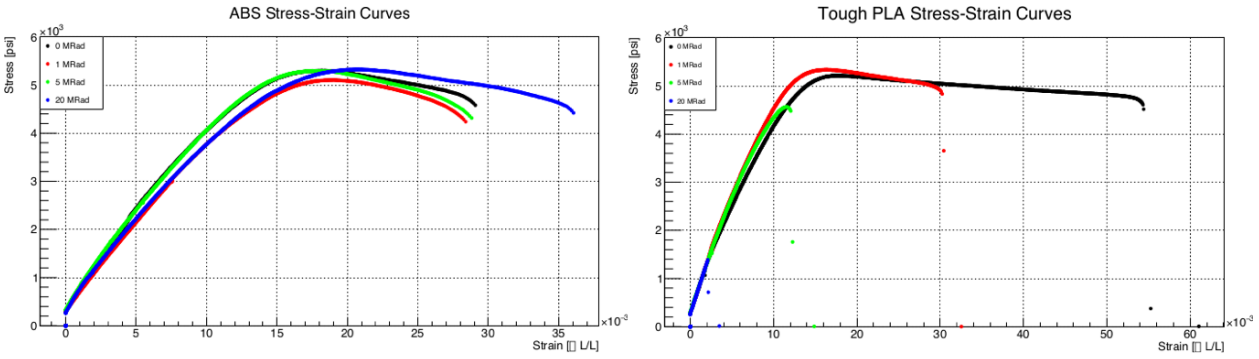

Figure 129: *Stress strain curves for 3D-printed plastics using ASTM-D638 type-I dogbones. ABS is on the left and tough PLA on the right. The different colors represent different dose levels given in the legend. The elastic moduli are unaffected by the radiation, but the yield strength of tPLA is systematically reduced.*

6.7.3 Front-end Electronics

The present version of the prototype base and preamplifier assembly shown in Fig. 113 has components that have been radiation tested at the MAMI facility in Mainz, Germany. Since the detectors need to be switched between single event mode and integration mode occasionally, to allow tracking mode runs, the base and amplifier gain and signal paths have to be switchable remotely. Previous versions of the assembly had adopted a complicated digital remote gain and signal path switching design, which included serial communication ICs and an amplifier offset DAC. That version of the design already had the same operational amplifiers that are being used in the current design. The design was tested beyond 86 kRad (the expected absorbed dose in the region around the front-end electronics is around 60 kRad).

It was determined that all of the digital electronics components that were needed to implement digital remote switching failed at 86 kRad, but that the passive components and the operational amplifier circuitry

continued to function. The design presented in Fig. 113 now implements an analog switching mechanism using reed relays (as described in Sect. 6.4.2).

7 Møller Scattering Asymmetry Extraction

Having laid out the requirements and technical specifications of the principal components of the apparatus, in this section we elaborate on how they facilitate the extraction of the helicity-correlated asymmetry in the Møller-scattered flux. Subsequent sections will describe the rest of the apparatus required to calibrate and evaluate normalization corrections to this asymmetry measurement to extract the parity-violating asymmetry in Møller scattering.

As described in Sect. 5.1.2, the spectrometer/collimator system directs Møller electrons to a region largely free of background. As then described in Sect. 6.2, an annular region spanning approximately 60 to 120 cm from the beam axis 27 m downstream of the target is populated with fused silica tiles. The light registered by these tiles is integrated to provide relative measures of the scattered fluxes and thence parity-violating asymmetries of the signal and background scattering processes.

We first provide the justification for how the various individual tile asymmetries are organized. We then describe how any corrections due to a residual transverse beam polarization are controlled. Finally, we describe how the spectrometer optics and the detector tile segmentation are exploited to evaluate the Møller and background asymmetries and dilution correction factors.

7.1 Raw Tile Asymmetries

The characteristics of Møller scattering kinematics drive the design of the spectrometer optics which in turn define the segmentation of the main integrating detector tiles. As shown in Fig. 56b in Sect. 5.1.2, the Møller-scattered flux is fashioned into a "peak" in the radial direction by the spectrometer at the detector plane approximately 26.5 m downstream of the target, forming a relatively thin annular ring (width ~ 8 cm) of approximately 94 cm radius. A ring of 84 quartz tiles (so-called Ring-5 detectors) that measures the flux traversing this ring comprises the primary Møller detector tiles.

However, these 84 tiles also register small contributions from scattering processes other than Møller scattering, as we describe in more detail in Sect. 7.3.1. In order to calibrate both the dilution factors and the asymmetries in background processes, 5 additional rings of detectors comprising 28 tiles each are instrumented, four rings at lower radius (1 thru 4), and one at larger radius (ring-6), with ring-5 being the main Møller ring. Driven by the optics of the spectrometer and the chosen segmentation, each ring's azimuthal segmentation is categorized as "open", "transition" and "closed" tiles, shown as different colors (red, green and blue respectively) in Fig. 55 in Sect. 5.1.2. The open tiles are along the mid-planes of the open acceptance semi-septants (see discussion around Fig. 54 in Sect. 5.1.1 for definition), the closed tiles are along the mid-planes of the closed semi-septants and the transition tiles are in between the two. There are thus 28 sectors in a ring, with ring-5 tiles further equally sub-divided by a factor of 3. Thus, ring-5 comprises 21 open, 21 closed and 42 transition tiles while the other rings are constituted with 7, 7 and 14 tiles respectively of each category.

Given the symmetry of the apparatus, spectrometer optics and the kinematics of the signal and background process, the open, closed and transition tiles on each ring contain a different mix of electrons from various scattering processes. Importantly, the kinematics in each tile category in each ring is identical and can be averaged to take advantage of azimuthal symmetry and thus cancel systematic effects. These averages result in 18 different asymmetry aggregates, each corrected for random and helicity-correlated beam fluctuations (see Sect. 3) that are then passed on for further analysis, described in Sect. 7.3.1 below to extract the signal and background asymmetries and dilution factors.

7.2 Transverse Asymmetry Control

A transverse polarization component to the beam on target would introduce an azimuthal modulation of the measured asymmetry due to the beam-normal single-spin analyzing power A_T. At MOLLER kinematics, the magnitude of A_T is large compared to A_{PV}. Averaging asymmetries over the full range of the azimuth greatly suppresses this effect. However, imperfect cancellation could lead to a significant systematic error unless the grand average transverse polarization is well below 1%.

The experimental design exploits the interesting kinematic dependence of A_T to further suppress this potential systematic correction during data collection. Due to CP symmetry, A_T as a function of the COM scattering angle, or equivalently $y \equiv 1 - E'/E$ must vanish (due to the two Feynman diagrams for identical particles) at $y = 1/2$, which corresponds to 90° scattering in the COM frame. The maximum A_T of around 12 ppm occurs at $|y - 0.5| \approx 0.2$, at the very edges of the scattered electron momentum acceptance. Consequently, A_T is of opposite sign at these two extremes.

There are two consequences of the aforementioned kinematic feature. First, because we accept both COM forward and backward angle scatters, the average A_T is suppressed by an order of magnitude from the peaks of 12 ppm. Figure 130a shows A_T as a function of E' for a beam energy of 11 GeV. Secondly, and equally importantly, the "open" (mixture of forward and backward angle scatters) and "closed" (virtually all backward angle scatters) sector tiles will measure A_T of opposite sign in a correlated way, which will be a powerful check of spurious systematic effects. Figure 130b shows the range of scattered electron energies accepted by the 3 different ring-5 tile categories. The convolution of these two characteristics leads to the result illustrated in Fig. 131, which shows the simulated average transverse asymmetry, with 100% transverse beam polarization, for the open, transition and closed tiles as a function of their position in the azimuth.

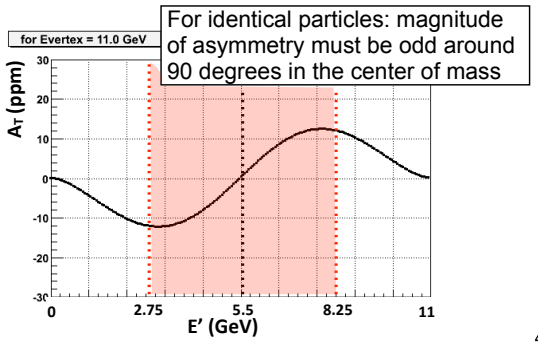

(a) Beam-normal single-spin asymmetry A_T vs. scattered electron energy

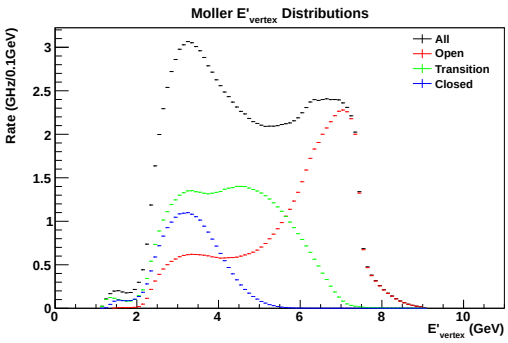

(b) Scattered electron energy distributions in ring-5 tile categories: red (open), green (transition) and blue (closed)

Figure 130: *The characteristic behaviour of the beam-normal single-spin analyzing power A_T in Møller scattering as a function of E' at 11 GeV beam energy (left figure with the shaded region showing the approximate acceptance) coupled with the different acceptances of the 3 different tile categories (right figure) leads so very different expectations of the beam normal-single spin asymmetry, as shown in Fig. 131*

The basic principle of the online systematic control is as follows. First, it is possible, by passive setup procedures, to limit the transverse component of the beam polarization at the target to be less than 1° at the start of physics running. One can then measure the A_T ϕ modulation to very high precision during production data collection within a few hours, by studying the azimuthal dependence of the raw detector asymmetry separately in each ring-5 tile category. Exploiting the important feature that the magnitude and sign of the modulation are correlated, even a relatively small transverse polarization component can

be reliably extracted, distinguishing potential modulation from other systematic effects such as helicity-correlated beam position fluctuations.

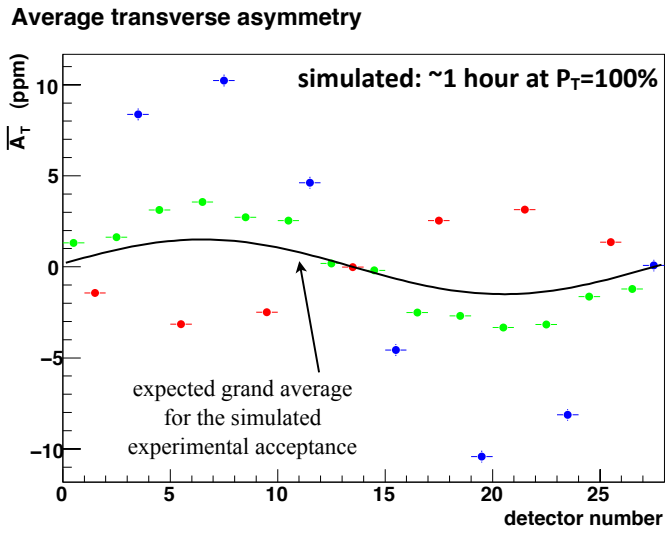

Figure 131: *Simulated values of the transverse asymmetries for* 100% *transverse polarization for the three different types of azimuthal detectors in the Møller ring - open (red), transition (green), and closed (blue). Even with the expected production transverse polarization of* $< 1-2\%$*, the expected transverse modulation is large enough that it can be measured within a few hours of production running, allowing for a "manual" feedback technique to minimize the transverse beam polarization.*

The statistical error on the inferred transverse polarization angle from a few hours of data will be well below 1°. It should therefore be possible to devise a "manual" feedback loop that would make small tweaks to the launch angle of the electron beam polarization at the low energy end of the machine based on the measured A_T every few hours. While the statistical "noise" in the inferred transverse polarization will be inserted into the launch angle set point, this algorithm should nevertheless lead to a rapid convergence of the total data set to zero average transverse polarization over a series of setpoint adjustments.

Ideally, the suppression of the initial launch angle (averaged over all the data) is expected go like $1/N$, where N is the number of adjustments. In principle, we should gain a factor of about 25 below the setup accuracy of 1° in a week. If one now further conservatively assumes a factor of 10 suppression in the grand average of A_{PV} over the full range of detectors, then the total correction to A_{PV} will be less than 0.06 ppb. Therefore, with the implementation of the manual launch angle feedback, it is our expectation that no correction for the transverse polarization will need to be made. We have assumed the entire value of the anticipated correction to be the systematic error in our projections. As a final control measure, if the aforementioned level of suppression is difficult to achieve in practice, some of it can be recovered by a slightly different re-weighting of the data from the various different azimuthal detectors with only a small loss in the statistical error in the extracted A_{PV}.

7.3 Background Corrections

7.3.1 Overview

Any high energy electrons that originate in the target and arrive at the detector plane after traversing the spectrometer/collimator system either scattered off target electrons (the signal Møller electrons), or target

protons, or nuclei in the target windows. The electrons that are created by the latter two categories are the irreducible backgrounds that we discuss first. As described earlier, we exploit how the signal and background contributions vary over the 18 different tile categories to infer both the dilution factors and asymmetry corrections. A more complete description of all these topics can be found in the backgrounds report [62].

7.3.2 Irreducible Backgrounds

The principal irreducible background under the Møller "peak" (see Fig. 56b) is radiative elastic electron-proton (ep) scattering, which constitutes about 8% of the signal averaged over the Ring-5 tiles. This background is well-modeled using Monte Carlo simulations and then verified explicitly with auxiliary tracking measurements (see Sect. 8.2) of the radial profile of the scattered flux. The theoretical prediction for the parity-violating asymmetry is also well known for this process, including the $\gamma - Z$ box radiative correction, explicitly calculated at 11 GeV [63].

An equally important background correction is due to the smaller dilution from inelastic ep scattering, as well as that same process from the Al target windows. Even though the contribution from the background to the detected rate is expected to be small, $\lesssim 0.5\%$, the asymmetry correction can be significantly larger due to the fact that the estimated coupling to the Z boson is more than an order of magnitude larger than Q_W^e. In Sect. 7.4, we describe how we extract the couplings directly from the data rather than rely on theory predictions.

The dilution and asymmetry from electron scattering off Al nuclei in the end windows of the target represent the final component of irreducible backgrounds. These processes include quasi-elastic scattering, inelastic excitations of the aluminum nucleus, and scattering off of impurities in the alloy planned for the target windows. Since the total correction from the target windows is estimated to be smaller than the ultimate statistical uncertainty of the main A_{PV} measurement, we estimate the asymmetries using theoretical input and dilution factors from the Monte Carlo simulations and perform a subtraction prior to the simultaneous fit described in Sect. 7.4.

7.3.3 Other Backgrounds

Negatively charged pions, heavier mesons and muons contribute at a small level to the signal in the detector tiles. The dilution from such backgrounds is estimated to be negligibly small, but the parity-violating asymmetry of this background will depend on the processes that create them, such as real and virtual photoproduction and electroproduction off target protons, and decays of hyperons. The correction is expected to be about 3%, so this will be treated in the same way as the aforementioned aluminum background prior to the deconvolution analysis with one important difference: the correction is informed and calibrated by the pion detectors (see Sect. 9.2): the asymmetry from simultaneous integrating data collection, and the dilution factor from special low current calibration runs.

There is a small contribution to the detector PMT signals from Cherenkov and scintillation light in the air lightguides, which have been estimated in dedicated test beam configurations. The system of collimators and collars as well as the lead shielding in the vicinity of the light detectors have been optimized to minimize contributions from other soft photons and neutrons. Special calibration studies, such as runs "blinding" the Cherenkov photodetectors and looking for the residual beam-correlated response, runs with the spectrometer magnets turned off and runs with a blocker in front of the main acceptance collimator, will provide the requisite accuracy to estimate these small dilution factors.

7.4 Tile Asymmetry Deconvolution Analysis

After correcting the raw helicity asymmetries in the scattered electron flux in the 18 different categories of tiles for beam fluctuations and then averaging each of them over the full range of the azimuth, we then carry

out the deconvolution analysis to extract the asymmetries in the aforementioned signal and background processes from the data. The large variations in the rates and parity-violating asymmetries in these tiles depending on the relative contributions from Møller, elastic e-p, inelastic e-p and elastic e-Al scattering enables our approach. In particular, the poorly known behavior of the inelastic electron-proton weak neutral current vector coupling as a function of inelasticity will be directly measured rather than relying on theoretical estimates.

First, we subtract out asymmetry and dilution components which are smaller or comparable to the ultimate statistical error i.e. of the order of 3% or less. These will include all subdominant components including those due to pion and neutral backgrounds. Then we carry out a simultaneous fit of the remaining components using dilutions determined from Monte Carlo simulations and extract independent parity-violating couplings for the chosen $e - X$ scattering processes. As we demonstrate in the following, the procedure results in acceptably small systematic errors associated with correcting for the irreducible electron background asymmetries.

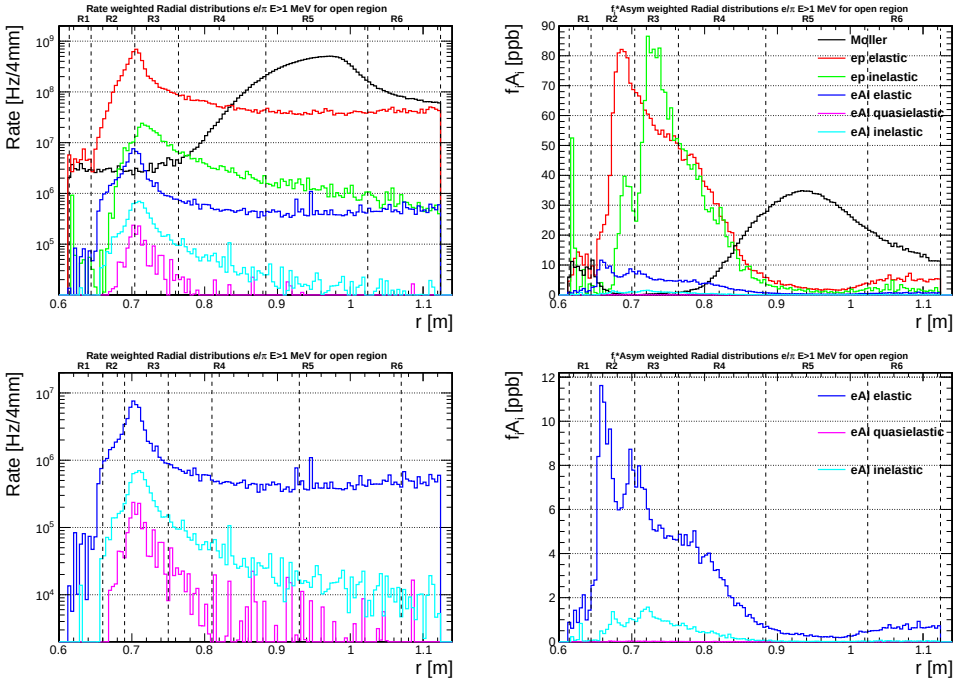

Figure 132: *Simulated signal and background vs. radial location of detected electron at the MOLLER detector ring. In all figures: the Møller electron signal is in black, background from elastic scattering on the proton is red, inelastic scattering from the proton in green, and elastic, quasielastic, and inelastic scattering from the Al target windows in blue, magenta and cyan, respectively. Upper left: rates, in Hz. Lower left: rates for just the Al contributions. Upper right: contribution to the total measured asymmetry, in ppb, for all processes ($f_i A_i$, where f_i is the dilution for the individual process). Lower right: as above, for Al contributions only. Note: the figures on the left have a log scale, while those on the right are linear scale. The boundaries of the 6 detector rings are indicated by vertical black dashed lines.*

Simulated electron distributions at the detector plane are shown in Fig. 132 from a full GEANT4 [64] simulation of interactions in the long liquid hydrogen target with relevant material features of the apparatus and 3-D spectrometer magnetic field map. Events were generated in the target from Møller scattering from electrons in hydrogen, elastic and inelastic scattering from protons in hydrogen, and elastic, quasielastic,

and inelastic scattering from the Al entrance and exit windows of the target, using appropriate cross sections and material thicknesses. The plots show the detected electron rates *vs.* radial location at the z-location of the MOLLER detector, as well as the dilution-weighted asymmetries $f_i A_i$. The dilution for a given process is defined as $f_i = N_i / \sum_j N_j$, where N_i is the rate of detected events from process i. The rates and asymmetries shown are summed over the full detected azimuth ϕ, and correspond to the maximum beam current of 65 μA and beam polarization of 90%.

For this fitting process, we provide as input (1) the cross sections and kinematics (and thus the dilution f_i) in each detector bin (radius,ϕ) for each process and (2) a model for how the asymmetry A_i varies with kinematics (Q^2 and W) over the detector acceptance (radius,ϕ) bin. Knowledge of the f_i is validated using high-granularity measurements of the total detected electron rates as a function of (radius,ϕ) using our tracking system, which will also extract the central kinematics of the experiment.

7.4.1 Treatment of Inelastic Electron-Proton Scattering

As described in detail in the full backgrounds report [62], we are able to exploit the radial and azimuthal segmentation in the detector tiles to account for a modest W-dependence of the Z_0 coupling. Our ansatz, which is grounded in theoretical input is to separate the kinematics for inelastics into three bins in W: (i) the Δ region, $1 < W < 1.4$ GeV (ii) the "resonance region", $1.4 < W < 2.5$ GeV, and the "continuum" $2.5 < W < 6$ GeV. We use the Christy-Bosted global fit [65] for the cross sections and model the inelastic asymmetry in these three bins using $A_{\rm inel} = K f(W) Q^2$ where K contains electroweak couplings, and $f(W)$ is assumed to be constant in each of the three bins in W. We then treat the three $f(W)$ as free parameters to be extracted from our data via the simultaneous fit to the asymmetries in 18 tiles categories. We thus minimize systematic uncertainty due to theoretical input on the inelastic asymmetries; we largely rely *on our data* to extract the inelastic contributions.

7.4.2 Toy Dataset Simultaneous Fit Results

The 18 asymmetries (6 radial rings, each with 3 ϕ sectors) produced in the full simulation, with statistics corresponding to the full beam time request of 344 days, were simultaneously fitted. The fit had 5 free parameters: the asymmetries for Møller, ep-elastic and e-p inelastic (3 W bins) scattering with appropriate Q^2 evolution for each. The f_i dilutions were taken from the simulation. The small contributions from elastic, quasielastic and inelastic scattering from the Al windows were subtracted before the simultaneous fit.

Table 26 shows the total predicted asymmetry in each tile category, A_m, and its statistical precision σ_A/A along with the fractional contributions to the measured asymmetries from each relevant process. One can see from this table the strategy of the simultaneous fit. Ring-5 tiles are dominated by the Møller scattered electrons. Rings-2, -3 and -4 tiles have very different contributions from ep-elastic and ep-inelastic scattered electrons, allowing these asymmetries to be disentangled. There are further important characteristics that contribute to efficient extraction of the various background couplings e.g. the contributions in the "open" and "closed" ring-3 and -4 tiles from the various W regions in inelastic ep-scattering.

The results of the fit are shown in Tab. 27. We see that the desired precision (2.10%) in the Møller asymmetry is achieved. Very similar results are found with a 4-parameter fit (where the ep-inelastics were assumed to have single asymmetry that scales as Q^2, independent of W), with a 2.05% precision on the Møller asymmetry. Table 28 shows the size of the correction for each background signal, as well as associated systematic error (due to the statistical uncertainties including correlations in the extracted couplings) from a similar fit as Tab. 27) but limited to just the Ring 5 results.

ring #	sector ID	$\frac{\sigma_A}{A}$ (%)	A_m (ppb)	Møller (%)	e-p elastic (%)	e-p inelastic (%)	e-Al elastic (%)	e-Al quasi-elastic (%)	e-Al inelastic (%)	pions (%)
1	0	67.80	-27.3	34.6	25.3	28.8	-3.0	0.0	-0.4	14.8
1	1	57.50	-18.6	43.8	39.3	9.8	-5.5	0.0	-0.5	12.9
1	2	48.77	-29.3	28.9	34.1	34.9	-4.4	0.0	-0.6	7.2
2	0	4.52	-209.4	2.5	54.1	44.1	-0.8	0.0	-0.8	1.1
2	1	1.52	-283.4	0.8	58.6	42.6	-1.5	0.0	-0.9	0.4
2	2	2.47	-91	0.4	77.7	30.9	-8.2	0.0	-1.0	0.1
3	0	2.51	-310.5	1.2	34.6	64.5	-0.8	0.0	-0.9	1.2
3	1	1.21	-219.9	0.4	47.0	56.0	-2.8	0.0	-1.0	0.4
3	2	1.73	-108.4	0.3	56.5	50.0	-5.9	0.0	-1.0	0.2
4	0	4.84	-128.1	4.8	35.3	48.4	-1.9	0.0	-0.4	14.0
4	1	2.75	-115.5	3.5	43.7	49.8	-3.1	0.0	-0.6	6.6
4	2	3.50	-54.7	27.3	39.8	35.1	-4.2	0.0	-0.5	2.5
5	0	4.86	-30.8	83.2	5.8	4.9	-0.5	0.0	-0.1	6.6
5	1	2.93	-34.2	85.6	6.6	4.7	-0.7	0.0	-0.1	3.8
5	2	2.67	-35.5	88.0	7.2	4.3	-0.9	0.0	-0.1	1.6
6	0	17.26	-26.9	56.3	16.1	13.6	-1.8	0.0	-0.2	16.1
6	1	8.53	-25.3	64.1	17.3	9.2	-2.0	0.0	-0.1	11.5
6	2	8.32	-24	67.8	21.1	8.3	-2.6	0.0	-0.1	5.5

Table 26: Total predicted asymmetry in each radial ring, A_m, and its statistical precision σ_A/A along with the fractional contributions to the measured asymmetries from each relevant process. "0" indicates that the fraction is less than 0.05%. The three ϕ sectors are defines as follows: "0", "1" and "2" are "closed", "transition" and "open" tiles respectively.

Processes	Expected A (ppb)	$\frac{\sigma_A}{\lvert A\rvert}$ (%)
Moller	-34.65	2.10
ep elastic	-26.94	6.72
ep inelastic (1)	-514.05	16.52
ep inelastic (2)	-521.64	7.48
ep inelastic (3)	-437.49	21.35

Table 27: *Results of the simultaneous fit to the 18 quartz tile asymmetries. The asymmetries for each signal (A_i) in the open sector of Ring 5 are given for reference, along with the statistical precision from the global extraction in %.*

Process	Correction (%)	Systematic Error (%)
e-p elastic	1.14	0.08
e-p inelastic ($W < 1.4$ GeV)	-1.34	0.22
e-p inelastic ($1.4 < W < 2.5$ GeV)	-1.54	0.11
e-p inelastic ($W > 2.5$ GeV)	-1.66	0.35
e-Al elastic	0.87	0.09
e-Al other	< 0.10	< 0.10

Table 28: *The fractional correction to the Møller asymmetry in Ring 5 and the associated systematic errors due to the extracted fit uncertainties shown in Tab. 27 are listed. The systematic error on the e-Al elastic contribution is assigned as a fractional error of* 10% *as discussed in the full backgrounds report [62]. The "e-Al other" contributions include quasi-elastic scattering and inelastic scattering from discrete excited nuclear states and the giant dipole resonance.*

7.5 Summary

We have quantitatively demonstrated how the MOLLER subsystem design and physics requirements are optimized to cleanly extract the parity-violating asymmetry in Møller scattering with an uncertainty that is dominated by counting statistics. The radial and azimuthal segmentation of the detector, combined with the toroidal spectrometer optics and the kinematics of the various background processes enables us to untangle the Møller asymmetry from those of the dominant background processes, without recourse to other data or theoretical predictions for those background asymmetries. The required inputs are the cross sections and simple expectations on the leading Q^2 (and, for inelastics, W) dependence of the asymmetries. A simultaneous fit of measured asymmetries making use of the radial and azimuthal segmentation of the detector determines the background asymmetry contributions to the needed precision. It also provides asymmetry measurements for these additional processes.

8 Tracking Detectors and Kinematics Calibration

8.1 Tracking System Overview

The MOLLER tracking system consists of four layers of Gas Electron Multiplier (GEM) detectors in each of the seven sectors, located immediately downstream of the drift region and just upstream of the main integrating detectors, for a total of 28 identical GEM detectors. (see Fig. 2). Each sector will also have two layers of plastic scintillator trigger counters, for a total of 14 identical scintillators. The trackers are mounted on a "GEM Rotator" which will allow the array to be rotated around the azimuth to permit measurements over the full azimuthal acceptance. The azimuthal size of the GEM module is constrained by the dimensions of available GEM foils, and corresponds to 27° of arc. Given dead zones due to the GEM detector frames, full azimuthal measurement capability will require at least two sets of "rotations" of the GEM system.

Also important for the tracking measurements is a sieve-hole diagnostic collimator (see Sect. 5.2.1) which will be inserted upstream of the spectrometer magnets, and which will be used in conjunction with the tracking system and thin solid targets for the kinematics verification, as well as a blocker collimator (see Sect. 5.2.1) used for studies of soft background and determination of the flux from pions.

The purposes of the tracking system are multifold: to i) verify the optical properties and acceptance of the toroidal spectrometer system, ii) verify the acceptance of the quartz detectors, iii) measure the position dependent light-output response of the quartz detectors, iv) measure the radial and azimuthal distributions of incident electrons in order to verify the fractional backgrounds from elastic and inelastic ep events in the integrating detectors, v) study neutral and "soft" backgrounds in the integrating detectors and vi) aid in the identification of pion events, in conjunction with the pion detectors, shower-max, and main detectors. Items i) and ii) are essential for verifying the expected kinematics of the experiment, iii) will be useful for searching for radiation damage effects in the main detectors, and iv)-vi) are important for measuring and constraining background contributions.

The tracking system will primarily be used during dedicated low beam-current runs with data taken in a "counting mode", as opposed to the standard integrating mode of asymmetry data taking.

A discussion of the kinematic verification procedure with the tracking system is provided below (see Sect. 8.3).

8.2 Tracking System Requirements

1. **Rate Capability and Radiation Hardness:** The tracking system will be run when the beam current is reduced by many orders of magnitude. At the peak of the Møller distribution the electron flux is 100 MHz/cm^2 at full beam intensity, far too high for individual track reconstruction with any present technology. Previous experience (with Qweak) has shown that stable beams can be delivered with currents as low as 100 pA, and the majority of the tracking measurements will be taken with beam fluxes of this order of magnitude, yielding peak fluxes from the hydrogen target of a few hundred Hz/cm^2. The tracking system detectors will be removed from the immediate path of the scattered flux during full beam-current integrating mode measurements. However, their electronics must be reasonably radiation-hard, so as to not be damaged during the tracking mode data-taking, nor by the ambient radiation in their "parked" locations during full current running.

2. **Spatial Resolution:** The spatial and angular resolution requirements of the tracking system are set by their use in the kinematics verification. In this procedure, we need to be able to separate events from different sieve holes which are in the same sector. Simulated track reconstruction studies indicate that this can be adequately done assuming $1\ \mathrm{mm}$ spatial and $1\ \mathrm{mrad}$ angular resolution. These detector resolutions are more than adequate to "image" the individual thin quartz detectors for use in studying the position dependence of their optical response, and sufficient to generate projected radial and

azimuthal rate distributions with fine enough binning for background deconvolution studies (eg. see Fig. 132). Because the tracking system will be operated in a magnetic field-free region, straight-line track fitting can be used. A four-layer tracking system is needed in order to allow for some small inefficiency, and still have at least 3-point tracks to allow a χ^2 test for valid tracks, and to suppress spurious hit combinations.

3. **Geometrical Coverage:** We must map the track distribution over the entire azimuth, and over the radial acceptance of all the integrating detectors rings (see Fig.132), to be able to identify any unexpected breakdowns of the seven-fold symmetry of the apparatus due to magnetic field or collimator imperfections beyond the expected tolerances. However, we do not require covering the full azimuth in a single measurement, so to reduce instrumentation costs, we can instrument a reduced fraction of the azimuth, and sequentially rotate the tracking detectors into different azimuthal locations. We require the ability to redundantly measure at least some azimuthal locations with different tracking detectors, in order to test our ability to "calibrate out" tracking detector inefficiencies. Coverage of a single septant requires relatively large tracking detectors (≈0.5 m^2 in area). The detectors should also be low-mass, so as not to introduce additional backgrounds in the main detectors during tracking measurements; we desire $< 8\% X_0$ from the detectors.

4. **Triggering:** We need to be able to trigger tracking readout independently of the main integrating detectors, so we ensure that all incident charged particles are measured; a high-efficiency trigger ($> 98\%$) based on charged particles (used in software veto mode) will be important for studying neutral backgrounds. We use two layers of trigger detector to reduce spurious triggers due to soft backgrounds. An "unbiased" pulser-trigger will be useful to study the trigger efficiency.

8.3 Kinematics and Optics Measurement

The challenge of measuring the acceptance and quantifying its uncertainty is non-trivial. Measuring the acceptance is crucial because the relative contributions of Møller-scattered events over the full range of acceptance, with proper weighting, is required to relate the measured parity-violating asymmetry A_{PV} to the underlying theoretical prediction via

$$A_{PV} = mE\frac{G_F}{\sqrt{2}\pi\alpha}\frac{4\sin^2\theta}{(3+\cos^2\theta)^2}Q_W^e = mE\frac{G_F}{\sqrt{2}\pi\alpha}\frac{2y(1-y)}{1+y^4+(1-y)^4}Q_W^e \ . \tag{18}$$

Here θ is the center-of-mass scattering angle, $y = E'/E$, and Q_W^e is the electron's weak charge.

One requires precise knowledge of the term which we define as the "kinematic factor" $\mathcal{A} \equiv A_{PV}/Q_W^e$, which is dependent on the beam energy E and the center-of-mass scattering angle θ through

$$\mathcal{A} \equiv \frac{mG_F}{\sqrt{2}\pi\alpha}\frac{4E\sin^2\theta}{(3+\cos^2\theta)^2} \ . \tag{19}$$

This kinematic factor must be averaged over the entire acceptance of the spectrometer and appropriate integrating main detectors, and weighted by the relative response of the main detectors.

Because of the very broad momentum acceptance of the spectrometer and the plan for accurate placement of acceptance-defining collimators, the problem simplifies greatly. If the momentum acceptance is uniform as a function of accepted angle, sufficiently accurate construction and placement of the acceptance-defining collimators, and knowledge of the incident beam energy, is all that is required. The purpose of the magnetic optics reconstruction in this context is to validate the underlying assumptions.

The multiple layers of GEM detectors in the tracking system, spaced along the beam axis, provide a lever arm to reconstruct not only the track positions, which we will denote with cylindrical coordinates r

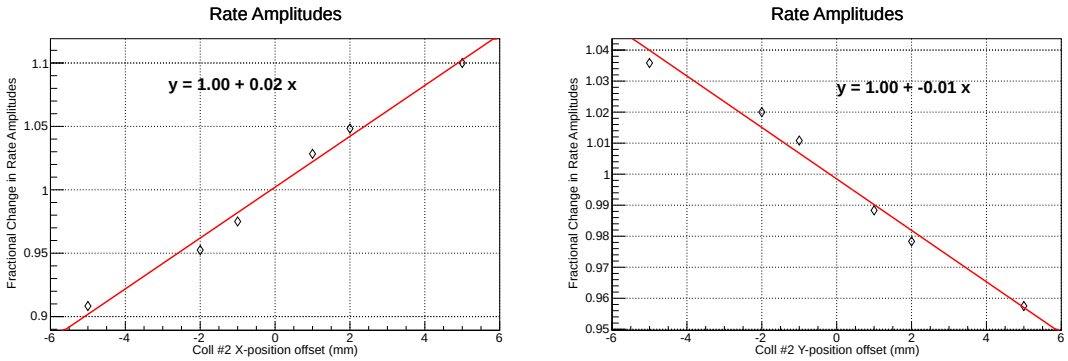

Figure 133: *A misplacement of the acceptance-defining collimator transverse to the beam produces a small azimuthal modulation in rate of about 2%/mm.*

and ϕ, but also the directions $r' = dr/dz$ and $\phi' = d\phi/dz$. These four independent variables map from the independent variables which describe the scattered particle, the lab scattering angle $\theta_{\rm lab}$, the scattered electron momentum E', the lab azimuthal angle $\phi_{\rm lab}$ and the reaction vertex position v_z (we neglect the v_x and v_y coordinates since these will be known event-by-event from the raster current and they represent small perturbations in the map).

To measure the acceptance of the apparatus, a model of the magnetic transport optics must first be obtained. Calibration of the optics over a relatively broad range can be performed by mapping out specific and identifiable points with defined polar and azimuthal angles, momentum, and target position. Interpolation between these points will complete the full acceptance map. Using events from nuclear elastic and from the Møller interaction with a well-defined beam energy differently correlates the momentum and polar angle (see Fig. 134).

With the use of a thin solid (^{12}C) target and a removable sieve collimator before the magnetic elements, the remaining variables can be constrained. The sieve is $\sim 28\ X_0$ thick to be able to sufficiently stop the highest-energy electrons, except for those passing cleanly through the sieve holes.

Absolute positioning of the acceptance-defining collimator can be done both by survey and cross-checked by measuring and then minimizing the azimuthal modulation of rates resulting from any small transverse displacement of the collimator. Figure 133 shows the amplitude of the rate modulation as a function of the collimator displacement. Assuming a modulation amplitude measurement to an accuracy of 2% of the average rate per sector, the positioning of the collimator can be determined to an accuracy ~ 1 mm. The impact of the residual uncertainty of 1 mm on the transverse position of the acceptance-defining collimator will be less than 1% on the average kinematic factor $\langle \mathcal{A} \rangle$, and thus negligible. Nevertheless, knowing the value of this shift is important for constraining other systematics, such as parity-conserving asymmetries and helicity-correlated beam trajectory differences which which could produce their own azimuthal modulations in the observed detector asymmetries.

By having a map of ($\theta_{\rm lab}$, p, $\phi_{\rm lab}$, v_z) $\rightarrow$ (r, ϕ, r', ϕ') at specific points the problem of optics reduces to interpolating between these points. The propagated uncertainty on $\langle \mathcal{A} \rangle$ is then dependent on the number of calibration points and the functional form of the acceptance used. The form of the acceptance must rely upon simulations and perturbations on various positioning and magnetic fields which can then be used for a maximum likelihood fit. This is also critical to take into account higher-order effects such as the beam raster, multiple scattering, and radiative effects, which will require Monte Carlo simulation benchmarked by the tracking data.

The calibration of the acceptance as a function of $\theta_{\rm lab}$ and E' will be done using nuclear elastic scattering

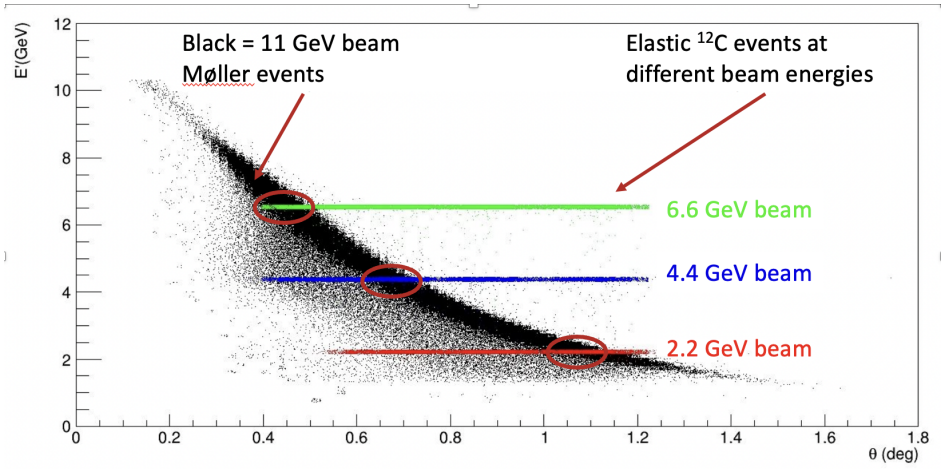

Figure 134: *E' vs. $\theta_{\rm lab}$ for Møller events at 11 GeV and ^{12}C nuclear elastic events at several lowered beam energies. The angular locations of three selected sieve holes are indicated. The black dots below the main Møller stripe are from radiative processes.*

from thin ^{12}C targets. Here we exploit the fact that at these kinematics the forward scattered electrons from nuclear elastic scattering at a given beam energy are essentially monoenergetic (see Fig. 134), because the nuclear recoil energy is tiny, in contrast with the Møller electrons. Thus tracking measurements taken with ^{12}C at lowered beam energies can determine the acceptance for selected points in the relevant (E', $\theta_{\rm lab}$) phase space for Møller electrons. We will take tracking data at three reduced beam energies (4.4, 6.6 and 8.8 GeV) with sieve collimator holes chosen to select events with appropriate angles (see Fig. 134), including holes that will sample the radiative tail region of the Møller acceptance. The fact that the relative cross section for nuclear elastic scattering vs. Møller scattering scales as Z^2 ensures that the ^{12}C data will not be swamped by Møller events.

The 21 different sieve hole locations are chosen to sample the entire range of $\theta_{\rm lab}$ for thin targets at both the z-locations corresponding to the upstream and downstream ends of the LH2 target. Some holes are offset from the center of the given semi-septant, in order both to ensure that events from different holes are cleanly separated at the GEM locations, and to study the $\phi_{\rm lab}$ dependent terms in the acceptance function.

Figure 135a shows the chosen hole pattern and Fig. 135b shows the simulated locations of the track arrivals at one GEM layer for both the nuclear elastic and Møller events from a ^{12}C foil target, for one of the reduced beam energies (2.2 GeV). Similar results hold for the other beam energies. The signals from each hole and from each process are clearly distinguishable with the chosen sieve hole diameter of 5 mm. The relative rates of nuclear elastic and Møller are also acceptable, so that the DAQ will not be overwhelmed by Møller events during 12C data-taking. Data from different combinations of the sieve holes will be obtained in different rotational positions of the GEM Rotator.

Least-squares fits of the GEANT4 simulated target kinematic variables $\theta_{\rm lab}$, E' $\phi_{\rm lab}$ and v_z to simple polynomial functions of the simulated variables at the GEM (r, ϕ, r' and ϕ'.) for the ^{12}C elastic tracks lead to acceptable results. The most critical is $\theta_{\rm lab}$, which was fit to

$$\theta_{\rm lab} = a + b_0 + b_1 r + b_2 r' + b_3 r^2 + b_4 r r' + b_5 r'^2 \tag{20}$$

and yields a track-by-track residual between the true $\theta_{\rm lab}$ and the fitted $\theta_{\rm lab}$ with a mean value of $(4\pm3)\mu$rad, consistent with zero, and $\sigma = 430$ μrad.

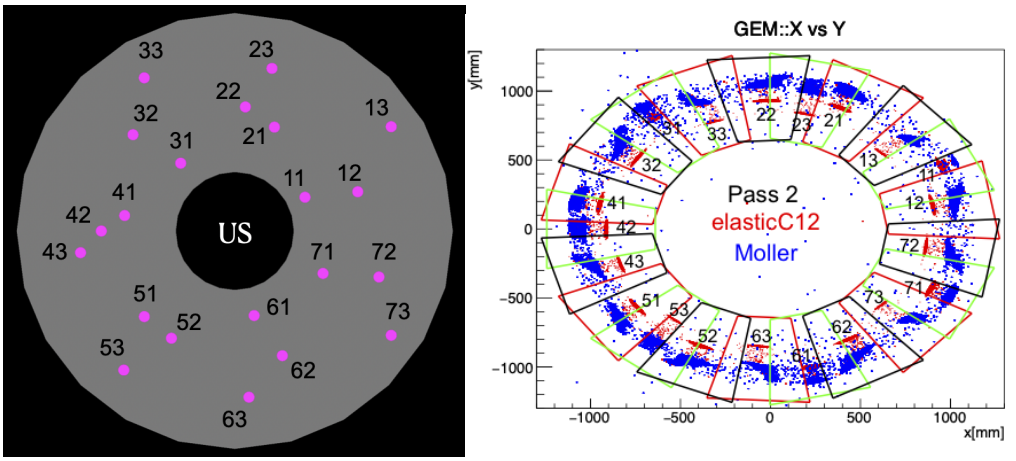

(a) *Sieve Collimator hole locations.* (b) *Track locations at GEM with sieve in place.*

Figure 135: *a) Sieve Collimator hole locations. The diameter of the holes is 5.0 mm. b) Track locations at GEM layer 4, with Sieve collimator in place, for 4.4 GeV electron beam (Pass 2). The corresponding sieve hole numbers are indicated. The green, red, and black trapezoids are the GEM acceptances in each of the three rotational positions. Note that both images face the upstream direction.*

8.4 GEM detectors

The MOLLER setup requires high resolution track reconstruction under high rate conditions over a large area. A cost effective solution for such requirements is provided by the Gas Electron Multiplier (GEM) technology invented by F. Sauli [66] in 1997. The GEM is based on gas avalanche multiplication within small holes (on a scale of 100 μm), etched in a Kapton foil with a thin layer of copper on both sides. The avalanche is confined in the holes, resulting in fast (about 10 ns rise time) signals. Several GEM foils (amplification stages) can be cascaded to achieve high gain and stability in operation. The relatively small transparency of GEM foils reduces the occurrence of secondary avalanches in cascaded GEM chambers. All these properties result in very high rate capabilities of over 100 MHz per cm^2 and an excellent position resolution of as good as 70 μm. Fig. 136 illustrates the principle of operation of a triple (three foil) GEM chamber. Triple GEM chambers have been successfully used in the COMPASS experiment at CERN [67], in SBS [68] and PRad [69] experiments at Jefferson Lab and may other experimental setups around the world.

The GEM detector coverage needed for each tracking wheel depends on its location along the beam propagation axis, with the detector wheels located further downstream requiring larger area in order to intercept the electrons in acceptance. The GEANT4 simulation has been used to determine the GEM coverage areas. The GEM coverage area necessary to intercept electrons in a given septant is determined by observing electrons that Møller scatter inside the target, and which arrive at the quartz detectors, as well as the ep scattering events. Because the strong ϕ-defocusing of the spectrometer results in electrons being swept across the septant boundaries by the time they arrive at the quartz detectors, the electrons that arrive at a particular septant in the simulation at the nominal location of the quartz detectors are selected and tracked upstream through each of the GEM planes in order to determine the sizes of individual GEM planes. The GEM detector shapes determined from this study are trapezoidal but with the parallel side at the inner radius replaced by a relatively thin (8 mm wide) arc, concentric with the beam pipe center. This thin inner arc is needed to ensure that the GEM active area can come close enough to the beam pipe to capture the full

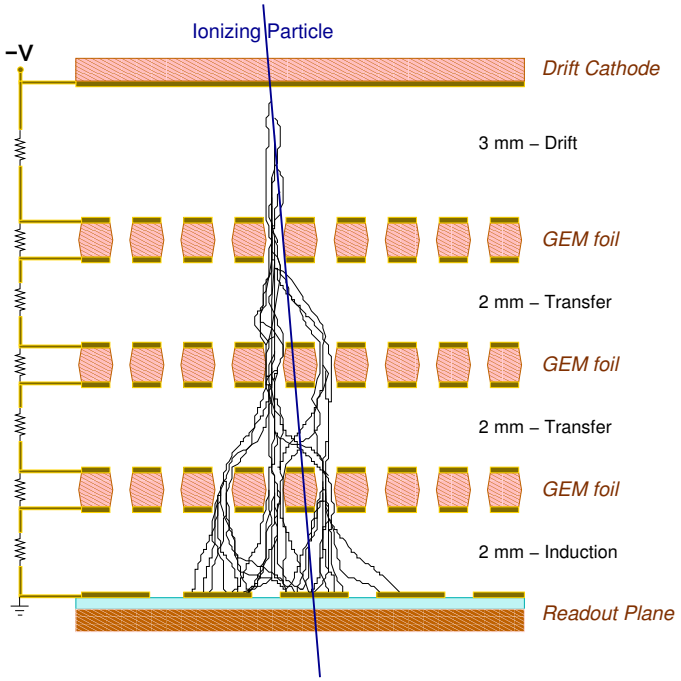

Figure 136: *Principle of operation of a triple GEM detector.*

charged particle envelope while fully excluding the photon envelope. The outer parallel side is kept straight, given mechanical and structural stability considerations.

The GEM detector required coverage determined as indicated above, and increased by a margin of 5 mm at the inner and outer radii, is presented in Tab. 29. These are the sizes required to intercept electrons from any one particular septant. Given that the radial extents for the four locations are not very different, 43.5 cm for the location 1 and 48 cm for the location 4, GEM modules of the same size with a radial extent of 48 cm have been designed for all 4 locations. Using the same size for all 4 locations greatly simplifies the GEM design and fabrication while reducing the number of needed spares. The radial placement of the GEMs varies slightly with each layer so as to capture the full acceptance for each layer.

The module designed to fit all four locations is shown in Fig 137a. The length of the active area along radial direction is 0.48 m to match the size of the envelope at the fourth location, and the azimuthal width

Table 29: *GEM coverage needed to intercept electrons incident on the quartz detector of a given septant.*

	z(m)	Inner rad(m) of charged envelope	Outer rad(m) of charged envelope	Outer rad (m) of beam pipe	$\pm\phi$(deg)
GEM #1	19.28	0.58	1.025	0.5185	31.0
GEM #2	19.78	0.60	1.010	0.5536	30.5
GEM #3	20.19	0.62	1.075	0.5728	28.8
GEM #4	20.69	0.64	1.120	0.5879	28.8

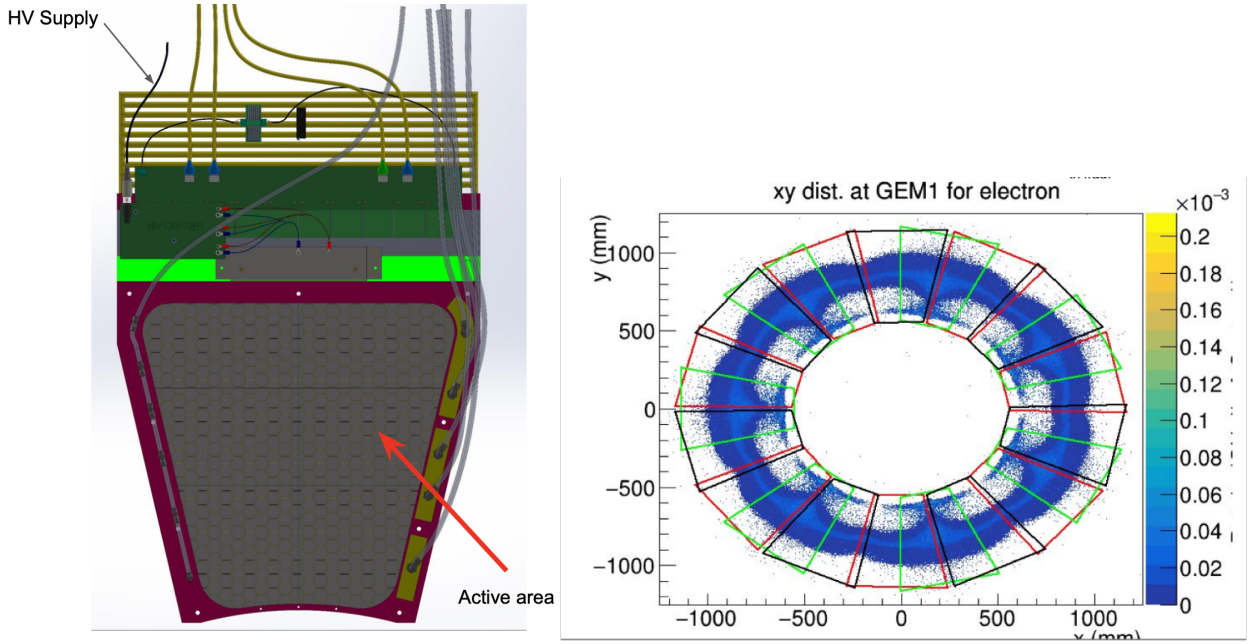

(a) *GEM detector front view.* (b) *GEM model front view*

Figure 137: a) GEM module front view, showing active area, frame, passive backplane, HV connections, HDMI cables (tan) and gas lines (gray); b) Simulated distribution of electron tracks at first layer of GEMs, overlaid with the coverage for three overlapping GEM rotation positions (red, green and black trapezoids).

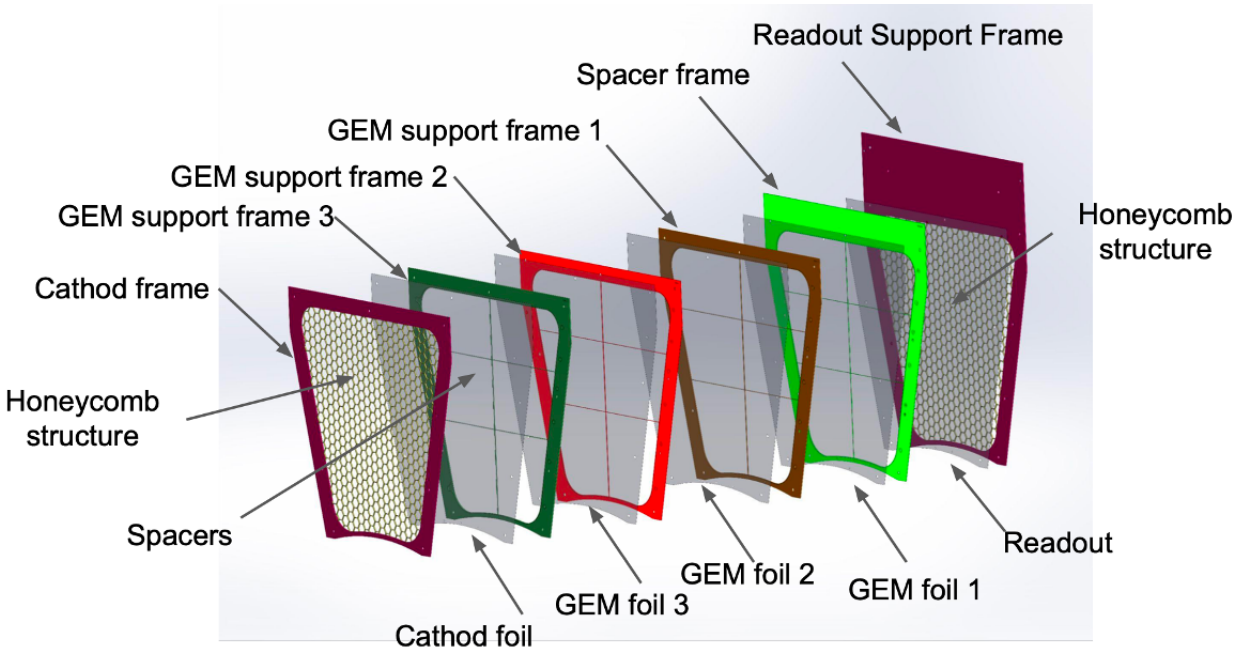

Figure 138: *Exploded view of single GEM module showing the three GEM foils and their support frames, the support frames for the cathode plane and for the readout board, and the lightweight honeycomb structures.*

is $\pm$ 13.35°, so that with two rotational movements of the wheel (three azimuthal settings) the GEMs will cover the full acceptance with plenty of overlap as seen in Fig 137b.

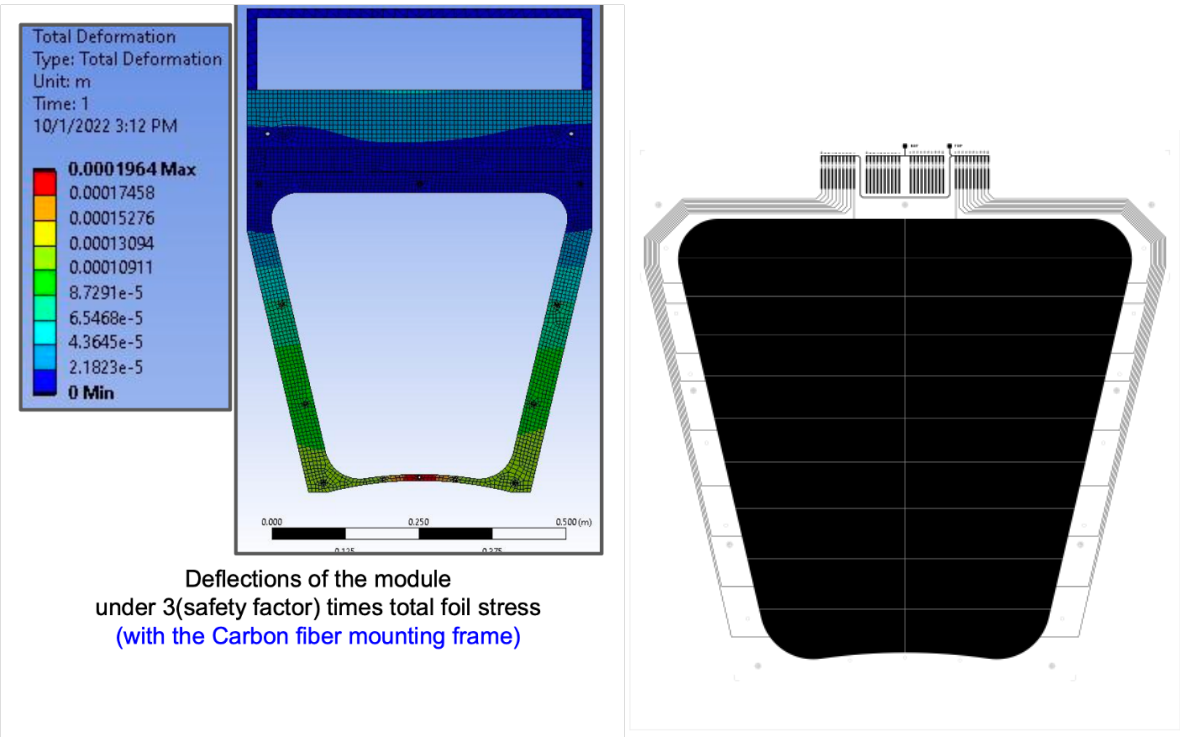

(a) *FEA deflections for GEM module.* (b) *GEM high voltage distribution.*

Figure 139: *(left): FEA results for deflections of the assembly GEM frame and carbon-fibre support frame, under 3× expected foil tension. (right): High voltage distribution for GEM module (20 sectors per foil).*

An exploded view of the components of a single GEM module is shown in Fig. 138. All support frames are made out of machined G10/FR4 material. Each GEM module is 16 mm in thickness, representing a total radiation length for normal incidence electrons in the active region of just 0.8% X_0. The readout support frame, made by gluing a lightweight 3 mm honeycomb layer on the G10 frame provides structural rigidity and flatness to the module. The spacers crossing the various support frames are for keeping the GEM foils from touching each other; these spacers are approximately 300 μm wide and contribute only about 2% reduction to the active area of the chamber. An external carbon-fibre mounting frame will allow the GEM module to be supported on the GEM Rotator, and provides additional rigidity to the assembly. Finite Element Analysis of the GEM assembly indicates that the deflections from the nominal dimensions, assuming 3 times the expected foil tension, are under 200 μm at the maximum, see Fig. 139a.

The high voltage distribution for each GEM foil, as shown in Fig. 139b, is divided into 20 independent sectors, to allow a large fraction of the active area to remain powered in the case of a localized electrical short in one foil. CFD simulations of the gas flow scheme within each module show excellent pressure uniformity and adequate gas flow velocity (see Fig. 140).

8.5 GEM electronics

The electronic readout of the GEM detectors will be done with an APV-25 chip based readout system [70] using the Multi Purpose Digitizer (MPD) architecture [71] originally developed by the INFN-Genova group

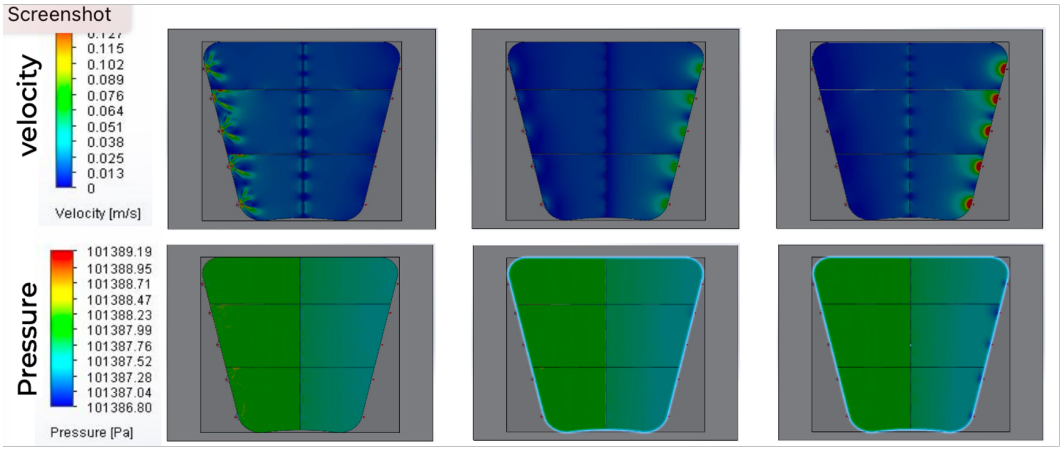

Figure 140: *CFD simulations of gas flow velocity and pressure for GEM module.*

for Super Bigbite Spectrometer (SBS) project experiments [68]. See Fig. 141 for details. This readout system has been fully integrated into the JLab DAQ framework and is supported by JLab DAQ professionals. The system is currently being used successfully for SBS data taking.

The readout strips are arranged in a U-V configuration, with each strip direction parallel to one of the two radial sides of the detector module. This design allows all the readout electronics to be at the large-radius (lower radiation environment) edge of each GEM, eliminates multiple scattering in the acceptance due to the readout card mechanics, and optimizes the dead-to-active area ratio of the detector, The U-V strip readout includes in its design a double-sided zebra connection technique that the UVa group developed to allow the connection of all readout strips to the front-end electronics at the outer radius side of the wedge-shaped large detector. Prototypes of this U-V configuration were constructed for EIC detector development and successfully tested with cosmic rays in the GEM Detector Lab at UVa and in 2018 with a high-energy proton beam at the Fermilab Test Beam Facility (FTBF). The U-V stereo angle is 26.5° (the small stereo angle is set by the need to have the readout all at the outer edge of the module). The readout pitch is 800 μm and the readout strips are 146 μm wide. There are 1200 total readout strips per module for U and V sides combined, yielding 33,600 readout strips for the 28 modules in the tracker.

The strips in module will be read out by 10 radiation-tolerant APV front-end cards. Fig 142-left shows the schematic details of the strip arrangement and the readout cards, while Fig 142-right shows the layout of the readout plane produced for the prototype-1. All cards on a module are connected and supported by a passive backplane board. On the backplane the analog output lines from the cards are organized into groups of four or less; in this case three groups of 4, 4 and 2. Each group is connected via an HDMI cable into a VME-based MPD module. This module manages the front-end cards and provides the ADCs to convert the APV25 pipeline-multiplexed analog signals into digital information. The MPD is connected to a JLab custom electronics Virtual Trigger Processor (VTP) module. The FPGA units of this module perform the preliminary processing of the converted data, such as pedestal subtraction, common-mode noise removal, and zero suppression (data sparsification).

Each front end card hosts one APV25 chip, which is able to read 128 channels. The APV25 has essentially a preamp & shaper stage, followed by a 192-cell analog pipeline which permits up to 3.4 μs trigger latency. Signals are sampled at 40 MHz (25 ns bins). Both the front end cards [70, 72] and backplanes are radiation tolerant. At the radial location where the APV25 front-end cards and backplanes will be located during the high-current integrating mode measurements (the "parked" position), the total ionizing dose over

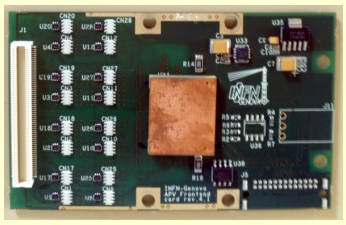

- 128 analog ch / APV25 ASIC
- 3.4 μs trigger latency (analog pipeline)
- Capable of sampling signal at 40 MHz
- Multiplexed analog output (100 kHz readout rate)

- **Up to 16 APV25 cards (2048 chs) on a single MPD (parallel readout)**
- Altera Arriga GX FPGA / RAM: DDR2 (128 MB)
- **Optical Fiber Link interface (Aurora ~2 Gb/s peak)**
- 100 MHz system clock and Front panel coax clock
- Used HDMI-A for analog and digital signals
- **VME/32, VME64, VME64-VXS compliant (up to 200 MB/s peak)**
- 4 high speed line on the VXS available for data transfer
- Firmware v. 4.0 (74% resources):
  - Finite-Impulse-Response Filter (16 parameters)
  - Zero Suppression (sparse readout)
  - Common mode and pedestal subtraction
  - Remore reconfiguration
  - ~2 ns trigger time resolution
  - VME / Optical Fiber simultaneous implementation

Figure 141: *The APV-25 front-end card (left top), and the MPD module (right).*

the full run is calculated (GEANT4 simulation) to be < 400 kRad. The APV25 chips have been demonstrated to operate successfully after doses of more than 20 MRad [70].

The backplane is a PCB for signal routing. It hosts two radiation-tolerant voltage regulators which provide the power to the cards. The backplane & front end cards are powered by a single voltage level of 3.3-3.5 V.

The MPD is designed to operate on a VME64x crate with the JLab compliant VXS extension; in addition, it can transfer the data through a high-speed optical interface to a JLab VTP or Sub System Processor (SSP) unit; we plan on using the VTP module. The following signals are exchanged by the MPDs and the Front-End cards:

- IN to the card: Trigger (1 differential line), Clock (1 differential line), common to all cards on the same backplane
- OUT from the card: Analog Output (1 differential line), one for each card
- BI-Directional: I2C (2 lines), common to all cards on the same backplane

All signals between the backplane and the MPD are transmitted along HDMI Type A cables. The MPD can receive an external trigger and clock either by the front LEMO connectors or the VXS bus; it provides the busy signal either from a front-panel LEMO connector or via the VXS bus.

The 28-GEM module tracking arrangement for MOLLER requires 280 APV cards and 28 MPD modules. The MPD modules will be hosted in two VXS crates housed in a radiation-protected bunker, located on the Hall A floor upstream of the GEM trackers, and upstream of the barite detector shielding wall (see

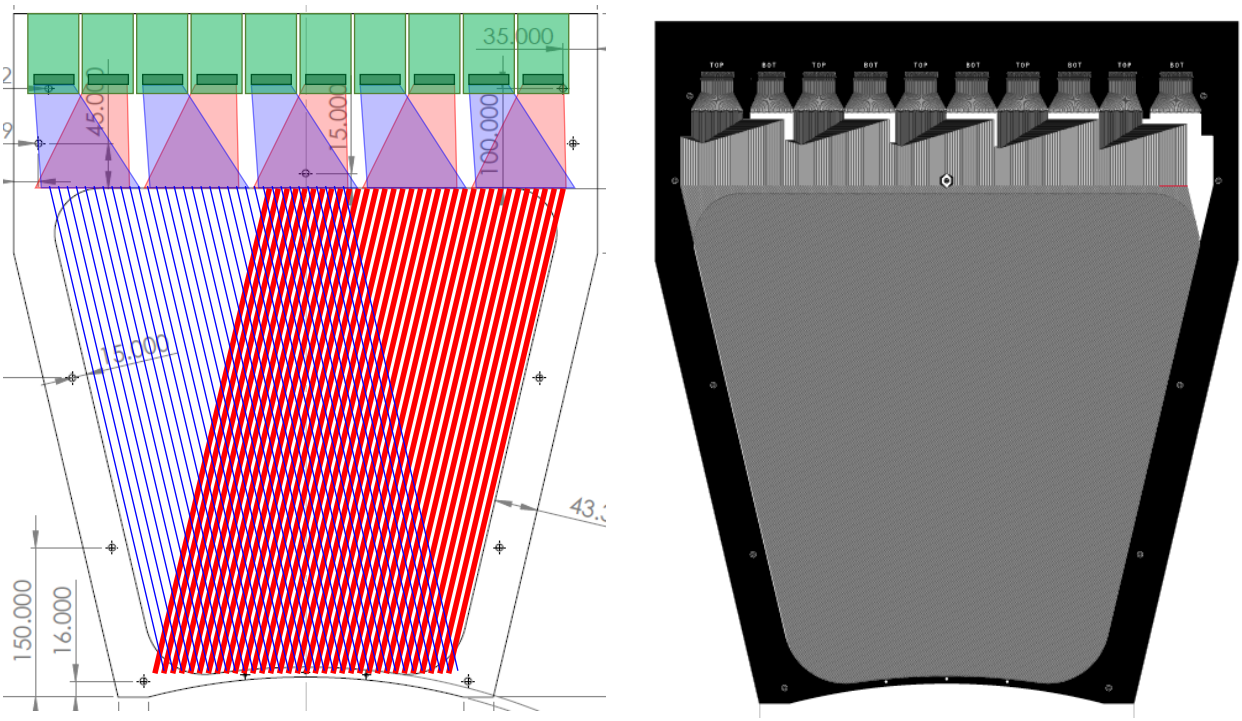

Figure 142: *(left) GEM readout strip schematic. The U strips are shown in blue, the V strips shown in red (the strip pitch is not to scale), and the dark and light green rectangles at the top show the connectors and APV front-end cards respectively. (right) Gerber layout for the readout board fabricated for MOLLER GEM prototype-1 (right).*

Sect. 12.2.6). The VTP modules (connected to the MPDs via fiberoptics) will be located in the upstream shielding house.

The distance from the front-end cards to the MPD bunker is limited by the readout pedestal noise induced by the HDMI cable length. Fig. 143 shows the strip-by-strip RMS pedestal noise levels measured in bench tests at INFN for five APV front-end cards. These data were taken with 25 m long HDMI cables. While the pedestal levels for most of the strips are around 10 ADC channels, the noise levels for the first few strips on each APV card spikes to over 100 ADC channels (to put these numbers in perspective, the average strip charge for a MIP detected in a GEM operating at nominal gain is about 200-300 ADC counts). Furthermore, cut is typically applied at five times the pedestal RMS, strip-by-strip, for zero and noise suppression during the analysis of GEM data. This noise spike is understood as being caused by the pipelined readout of the APVs: signal from the digital header word which precedes the sequential strip-by-strip readout can bleed into the first channels of analog data if the impedance is not perfectly matched. The height of this noise spike increases with the HDMI cable length, while the noise levels for the rest of the strips remain about the same. In order to keep the noise levels for the first few strips down to a manageable level, the HDMI cable lengths for GEM readout in the SBS experiment were limited to 10 m. We will address this issue in MOLLER GEM readout by leaving the high noise first 8 channels in each APV card unconnected to strips. This is possible given the 1280 available channels in the 10 APV cards to read the 1200 channels. With this solution, the MOLLER GEM readout will be able to function with HDMI cable lengths up to at least 30 m. Recent bench studies at INFN Rome have demonstrated that the signal attenuation and noise increase (when

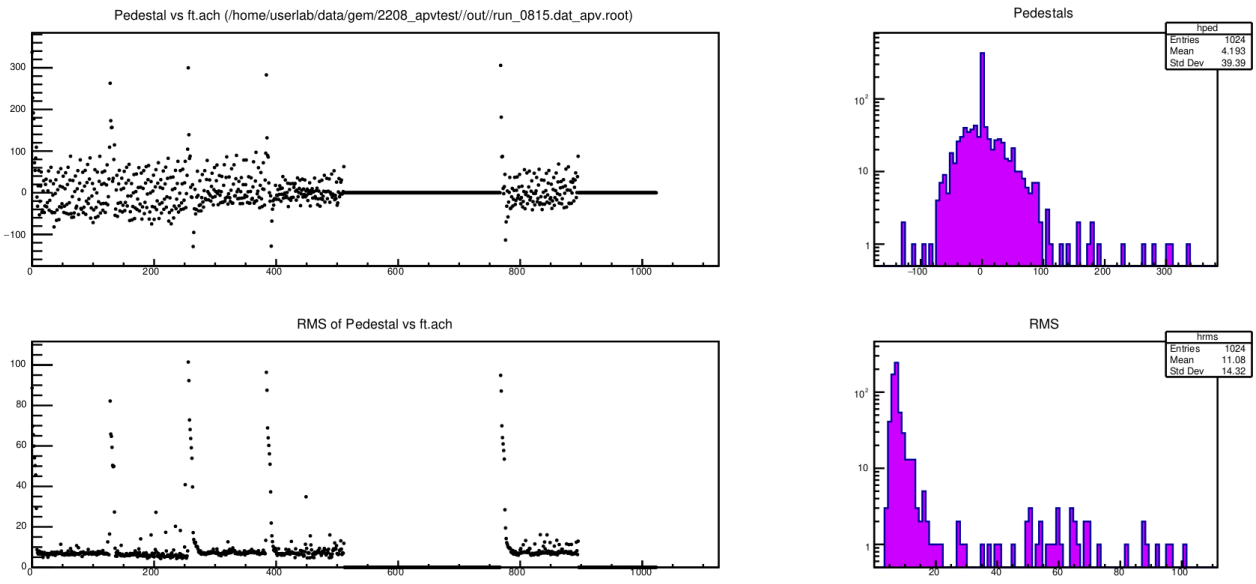

Figure 143: *GEM readout strip pedestal values (top) and RMS pedestal noise (bottom) in ADC units for bench studies with 25 m long HDMI cables. The spikes to large values of RMS noise are the first 80-10 channels in each APV front-end card. In our design, the first 8 channels for each APV front-end card will not be instrumented. Typical signal pulse heights are 250 ADC units.*

the first 8 channels are discarded) for 25 m (and even 45 m HDMI cables) is acceptable. This scheme will be further tested and verified with the prototype MOLLER GEMs.

Of the 280 APV front-end cards and 28 MPD modules needed, 210 cards and 8 MPD modules have been procured using MOLLER-NSF funds. The remaining front-end cards and MPD modules will be acquired from the SBS GEM readout system when SBS running is completed in 2024. The SBS readout has over 900 front-end cards and about 100 MPD modules. After over a year of running, no loss of APV cards due to radiation damage has been observed in the SBS experiment. The 10-slot backplanes have been designed and will be fabricated soon.

A real-time zero-suppression is needed to keep the output data volumes at a manageable level. The zero suppression method for the SBS GEM readout was developed and optimized before the SBS-GMn experiment last year. This technique worked very well during the experiment, apart from a few minor issues. These issues have been corrected for the upcoming SBS-GEn-II run.

8.6 GEM Rotator

The GEM Rotator and stand, see Fig.144a, will support the 28 identical GEM modules (4 layers of 7 GEMs) and the 14 identical trigger scintillators (2 layers of 7 scintillators) in a symmetrical array around the beam line, just downstream of the drift region exit window, and upstream of the main integrating detectors. The requirements for the GEM Rotator include the need to avoid ferrous materials in regions of significant electron flux, minimal mass within the acceptance region, the need to rotate the GEMs to different azimuthal stations for the tracking measurements, and the need to remove the GEMs entirely from the scattered beam acceptance for the main integrating mode asymmetry measurement (”parked position”) via radial motion to a larger radius, see Fig.144b. At this radial location the APV front-end readout cards for the GEMs will be in a relatively low-radiation environment. The height from the hall floor to beamline center is 3000 mm. Both motion systems (rotational and radial) must be operable remotely.

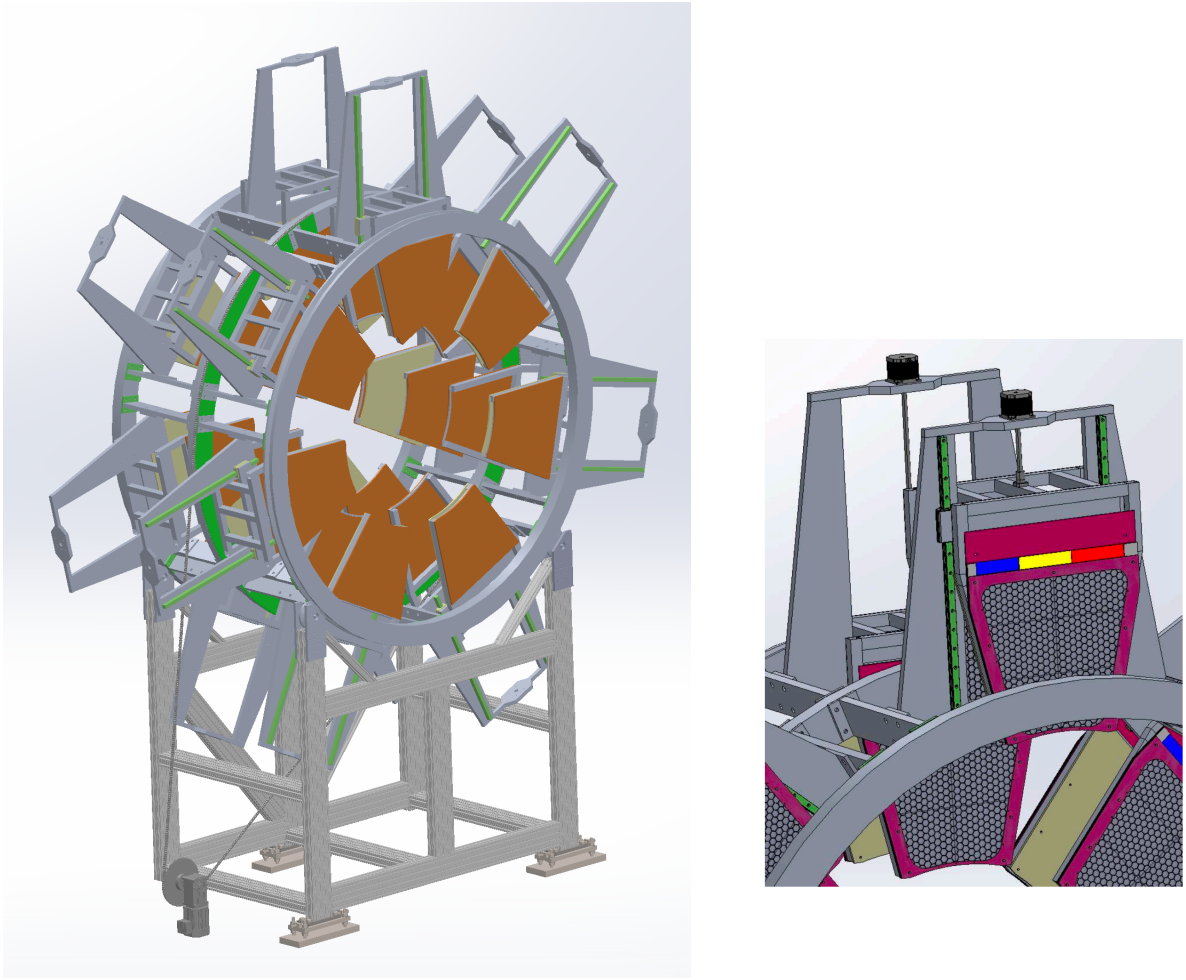

(a) *GEM Rotator and stand.* (b) *GEM Radial Motion.*

Figure 144: *a) GEM Rotator and stand, showing GEMs in the inserted (measurement) position. The GEMs are in brown and the trigger scintillators in tan. The chain drive and rotational motor are shown; the radial motion mechanism is not shown. b) Detail showing radial motion mechanism for GEMs, with a GEM module pair in the parked position (top foreground) and the other modules in the tracking mode measurement position. The linear guide rails are in green.*

The Rotator consists of three identical wheels connected together to form a Ferris-wheel structure. The wheels are 2654 mm in outer diameter, 2400 mm in inner diameter, 76.2 mm thick and are made from 6061-T6 aluminum. The two end wheels sit on four rollers mounted on the support stand. The center wheel has sprocket segments which are used to attach to a chain drive to actuate the rotational motion. A V-groove on one end wheel holds the z-position of the Rotator. Two layers of GEM modules and one layer of trigger scintillator are attached between wheels 1 & 2, and two layers of GEM modules and one layer of trigger scintillator are attached between wheels 2 & 3. The spacing in the z-direction between pairs of GEM layers is approximately the same (393.7 mm for layers 1 & 2 and layers 3 & 4, and 401.8 mm for layers 2 & 3). The total mass of the three wheels is 608 kg, and the Rotator assembly with GEMs and scintillators is 1800 kg. As the Rotator will need to be assembled around the previously-installed beam pipe, each wheel will the manufactured in two halves, and bolted together around the beam pipe, on the support stand.

The Rotator stand on which this assembly sits is made from commercial Bosch 80/20 T-slotted aluminum (6105-T5) members, bolted together, see Fig. 144a. The stand will be supported on three adjustable base-leg adjusters (two at the upstream side, and one at the downstream side), grouted into the Hall A floor, which will allow adjustment of the stand height and location in the horizontal (transverse to the beam) direction, as well as the pitch and yaw angles. The precise location of the Rotator in the beam direction is not critical to set, and the roll angle for the GEMs is adjustable by the rotation mechanism. The base-leg adjusters follow designs commonly used in Hall A at JLab for adjustable mounting of heavy equipment. The weight of the stand is 250 kg. Buckling analysis of the fully-loaded system gives a safety factor of > 102.

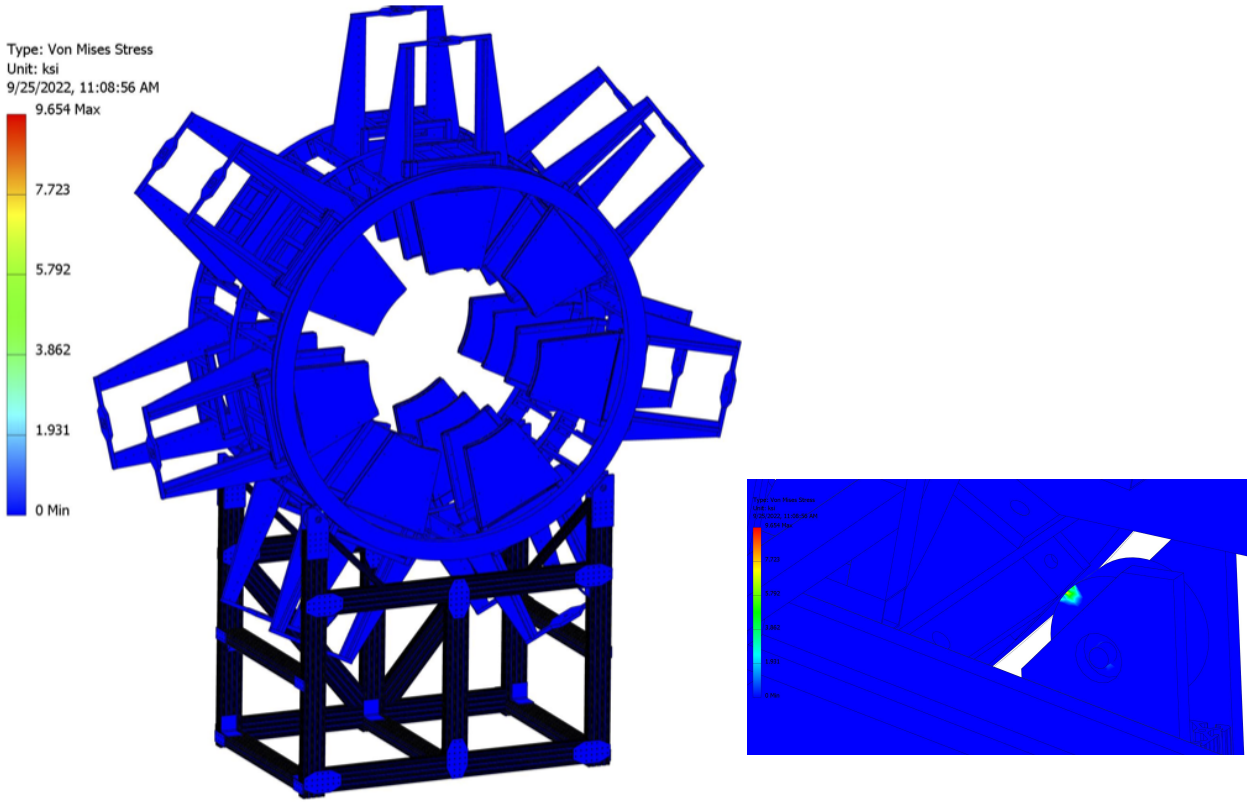

(a) *Rotator and Stand* (b) *Maximum stress location at wheel/roller contact.*

Figure 145: *FEA analysis results for stresses in fully-loaded GEM Rotator and stand.*

The radial motion of the GEM modules to move them between the measurement position (tracking data-taking) and the parked position (integrating data-taking) is accomplished by 14 ball-screw linear stepper motor actuators, see Fig.144b. Each actuator moves a pair of GEMs and a single trigger scintillator along non-magnetic linear guide rails. The weight of a module consisting of a GEM pair, trigger scintillator and holding frame is 25 lbs. The guide rails selected are Franke FDD guides, where the rail body is anodized aluminum, the raceways are non-magnetic steel and the rollers are non-magnetic bearing steel. The trapezoidal frames supporting the linear motors and guide rails is 6061-T6 aluminum. The ball screw is stainless steel. The radial motion stroke is 760 mm for the first two GEM layers and 720 mm for the second two, and will be limited by hard stops at both extremes, which should provide better than the required 1 mm positioning repeatability in the radial direction. The 14 linear actuators will operate independently, which will allow insertion of a single pair of GEM detectors in a particular semi-septant, to allow the study of any

backgrounds in the main detectors caused by the tracking system's insertion. The holder frame for the GEM and scintillator modules is made from aluminum and carbon fibre.

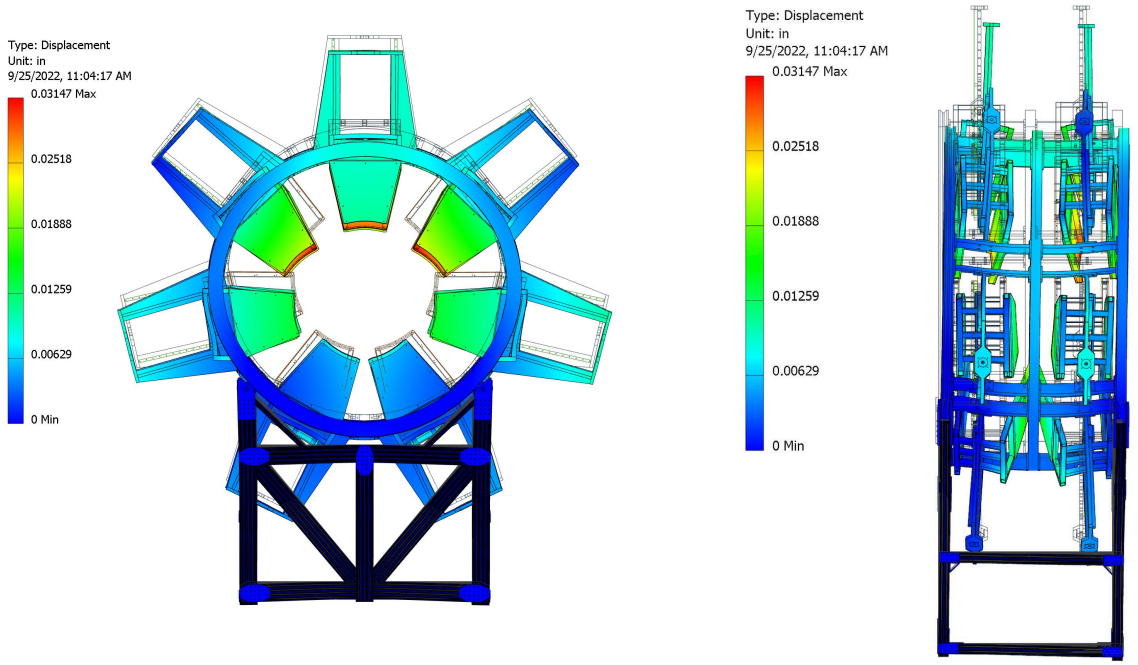

(a) *Displacements: Front view* (b) *Displacements: Side view*

Figure 146: *FEA analysis results for displacement from nominal for GEM Rotator and stand. Black and white outlines are nominal locations, displacements are exaggerated for visualization.*

In the measurement position, the radial distance from the innermost edge of the GEMs to the closest location on the beam pipe is 35 mm, including tolerances from manufacturing, vacuum loading and seismic events on the beam pipe (but not including tolerances from the Rotator positioning or manufacturing).

The rotational system is required at minimum to move the GEMs by 1/7 of 2π (51.4°) to enable sequential azimuthal measurement positions to cover the full detector acceptance. The present design provides 103° rotation, which will allow selected azimuthal measurement positions to be made by two different sets of GEMs, which will be useful to verify that individual detector efficiency variations have been properly calibrated out. It will also be useful in the installation process. The rotation system uses a 316 stainless steel chain of 0.5" pitch wrapped around the exterior of the center wheel, connected via sprockets. The chain is driven via a low speed motor with high starting torque, located at the Hall floor level (see Fig.144), sufficient to drive the maximum torque caused by unbalanced loads during GEM installation (2070 lb-inch, caused by a single GEM pair and scintillator), requiring a chain tension of 40 lbs.

Finite Element Analysis (FEA) of the Rotator and its support stand was done with the Rotator fully loaded with GEMs and trigger scintillators and their associated front-end electronics. The stresses were found to be acceptably small (see Fig. 145). The maximum Hertzian stress at the contact of the wheel with

the rollers is 170 MPa, which for 6061-T6 aluminum should not exhibit significant wear until the number of rotations exceeds 10^5. The expected number of rotations of the system is of the order of a few 10^2.

The FEA predicted displacements of the GEM modules from nominal are under 0.8 mm, within the design 3 mm tolerance (see Fig. 146).

8.7 Trigger Scintillators

The 14 plastic scintillator trigger counters follow the same footprint as the GEM detectors, so as to cover the full acceptance of the GEMs. Thus they are trapezoids with a curved inner edge, like the GEMs. Each scintillator is made from EJ-208 from Eljen Technology, and will be 1 cm in thickness (2.3% X_0). EJ-208 was chosen due to its long absorption length and good light output. In each azimuthal location, the upstream scintillator is located just downstream of the first GEM, mounted on the same frame that supports the GEM, and the downstream scintillator will be located just upstream of the fourth GEM, again mounted on the same frame.

The timing requirements for the trigger scintillator are not stringent, as the read out of the tracking GEMs will be with a time binning of 25 ns. We desire at least 2 ns σ time resolution. The most important performance characteristic of the scintillators is to have a detection efficiency for minimum-ionizing particles that is uniform at the $\pm 2\%$ level over the active area of the GEMs (reduced efficiency at the edges of the scintillators where they cover the inactive GEM frames is not a problem). The uniformity of efficiency is needed in order to avoid trigger biases in the reconstruction of the track distributions at the main detectors and in the spectrometer optics calibrations.

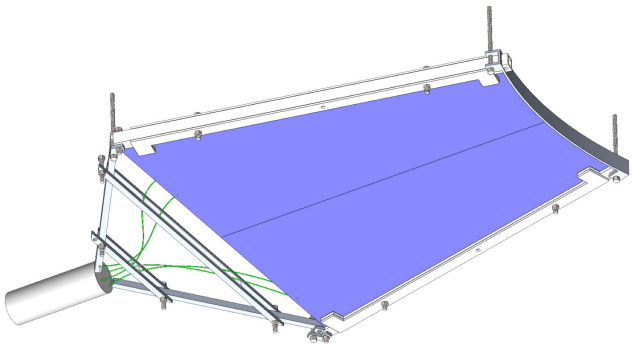

Figure 147: *CAD of Trigger Scintillator and holding frame.*

An overall efficiency in the active region of $> 98\%$ is desired, mainly for purposes of special runs in which the trigger scintillators will be used in veto mode, in order to identify backgrounds in the main detectors, Shower-max, or pion detectors that do not arise directly from Møller or ep electrons, *i.e.* soft neutrals or events originating in the beam dump or beamline.

The rate capability requirements of the trigger scintillators are not taxing. There will be two primary operating modes of the scintillators, a) measurements with the full LH2 target and no sieve collimator, at a beam current of 1 nA, and b) measurements with the sieve collimator inserted and pairs of 1-mm thick ^{12}C optics targets at a beam current of 100 nA. The maximum rate per sector of the scintillators in these two modes will be 1.3 MHz.

In the original design concept, light was read out from the scintillator using a trapezoidal acrylic light guide connected to the large-radius edge of the scintillator, coupled to a single 2" diameter PMT. This concept has been discarded in favor of WLS (wavelength shifting fibre) readout, which is more compact, and for which optical simulations in GEANT4 predicts superior light output and uniformity of optical response across the scintillator area than for the light guide option. The selected WLS fibre material is Kuraray Y-11, which is chosen because its absorption peak (430 nm) is well-matched to the EJ-208 wavelength of maximum emission (435 nm).

The fibres will be placed in grooves cut in one large face of the scintillator. The present design has 6 parallel rows in the approximately radial direction, spaced by 50 mm (the exact number of fibres per scintillator is being optimized). The option of increasing the number of embedded fibres by machining grooves into both the front and back faces of the scintillator is being explored. The present selection for a PMT is the ET Enterprises 2" diameter 9814B PMT and the RB1102 base. A gain switchable base is not needed for the trigger scintillators, as they will only be operating in counting mode data-taking.

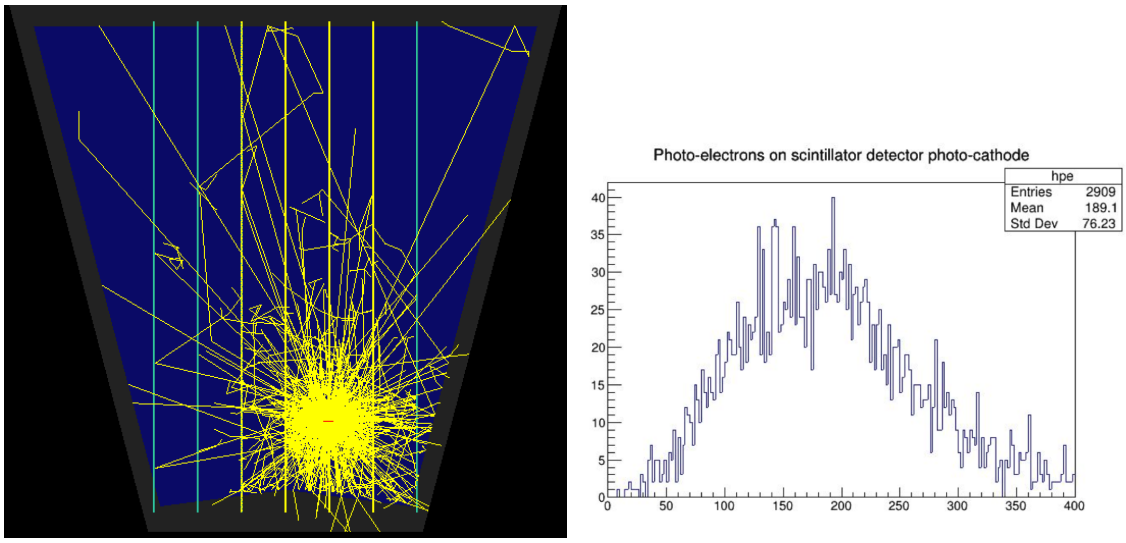

(a) (b)

Figure 148: *Simulated results (GEANT4) for Møller electrons on a trigger scintillator paddle, read out via WLS fibres. a) single event, optical photons in yellow; b) number of photoelectrons seen by PMT.*

Initial prototype testing is underway to study the WLS-based readout and to benchmark GEANT4 optical simulations. The prototype uses a rectangular 30 x 40 x 1 cm tile of EJ-208 with two grooves in which are embedded a single WLS (looping back outside the scintillator), which is connected to a PMT. The prototype uses older 1.2 mm diameter Y-7 (175) fibres from Kuraray, borrowed from W&M collaborators from the Minerva collaboration. Initial results are that the light output is maximized when the reflective mylar wrapping does not whet the scintillator surface.

8.8 Triggering and data rates

We need to be able to trigger the tracking readout independently of the main integrating detectors, so as to ensure that all incident charged particles are measured; the default trigger in the counting mode measurements will be an "OR" of the coincidence between the upstream and downstream scintillators in a given one of the 7 GEM sectors. Two scintillator layers are required in order to suppress spurious triggers due to soft backgrounds. In the majority of the tracking data-taking modes, the triggers will be completely domi-

nated by good Møller electrons or electrons from elastic e-p scattering (or e-^{12}C scattering in the case of the optics targets), and so the triggered data set will have high purity. As discussed above (Sect. 8.7) the raw trigger rate will be reduced by reducing the beam current. The trigger will also be highly pre-scaled to avoid saturating the DAQ.

An "unbiased" pulser trigger is also useful to study the trigger efficiency in test runs, and a trigger based on an "OR" of the main detector signals, and in which the trigger scintillators are used in software veto mode, will be important for studying neutral backgrounds. Finally, a trigger based on an OR of the pion detectors in coincidence with the trigger scintillator pair from any sector will be used in counting-mode measurements of the pion background flux.

9 Auxiliary Detectors

Several auxiliary detector systems are used to monitor and help ensure the quality of the experimental setup and production data. These systems are described in this chapter and include the Shower-max detector ring, Pion detector ring, and various beam scattering monitors and scanner detectors. These systems enable increased understanding and control of systematic effects and background asymmetries. The design and function of each system are driven ultimately by the goal to reduce systematic error in the main integrating detector Ring 5 asymmetry measurement. Each system plays a vital role in monitoring for specific systematic, beam-correlated or background effects and correcting for them if necessary.

The Shower-max and Pion detector rings are positioned to intercept the peak Møller scattering flux after it passes through the Ring 5 acceptance. In addition, there are two beam scattering monitor rings called the Large Angle Monitor (LAM) and Small Angle Monitor (SAM). The LAM is installed upstream of the GEM rotator and is positioned to intercept scattered flux at the outer edge of the collimated primary flux envelope. The SAM is installed around the beamline near the Hall A beam dump entrance and is designed to monitor the rate of very small angle ($\sim 0.1^\circ$) scattered flux coming from the target. There are also four downstream (DS) linear scanners positioned just upstream of the SAM, as well as a small upstream (US) 2-D scanner positioned just upstream of the main detector barrel. The DS scanner's primary purpose is to validate the baseline optics of the spectrometer – position, alignment and function of collimator systems and magnet coils. The US scanner's purpose is to map, in two dimensions, the event distribution impinging on the main detector array.

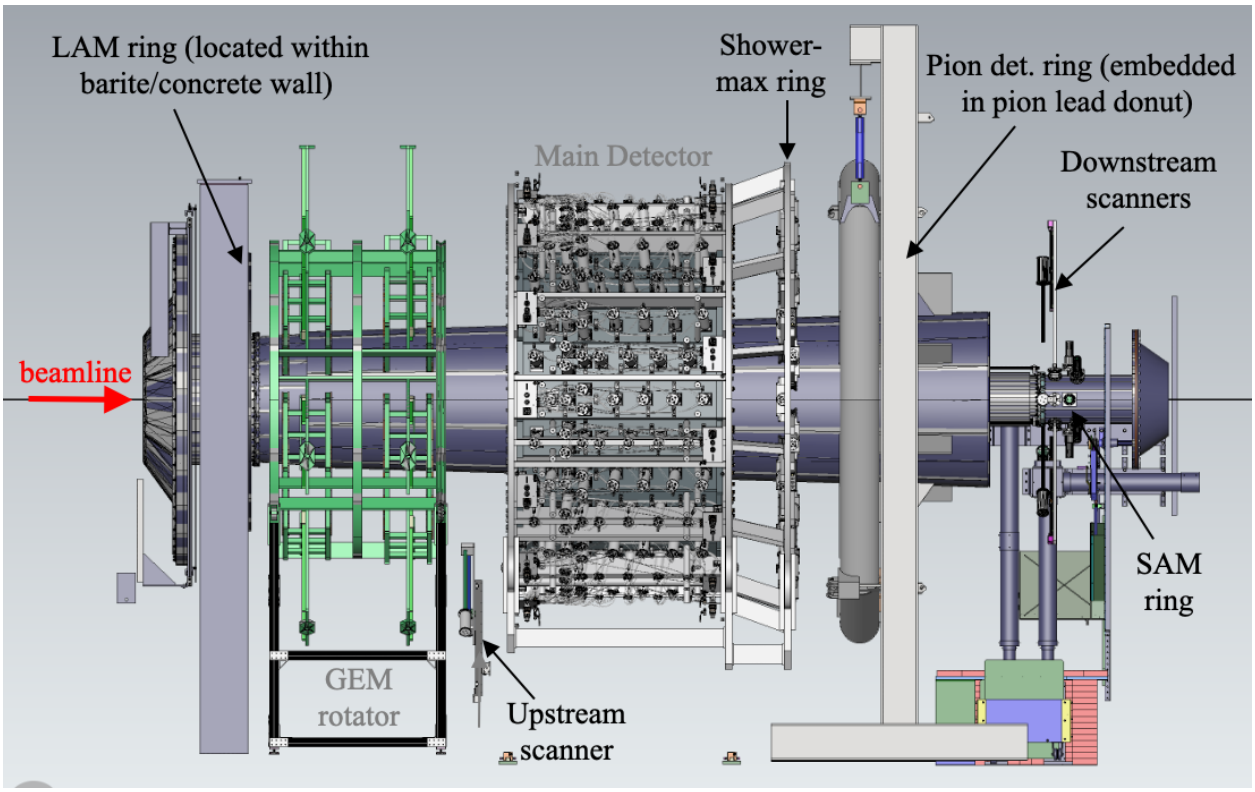

Figure 149: *Beamline detector CAD highlighting the auxiliary detector packages.*

9.1 Shower-max

9.1.1 Overview

The purpose of the Shower-max (SM) detector system is to provide an additional measurement of the Møller peak signal flux intercepted by the main Ring 5 detectors. The SM ring provides an independent measurement of the Ring 5 flux asymmetry. The different analyzing power and background systematics for the SM measurement make it a powerful cross check of the main measurement. The SM ring support structure is integrated into the downstream end of the main detector barrel structure; it is centered on the beamline with a z-location approximately 1.7 m downstream of Ring 5. The inner diameter of the SM detector ring is ~ 2 m. There are 28 individual SM detectors (modules) instrumented around the ring giving full azimuthal coverage. There is a 3-fold reduction in the azimuthal segmentation of the SM ring compared to Ring 5, but otherwise the segmentation patterns are matched; each SM module covers the acceptance of three adjacent Ring 5 modules in either an Open, Closed, or Transition semi-septant region.

The Shower-max detector is an electromagnetic sampling calorimeter designed to have an energy proportional response with at least 25 % detection resolution for individual, incident electrons with energies in the range of 2 – 8 GeV. The detector can operate in both integrating (production) mode and event mode for routine low-current calibration studies. Given the high rate of intercepted particles, an important design consideration is the radiation hardness of SM optical components over the lifetime of the experiment. The accumulation of radiation dose to active components discussed in Sect. 6.7 is significantly higher for SM than for the main detector rings. This requires the use of high-purity fused silica (HPFS) Cherenkov radiators as well as additional mitigation strategies to control radiation damage effects on the long term performance of SM. Radiation-hard, air-core aluminum light guides are used to direct the Cherenkov light from the radiator to a 3 inch photomultiplier tube (PMT) located 25 cm away in a low radiation region.

9.1.2 Design Concept

The Shower-max detector concept uses a conventional layered sandwich design consisting of four layers of HPFS (referred to interchangeably as quartz) interleaved with four layers of high-purity tungsten. This sandwich of quartz and tungsten is referred to as the "stack." The total thickness of the stack along the beam direction is approximately 9.5 X_0. This allows the electromagnetic shower to grow to near maximum size, with ≈ 1.1 cm Molière radius, before exiting the downstream end of the stack towards the lead pion donut and pion detector ring. As the electromagnetic shower develops, its growing number of charged, relativistic particles traverse the successive quartz layers and generate Cherenkov light. The quartz layers are essentially DIRC-style detectors that use total internal reflection inside the quartz to efficiently direct the generated Cherenkov light cone to a 45° bevel cut along one surface where it escapes into the light guide volume. The light guide is designed to direct most of the light to the PMT in a single reflection.

9.1.3 Individual Detector Module

All 28 detector modules each have the same design and material construction. Each module consists of four quartz and four tungsten layers cradled in an aluminum chassis with reinforced side struts that rigidly connect the stack to the PMT. Some CAD views of the detector module are given in Fig. 150.

Geometry, materials & components The Shower-max chassis is made from all 6061 aluminum parts with brass and aluminum hardware. The light guide is made from 0.020 inch thick sheets of Anolux MIRO-IV. This material uses an Alanod aluminum base material with an electrolytically bright anodized and PVD-coated aluminum surface. The light guide material candidates for Shower-max are MIRO-Silver and MIRO-IV. Both are poor reflectors in the UV which is preferred for Shower-max given its large light yields and

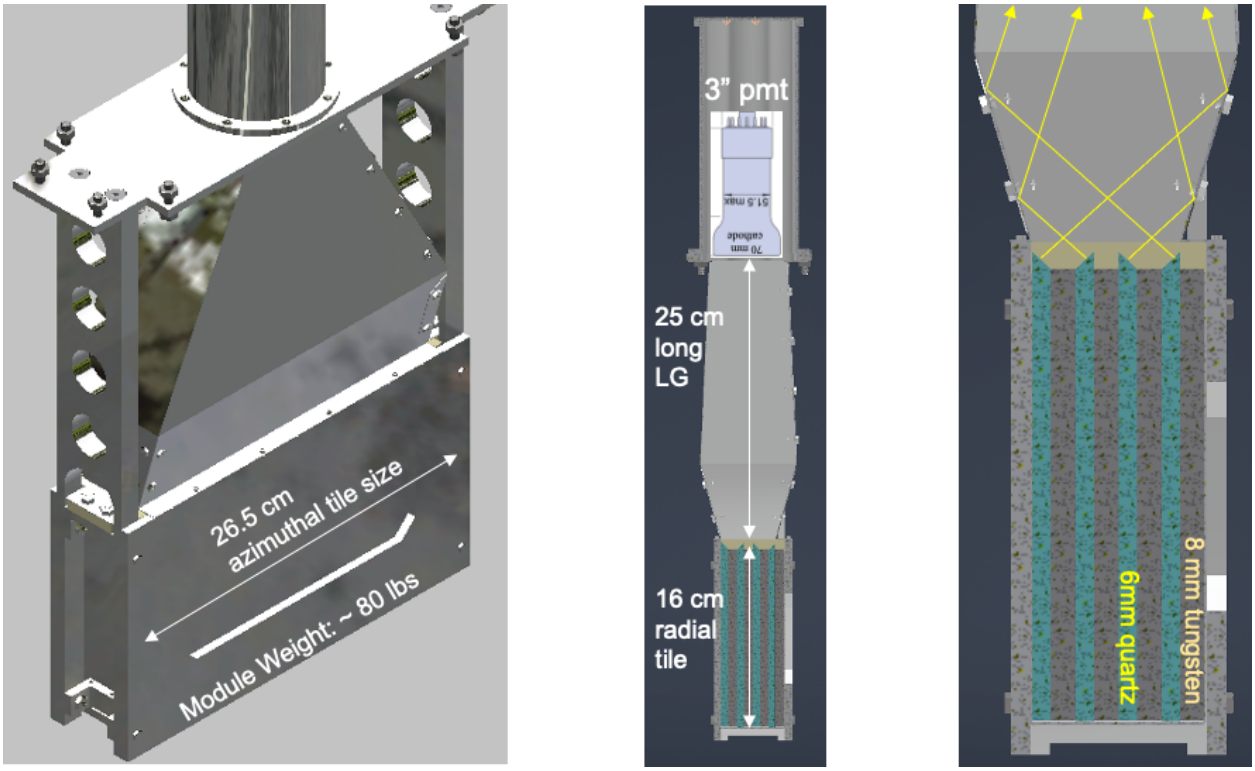

Figure 150: *(left) Shower-max module design views. The chassis and light guide are aluminum. (middle and right) Side-view of Shower-max showing details of the stack and light guide; yellow rays depict the dominant direction of Cherenkov light exiting the quartz. Impinging electrons pass through the stack from right to left in these views.*

radiation damage effects in the UV spectrum; MIRO-IV was chosen to avoid the use of silver in the material. The chassis and light guide parts are all precision CNC machined.

The preferred type of HPFS for Shower-max is Heraeus Spectrosil 2000 with H_2 doping. The choice is based on radiation hardness testing of various HPFS samples (see Sect. 6.7). The active area of each quartz tile is 265 mm (azimuthal) by 160 mm (radial) and is 6 mm thick (along beamline). The tungsten layers (or plates) are 99.95 % pure and are each 265 mm $\times$ 160 mm $\times$ 8 mm (and have no 45° cut). The dimensional tolerances of the tungsten are ± 0.005 inch. The dimensional and angular tolerances for the quartz tiles are given in Tab. 20 of Sect. 6.3.1.

Mechanical design, Chassis and FEA Given the weight of the tungsten plates and vertical ring configuration, the stack components are encased in 1/4-inch thick aluminum chassis parts and supported securely along the edges and corners. A list of parts with shop drawings is given in Fig. 151. The outer (radially) edges of the stack are supported by the "ledge" parts, while the inner stack is supported by the "floor plates" and lower U-channel parts. CAD views of these SM parts are given in Fig. 152. The azimuthal stack support and fitment rely on precision CNC parts with tight-fitting, through-hole bolted assembly connections. An important design consideration is to minimize deformation stresses on the light guide both during ring assembly and while deployed during MOLLER. A specialized hole mount for a fiducial fixture will be incorporated into a selected chassis part to facilitate survey and alignment of each module in the ring during installation.

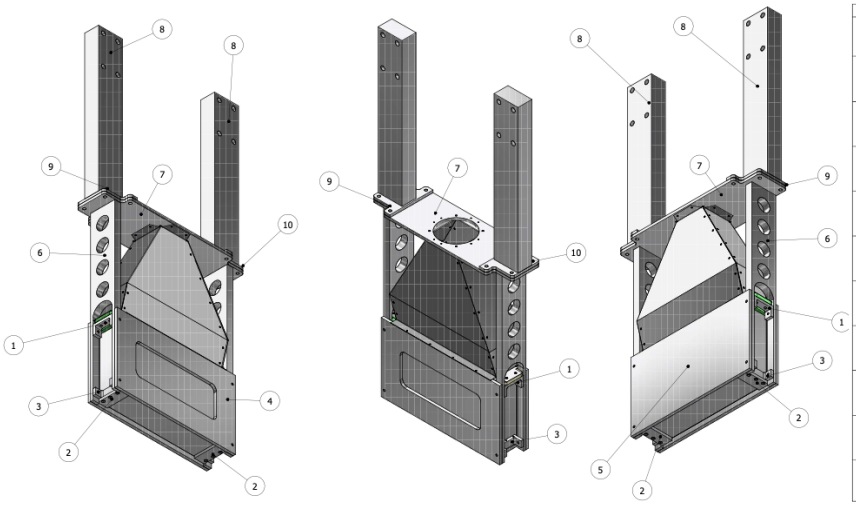

SHOWER MAX PARTS		
ITEM NO.	PART NAME/MATERIALS LIST	Material
1	UPPER U CHANNEL	(1/4)" x 2" ALUMINUM 6061
2	FLOOR PLATE	0.25 (1/4) THICK 6061-T651 ALUMINUM PLATE
3	LOWER U CHANNEL	0.25 (1/4) THICK 6061-T651 ALUMINUM PLATE
4	FACE PLATE	0.25 (1/4) THICK 6061-T651 ALUMINUM PLATE
5	BACK PLATE	0.25 (1/4) THICK 6061-T651 ALUMINUM PLATE
6	WEB PLATE	0.625 (5/8)" THICK ALUMINUM 6061
7	TOP PLATE	0.25 (1/4) THICK 6061-T651 ALUMINUM PLATE
8	SUPPORT STRUT	1.5 (3/2)" THICK ALUMINUM 6061
9	LEFT FOOT PLATE	0.25 (1/4) THICK 6061-T651 ALUMINUM PLATE
10	RIGHT FOOT PLATE	0.25 (1/4) THICK 6061-T651 ALUMINUM PLATE

Figure 151: *Shower-max chassis parts.*

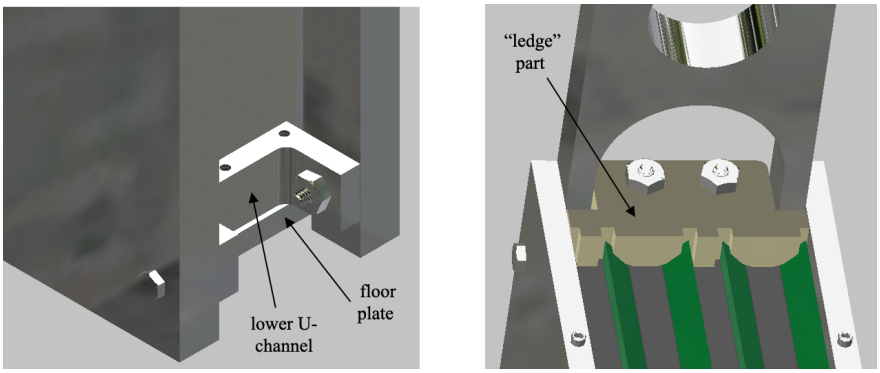

Figure 152: *Shower-max stack support parts. (left) Shows the inner (radially) stack support parts. (right) Shows the outer stack support concept with ledge part. This part secures the outer stack in place by supporting 2 mm of quartz and tungsten at both ends.*

Based on analysis of the initial chassis model, the radial struts were stiffened to reduce weak-axis deformations during assembly. This resulted in the current design and use of the "web plate" part. Finite element analyses (FEAs) have been performed on the SM module chassis and ring assembly, as well as modal analyses of the ring structure. The SM module weak-axis FEA is presented in Fig. 153. While these stresses are not relevant while suspended in the vertical ring, they are important for assembly and installation considerations. Using the web plate reduces maximum deflections to less than 0.5 mm.

Optical design, quartz and light guide The optical components of Shower-max consist of quartz, light guide, fused silica PMT window and bi-alkali photocathode. The optical properties of these components have been carefully referenced and/or measured on the bench and incorporated into a GEANT-4 optical simulation framework. This framework drives much of the Shower-max design concept and its model parameters are benchmarked to test-beam data from prototype R&D.

The use of high purity fused silica (or quartz) is required due to its resistance to radiation damage. The quartz tiles must be optically polished on all six surfaces and have a fair degree of parallelism between the

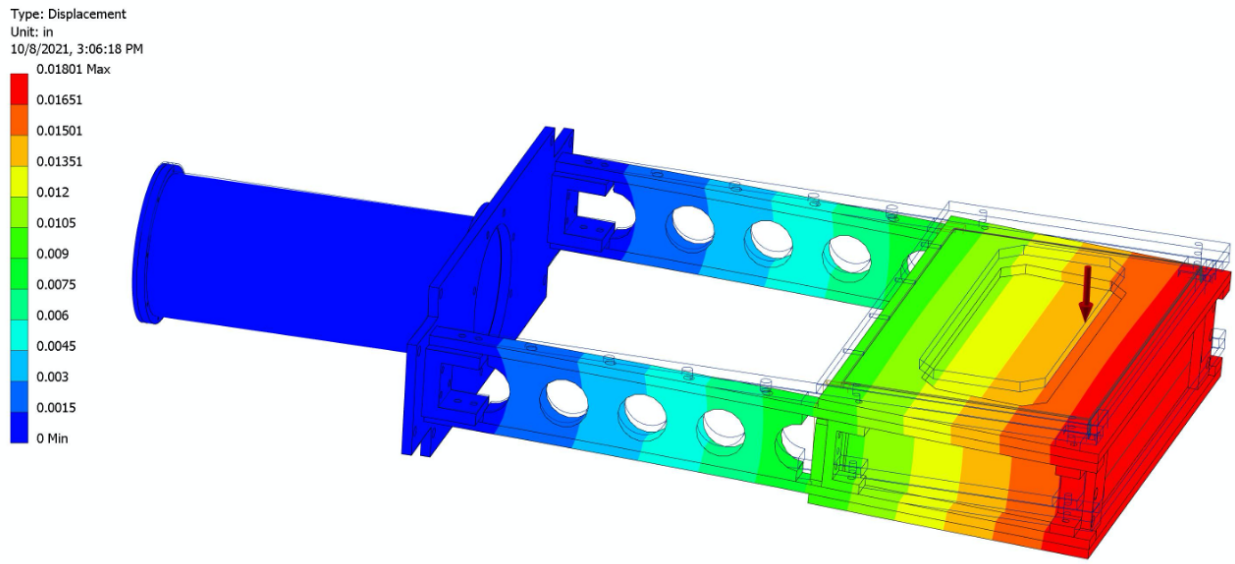

Figure 153: *Shower-max module weak-axis FEA from L. Bartoszek. These stresses are relevant during module assembly, handling, and installation in the ring. The maximum deflection is 0.018 inch and deemed acceptable.*

large faces. A 45° angle cut is made along one long side to break the total internal reflection and allow Cherenkov light to escape; a schematic of the radiator geometry is given in Fig. 154. As discussed in Sect. 9.1.6, due to very high doses on the various SM quartz layers, the UV light component of the SM signal will be eliminated from the start. This is accomplished using a long-pass filter in front of the PMT window. The long pass filter is 78 mm diameter, 3 mm thick and made of Corning 7980 UV grade HPFS.

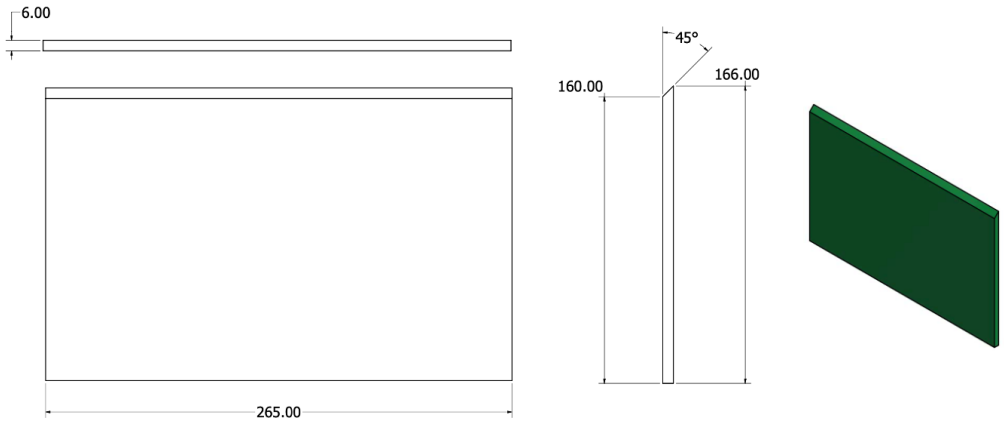

Figure 154: *Shower-max quartz geometry in mm. Note that the tungsten geometry is identical to this, except that the 45° angle cut is removed.*

The Shower-max light guide parts list with shop drawing is presented in Fig. 155. Reflectivity measurements (at normal incidence) of several light guide materials have been performed and are shown in Fig. 156 along with the reflectivity of MIRO-IV for several different angles. Most of the light rays exiting the quartz strike the light guide funnel mirror with $\sim$30° angle of incidence with respect to the mirror plane. At this

angle, according to Fig. 156, the light guides give 60 to 70 % reflectivity through the visible range, with an abrupt drop off below 350 nm.

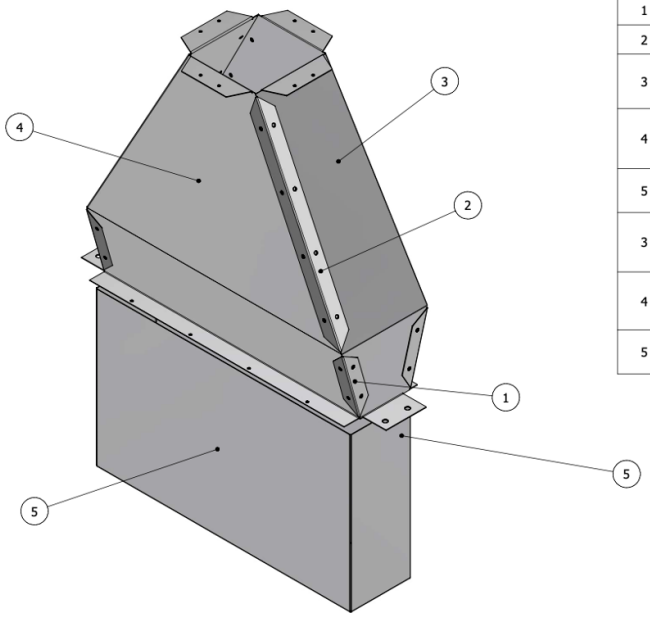

ITEM NO.	PART NAME	MATERIAL
1	SHORT FLAP	0.02" ANOLUX MIRO-SILVER OR MIRO - IV MATERIAL DOES NOT MATTER
2	LONG FLAP	0.02" ANOLUX MIRO-SILVER OR MIRO - IV MATERIAL DOES NOT MATTER
3	LIGHT GUIDE BACK	0.02" ANOLUX MIRO-SILVER REFLECTIVE ALUMINUM SHEET CAUTION: NO SCRATCH SURFACE REQUIRED
4	LIGHT GUIDE FRONT	0.02" ANOLUX MIRO-SILVER REFLECTIVE ALUMINUM SHEET CAUTION: NO SCRATCH SURFACE REQUIRED
5	SUITCASE	0.02" ANOLUX MIRO-SILVER REFLECTIVE ALUMINUM SHEET CAUTION: NO SCRATCH SURFACE REQUIRED
3	LIGHT GUIDE BACK	0.02" MIRO- IV REFLECTIVE ALUMINUM SHEET CAUTION: NO SCRATCH SURFACE REQUIRED
4	LIGHT GUIDE FRONT	0.02" MIRO- IV REFLECTIVE ALUMINUM SHEET CAUTION: NO SCRATCH SURFACE REQUIRED
5	SUITCASE	0.02" MIRO- IV REFLECTIVE ALUMINUM SHEET CAUTION: NO SCRATCH SURFACE REQUIRED

Figure 155: *Shower-max light guide parts. Each light guide is constructed from two flat cut-outs that are folded by hand and assembled with brackets and small aluminum screws. The suitcase parts are primarily for light tightness.*

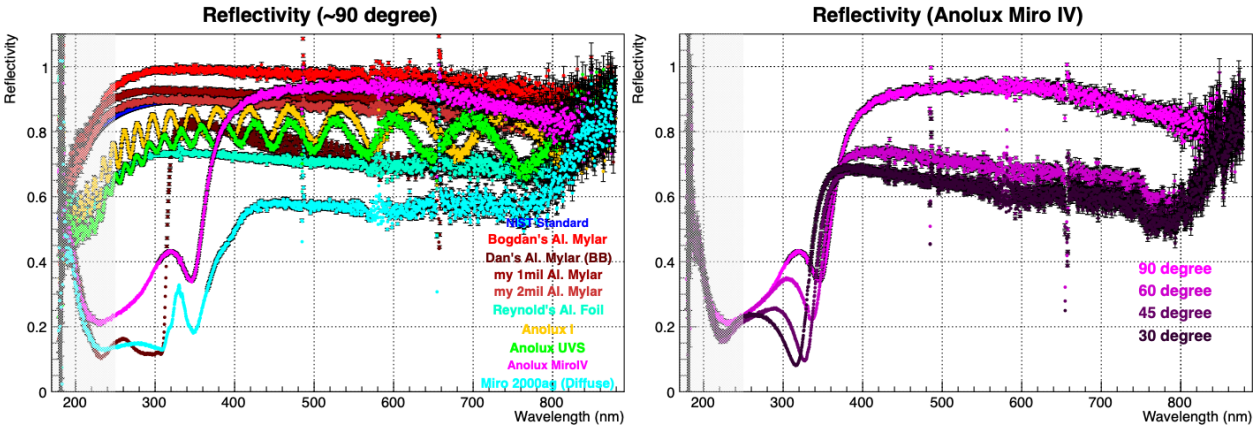

Figure 156: *(left) Reflectivity measurements calibrated with traceable NIST mirror standard. (right) Reflectivity measurements for Miro-IV (top) for 90°, 60°, 45°, and 30° angles relative to the mirror plane.*

Rates, yields and PMT operation The Shower-max detectors use the same 3 inch PMTs as the main detectors – Electron Tubes 9305QKB. Both event and integration mode PMT voltage divider, preamplifier and signal acquisition electronics have the same design as for the main detectors. The difference for Shower-max is that the PMT photocathode currents will be higher during integration mode, requiring the use of

different PMT and preamplifier gain combinations compared to any of the main detectors. Extra care will be needed to assure good linearity on the bench for the operating conditions of the SM PMTs.

The anticipated rates of intercepted particles per SM module are high, especially for the Open semi-septant detectors. These high rates, combined with the much higher SM PE yields, create uncomfortably high PMT cathode currents for integration-mode data taking. Table 30 summarizes these numbers for each semi-septant detector. To address the high cathode currents, long-pass filters are used to limit the currents to below 100 nA.

	Open		Closed		Transition		Ring Total	
	e^-	γ	e^-	γ	e^-	γ	e^-	γ
Rate [GHz]	9.3	83.3	3.9	29.4	4.8	50.9	159.8	1501
Mean PE yield [PEs]	564	3.8	320	3.1	352	2.7		
partial Cathode I [nA]	840	51.0	200	14.7	271	22.1		
Cathode current [nA]	891		215		293			

Table 30: *Simulated Shower-max rates, mean yields and photocathode currents for electrons and gammas in individual semi-septant detector modules with no long-pass filter. Rates from electrons and gammas come from Møller and elastic and inelastic e-p event generators. The total ring rates are also given.*

9.1.4 Ring Assembly

The Shower-max ring consists of 28 modules: 7 Open, 7 Closed and 14 Transition semi-septant detectors. The inner and outer radial location of the detector active area is 1020 mm and 1180 mm, respectively. Note this is only technically true along the mid-plane of each module. The z-location of the Shower-max ring along the beamline is centered at 23920 mm from hall center and is approximately 1.7 m downstream of Ring 5; the pion detector lead donut is 0.5 m downstream of SM. A beamline view of the SM ring assembly and iso-view of an individual module is given in Fig. 157; these models come from simulation geometry definition GDML files. A CAD model view of the SM ring is given in Fig. 158 showing the staggered configuration of the modules around the ring. The Open and Closed modules mount to the upstream surface of the support ring, while Transition modules attach to the downstream surface.

Installation of SM modules into the ring structure will take place within Hall A. SM modules will be installed at the same time as the main detector segments using the same process. The main barrel and SM ring support structure is first installed around the beamline and detector beampipe. Each SM module is lowered into position vertically one at a time, using a small jib crane for example, and bolted into position on the ring. The ring will then rotate into a new position and the next SM module is installed, and so forth until the ring is complete. Each SM module weighs approximately 80 lbs including the two aluminum bars that attach the module to the support ring.

Support structure design, FEA The Shower-max ring support structure is cut out from a 2 inch thick 6061 aluminum plate. The ring has inner and outer radius of 68 and 78 inch, respectively, and is split into two halves (for installation around beamline). The ring sits on its own set of aluminum (7075-T6) roller bearings and is connected to the main detector barrel with fourteen aluminum cross supports equally spaced around the ring. The SM rollers use the same drive mechanism and motor as the main detector rollers. The two SM support ring halves, without any modules installed, weigh 1000 lbs, and when fully instrumented weigh 3240 lbs. An FEA of the SM ring combined with the main detector barrel is presented in Sect. 6.6.3. The results are also presented here in Fig. 159 with a cutaway view of half the detector assembly looking upstream at Shower-max. Maximum SM deflections are near 0.5 mm and occur in the beam-left and -right

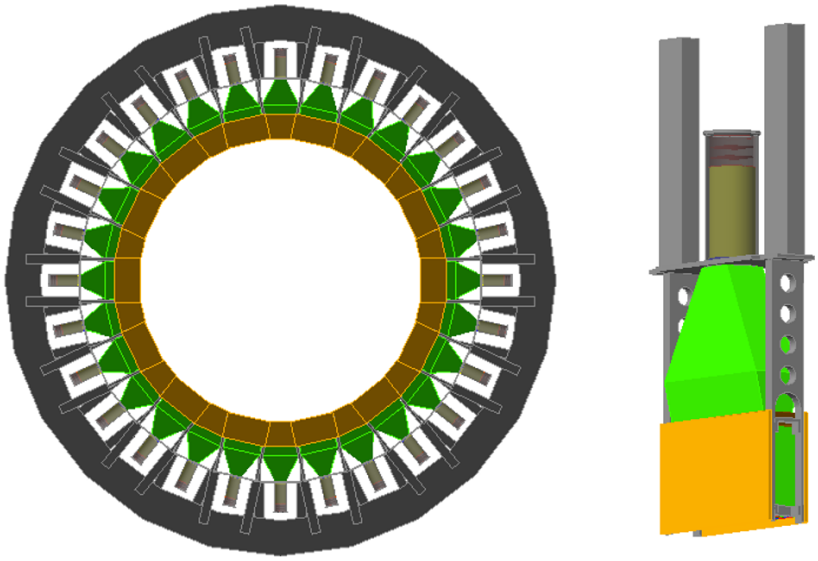

Figure 157: *(left) View of the Shower-max detector ring GEANT-4 simulation model (GDML) with support framing. (right) SM model implemented in simulation.*

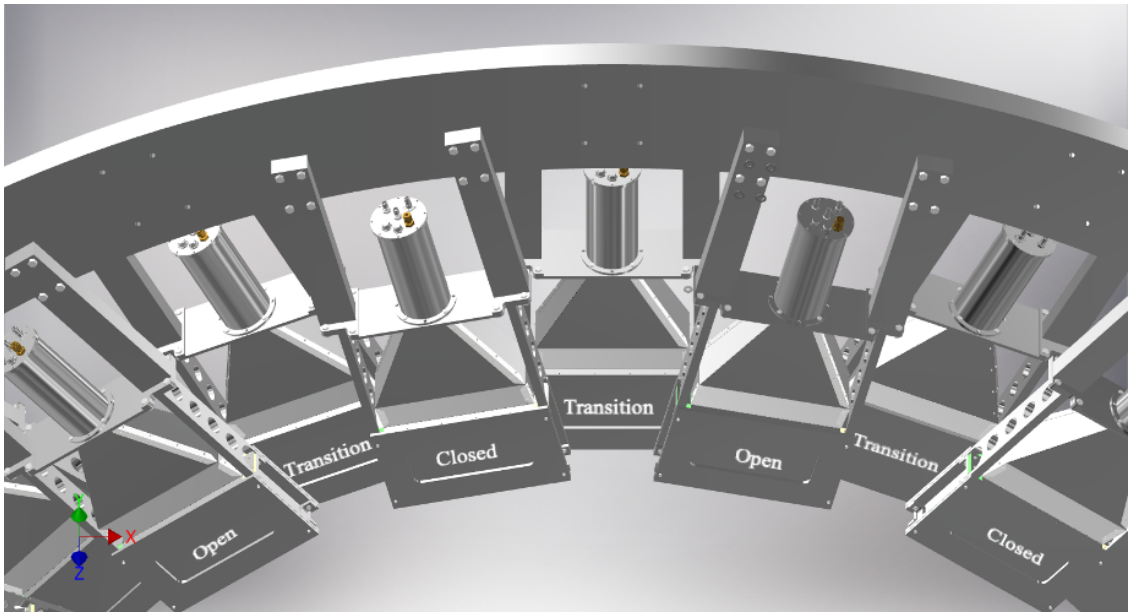

Figure 158: *Shower-max ring structure CAD. Downstream view of the Shower-max ring showing aluminum support structures and attachment of modules to the ring. The Open and Closed semi-septant detectors are upstream of the Transition detectors. There is a small triangular-shaped region of overlap between adjacent detectors to prevent gaps.*

few modules, with corresponding minimum deflections directly above and below the beamline. The size and pattern of deflections indicate the ring support design is robust and to reduce deflections further would require stiffening the module chassis.

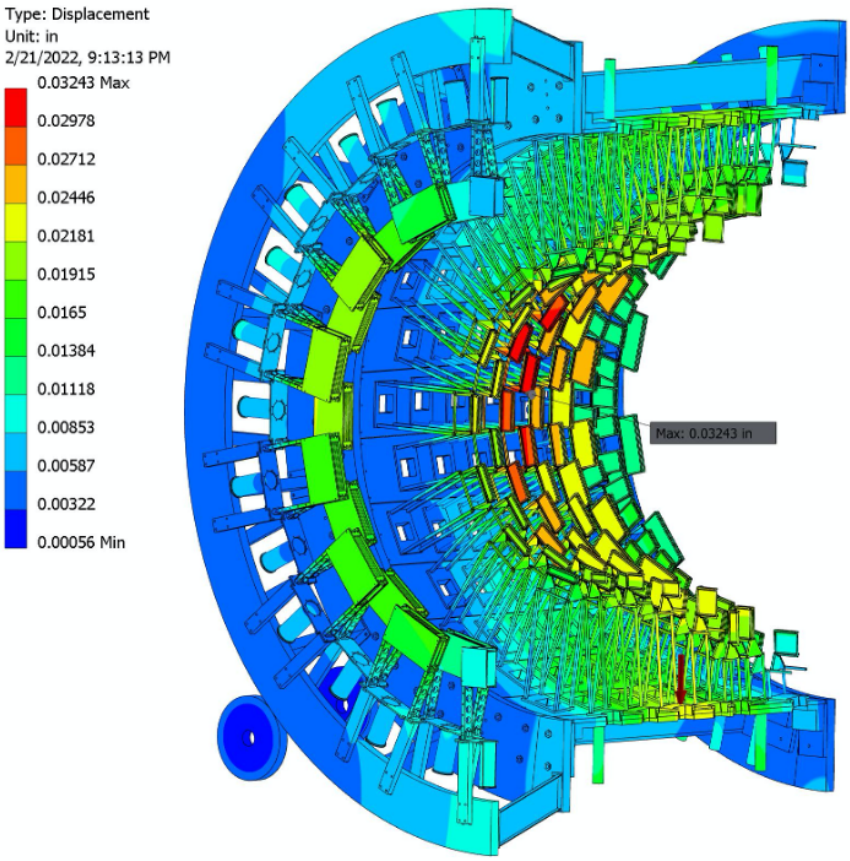

Figure 159: *Detector support structure FEA by L. Bartoszek with view looking upstream at Shower-max.*

9.1.5 Requirements and Projected Performance

The requirements for Shower-max are the same as for the main integrating detectors outlined in Sect. 6.1.1. However, given the energy-dependent detector response and resolution of the SM signal, combined with the relatively broad energy acceptance of each semi-septant module, the design of the stack configuration and thickness was tuned to provide $\leq$ 25 % resolution for individually detected mono-energetic electrons between 2 - 8 GeV. Simulated distributions of the energy acceptance and energy dependent photoelectron (PE) yield responses and resolutions for each semi-septant region are given in Fig. 160. While the single-electron detector response resolutions are key performance parameters, the overall finite resolution of the detector during MOLLER, which drives its excess statistical noise during the integrating measurement, is a more complicated convolution of the accepted rate-weighted energy distribution of each detector and its response to those energies.

To predict the detector performance and resolutions, simulations are run for each semi-septant detector with incident electron energy and momentum matching the red, blue, and green distributions in the left plot of Fig. 160. The results of this study, given in Fig. 161, show PE response distributions with 25 - 30% relative widths (or resolutions) for the three semi-septant regions. A Shower-max detector with 30% overall finite resolution (per helicity window "event") leads to 4.4% error inflation in the integrating asymmetry measurement. The Ring 5 thin quartz detectors will have better resolution and less excess noise than the Shower-max detectors due to their energy independent response. However, while the energy-proportional

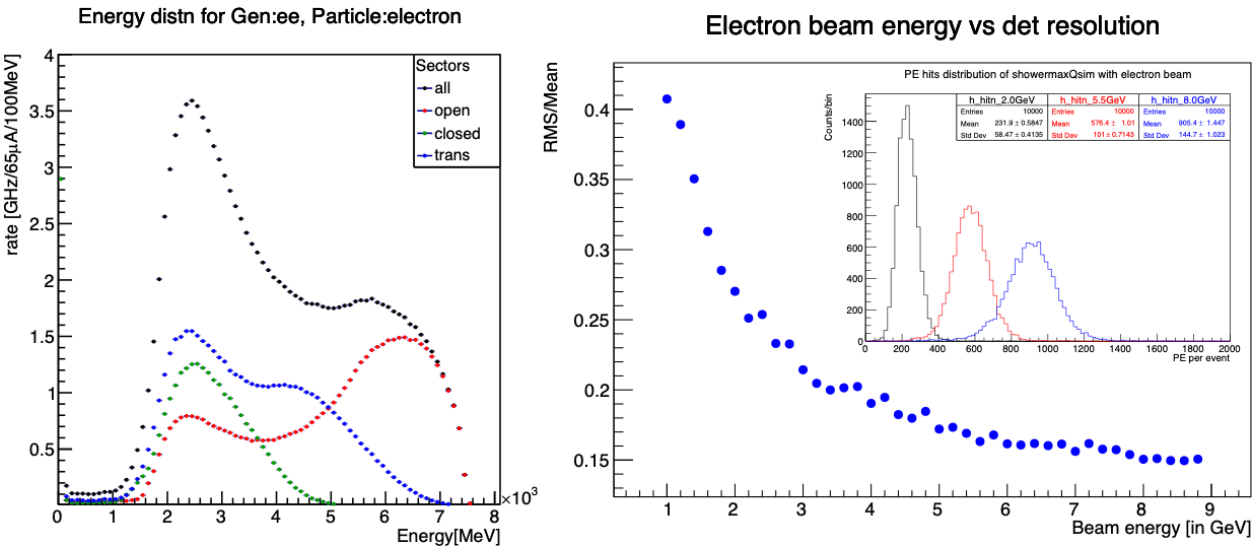

Figure 160: *(left) Rate distribution of Møller electron energies accepted in the Open, Closed, and Transition region Shower-max detectors. (right) Simulated detector resolution versus energy with inset plot of the SM response for 2, 5.5, and 8 GeV mono-energetic, single electrons.*

response of the Shower-max inherently worsens its finite resolution, it makes it less sensitive to hadronic and low-energy electromagnetic backgrounds.

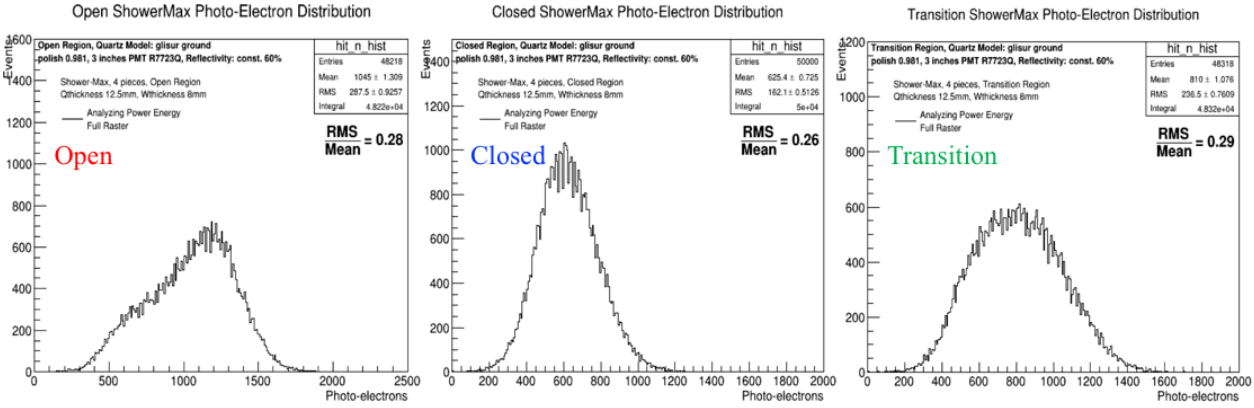

Figure 161: *Simulated analyzing-power and energy rate weighted PE responses for the three semi-septant SM detectors. These results show overall resolutions are in the ∼25 - 30% range.*

The SM rate-weighted gamma-ray energy acceptance and PE yield response to a few select gamma energies are given in Fig. 162. Background flux is dominated by low-energy gammas, as expected, which give a proportionally low SM PE response. So although there are 10 times more gammas than electrons impinging on the detector, they make on average 100 times fewer PEs. In a given helicity window, the detector signal contribution from gamma rays is predicted to be ∼5.5 – 7.5 % of the signal from electrons. Other backgrounds include pions and muons. Mean PE responses to these are given in Tab. 31. These responses are 10 – 20 times lower than for an equivalent energy electron or gamma-ray.

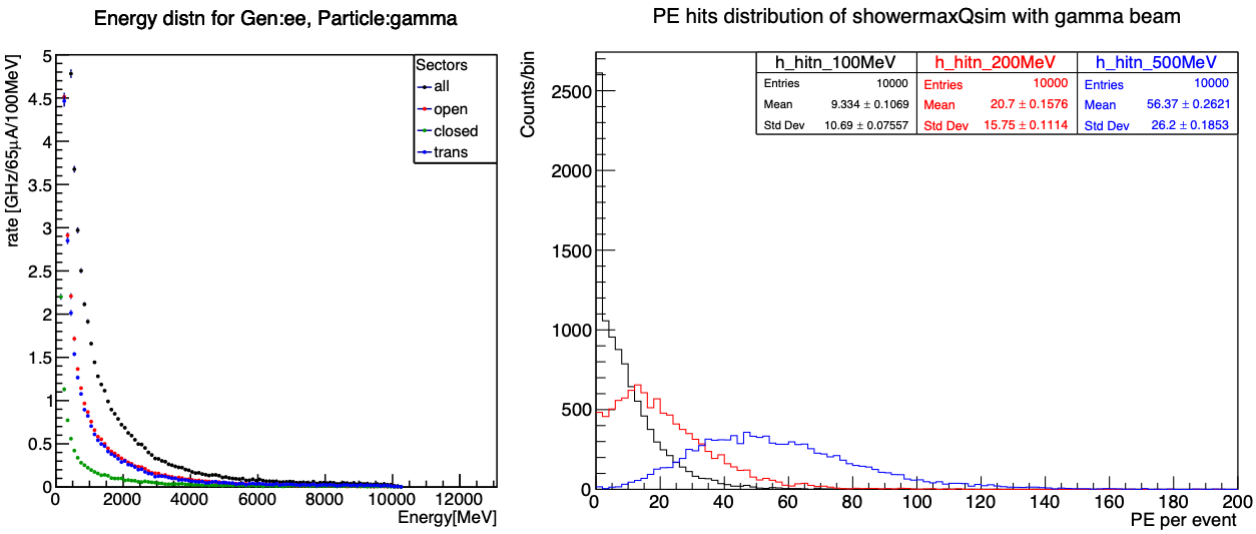

Figure 162: *(left) Rate distribution of gamma energies accepted in the Open, Closed, and Transition Shower-max detectors. (right) Simulated detector response for 100, 200, and 500 MeV single electrons.*

	Mean PE Response: [PEs]	
Energy	Pion	Muon
2 GeV	37	33
5 GeV	60	34
8 GeV	93	33

Table 31: *Shower-max PE response for pions and muons at various energies.*

9.1.6 Risks and Mitigation

Shower-max has two challenges to overcome in order to achieve long term stable operation during MOLLER. The challenges are how to manage the unavoidable, significant radiation damage to its quartz tiles, and how to manage its exorbitant photocathode currents due to high light yields and particle detection rates. Both of these challenges are addressed by the use of long-pass filters in front of the PMT window and cathode. The filter cutoff is selected to prevent UV light from reaching the cathode, thus significantly reducing average PE yield and cathode current, as well as reducing much of the potential long-term impact of quartz radiation damage effects on the SM signal.

Simulations of radiation loads (or doses) on the various optical and electronic components of Shower-max have been performed. We find peak lifetime dose densities in the SM quartz can be ∼10 times higher than for the main detectors (see Sect. 6.7 for radiation effects on the main detectors). The approximate peak dose densities in each SM quartz layer are given in Tab. 32. Doses range from 150 Mrad/5x5 mm^2 in the last layer of the Closed semi-septant modules to 1.3 Grad/5x5 mm^2 in the second layer of the Open modules. The maximum dose level achieved during the quartz radiation hardness tests was ∼0.5 Grad/5x5 mm^2. At this level no changes in visible light transmission were recorded, however, most all the light below 300 - 350 nm was absorbed. Note that we know of no optical absorption center defect mechanisms in the visible spectrum for high-purity fused silica.

The SM longpass (LP) filter, PMT window and sensitive electronics have also been modeled in simulation for radiation-load studies. The results are given in Tab. 33. Candidate 400 nm LP filters, made of Corning 7980 UV grade HPFS, were radiation damage tested to 7 Mrad/5x5 mm^2 peak dose with no mea-

Lifetime peak dose/pixel [Grad/5x5 mm^2]				
Quartz layer	First	Second	Third	Last
Open	0.7	1.3	1.1	0.7
Transition	0.4	0.65	0.55	0.3
Closed	0.25	0.4	0.3	0.15

Table 32: *Lifetime peak dose density in Shower-max quartz layers for each semi-septant module.*

surable loss in filter performance; this dose level is 3 - 5 times higher than anticipated. The PMT window is fused silica and is also expected to maintain transparency under the anticipated radiation loads. The PMT amplifier electronics are modeled using 0.5mm thick planes of silicon located in two different regions of the PMT can. The simulated, position-dependent doses are tallied in 5x5 mm^2 bins (referred to as pixels) across the plane of the material. We note that we are predicting lifetime radiation levels for SM PMT electronics that are approaching a questionable threshold for commercial-grade ICCs. Also, SM PMTs have no dedicated, local shielding by design. They rely on being located in the shadow of the main detector PMT region. For the Open semi-septant, we plan to have replacement PMTs, PMT electronics, filters, and 7 replacement SM modules on hand as needed.

	PMT component lifetime mean dose/pixel [kRad/5x5 mm^2]			
semi-septant	LP filter	window	Si chips region1	Si chips region2
Open	3300	1200	75	70
Transition	2200	890	71	62
Closed	1400	550	53	47

Table 33: *Predicted lifetime mean dose density in Shower-max PMT components for each semi-septant module. Si chips region1 and 2 represent integrated circuit chips that are part of the integrating- and event-mode amplifiers which are all housed in the PMT can.*

9.1.7 Prototyping

The first round of Shower-max prototyping took place in 2018 with MOLLER pre-R&D funding. Two prototypes with different stack configurations were constructed and tested at the SLAC End Station A Test Beam (ESTB) facility; the test-beam run was designated T-577. Three different electron beam energies were used: 3, 5.5, and 8 GeV. The rate of single test-beam electrons was extremely low ($\lesssim$ 1 Hz average). Combining several runs, the PE yield results for 5.5 GeV electrons are given in Fig. 163 along with a photograph of the two prototypes. Both prototypes used 8 mm thick tungsten, and one used 10 mm thick quartz layers while the other used 6 mm thick layers. The latter matches the current design, the only difference being the smaller active area of 246 mm by 105 mm compared with 265 mm by 160 mm. We note that the PE yield from the SLAC test beam data is $\sim$ 3 times lower than anticipated, however, it is still quite high and more than sufficient for MOLLER. The low yield is thought to result from TIR losses in the quartz due to using black polyimide Kapton film wrapping. This will be tested in follow-up beam tests and the wrapping will be replaced with aluminized mylar.

The second Shower-max test beam takes place at the Mainzer Microtron (MAMI) at the University of Mainz, Germany. The MAMI test beam is an 855 MeV CW electron beam capable of delivering high and tuneable rates of single electrons. The new prototype to be tested is shown in Fig. 164. Different stack assembly techniques using various wrappings and spacers will be tested, as well as the effect of using different long-pass filters. Given the low energy of the test beam, our simulated PE yields are relatively

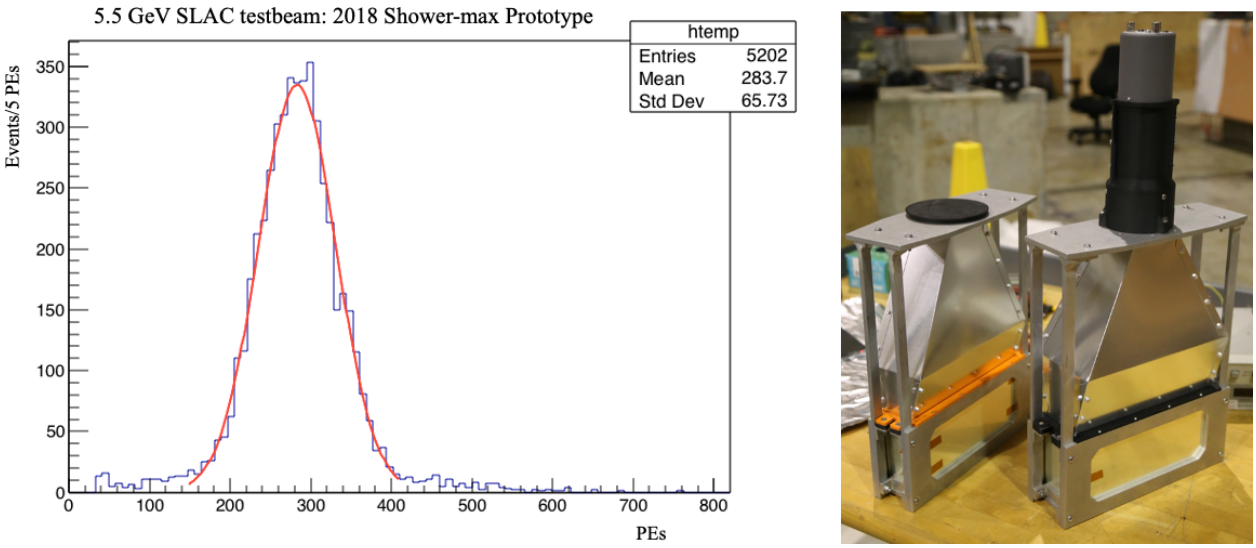

Figure 163: *2018 SLAC test-beam results and prototypes. The red curve is a Gaussian fit to the data and has a 17% relative width. The shoulder events above and below the peak are from misidentified 0-electron and 2-electron events.*

low ($\sim$ 100 PE mean) with larger relative widths ($\sim$ 40%), however, these are sufficient to benchmark the performance of the prototype, as well as to calibrate the optical simulation parameters and output.

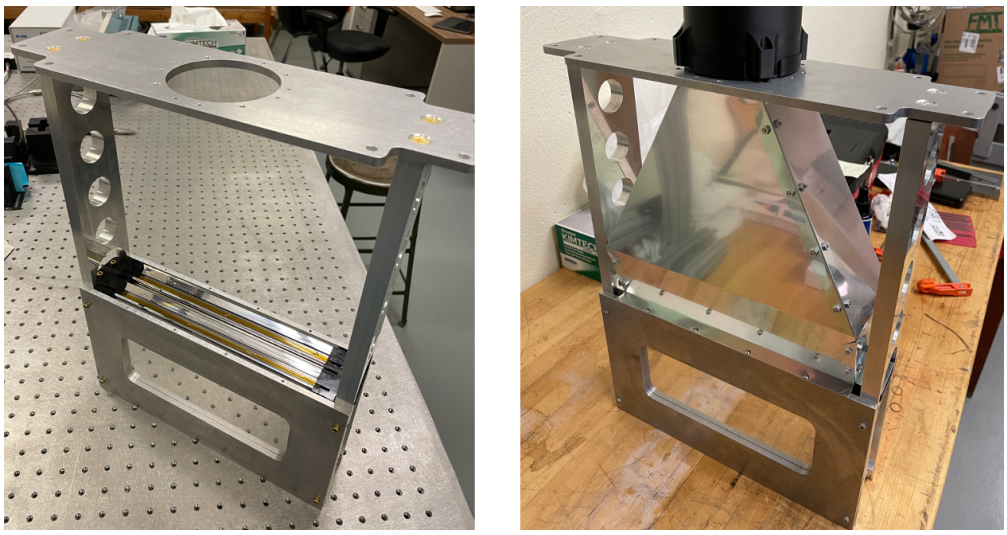

Figure 164: *Shower-max prototype constructed for MAMI test beam.*

9.2 Pion Detectors

9.2.1 Overview

GEANT4 simulations, using the Wiser parameterization for pion production [73], indicate that a flux of π^- per Møller scattered electron of $\pi^-/e^- \approx 10^{-3}$ will be incident on the main detectors. Any background asymmetry caused by these π's (and their subsequent decay-in-flight μ^-) must be measured and corrected

for. Various model estimates suggest that this asymmetry could be large (of order 500 ppb). We desire to measure the pion asymmetry to a 100 ppb statistical precision in about 50 days of data-taking, assuming that the pion fraction is 10^{-3} of the Møller electron flux.

The pion detector system consists of 28 identical acrylic Cerenkov detectors, located downstream of the Shower-max detectors and encased in a Pb absorber "donut". The pion detector system requires the ability to suppress the Møller electrons by a factor of $> 10^3$ while retaining a significant fraction of the incident pions, so as to have the pion detectors measure the asymmetry of a roughly equal mixture of pions and Møller electrons assuming the predicted initial π^-/e^- ratio. This is accomplished using a Pb absorber "donut" such that the total Shower-max detectors and the Pb absorber corresponds to a total $45X_0$ in thickness.

9.2.2 Pion Detector Angular and Radial Coverage

There may be significant azimuthal variation in the measured pion asymmetries, due to the combination of any residual transverse beam polarization and the possibly large single-spin asymmetries in pion production [74]. Therefore we must instrument the entire azimuth for the pion asymmetry measurement. Only pions incident on the Møller ring need to be measured, so the radial coverage of the pion detectors only needs to assure a fair sample of those pions. It is useful to subdivide the pion detectors in azimuth so as to look for pion asymmetry variation with kinematics, so we segment by 28 in ϕ , in order to have pion detectors measuring separately the "open", "closed" and "transition" regions of the Ring 5 acceptance for each semi-septant. In contrast, no significant azimuthal variation is expected in the pion flux, so we only need to measure the pion background fraction (in counting mode) in one semi-septant of each type (open, closed, and transition).

9.2.3 Pion Detector Cherenkov material

The incident charged particle flux of 50 MHz expected on the pion detectors is $\sim 10^{-3}$ of that incident on the Ring 5 integrating detectors (after the electrons are ranged-out by the Shower Max detector and the Pb absorber), thus the pion detectors do not have the same stringent requirements for radiation hardness as do the integrating detectors of the Shower-max detectors. The ability to tolerate a dose of 0.2 MRad without significant degradation of the detector response is required. Experience using UVT acrylic for similar detectors during the first parity-violating electron scattering experiment at JLab, HAPPEX-I [75], as well as HAPPEX-III [76] was positive. The design material chosen is Eljen UVT acrylic (BC-800) or equivalent. This material has been shown to lose less than 50% of its optical transmission after a radiation dose of 5 MRad, 25 times the anticipated total dose.

Each detector is rectangular in shape, with an active volume of 210 mm (azimuthal) $\times$ 25.4 mm (radial) $\times$ 70 mm (thickness along z), with the inner edge located at a radius of 1168 mm. Each detector is read out optically by a 1" PMT, epoxied directly to the center of the downstream edge of the acrylic. The Pb absorber is an annulus of inner radius 1050 mm and outer radius 1260 mm and 400 mm in depth. Each pion detector is located in an individual light-tight enclosure, which is recessed in a cavity in the downstream face of the absorber donut. The upstream face of the detector follows 200 mm of Pb absorber (35.5 X_0), along with the Shower-max detectors (9.5 X_0), provides a total radiation length of 45 X_0 of absorbing material, sufficient to largely range out the Møller electrons.

9.2.4 Pion Detector shielding and optical design

The design of the Pb absorber donut was driven by extensive GEANT 4 simulations studying the photoelectron background generated in the pion detectors by the Møller electrons. Showers generated by the Møller electrons in the Shower-max detectors can generate e^-, e^+ and γ's which can cross sectors to interact with

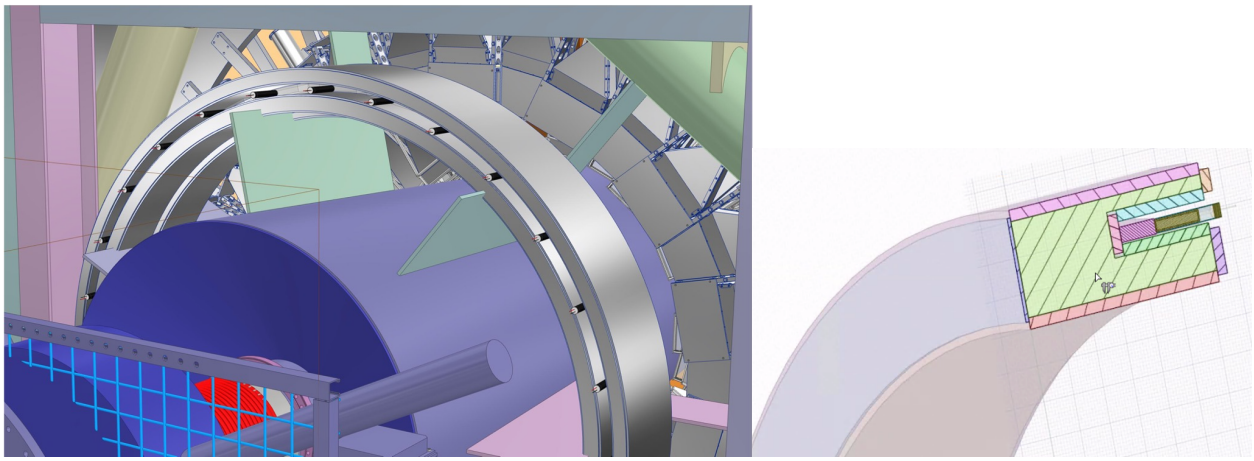

(a) *Pion Detector System and Pb Donut.* (b) *Section view of Pb donut.*

Figure 165: *a) Pion Detector system mounted inside Pb pion donut (grey cylindrical sections), view from downstream. Several of the pion detector PMTs are visible. The (green) fins support the downstream beam pipe (purple) from the Pb donut. b): Section view of Pb donut, and installed pion detector (view from upstream). Pb (light green) encased in aluminum shell, acrylic detector medium (violet), and PMT (dark green).*

detectors near 180° away in azimuth, hence the need to shield the pion detectors on their inner-radius sides and downstream of their front faces. Secondary and tertiary shower remnants can scatter into the detectors from larger radii, hence the need also for shielding at their outer-radius sides. The thickness of the detectors in the radial direction (2.54 cm) was chosen to balance between maximizing the fraction of the optical signal arising from the through-going pions and their decay muons while maintaining an adequate total flux of pions. This lead to our design with the pion detectors enclosed within a cavity in the Pb absorber donut (only the downstream face is unshielded), see Fig. 165. The remaining background arising from Møller electrons is dominated by conversion in the acrylic of the copious flux of low-energy (< 2 MeV) γ's that emerge from the shielding. These γs each produce an average of only 2.3 photoelectrons, but in total they account for 70% of the photoelectrons in Møller-generated events (low-energy electrons/positrons and neutrons account for most of the remainder). In contrast, the average simulated signal size from a pion (or decay muon) is 425 photoelectrons. The predicted signal/background of (photoelectrons from pions)/(photoelectrons from Møller electrons) in the pion detector is 107% with this geometry.

The detected flux of pions (and decay muons) is 0.75 MHz/detector at 65 μA beam current, for a total of 20 MHz detected pions in the 28-detector ring. The total ionizing dose is twice this, including the Møller electron generated events, yielding a total integrated dose of 75 kRad for the entire data-taking. We require a detector resolution of better than 25%, so as not to significantly degrade the statistical width of the asymmetry measurement. With the expected photoelectron signal from pions this resolution should be readily achievable.

GEANT-4 simulations indicate that the designed pion detector system will measure an essentially unbiased sample (*i.e.* the same kinematic distributions) as those pions detected in Ring 5 and the Shower-max detectors, see Fig. 143.

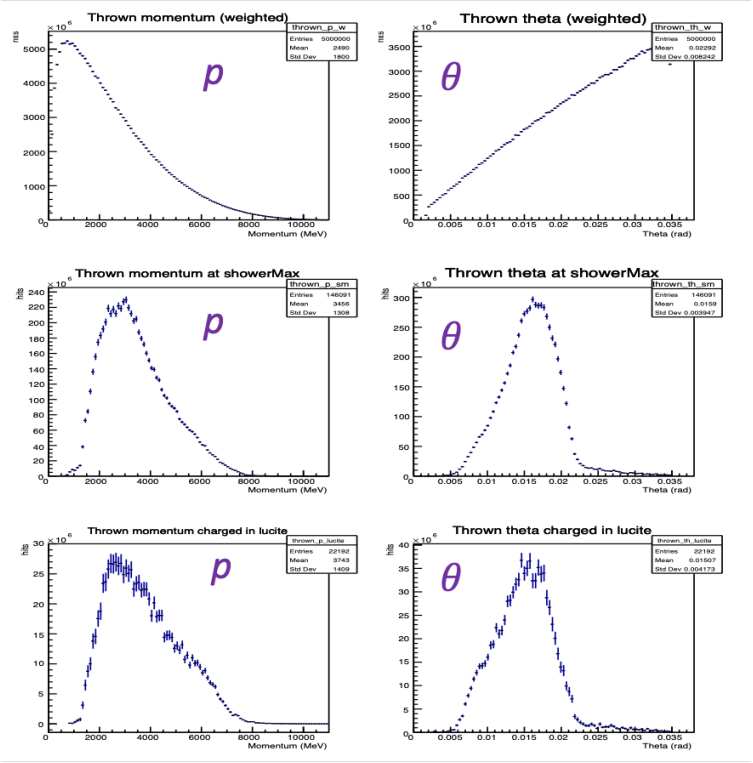

Figure 166: *Pion kinematics (left: scattered momentum, right: scattering angle) for generated pions (top), pions seen in Ring 5 and the Shower-max (middle), and pions seen in the pion detectors (bottom).*

9.2.5 Pion Dilution measurement

In order to correct the measured Ring 5 (and Shower-max) asymmetry for the background from pions, the flux of pions (and their decay muons) incident on these detectors must be measured. This will be done during low beam-current "counting mode" data-taking, largely done in parallel with counting mode data-taking with the Tracking system (see Sect. 8).

Pions seen in Ring 5 will be identified by their large pulse-height in a pion detector and their small signal in the corresponding Shower-max detector (in contrast to the much larger signal from Møller electrons, see Tab. 31). A valid track in the GEM tracking system which projects to the Ring 5 detector and Shower-max detector that fired, as well as hits in the tracking system trigger scintillators will also be required in software. Møller electrons in Ring 5, in contrast, will be identified by a large signal in the Shower-max, and at most a few photoelectron signal in the pion detector, again, associated with a valid track and trigger in the tracking system pointing to the appropriate Ring 5 and Shower-max detector. In one semi-septant of each type (open, closed and transition), a plastic scintillator located just downstream of the pion detector will provide an additional input to the pion identification, as 83% of the pions and muons seen in the pion detector will pass through the acrylic to reach the scintillator, but only a modest fraction of low-energy background from Møller electron showers in the Pb donut will do so.

Additional counting-mode data-taking with an enhanced pion fraction will be done using one of the movable diagnostic collimators, the "blocker" collimator (see Sect. 5.2.1). This collimator will cover the entire acceptance for events scattered from the target with a 20 X_0 thickness of 90/10 W/Cu, which will suppress the Møller and ep electron signal by a factor of 5×10^{-5}, while reducing the pion flux at the pion detector by only a factor of 0.55. This will provide additional information to verify our pion identification algorithm.

The pion detector PMTs will use switchable-gain bases, as designed for the main integrating detectors, to allow pulse-height measurements in counting mode data taking at low beam currents for these pion dilution studies.

9.3 Scattered Beam Monitors

A set of detectors, referred to as scattered beam monitors (SBM) will be installed at various locations to monitor potential false asymmetries in irreducible background that results from the primary scattered beam interacting in downstream collimators, beampipes, and shielding. Small and large angle scattered beam monitors (SAM and LAM) - also referred to as luminosity monitors - will be located in regions where the scattered rate is estimated to be comparable to or larger than the main Møller rate, but the physics asymmetry is expected to be smaller. These detectors will consist of quartz Cherenkov radiators and air-core aluminum light guides to transport the light to photomultiplier tubes. Diffuse scattered beam monitors (DBM) will be deployed in locations where the expected scattering rate from primary target interactions is small, so the majority of the signal would come from secondary interactions. These detectors will include detectors with photomultiplier tubes coupled directly to quartz Cherenkov radiators and detectors with bare photomultiplier tubes. Detectors of this type proved very useful in the Q_{weak} experiment [12] to correct for an observed beamline background asymmetry, which was a false asymmetry caused by secondary events scattered from the beamline and the tungsten beam collimator.

9.3.1 Large Angle Monitors

The large angle monitor (LAM) detectors are located at a distance of ∼23.6 meters downstream of the hydrogen target, just upstream of the GEM rotator. They are integrated with the lead collar 2 assembly, which is housed in the barite/concrete wall located downstream of the drift pipe exit window. A 2D scattered flux plot of the electrons at the LAM plane and a radial rate plot are shown in Fig. 167. The lead collar 2 assembly was designed to shield the region downstream of the drift pipe exit window from scattered flux at larger radii than flux that is intercepted by the main detector array. This flux would otherwise make background in the air between the drift pipe exit-window and the main detector. There is substantial flux at that location with a large rate but small expected physics asymmetry.

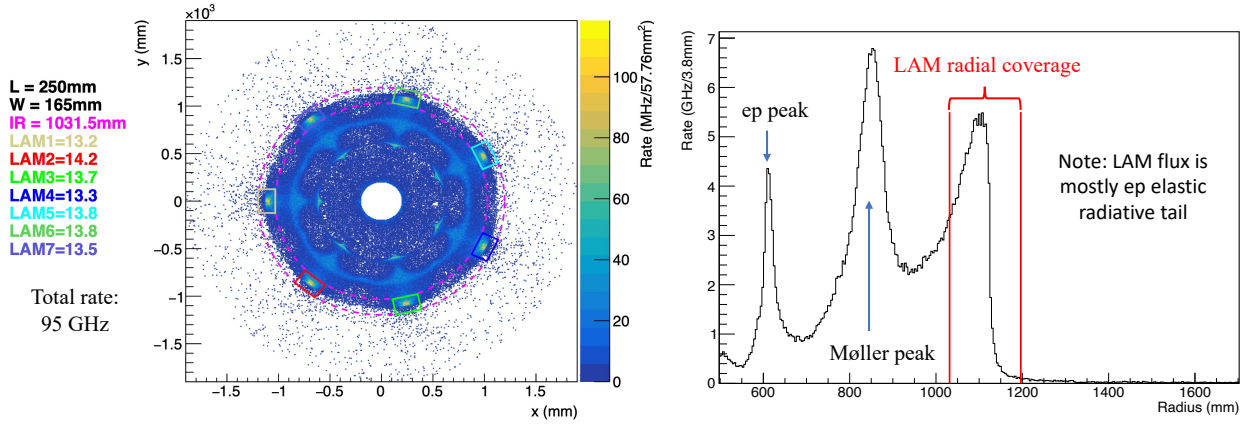

Figure 167: *The left figure shows the 2D rate-weighted distribution of electrons at the LAM plane. The rectangles show the location of the LAM quartz radiators. The right figure shows the radial rate profile (integrated over the full azimuth at the LAM plane) and the region of LAM coverage.*

The LAM detectors consist of seven modules designed as shown in Fig. 168. Each module consists of a 25 x 16.5 x 1 cm^3 fused silica radiator housed in a 3D-printed plastic exoskeleton. The detectors are installed such that the 45° bevels are at the outermost radius. For normally-incident charged particles the Cherenkov light will be mostly contained and primarily exit the quartz when encountering the bevels. The two bevels are each next to the photocathode of a 3" Electron Tubes 9305 QKB photomultiplier tube, which is the same PMT choice as the main and Shower-max detectors. The LAM detectors are mounted as shown in Fig. 169. They will mount on the downstream side of the outer lead collar ring in the middle of the seven "open" sectors. The fused-silica radiator is positioned upstream of the inner lead collar ring, where they intercept the scattered flux that is shielded from the main detectors by the collar. The photomultiplier tubes extend downstream at a larger radius than the inner lead collar ring. They are designed to be removable for servicing without the need to remove the fused silica and its housing.

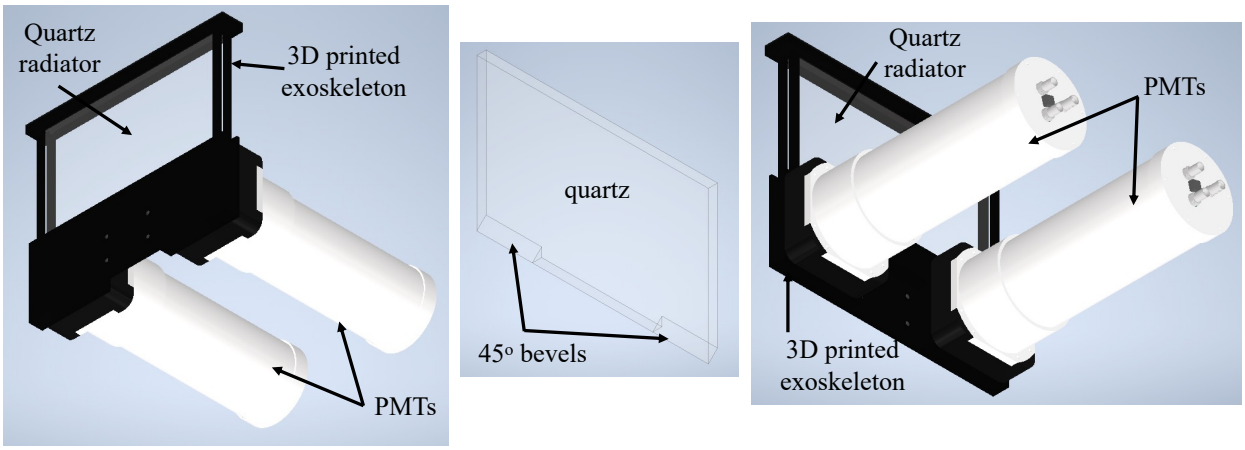

Figure 168: *Design views of the large angle monitor (LAM) modules and fused silica radiator.*

The simulated rate in each LAM detector is $\sim$ 13.6 GHz. The total rate summed over all seven LAM detectors is 95 GHz. The contributions to that rate, and the asymmetry from each contribution are: radiative tail of Møller scattering (19 GHz and 10 ppb), radiative tail of e-p scattering (76 GHz and 4 ppb), and inelastic e-p scattering (0.2 GHz and 332 ppb). The resulting total asymmetry of 6 ppb is smaller than the Møller physics asymmetry in Ring 5 of 32 ppb. To estimate the expected statistical error per window-pair, electromagnetic showering of the incident flux in structures upstream of the LAM detectors must be properly accounted for. The geometry and position of these structures relative to the LAM detectors are shown in Fig. 170. All of the primary flux from the target incident on the LAM passes through the 6.35 cm thick aluminum flange that mounts the downstream window. Some of the primary electrons shower in this aluminum resulting in more than one $>$ 1 MeV charged particle incident on the LAM quartz for that event. The collar 2 outer ring is a lead ring 15 cm (27 X_0) thick that covers about half of the LAM quartz radially. The primary flux that passes through this ring showers also, with higher multiplicity than the events passing through the aluminum flange. Simulation shows that the relative rates are: 50% from target (with multiplicity 1), 25% of the rate from the aluminum flange (with multiplicity 1.3), and 25% of the rate from the collar 2 outer ring (with multiplicity 3.0). Thus, taking account of the correlations in EM shower events, the effective primary rate is 70 GHz. When Cherenkov photon transport and detection is implemented in the simulation, the resulting photoelectron spectrum (summed over both photomultiplier tubes) is shown in Fig. 171. The mean photoelectron yield per event summed over both photomultiplier tubes is 59. The PE distribution has a large width due to the events that shower in the lead collar. Combining

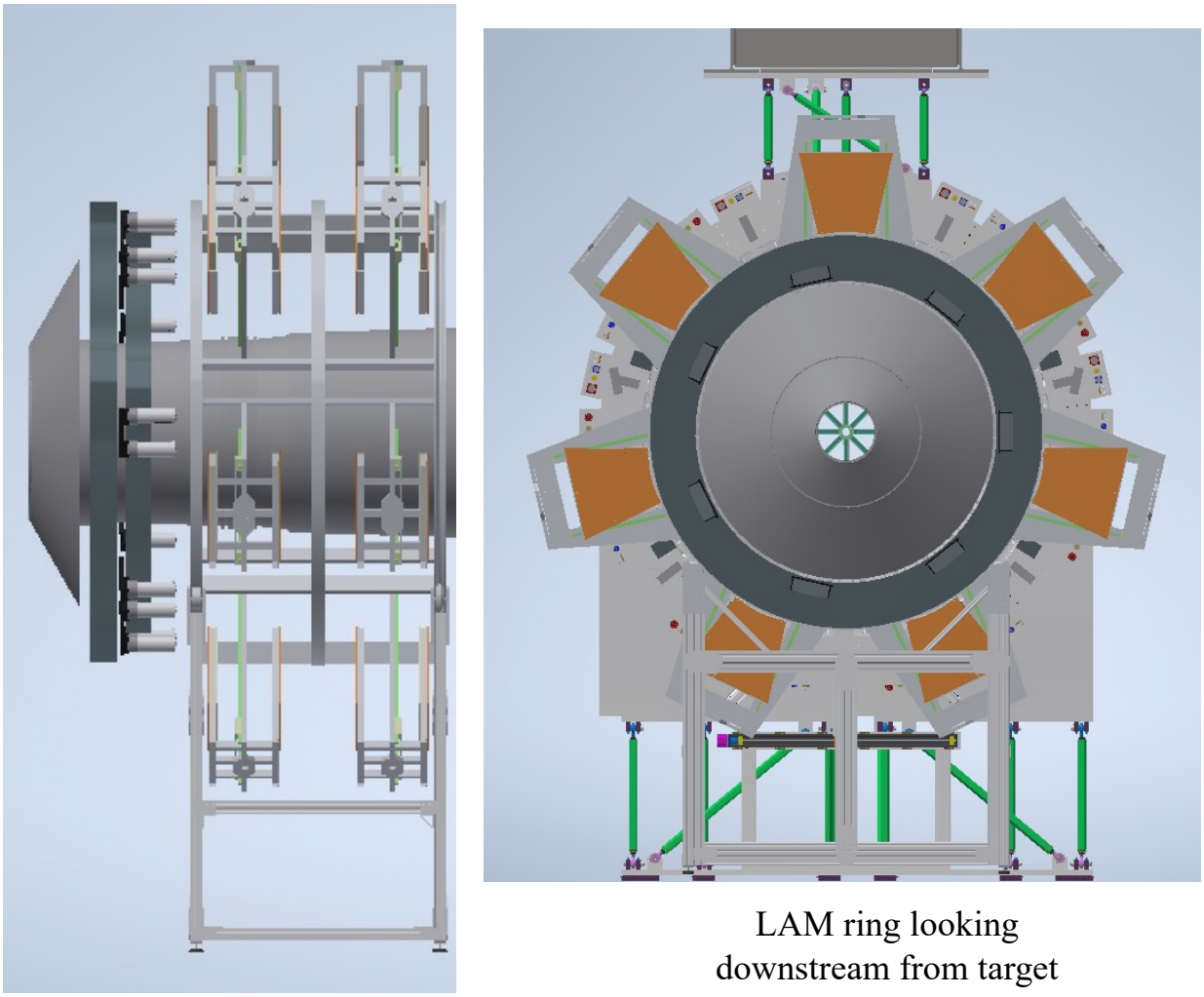

Figure 169: *Installed location of the large angle monitor (LAM) detectors. The left image shows the detectors mounted on the outer lead collar ring. The barite/concrete wall that houses the lead rings is not shown. The right image shows the view looking downstream from the target, with the fused silica radiators visible upstream of the inner lead collar ring, but the photomultiplier tubes being shielded by the outer lead collar ring.*

these considerations, the predicted statistical width per window-pair is 176 ppm, as compared to the 91 ppm of the Ring 5 main detectors.

The estimated integration-mode PMT currents will be about a factor of two larger than those of the Ring 5 main detector PMTs. For a given PMT, the rate will be 10 GHz with an average of 29 photoelectrons/event. This will result in a cathode current of $\sim$ 46 nA. With a PMT gain of $\sim$ 539 the anode current will be 25 μA, which will result in a 2.5 V output from an I-V pre-amplifier with gain setting 0.1 MΩ.

9.3.2 Small Angle Monitors

The small angle monitor (SAM) detectors are located at a distance of $\sim$ 30.7 meters downstream of the hydrogen target, just upstream of the beam dump. There are eight SAMs spaced uniformly around the

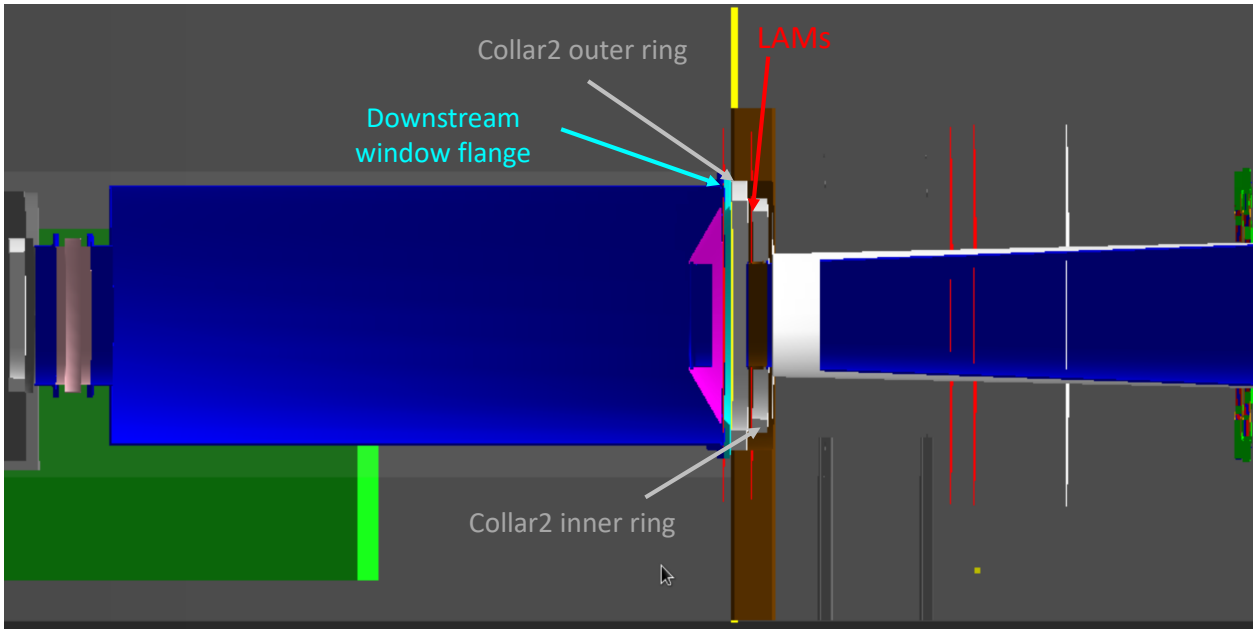

Figure 170: *The figure shows a GEANT-4 geometry image that shows the relation between the location of the downstream window aluminum flange and the outer lead collar to the LAM detectors.*

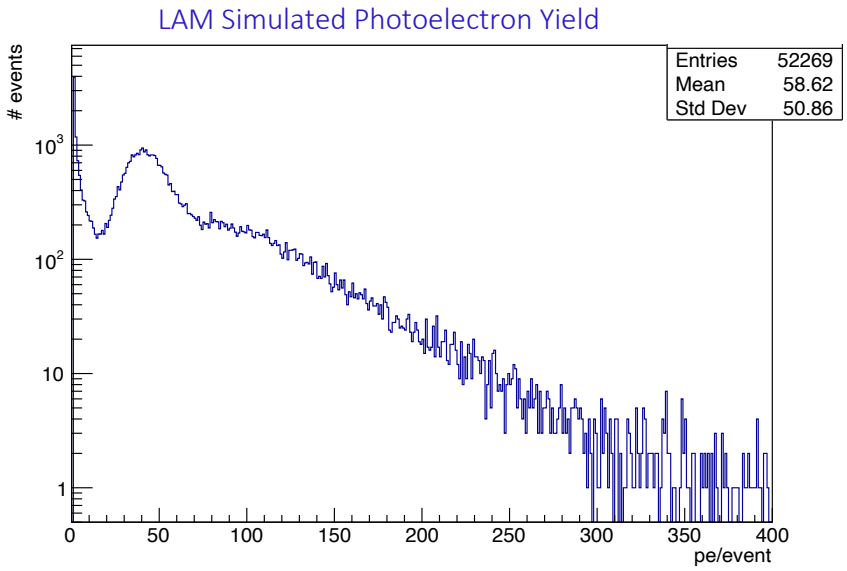

Figure 171: *Simulated large angle monitor photoelectron yield summed over both photomultiplier tubes attached to a LAM module.*

azimuth. The active element for each is a small fused-silica radiator located at a small scattering angle of $\sim$ 2 mrad. Both a 2D scattered flux plot of the electrons at the SAM plane and a radial rate plot are shown in Fig. 172. Each SAM detector has an extremely high rate, $\sim$ 475 GHz per detector. They will have smaller statistical width than the primary Møller flux in Ring 5, so they can serve as a sensitive diagnostic of target density fluctuations, beam fluctuations, and electronic noise. Because of the small scattering angle, they are

estimated to have a small physics asymmetry of $\sim$ 3 ppb, an order of magnitude smaller than the Møller parity-violating asymmetry. Thus they can serve as a "null asymmetry monitor."

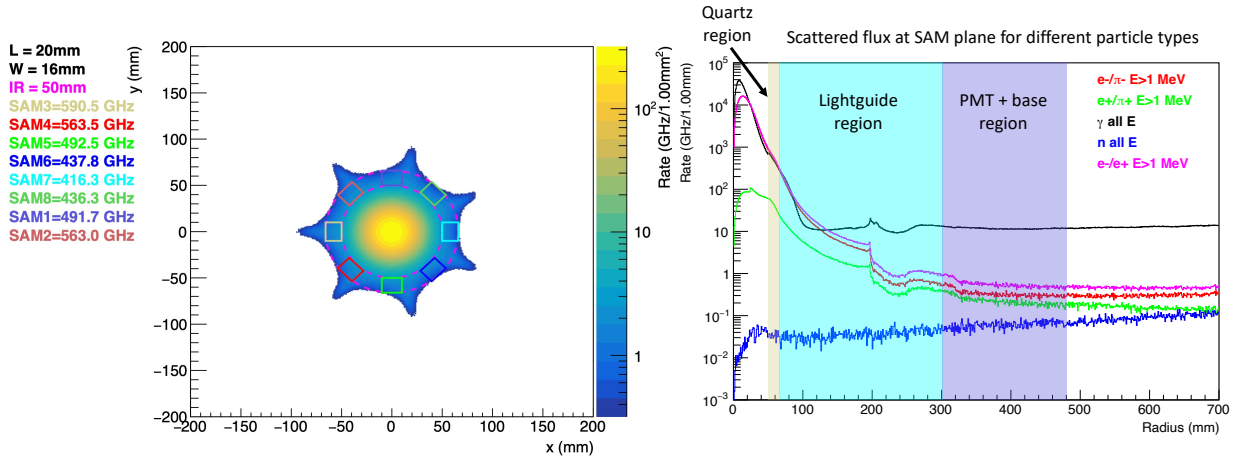

Figure 172: *The left figure shows the 2D rate-weighted distribution of electrons at the SAM plane. The rectangles show the location of the SAM fused-silica radiators. The right figure shows the radial rate profile (integrated over the full azimuth at the SAM plane), the region of the SAM quartz coverage, and the regions where the air light guide and PMTs are located.*

The SAM detectors consist of eight modules designed as shown in Fig. 173. Each module consists of a small fused silica block (1.0 x 2.0 x 0.6 cm^3) with a 45° bevel to allow the Cherenkov light to escape and transmit through a 26 cm long air light guide. The photomultiplier tube will be a 2 inch Hamamatsu R375 tube. The SAM detectors are mounted as shown in Fig. 174. The beam pipe where they are installed will be manufactured with eight ports. Mounted to each port flange will be a flange with an aluminum insertion tube with 0.065" wall thickness, except at the smallest radius where there is a hemispherical dome with a thinned-down wall thickness of 0.012". The SAM detector module itself mounts within this aluminum insertion tube.

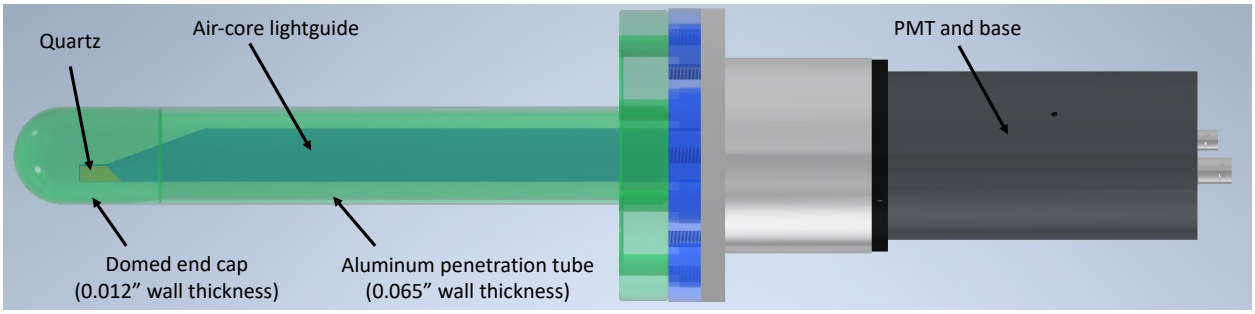

Figure 173: *Design view of the small angle monitor (SAM) modules.*

The simulated photoelectron yield for the simulated scattered flux incident on the quartz blocks is shown in Fig. 175. The mean is about 7.9 photoelectrons per event with an expected rate of $\sim$ 475 GHz per detector. This results in a photocathode current of $\sim$ 600 nA. For such a large photocathode current, we will use a unity-gain base, with all the dynodes tied together. This configuration worked well with the chosen model

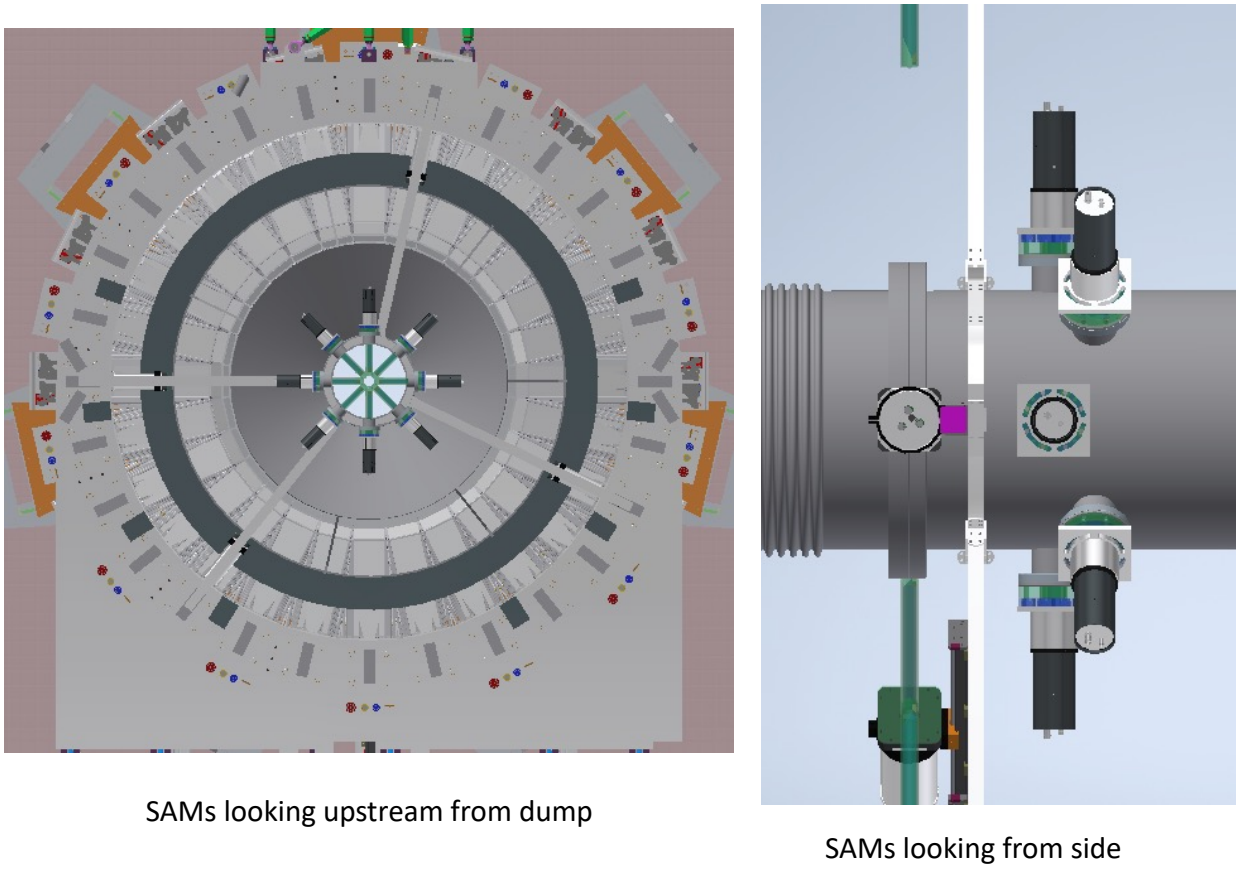

Figure 174: *Installed location of the small angle monitor detectors. The left image shows the view of the detectors and their insertion tubes from the beam dump. The right figure shows the SAM beampipe with its eight ports where the SAM insertion tube flanges will mount.*

of photomultiplier tube during both Q_{weak} and CREX. Using an I-V preamplifier with a gain setting of 2.0 MΩ would result in an output voltage of 1.2 V.

A technical risk with the SAM detectors is the high radiation dose that will be received by the fused silica blocks over the course of the production run. For the full 8256 hours of production running time at 65 μA, the estimated dose per fused silica block is $\sim$ 170 Grad. The similar size and material (Heraeus Spectrosil 2000) used during the Q_{weak}experiment showed no evidence of radiation damage up to $\sim$ 35 Grad. There is no reason to believe that there will be any degradation as one goes beyond 35 Grad. However, periodic replacements can manage most of this risk, if needed. The production running will be broken up roughly into 3 calendar years, between which SAM fused-silica replacements could be done. This would limit the dose in each period to $\sim$ 57 Grad. It should also be noted that there is an additional safety factor, because the SAM PE yield could drop from $\sim$ 8 PE per event down to 1 PE per event, and the detector would still satisfy the requirements, because the statistical width per detector would still be less than the main detector Ring 5.

9.3.3 Diffuse Beam Monitors

Diffuse scattered beam monitors (DBM) will be deployed in locations where the expected scattering rate from primary target interactions is small, so the majority of the signal would come from secondary interac-

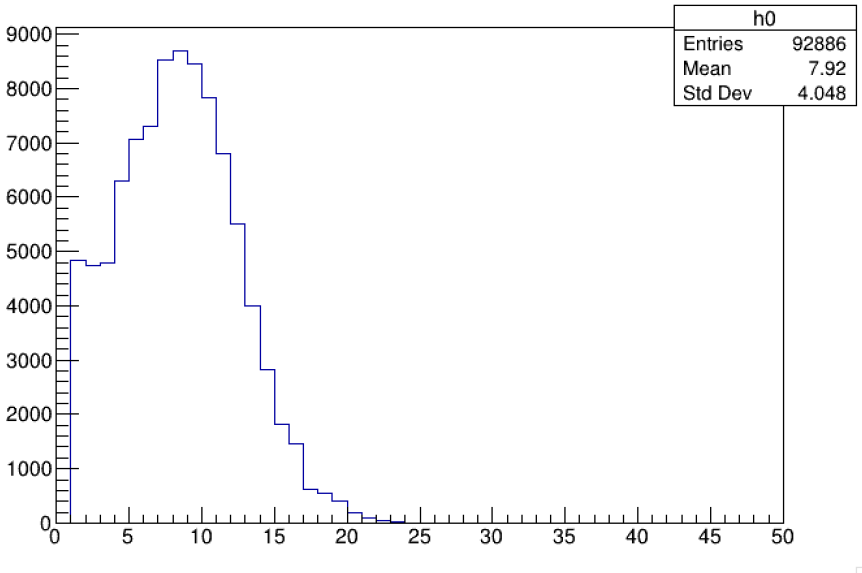

Figure 175: *Simulated small angle monitor photoelectron yield.*

tions. The DBM detectors consist of fourteen modules designed as shown in Fig. 176. Each module will consist of a bare 3" Electron Tubes 9305 QKB photomultiplier tube and this same type of PMT bonded to a 10 x 7.1 x 1.0 cm^3 fused silica block with SES406 (Shin-Etsu) optical glue, which was used successfully for the main detectors in the $Q_{\rm weak}$ experiment. The monitors will be located just upstream of the main detector array at a radial location that is in the shadow of lead collar 2. They will be placed azimuthally in the middle of both open and closed sectors. The simulated radial rate profile at that location is shown in Fig. 177. The fused silica blocks will be located at a radius that is upstream of the radial location of the main detector photomultiplier tubes, which are protected by a lead shielding ring. The simulated rate in each fused silica DBM detector is $\sim$ 36 MHz, dominated by secondary interactions. The estimated photoelectron yield from the fused silica block is $\sim$ 86 pe. This corresponds to a photocathode current of $\sim$ 0.5 nA. At a PMT gain of $\sim$ 5000, a 2.5 μA anode current will result. With an I-V preamplifier gain of $\sim$ 1.0 MΩ, a 2.0 V signal will be obtained.

9.4 Scanner Detectors

Small movable detectors that can operate at both the full beam current and at the low beam currents needed for the tracking measurements will be used at two locations in the experiment. Such scanners have been used for E158 [77], HAPPEX-II, and $Q_{\rm weak}$ [32].

9.4.1 Upstream Scanner

The upstream scanner is located between the GEM detector array and the main detector array, as shown in Fig. 149. Its design is shown in Fig. 178. It consists of two small overlapping fused-silica radiators (1 cm^3), coupled to 80 cm long, 51 mm diameter air light guides read out by 3" Electron Tubes 9305 QKB photomultiplier tubes. To eliminate the background from events creating Cherenkov and scintillation light in the air of the air light guide, the tube containing them will be evacuated to rough-pump vacuum level during the brief periods when the scanner is operational. They will be instrumented to be read out either in event mode or in integrating mode. They are mounted to an xy motion stage that allows coverage of one sector in

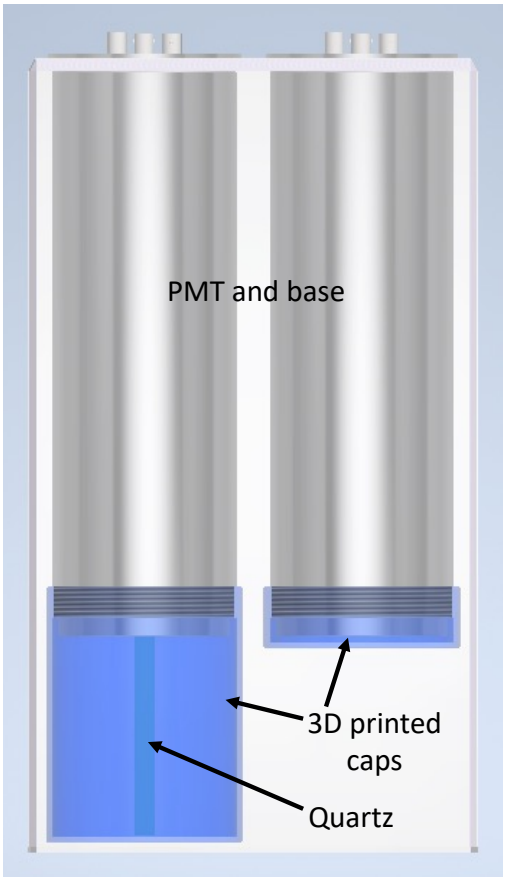

Figure 176: *Design view of the diffuse beam monitor (DBM) modules.*

less than one hour. The 2D linear motion system consists of two stainless steel ball-screw driven tables (a likely choice is the Velmex BiSlide positioning stages with 50" travel in one dimension and 30" in the other) to cover an active scan area of 120 cm x 60 cm. Two linear-displacement draw-wire potentiometer position sensors measure instantaneous detector positions (a likely choice is sensors from the A-Tech Instruments Limited Series). The scattered flux profile at the plane of the upstream scanner is shown in Fig. 179. The figure shows both the expected normal scan coverage and the possible full range of motion.

The upstream scanners have two purposes. Since they can operate both at low and high beam current, they can be used to confirm that the rate distribution measured at low beam current by the Tracking system is not significantly different than that seen at full luminosity. They can also allow periodic monitoring of the scattered flux distribution during production data-taking, to ensure stability of the effective kinematics and to monitor any changes in backgrounds. A design requirement is that the system be able to monitor for shifts of $\sim$ 0.5 mm in the profile, since this type of shift can occur from a drift of 10^{-3} in the B*dl of the spectrometer field.

The peak rate expected from the upstream scanner over the nominal scan area is $\sim$ 2.6 MHz/μA. In integration mode during production running, the highest rate will be $\sim$ 170 MHz. The simulated photoelectron distribution is shown in Fig. 180, with an average of 4.8 pe/event. The estimated photocathode current is 0.13 nA. With a PMT gain $\sim$ 15,000, a 2.0 μA anode current results. With a 1.0 MΩ gain I-V preamplifier, this results in a 2.0 V output signal. In counting mode at 10 nA, the highest rate is 26 kHz, which is manageable with conventional counting mode electronics.

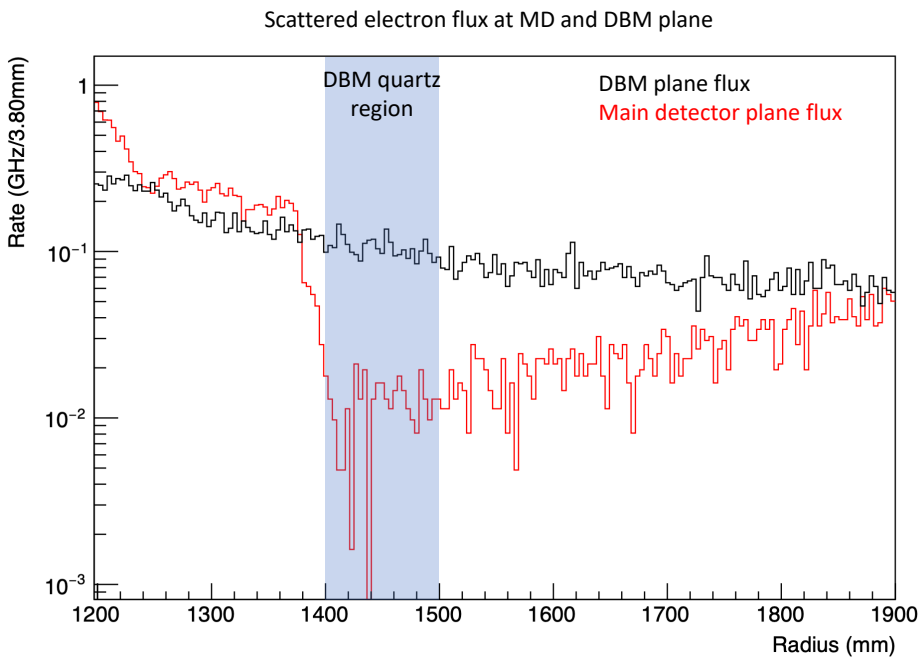

Figure 177: *The simulated radial rate distribution is shown both at the DBM plane and at a plane located within the main detector array. The drop in the main detector flux is due to lead shielding in the PMT region of the main detector array. That same flux will be detected by the fused silica radiator of the DBM before that shielding.*

The motors that drive the motion stages will have a significant amount of ferromagnetic material in them. Careful attention is being paid to all materials in the experiment that potentially have magnetically permeable material in them. A careful study was done of the amount of rescattered flux from these motors in their parked location that would make it into the main detector array. The collaboration has established a goal that the potential background asymmetry from any contribution of this type is < 0.1 ppb. The amount that could be attributed to the smallest radius motor in its parked position is 20 times smaller than this.

9.4.2 Downstream Scanners

The downstream scanners are located between the pion detectors and SAM detectors, as shown in Fig. 149. The detector design is the same as that of the upstream scanner detectors, which the only difference being that the air light guide is 50 cm (rather than 80 cm) long. These detectors will only be read out in integrating mode. They consist of four linear scanners mounted in open sectors and configured to scan radially. Their purpose is to make a beam-based verification of the alignment of the primary acceptance defining Collimator 2 to a precision of 1 mm. Each scanner detector is mounted to a linear motion stage that moves the fused silica cube over a range of 25 – 70 cm from the beam centerline. The likely choice for the motion system are stainless steel ball-screw driven Velmex Xslide units with 24 inch travel. Linear-displacement draw-wire potentiometers sensors will measure the instantaneous detector positions (likely choice is sensors from A-Tech Instruments Limited Series).

The simulated radial scattered flux rate distribution at the upstream scanner plane for spectrometer magnets off and a 4 cm Carbon target are shown in Fig. 179. Under these special conditions, the outer edge of collimator 2 is very clearly indicated with a sharp drop in rate at a radial distance of ~ 65 cm from the

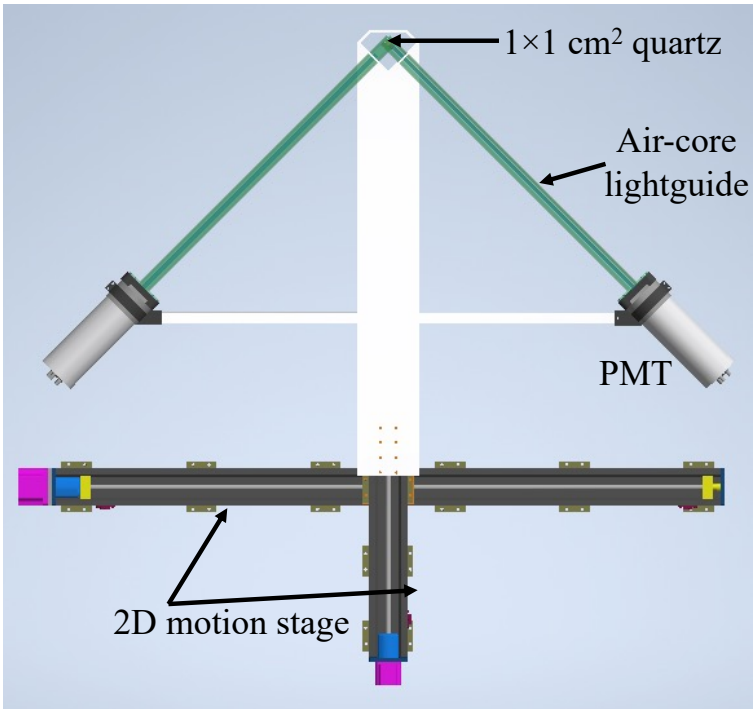

Figure 178: *Design view of the upstream scanner.*

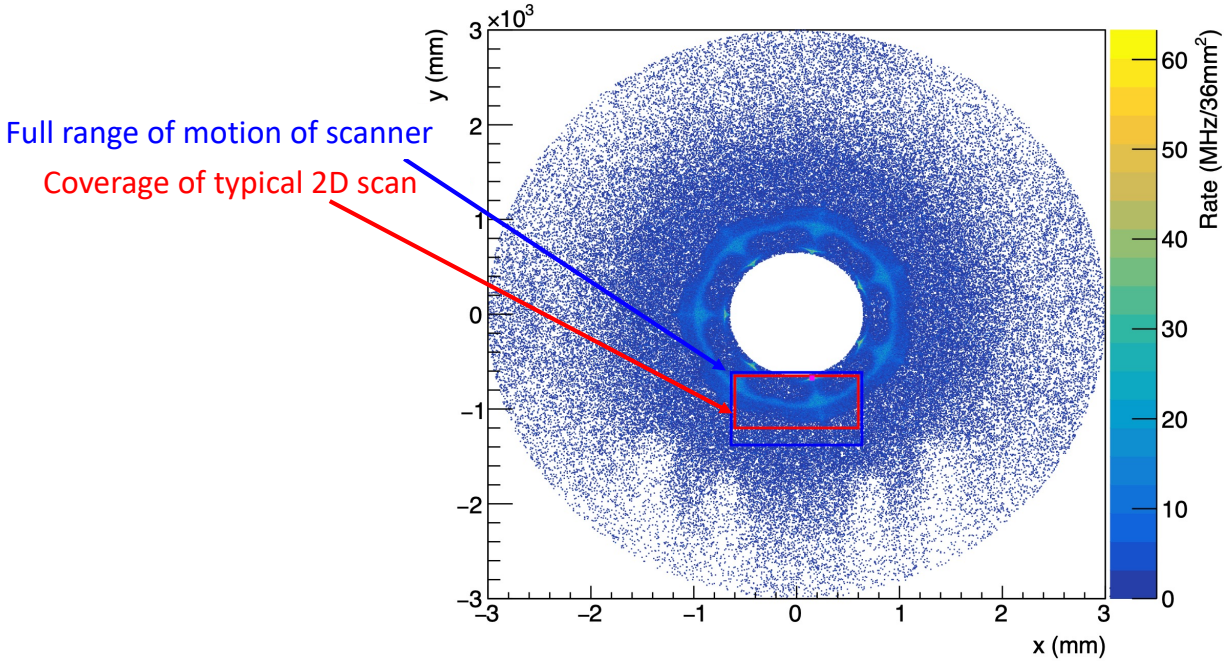

Figure 179: *The simulated 2D rate-weighted distribution of scattered electrons at the upstream scanner plane. The red box shows the range for the fused-silica radiator cube during a nominal scan. The blue box shows the full possible range of motion.*

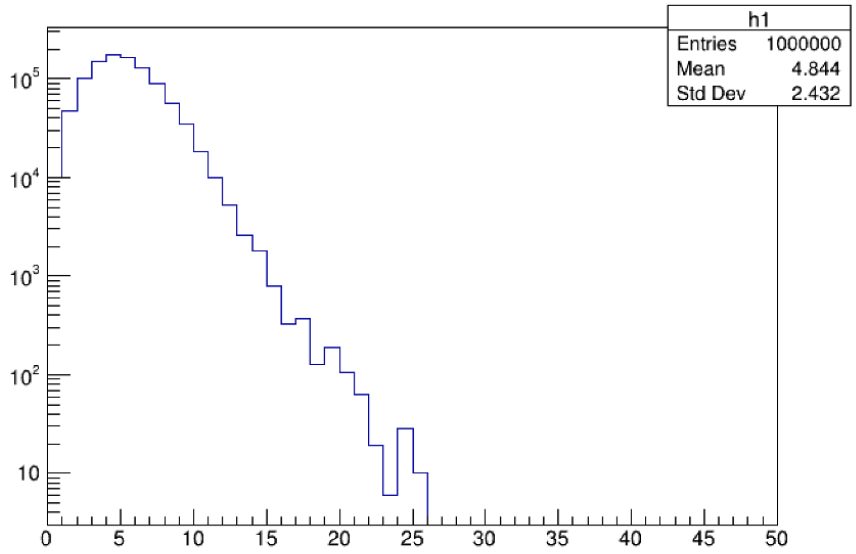

Figure 180: *Simulated upstream scanner detector photoelectron yield.*

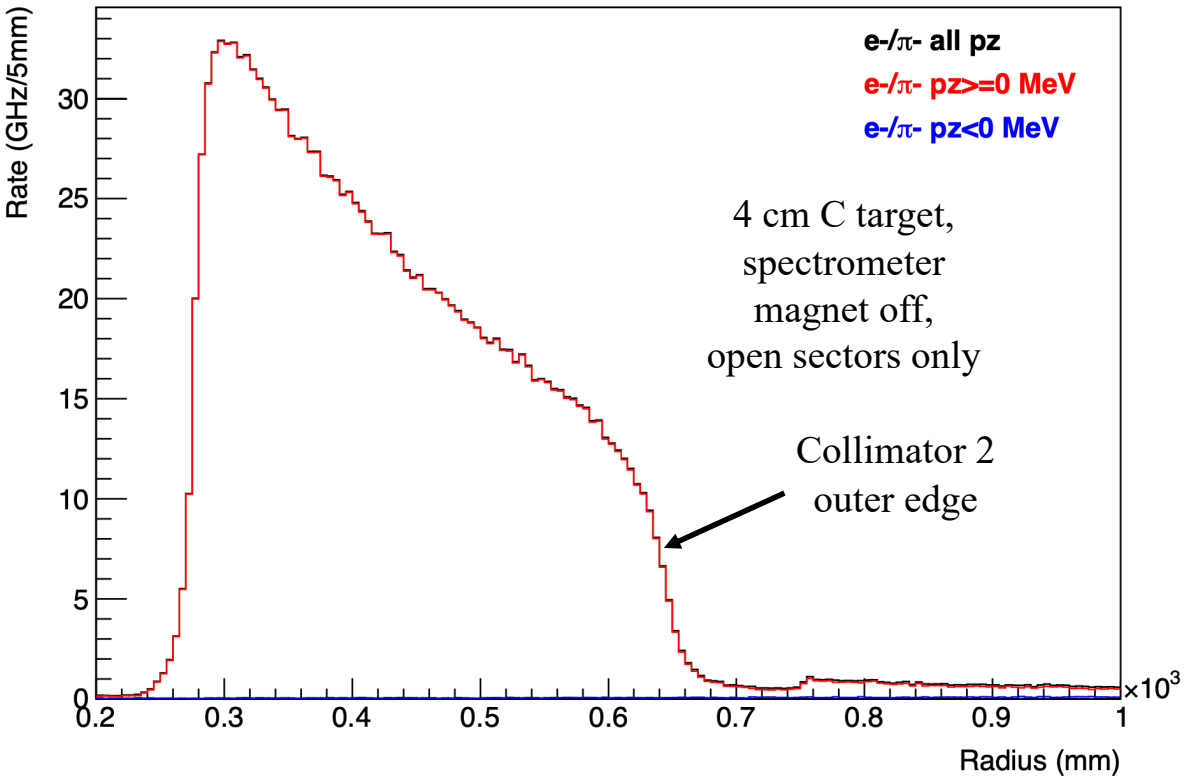

Figure 181: *The radial scattered flux rate distribution at the downstream scanner plane with spectrometer magnets off and a 4 cm thick Carbon target.*

beam centerline. By determining that radial transition location precisely at four points around the azimuth the centering of Collimator 2 with respect to the beam can be determined to within 1 mm.

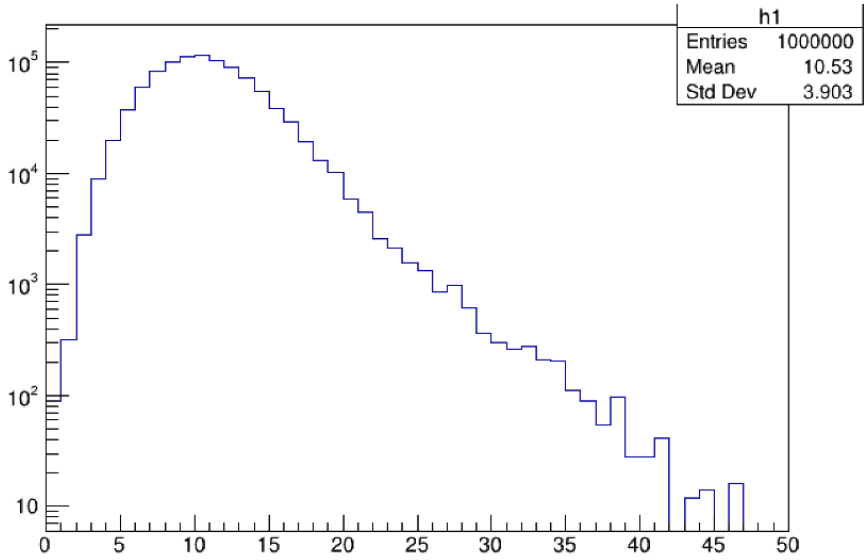

Figure 182: *Simulated downstream scanner detector photoelectron yield.*

The peak rate expected from the downstream scanner over its nominal scan range is $\sim$ 1.4 GHz for the special magnets off, carbon target conditions described above. The simulated photoelectron distribution is shown in Fig. 182, with an average of 10.5 pe/event. The estimated photocathode current is 2.3 nA. With a PMT gain $\sim$ 1700, a 4.0 μA anode current results. With a 0.5 MΩ gain I-V preamplifier, this results in a 2.0 V output signal.

9.5 Ring 5 HVMAPS profile detectors

The 84 Ring 5 main detector tiles will each be equipped with an array of 28 2×2 cm^2 high voltage monolithic active pixel sensors (HVMAPS) that will be used to monitor the event profile in the main Møller region at any beam current. While the scanner detectors described in the previous sections can scan the entire main detector region for one septant, they do so by scanning the region in 1×1 cm^2 areas at a time. In contrast, the HVMAPS can be used to study the evolution of the detector profile as the beam current is changed, simultaneously for all of the Ring 5 detectors, around the entire azimuth. They can also be used as an additional tracking detector located directly at the Ring 5 plane, in combination with the GEMs. The HVMAPS are implemented only for Ring 5, because of cost and the rather significant resources required for the associated DAQ.

9.5.1 Module design

Figure 183 shows the Ring 5 module, with the associated HVMAPS module mounted, and the HVMAPS module by itself. Figure 184 shows a partially exploded view of the module, showing some of the individual parts. To cover the Ring 5 tile area, 28 of the 2×2 cm^2 sensors shown in Fig. 185 are required. The sensors that will be used for MOLLER are based on a near identical design for the Mu3e experiment, which is called the MuPix chip [78]. This is a very mature chip design (version 11 now), which has been tested in many test beams, including for radiation hardness up to 300 MRad (protons). The sensors are based

on CMOS technology, incorporating an amplifier and a ToT double comparator for digitization, for each of the 64,000 80×80 $\mu\mathrm{m}^2$ pixels per sensor and the readout digital logic at the chip periphery. The chip design modifications for MOLLER include a different PLL (clock frequency) to match the CERN-developed readout electronics that will be used, and the implementation of a gate signal, which allows the operation of the chips at very high event rates, without saturation loss. The same design will also be used in the P2 experiment [79] as the exclusive tracking detector.

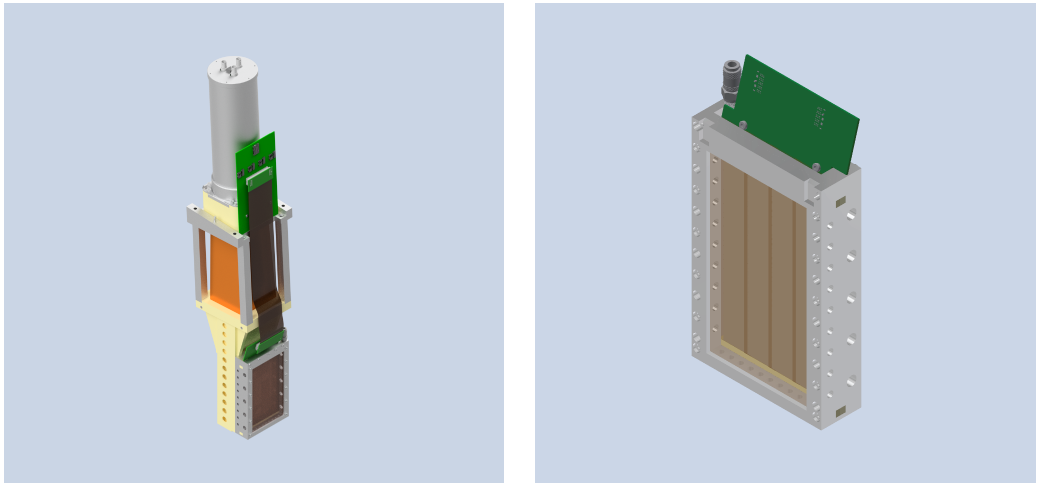

Figure 183: *Left: CAD image of the Ring 5 module with the HVMAPS module attached behind the quartz tile. Right: The HVMAPS module by itself.*

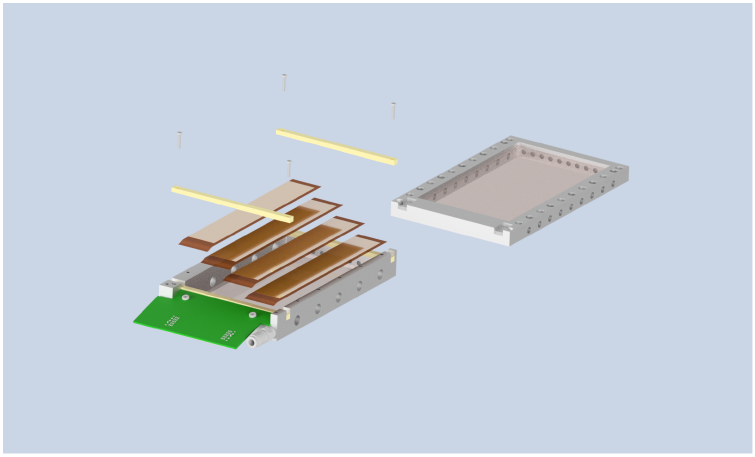

Figure 184: *Partially exploded view of the HVMAPS module.*

The module design for Ring 5 consists of 7 sensors bonded to each of four HDI flexprint strips that are stretched on a frame. The frame consists of a front and back part, each of which incorporates airflow channels for cooling and a Kapton window to protect the sensors and guide the airflow along the flexprint. Figure 186 shows the bonding plan and the design for a 6 chip flexprint layout. A layout for 7 chips (read out to one side only) is underway. The sensors can be thinned to about 50 $\mu\mathrm{m}$, depending on the applied bias voltage. The flexprint has a thickness of about 80 $\mu\mathrm{m}$ and for the windows we can use Kapton with a

thickness of $50\ \mu\mathrm{m}$. Assuming a sensor thickness of $100\ \mu\mathrm{m}$, the module will contribute a radiation length of $\sim 2 \times 10^{-3} X_o$ for an estimated $X_o \simeq 29\ \mathrm{cm}$, which is negligible compared to the radiation length of other materials in the path of the electron and won't affect the signal downstream of the module.

Each Ring 5 module has a separate air inlet to allow chilled air cooling of the sensors, which each produce about $1\ \mathrm{W}$ of power. The frames are designed to distribute the air flow in front off and behind the sensor flexprint assembly to avoid differential pressure and efficient cooling. The flexprints are bonded at one end to an interposer PCB that will incorporate a high density FMC connector, connecting to a readout board at the main detector barrel segment plate via a high density flexprint ribbon cable. The HVMAPS modules will be attached to the back of the Ring 5 modules with clamps, such that they are mountable/removable with the Ring 5 module installed in the segment and the entire detector array.

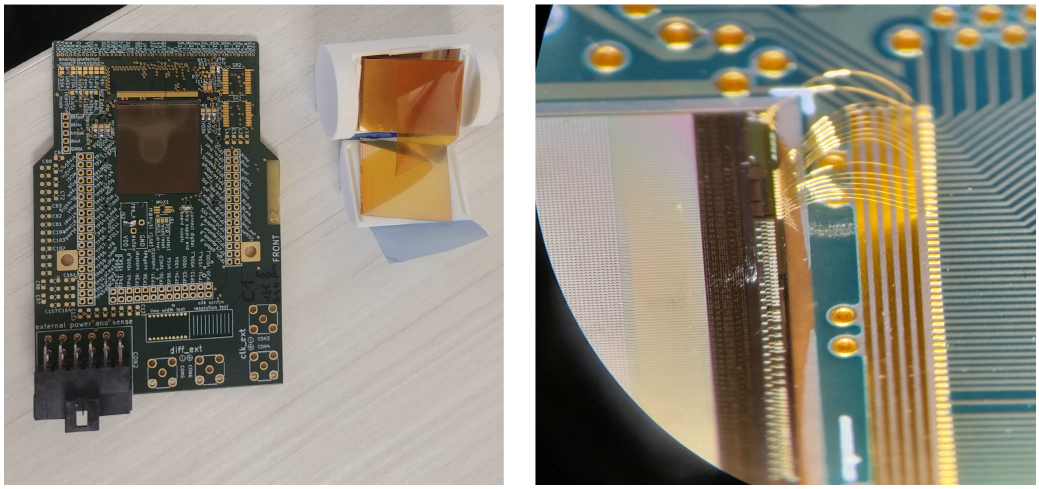

Figure 185: *Left: MuPix10 Prototype sensors. One is bonded to a prototyping board. Right: Partially bonded sensor*

9.5.2 Readout

The left side of Fig. 186 shows the bond connections for prototyping setup, with a large number of readout and control signals. This will be reduced to 38 connections per flexprint strip, for a total of 152 signal and control lines per HVMAPS module or per Ring 5 tile. This includes several LVDS readout lines, slow control, gate, clock, and LV lines for operation and an HV line for biasing (in the range of $60 - 100\ \mathrm{V}$). Figure 187 shows the readout and control layout for one module. The 152 control, bias, and signal lines are connected to a readout board at the location of the PMTs. The signals from each strip will be handled by serializer/de-serializer chip (CERN-developed lpGBT chip) and 4 of them connect to a single SFP+ fiber optic connection via a radiation-hard transceiver (CERN developed VTRX+ chip), and from there to an FPGA board that is located away from the detector array, in the shielded DAQ bunker. The clock, gate, and slow control, will be driven by the FPGA module, which will run a ROC with the JLab CODA system and a trigger interface. The LV bias for the digital and analog electronics on the sensor, as well as the sensor bias voltage, will be supplied by remote power supplies, to avoid noise and power fluctuation issues associated with DC-DC voltage converters.

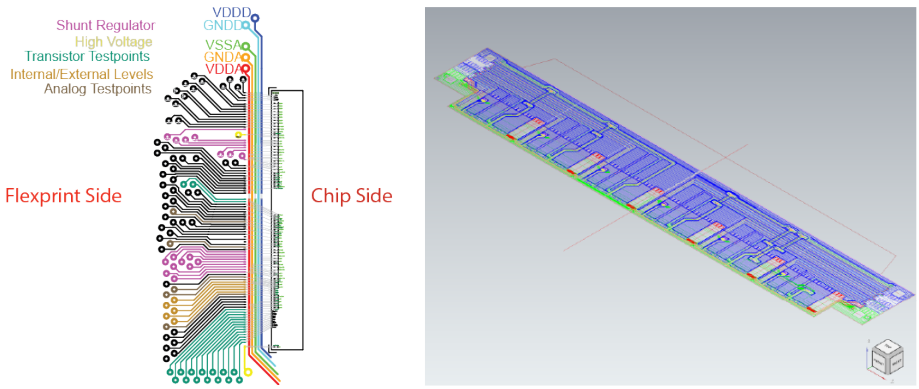

Figure 186: *Left: Schematic of connections from the chip to the flexprint for the prototype. There are many diagnostic connections that will not be connected in the final detector. Right: A six chip flexprint design that is read out at both ends. A 7 chip flexprint that is read out at one end is being designed. This can be achieved by omitting the number of diagnostic lines.*

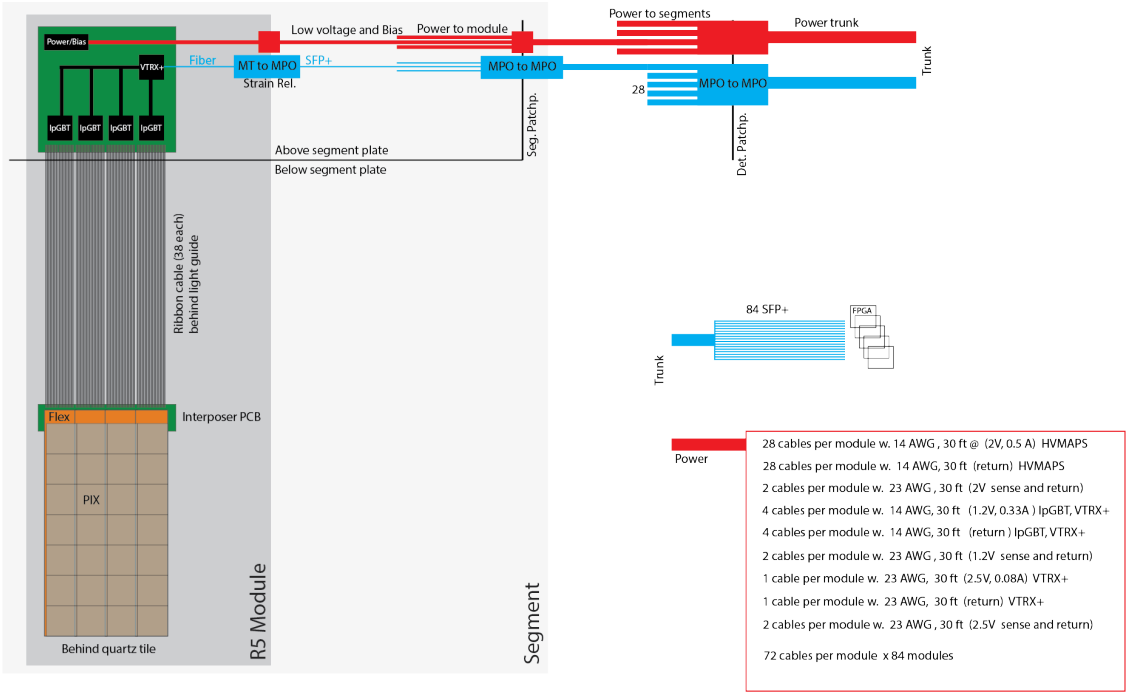

Figure 187: *Layout of the control and readout logistics for each of the Ring 5 HVMAPS modules. All low voltage supplies and bias lines are controlled by remote power supplies, to avoid noise problems.*

10 Electronics, DAQ, and Computing

10.1 Overview and requirements

This subsystem consists of several components: data acquisition and trigger, which are further divided into the integration mode and the counting mode systems; and online computing, consisting of computers, software, disks, and network to be able to record data to disk, send the data to tape, and analyze data online. Offline computing will be closely related to the online computing systems.

The integration mode and counting mode trigger and data acquisition systems are independent, and run in the CODA (CEBAF Online Data Acquisition) framework, the Jefferson Lab DAQ toolkit. Each DAQ system contains a module that accepts the trigger inputs, makes a trigger decision, and initiates an accepted trigger and readout event (this module will be referred to as a TS, or Trigger Supervisor). Connections between the TS and Trigger Interface (TI) units convey accepted triggers to the front-end electronics and ensure event synchronization. A TS module can support up to eight TI connections; for larger numbers of TI connections, Trigger Distribution (TD) modules are needed. The event fragments are gathered via a standard TCP/IP network to a workstation where events are built, written to disk, and subsequently stored in the Mass Storage System (MSS).

Both data acquisition systems will interface with the EPICS slow-control system [80] to ensure that parameters important to the analysis of the data will be archived in the data files.

10.1.1 Integration mode

The integration mode data acquisition system primarily interfaces with the integrating ADC modules, which are described in Sect. 10.3.1. In this mode, detector and beam monitor signals are integrated over the "helicity window" (about 0.52 ms long) at the nominal repetition frequency of 1920 Hz. Information identifying the beam helicity state, provided by the electronics in the polarized electron source, is recorded for each of these windows. The helicity windows are grouped in helicity patterns, as discussed in Sect. 3.2.1, over which the asymmetries will be calculated. During initial beam delivery and occasionally thereafter, the integrating ADCs are operated in a diagnostic mode in which all of the subsamples are recorded and reported, providing a waveform of the signals within the helicity window.

The trigger source for the integration mode is the T_{settle} signal from the helicity electronics, which indicates when the helicity state may be changing or settling after a change, as discussed in Sect. 3.2.1.

In the integration mode DAQ, the integration windows for the detector and beam monitor signals must be synchronized with the period of stable helicity as generated by the electronics in the polarized electron source. Due to differences in signal propagation time for the detectors and beam monitors, the relative gate timing of individual integrators must be adjusted by up to several μs and controlled to $\sim$60 ns. In production running, the integration DAQ must collect and transfer 100% of the helicity windows, without deadtime losses. The integration DAQ must also support the diagnostic mode of the integration ADCs, but this mode does not require 100% throughput or deadtimeless operation.

10.1.2 Counting mode

The counting mode data acquisition system is used for low-beam-current measurements in which individual electron scattering events can be observed, e.g. for verification of the kinematics using the tracking system. It includes amplitude and timing measurement of all of the detector channels, digitization of a subset of the beam monitor signals, and readout of the GEM tracking detectors.

The primary trigger for the counting mode comes from scintillators positioned to intercept electron trajectories through the GEM detectors (see Sect. 8.7). An important alternate counting mode trigger is the

use of individual quartz detectors or combinations, to investigate signals in the quartz which are not directly related to electron trajectories.

The counting mode trigger must support trigger decisions based on input rates between 10 kHz and 300 kHz (assuming beam currents down to $\sim$10 pA). It must have flexibility to generate triggers from either the dedicated trigger scintillators, or from any combination of the quartz detector signals. One of the main difficulties in the counting mode is to get an accepted trigger rate low enough to match to the highest rate possible with the GEMs, which is 5 kHz. The trigger inputs will be prescaled in order to achieve these acceptable event rates.

10.1.3 Online computing

Online computing includes both the systems involved in recording data and online analysis systems such as those providing feedback to the polarized source to control helicity-correlated beam parameters and those providing beam-parameter-corrected asymmetries for diagnostic purposes and evaluation of online data quality.

The networking and event building systems must support a data rate of about 130 MB/s during the production integration mode data collection to maintain 100% throughput without deadtime. Online analysis of helicity-correlated beam parameters and communication of feedback changes to the injector must occur with nearly 100% throughput and without impacting the data acquisition deadtime. Online analysis of fully-corrected detector asymmetries must occur with nearly 100% throughput and without impacting the data acquisition deadtime. Disk storage must be sufficient to hold the helicity-pattern-level asymmetry results spanning several days, to enable monitoring of changes in signal responses and correlations.

10.1.4 Offline computing

The analysis software used for the offline analysis of the integrating mode CODA data files will be identical to that used in the online computing. The specific challenge for offline computing for the integration mode will be the efficient aggregation and collection of the results over the full experimental periods.

10.2 Beam current and position monitor readout systems

Signals from the beamline elements will need to be recorded by the DAQ. These include beam position monitors, beam current monitors, and EPICS variables for controls of magnets and other equipment. The beam position and beam current monitors are discussed in Sect. 3.4. As described in Sect. 3.3.2, the experiment will use a beam modulation system to make small variations in the position, angle, and energy of the beam in order to measure the detector sensitivity to beam fluctuations. The DAQ will interface with this beam modulation system, sending the signals to control it and reading back its status. There will be scanner detectors, small-angle detectors (SAM) and diffuse beam detectors (DBM) to measure the beam profile and look for backgrounds. These detectors are typically a piece of quartz connected via a lightguide to a PMT. They will need to be read by the DAQ. The beam asymmetry feedback systems, described in Sect. 3.3.1 depend on a realtime analysis of the beamline data to calculate the needed changes in the injector settings and communicate them over EPICS to the helicity-control devices in the injector.

10.2.1 JLab Switched Electrode Electronics (SEE) BPM receiver

Most of the 4-wire beam position monitors are instrumented with SEE receivers [81]. The signals from each wire-pair used to calculate the X and Y positions are multiplexed, and analog outputs for each wire are provided by the sample-and-hold (S/H) module, with an effective analog bandwidth of 27 kHz. The analog

outputs are a voltage signal, with a typical signal of 3 V, but which can vary between 1–5 V. The S/H outputs will be input to integrating ADC or FADC channels, with in-line attenuators to adapt the signal level.

10.2.2 JLab digital BCM/BPM receiver

The current standard instrumentation for newer BPMs and BCMs at JLab uses a common digital receiver. The older analog SEE receivers described above are being gradually replaced by these new units. Like the SEE receivers, the new digital receiver modules have two channels, requiring multiplexing of the wire-pairs. The signal multiplexing is done with a 1 MHz cycle, allowing the most rapid complete measurement of beam properties to be at 1 Msps. The receiver modules use digital signal processing on this data stream, and provide an optical output of the digital data or output of analog signals proportional to the extracted signal magnitude. The analog outputs are provided by four 18-bit DACs running at 1 Msps which then go through a four-pole filter with a 100 kHz cutoff. This should be sufficient to resolve the expected minimum 10 μs T_{settle} period. This analog output would be used as an input to the integrating ADC or FADC channels, with in-line attenuators to adapt the signal level where needed.

Ongoing development efforts are underway to develop a module to decode the digital data stream from the receiver up to the full 1 Msps, which would then allow the beam properties to be measured with an effective bandwidth of approximately 500 kHz. This digital beam monitor readout development is desired by other Hall A and C experiments, not just MOLLER, and is being conducted outside the scope of the MOLLER project. This development of digital readout of the beam monitors is proceeding using CAEN V2495 FPGA modules to receive the digital data stream, and then accumulate the samples to form results for the beam monitors at longer time scales, such as the integrated value over a helicity window.

10.2.3 Berkeley digital BCM receiver

The development of new digital BCM receivers by collaborators at UC Berkeley and LBNL was discussed in Sect. 3.4.3. These receivers differ from those developed at JLab in that they directly digitize the 1.5 GHz signal from the beam cavities rather than using a local oscillator. The RF would be digitized at 3 Gsps, and the measured amplitude and phase would be extracted at a few Msps. The FPGA in the receiver would utilize a copy of the integration gate from the TI system to be able to form the integral of the beam current over each helicity window. The triggering and readout of the BCM receivers would be otherwise similar to that of the integrating ADC modules, described below. The FPGA will receive the start-of-window signal from the trigger distribution system, and will accumulate a number of samples which has been specified to span the stable helicity window.

10.3 Integration mode front-end

The primary front-end modules in integration mode are the integrating ADC module being developed by TRIUMF and the University of Manitoba. A full-scale prototype module has been used in several beam tests at MAMI as part of the development and testing. Scalers and IO registers would be used for diagnostic signals and to keep track of the helicity state of the beam in each helicity window.

10.3.1 Integrating ADC module

Each integrating ADC module will support sixteen input channels, as depicted in the block diagram of Fig. 188, and has been designed to connect to the detector preamplifier as described in Sect. 6.4.4. Each input signal passes through the anti-aliasing filter and is then digitized by an ADC chip. The ADC sample clock is supplied through the FPGA, which also queries the ADCs, collects the data and facilitates the readout.

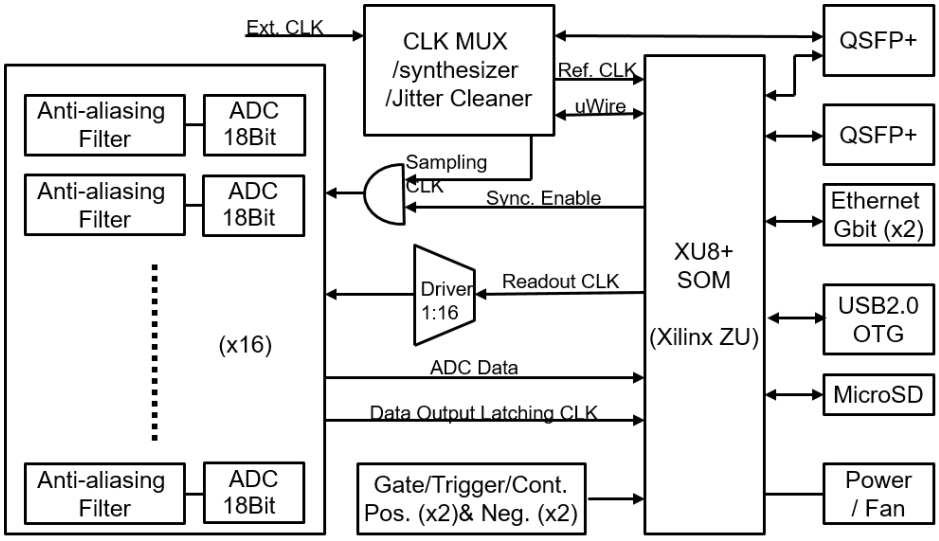

Figure 188: *Block diagram of the 16-channel integrating ADC being developed by TRIUMF and the University of Manitoba. The anti-aliasing filter, 18-bit ADC, and the FPGA (the XU8+ SOM in the diagram) are discussed in more detail in the text.*

Anti-aliasing Filter The ADC inputs pass through an anti-aliasing filter to reject common-mode noise coupled onto the cable from the detector and preamplifier. A 5-pole filter with a cutoff frequency of 1 MHz serves to limit the bandwidth well below the sampling rate of the ADC chip (15 Msps).

Analog-to-digital Converter The newly released, cutting-edge technology analog-to-digital converter (ADC) chip, LTC2387-18 from Linear Technology [82], was selected as our ADC candidate. It is a low noise, high speed, 18-bit successive approximation register (SAR) ADC with excellent linearity, and large signal bandwidth. It features a serial LVDS digital interface to support high speed operation while minimizing the number of data lines, allowing us to integrate multiple channels in a single board. The 18-bit ADC can operate at a selectable sampling rate up to 15 Msps. The sample rate is several times the anti-alias filter cutoff frequency and is a multiple of 60 Hz so as to reject power line noise.

FPGA The ADC sampling clock is controlled by signals derived from an external clock and gate signals. The output of each ADC in the module is summed over a selectable number of samples inside an FPGA and made available to the DAQ system through several Gigabit Ethernet interfaces per board.

The selected FPGA for the ADC board is the Zynq UltraScale+ from Xilinx [83]. The FPGA will be implemented as a System-On-Module (SoM Mercury-XU8 produced by Enclustra [84]) rather than by incorporating the FPGA directly in the board, which is easier to handle during layout design and makes the FPGA replaceable if it gets damaged. The Ultrascale+ FPGA is a complete System on Chip (SoC), featuring a quad core ARM Cortex-A53 processor system (PS), allowing embedded Linux running on the FPGA. The Mercury UX8 module adds several additional storage and interface modules, including DDR4 ECC SDRAM, eMMC, flash, dual Gigabit Ethernet, and dual USB 3.0. The full ADC board will be configured for 10 Gigabit Ethernet transfer via several fiber-optic links, allowing full streaming mode operation of all 16 channels per board, for diagnostic purposes. The slow control of the FPGA will be communicated via Gigabit Ethernet.

Data processing In the production running mode, the FPGA will receive the start-of-window signal from the trigger distribution system. After a programmed delay to allow for signals with different latency, the FPGA will begin accumulating the number of ADC samples which has been specified to span the stable helicity window. Several quantities will be accumulated from the ADC samples: the sum, the sum of squares, the minimum sample, the maximum sample, and the number of samples accumulated. These will be stored as a block of six 32-bit data words. We will also accumulate these quantities over fractions of the helicity window (which we call subblocks); the sums of the subblock values should be identical to those accumulated over the full window, allowing a cross-check of the data integrity. We plan to accumulate four subblocks, plus the full helicity window. Along with an 8-byte timestamp, this will result in a 128 byte data record per channel per helicity event, or 2048 bytes per module (16 channels) per event.

Physical footprint, power, and data transfer The integrating ADCs will be packaged as a 2U rack-mount module, with 16 channels per module. The module dissipates 28 W, which can be supplied either through Power over Ethernet (PoE++) or by an external $\sim$48 V power supply. We expect to use PoE++. The primary data transfer from the module will be through 10 Gbps Ethernet over optical QSFP. The copper RJ45 connection used for the PoE++ also provides 1 Gbps data transfer for slow controls on the module. The choice of PoE++ supply has not been finalized, but a possible candidate PoE++ supply unit would support 8 ADCs and would itself be in a 1U chassis.

10.3.2 Scaler

Additional diagnostic signals, such as from beam halo counters or V/F pulses, would be recorded in scalers such as the Struck SIS3820 32-channel VME scaler.

10.3.3 Helicity readout

The helicity generator board in the injector provides logic signals on optical fiber for the reported helicity of the beam, the first event of a helicity pattern, and the time period during which the helicity state may be changing (referred to as T_{settle}). The helicity reported to the experiment would be a delayed copy of the true helicity signal applied to the Pockels cell. The true helicity for a helicity window can be determined either by matching against the reported helicity in the window after the delay, or by accumulating the history of reported helicities to determine the pseudorandom seed used by the helicity generator board.

10.4 Integration mode DAQ system

An overview of the integrating DAQ layout is shown in Fig. 189. The integrators are the 18-bit ADCs described above, twenty-six of them in Hall A and six in the injector service building. We have approximately 500 integrating ADC channels; about 300 are used for the detector signals, about 100 for beam monitors in Hall A, and about 100 for beam monitors in the injector. Scaler modules are present in both the Hall A and injector crates. CAEN V2495 modules are used to receive digital data from the JLab digital BCM/BPM receivers as described in Sect. 10.2.2.

10.4.1 Trigger and timing

The primary integration-mode trigger is derived from the T_{settle} signal from the polarized electron source, which marks the period in which the beam helicity state is being changed. The timing of the T_{settle} signal is adjusted by digital delays in the TI connections to form the start signal for each integration module's integration period. To calibrate the trigger delays, we would use tune-mode beam, which has a narrow beam pulse that repeats at 60 Hz. We would then use the integrating ADC diagnostic mode to resolve the detector

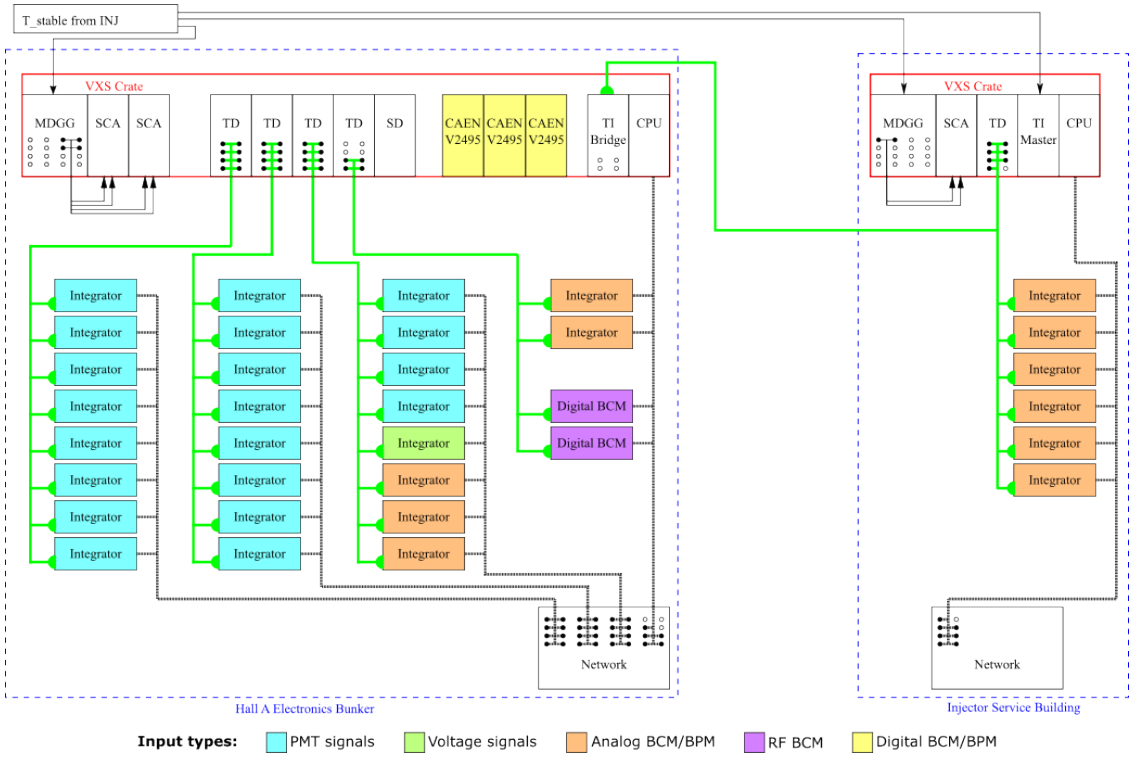

Figure 189: *Trigger and data connections in the integrating DAQ system. The bright green traces represent the trigger distribution on optical QSFP connections, and the dashed black traces represent Gigabit Ethernet on optical QSFP connections. The integrating ADC modules are color-coded to indicate the types of signals input to the module. Twenty modules instrument the signals from the detector PMTs (cyan), one instruments a mixture of PMT and voltage signals (pale green), and eleven (5 in hall A and 6 in injector) instrument the analog signals from beamline monitors. Also shown are the digital BCM receivers (purple) and FPGA modules receiving the digital outputs from the JLab beamline monitors (yellow).*

and beam monitor response of the tune mode pulse within the helicity window, allowing the determination of the relative timing offsets between the different systems.

10.4.2 Event building and data storage

As described at the end of Sect. 10.3.1, we plan to use four subblocks in the integrating ADCs, which at a helicity event rate of 1920 Hz will give about 4 MB/s in each of the 32 integrating ADC modules for a total of about 130 MB/s. This is well within the capabilities of using a single computer as the event builder, which has a maximum accepted data rate to about 900-1000 MB/s. Recent experiments in Hall A, such as SBS, have sustained even higher data rates by using multiple event builders in parallel, but that will not be required for the integration mode data.

At the 130 MB/s rate, an hour-long run would be about 500 GB. We would likely split the data into file segments of 10-20 GB each. Data files would be written to a local disk on the event builder computers, and would then be transferred automatically to the JLab MSS tape silo.

10.5 Counting mode front-end

10.5.1 FADC

In counting mode, the PMT signals and beamline monitor signals will be instrumented by JLab FADC250 flash ADC. The FADC250 uses a 12-bit ADC sampled at 250 MHz; either a pulse waveform, or integrals of the signal can be reported. The FADC250 modules have 16 Lemo input connectors, terminated in 50 ohms. The modules can be set in three full-scale input ranges, all negative going: -0.5V, -1V, and -2V. The offset can be controlled by DACs in a +/-10% full-scale range.

The PMT base design incorporates a dual mode amplifier, described in Sect. 6.4.4, allowing the signals to be switched between the integrating ADCs and the FADC250 modules. There will be two signal cables for each PMT, one going to the integration electronics and one going to the counting electronics. Both the signal and the ground connections to the cables will be switched at the base to avoid introducing a ground loop.

10.5.2 VTP

The VXS Trigger Processor (VTP) module [85] is a JLab-designed VXS switch card FPGA module which participates in the level-1 trigger in front-end VXS crates and as part of the global trigger. Additionally, the VTP has an ARM processor capable of running a Linux CODA ROC, and a QSFP 10/40 Gbps Ethernet connection for data readout. Data from each of the 16 VXS payload modules are communicated via a set of four 8.5 Gbps duplex serial lines on the VXS backplane [86], for a maximum data throughput of 34 Gbps per payload module. The VTP modules in VXS crates #1 and #2, as shown in Fig. 191, will be used to form trigger signals from their respective instrumentation channels, and will send these as trigger inputs to the master TI in crate #2.

10.5.3 GEM readout

The GEM readout will be a copy of the SBS system and is discussed in detail in Sect. 8.5. In this system, data from the APV25 front-end cards on the GEM detectors is digitized in a total of 28 MPD modules. The digitized MPD data are sent over fiber optical links to a single VTP module responsible for communicating with the rest of the DAQ system. The sample clock and trigger signals for the MPD cards are generated by the DAQ trigger system and distributed to the MPDs over BNC cables from the CAEN V2495 module shown in VXS#3 of Fig. 191.

Readout through VTP The data from the MPD modules is transmitted to a VTP module via an optical link. The links from four MPD modules will connect to the QSFP transceiver on a VXS_QSFP payload module, which in turn communicates via the backplane serial lines to the VTP, as shown in Fig. 191. The 28 MPDs require seven VXS_QSFP modules. The VTP will run a CODA ROC to handle pedestal correction and zero suppression of the GEM data, and to transmit the resulting event data over the optical Ethernet link to the event builder.

10.5.4 HVMAPS readout

The HVMAPS provide a fine-pitch pixel map across each of the Ring-5 tiles, as described in Sect. 9.5. For each tile, 28 HVMAPS chips would send their data through CERN lpGBTs and VTRX+ chips to drive an optical SFP link. The 84 SFP links from all of the Ring-5 tile HVMAPS would connect to a FPGA-based Arista switch (Arista 7130 96L) which would also connect to the TD/TI system to receive triggers. In counting DAQ mode, the HVMAPS would be part of the event readout, allowing comparison of the tracks

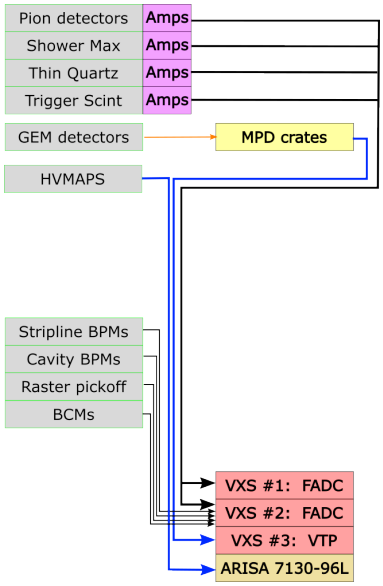

Figure 190: *Signal connections in the counting DAQ system. The black traces represent signals on BNC cables from the PMTs and from beamline instrumentation modules. The orange trace represents the HDMI cables between the GEM APV25 cards and the MPD modules. The blue traces represent optical SFP connections between the MPD modules and VTP, and between the HVMAPS and the Arista switch.*

from the GEMs to the struck pixels in the HVMAPS. In integrating mode, the HVMAPS would be operated as a stand-alone system with multiple samples taken independently of the helicity window trigger, and would provide a map of the hit distribution across each quartz tile in Ring 5.

10.6 Counting mode DAQ system

The signal connections and crate layout of the counting mode DAQ are shown in Figures 190 and 191 respectively. The primary triggers will be formed from the passage of particles through scintillators. We will read out 23 FADCs to accommodate all the signals from detectors and monitors. We will also read out the GEM detectors with a system like the one being used in the SBS DAQ, as described above. The trigger rates may vary from 10 kHz to 300 kHz (the latter high rate will only be used for studies in which the GEM detectors are not read out). The trigger definition will be flexible, controlled by the VTP FPGA firmware and programming. The event sizes without the GEM readout will be about 5 kB, hence the data rate of 50 – 1500 MB/s. The full data rate from the GEMs would be 230 kB/event, but zero suppression will give a substantial reduction.

10.6.1 Trigger and timing

As discussed in Sect. 8.8, the counting mode trigger will be based on either single FADC channels (such as individual thin-quartz tiles) or coincidences between FADC channels (such as a pair of trigger scintillators). The maximum input signal rates from the scintillators, as described in Sect. 8.7, are 1.3 MHz, but this will be prescaled to reach accepted event rates. The trigger timing will have 4 ns granularity due to the FADC sample period, but this will be sufficient for forming the scintillator coincidence trigger. The GEM signals are digitized in the APV25 with a 25 ns period. The tracking system does not require high-precision timing.

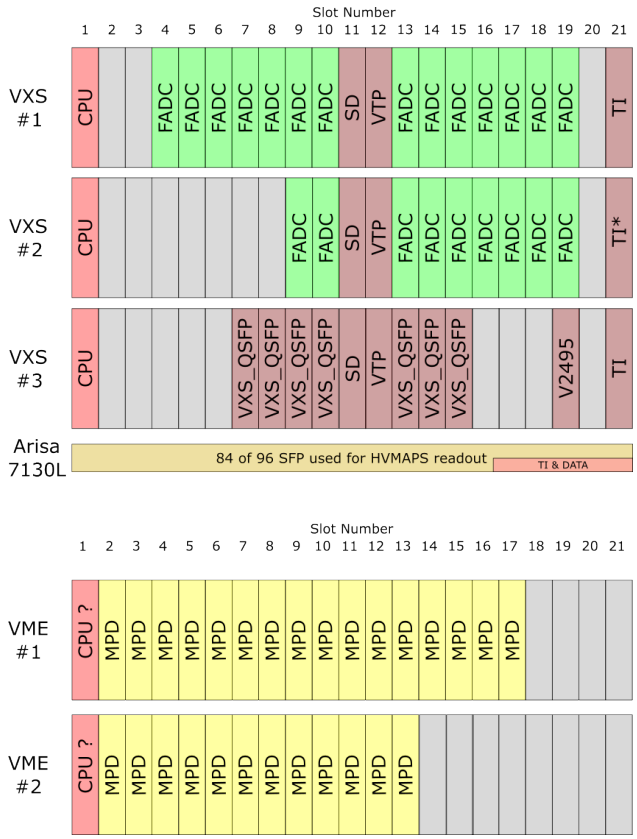

Figure 191: *Crate layout in the counting DAQ system. The three VXS crates and the Arista switch would be located together in the main electronics bunker. The two crates of MPD modules would be located in small shielded areas near the GEM rotator.*

Pulse fitting within the FADC will provide a more precise measure of the arrival time in analysis than the FADC sample clock.

10.6.2 Event building and data storage

We anticipate prescaling the event triggers to achieve an event rate of about 5 kHz, which is the highest event rate that the APV25 cards can support. The counting mode data rate will depend upon the occupancy in the GEM detectors; without zero suppression the GEM data rate would be about 2.3 GB/s. We expect that the actual occupancy to be 5%-10% for the highest luminosity counting mode running, giving an expected maximum data rate for the GEMs of about 230 MB/s. The FADC modules will likely be operated in pulse-integral mode, but if we included the full readout of all FADC samples, we would anticipate a data rate of about 160 MB/s. Together, this suggests a maximum counting DAQ data rate of $\sim$400 MB/s, which can be well supported by a single event builder computer. We can control the occupancy and data rate by either reducing the beam current or prescaling the triggers further.

10.7 Computing

10.7.1 Overview and requirements

The computing subsystem includes the network and computers, as well as the software, used to collect and analyze the data. The realtime and prompt analysis processes will run on computers in the counting house for feedback and monitoring data quality. The offline analysis would be performed on the Jefferson Lab computer farm. The same software will be used for the online (both realtime and prompt) and offline analysis.

Physics analysis software will be a research contribution from the user community. The integration mode analysis is expected to be based on the JAPAN (Just Another Parity ANalysis) framework [87], which was used for the Qweak, PREX-2, and CREX experiments.

In the analysis of an integrating parity experiment like MOLLER, the raw signals from the detectors in each helicity window are first normalized by the integrated beam current, and then they are combined with values from adjacent helicity windows to form an asymmetry in a single helicity pattern. Asymmetries are calculated on all normalized detector signals and on all beam parameters, and a correlation analysis between the detector and beam parameter asymmetries is carried out. In most of the data collection, the correlations are determined from natural fluctuation in the beam parameters, but in a small fraction of the data we "dither" the beam parameters by deliberately modifying them one-by-one (using the beam modulation system mentioned above). For each helicity window, two different corrected asymmetries are computed, using the "natural" and "dither" correlations, and then these results can be accumulated either singly in output files or by averaging helicity window asymmetries together to produce a mean value and uncertainty on the asymmetry.

10.7.2 Realtime processing: integration mode

Section 3.3 describes three tasks requiring realtime processing of the data: helicity-correlated feedback, beam modulation, and control of transverse beam polarization. Helicity-correlated feedback uses the measured charge asymmetry and position differences of the beam in the hall to modify the settings of the helicity control devices in the injector. Monitoring of the detector correlations to the beam parameters, and the correlations between the beam parameters, can provide an early indication of problematic changes in the beam tune. Additionally, the analysis to determine the transverse polarization must be done using asymmetries that are corrected for beam parameter fluctuations, which also appear as azimuthal asymmetry variations.

10.7.3 Prompt resource requirements: integration mode

The parity analyzer used for the PREX-II experiment maintained an analysis rate of about 400 events per second (data throughput of about 1.5 MB/s) for the full analysis chain. Scaling for MOLLER's 4 times larger number of integration channels results in a predicted analysis rate of 100 events per second, about 20 times slower than the collected event rate. Because the data per channel from the MOLLER electronics is larger than in PREX-II, a scaling estimation based on the 130 MB/s data rate and PREX-II analyzer throughput yields an analysis rate about 80 times slower than real time. Taking the simple average of these two estimates, we expect that, using the PREX-II analysis as a baseline, a total of 50 concurrent analysis processes are needed for a full real-time analysis to stay current with the data collection. Of the set of ten workstations, two are reserved for event building and helicity-correlated feedback, leaving eight across which to distribute these 50 real-time processes.

With a data rate of 130 MB/s, each hour-long run results in a raw data volume of about 450 GB. The calculation and storage of signal averages and asymmetries for each helicity-pattern does not generally result in data reduction, and thus the output data volume can be increased. For example, in PREX-II, an output

ROOT file was about four times larger than the original data file. For the experiment-long accumulation, we can keep averages of these quantities at about the minute time-scale, resulting in a data reduction of a factor of several thousand. However, to evaluate correlations between the beam parameters and the detector signals, and to monitor the correction process, we require keeping the results for each helicity pattern for several days. Assuming a full output file size of 1.8 TB per hour (four times the raw data size), a 100 TB staging disk allows about 2.5 days of history for this correlation/correction evaluation.

10.7.4 Offline software: integration mode

As mentioned in Sect. 10.1.4, the challenge for offline computing will be the efficient aggregation and collection of the results over the full experimental periods. The Qweak experiment used a MySQL database to store the analyzed results from each "runlet" (about 5-minutes of data), and from that database carried out much of the physics analysis. However, the final analysis of beam correlations and corrections required going back to the event- and pattern-level data stored in individual ROOT files for each run. The PREX-II and CREX experiments used ROOT files throughout the analysis process rather than using a database. MOLLER will need to research what works best for doing the aggregation and comparison of the full data set, but some sort of data reduction will certainly be needed.

10.7.5 Offline software: counting mode

For the counting mode, we plan to build on the analysis software developed for the PREX/CREX and SBS experiments. This software is based on the Hall A C++ Analyzer [88] with additional classes supporting the GEM trackers.

The counting mode data collection is estimated to be about 5% of the total experimental period, with an estimated raw data total over the full experiment of 1.25 PB. The data analysis speed is estimated to be about 100 events per second, based on experience with SBS data at low occupancy in the BigBite GEMs, and so would be about 50 times slower than the maximum accepted event rate of 5kHz. Since this is similar to the ratio of data analysis to data collection time we have projected for the integration mode, the counting mode resource needs are projected to be also at about 5% of the needs in integration mode.

10.7.6 Offline resource requirements

The tape storage estimate is 9.5 petabytes (PB) for the integrating-mode raw data plus the Compton polarimeter raw data, 2 PB for the results from the integrating mode and Compton polarimeter analysis, 1.5 PB for the counting-mode raw data and analysis results, and 1 PB for simulated data, for a total of 14 PB, which needs to be stored permanently on tape.

For the MOLLER offline analysis, we anticipate a need of 2000 (FY18) cores for a six-year period. This is about 40 times the computing power that was required for the Qweak experiment. Furthermore, we estimate another 2000-cores requirement for simulations. Altogether, the 4000 cores roughly translates to a 30% fraction of the Jefferson Lab computer cluster as of 2018 when the estimates were made. This is more than the usual allocated 10% for Halls A and C data analysis; however, this percentage will likely decrease over time with newer cores being faster and with the projected increase of the JLab cluster.

11 Polarimetry

The longitudinal polarization of the 11 GeV electron beam is expected to be about 90%, with some variation depending on the specific details of the GaAs photocathode at the polarized electron source. The beam polarization may vary at the 2% level over the duration of a specific photocathode's lifetime. The polarization will be oriented to within a degree of longitudinal to avoid an azimuthal scattering asymmetry associated with transverse polarization components (see Sect. 7.2). Since the measured parity-violating asymmetry is directly proportional to the electron beam longitudinal polarization, it is important to measure the polarization to high precision. The average polarization will be measured to a precision of 0.4%, with robust control of systematic uncertainties. This polarization will be continuously monitored for significant variations during data collection.

Members of the MOLLER collaboration have accumulated extensive experience with existing Møller and Compton polarimeters in Hall A which will be used to meet these goals. In particular, the recent precision neutron skin experiments, PREX-2 and CREX [89], provided essential insights into both polarimetry techniques, and clarity on improvements that are required to meet the precision polarimetry goals for MOLLER. During PREX-2 the Møller polarimetry team discovered how to choose the spectrometer tune to reduce the so-called Levchuk correction and nearly eliminate sensitivity to precise spectrometer field settings. A key improvement for the Compton polarimeter implemented during PREX-2 and CREX allowed for precise determination of the laser polarization inside the optical cavity allowing its determination to $\pm 0.45\%$. This technique will be refined with further characterization of the optical components prior to MOLLER with an expected reduction in this key systematic by a factor ~ 2. This reduction along with the addition of a functioning electron detector are the key improvements before MOLLER that will allow Compton to reach 0.4% uncertainty. The Møller polarimeter precision is expected to be greatly reduced by focusing on the two largest uncertainties i.e. directly measuring the current dependence of the beam polarization and degree of saturation of the target foil with dedicated studies with the electron beam during the experiment will diminish the two leading systematic errors each set at $\pm 0.5\%$ during CREX. The remaining systematic errors for Møller polarimetry during CREX totaled only 0.47%. The total combined (Møller and Compton) systematic error on polarimetry for CREX came in at $\pm 0.44\%$, building confidence that our precision goals are, in fact, achievable.

Two independent polarimetry techniques will be used for the MOLLER experiment. Compton polarimetry is a well established technique for high precision polarimetry at beam energies above a few GeV. However, MOLLER requirements will take this technique to precision levels not yet realized. Beam interactions with a photon target are non-disruptive, so Compton polarimetry can be employed at high currents as a continuous polarization monitor. The photon target polarization can be measured and monitored with a very high precision, and the scattering between a real photon and free electron has no theoretical uncertainty, such as the atomic or nuclear effects which can complicate other polarimetry techniques. Radiative corrections to the scattering process are at the level of 0.3% and are very precisely known. Compton polarimetry at JLab has previously achieved 0.5% precision on electron beam polarization and provided the basis for estimating that this technique is capable of achieving precision at the level of 0.4%. Several important upgrades to the Hall A Compton polarimeter will be completed by JLab before MOLLER operations begin.

The Møller polarimeter measures the scattering of beam electrons from polarized atomic electrons in a ferromagnetic foil. The use of a solid target is disruptive to the beam and limits the technique to low average beam current, but the approach provides a rapid, high statistics measurement with systematic uncertainties that are entirely independent from Compton polarimetry. The Hall A Møller polarimeter is operationally robust and commonly used by experiments with polarized scattering. An upgrade to the detection and collimation of the Møller polarimeter will be completed to support the MOLLER experiment.

In addition to the two polarimeters to be used in Hall A, a high precision Mott polarimeter in the low energy injector [90] will also be employed to cross-check those results. While this polarimeter is essential

for the configuration of the spin manipulation in the injector using relative measurements, the knowledge of the absolute analyzing power normalization has also been closely studied. The Mott polarimeter can reach 0.61% precision, with the dominant uncertainty contribution being due to the Sherman function, that is, the theoretical calculation of the analyzing power in Mott scattering. This polarimeter will provide a valuable cross-check, as the depolarization between the injector and the high energy hall is expected to be negligible.

The existing Hall A polarimeters and these plans for future improvements are described below.

11.1 The Hall A Compton Polarimeter

As pictured in Fig. 192, the Hall A Compton polarimeter [91] is located in a chicane, about 15 meters long, which deflects the beam to intersect with a laser cavity 21.5 cm below the primary (straight-through) beamline. After passing the electron-photon interaction point, the electron beam is bent about 2.3 degrees by the third chicane magnet to be restored to the primary beamline. Electrons scattered from the photon target are separated from the primary beam by this bend and detected using silicon microstrips just before the fourth chicane magnet. Scattered photons pass through the bore of the third chicane magnet to be detected in a calorimeter.

The photon target is a 0.85 cm long Fabry-Perot cavity crossing the electron beam at an angle of 1.4°. The laser system produces green (532 nm) light. Power levels of 10 kW have been stored in this resonant optical cavity for intersection with the electron beam, while more typical operation uses about 2 kW of stored power. The laser light can be toggled between opposite polarizations of highly circularly polarized light. The feedback loop which locks the laser to the cavity resonance can be disabled to dump the stored light and enable measurements of background from all non-Compton-scattering processes. To reduce overhead from the time required to re-lock the cavity, the transition between laser states is typically performed with a period of 1-2 minutes. The polarization of the transmitted light from the locked cavity and the reflected light from the unlocked cavity are each monitored and are used to characterize the laser polarization at the interaction point.

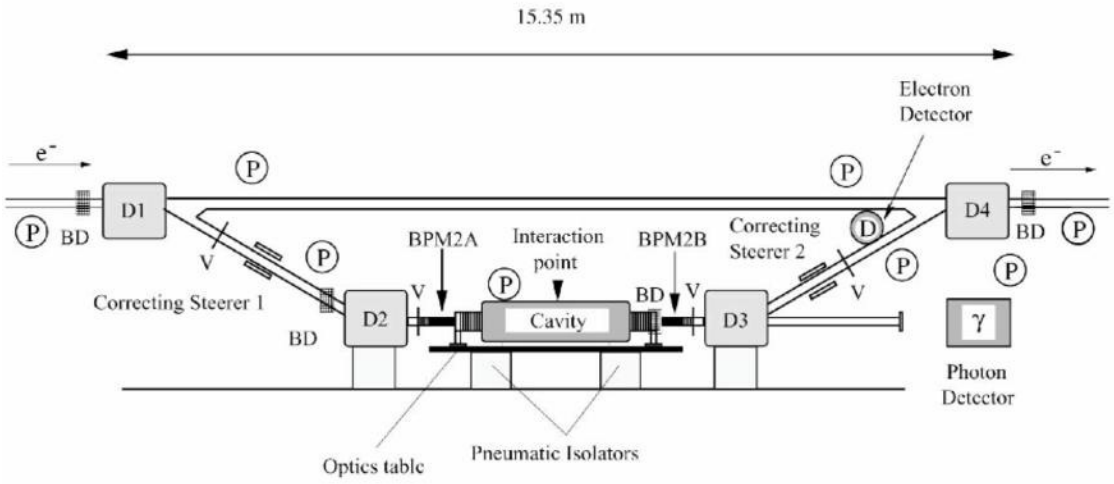

Figure 192: *Schematic of the Hall A Compton polarimeter. Figure from [91].*

At 11 GeV, with 2 kW stored laser power, the Compton-scattered rates will be approximately 1.5 kHz/μA and the asymmetry will range from 32% to -7% over the energy spectrum. If backgrounds remain compara-

ble to recent operation, statistical precision of 0.4% would be possible in about 5 minutes, depending on the specific detection and analysis approach which is considered.

The vacuum in the interaction region is at the level of few $\times 10^{-8}$ torr, implying a photon background rate due to Bremsstrahlung scattering from residual gas of around 5 Hz/μA. The dominant source of background in the photon detector is thought to be tails of the beam halo distribution interacting with the apertures in the interaction region. In contrast, for the electron detector the background is thought to be dominated by energy tail or position halo of the primary beam since electrons from aperture scattering would presumably not cleanly transit the third dipole. When well-tuned, the background rates in the photon and electron detectors have been seen to be roughly similar: around $<$100 Hz/μA in recent use.

There is a long operational history for the Hall A Compton polarimeter, including measurements during the 2009-2010 runs of HAPPEX-III [76] (3 GeV) and PREX [92] (1 GeV beam energy) with precision better than 1% [93]. One significant innovation since 2010 has been the implementation of a technique for determining the laser polarization inside the resonant optical cavity with high precision [94]. A photon calorimeter matched to the higher energy was installed. Additional collimation and magnetic extensions were added to reduce the synchrotron light flux and energy into the photon calorimeter. The polarimeter has also been operated since the energy upgrade with a 10.6 GeV beam during the 2016 run period and functions with expected backgrounds and sufficient control of synchrotron light.

Jefferson Lab is committed to high precision polarimetry in support of the physics programs chiefly in its two high current experimental halls, A and C. To increase the reliability and precision of the Compton and Møller polarimeters in both halls, JLab launched its High Precision Polarimetry (HIPPOL) program in 2020 with the intent of increasing functionality and reliability by upgrading the electron detectors in both halls as well as the laser system and DAQ in Hall C. As a result of the HIPPOL project, the Hall A and Hall C Compton polarimeters will converge on common laser and detector solutions and many of the key components and spares for the systems work equally well for both halls; the components of one can even be removed temporarily to replace a broken part in the other. For example, the laser systems will be identical in both Halls A and C. Work is ongoing to produce an FADC-based DAQ that is sufficiently flexible to meet the needs of all four polarimeters. The default electron detector system will make use of diamond strip detectors in both halls. The electron detector system will be discussed in further detail next.

Compton Laser System The laser system comprises a 200 mW 1064 nm seed laser, a 10 W fiber amplifier, a temperature-controlled doubling crystal as well as a variety of optical components installed on an optics table underneath the beam line which are used to transport and mode-match the laser to the Fabry-Perot optical cavity as well as to measure the polarization characteristics of the beam. The seed laser which typically runs at a few mW, feeds the fiber amplifier. The laser beam is frequency doubled to green at 532 nm via the temperature-controlled doubling crystal. Spares exist for each of these components including the temperature controller. Most optical components on the laser table are robust and replacements are available within days from suppliers such as Newport and Thorlabs. The optical cavity proper requires high reflectivity mirrors. Experience in the 6 GeV era suggested that the mirrors in the Fabry-Perot cavity needed to be replaced intermittently (typically on a time scale of one to years) likely due to radiation damage. In the 12 GeV era, similar lifetimes have been observed although in at least one instance, the mirrors had to be replaced sooner than expected due to a vacuum incident in the downstream beamline. Replacement mirrors will be purchased by Hall A well in advance of MOLLER.

The locking electronics currently in use are custom boards developed by the University of Basel two decades ago. These electronics still work well and a complete set of spare boards exist; however, the spares have not been tested recently. An investigation is currently underway to test the viability of using a commercially available set of locking electronics similar to that used in the Hall C laser system.

Compton Electron Detector A new electron detector is required to meet the precision goal for MOLLER and Jefferson Lab has decided to fund this upgrade through its HIPPOL program. At present, electrons are detected in 4 planes of silicon microstrip detectors located just before the 4th dipole. Custom readout electronics pre-amplify and discriminate signals from the microstrips for readout with an FPGA DAQ module. The system is operating with low efficiency and excessive noise, and cannot provide the required uniform and efficient detection. Two solutions are currently being investigated.

The primary design being pursued via the HIPPOL project is a diamond microstrip detector, similar to those which were successfully used for the Hall C Compton polarimeter during the $Q_{\rm weak}$ experiment [94]. In this design, the diamond planes are mounted on alumina substrate and have thin metal alloy strips glued to the surface with a pitch of a few hundred microns. A bias voltage between the substrate and the strips causes the electron holes created by a passing electron to drift towards the nearest strip which is then read out giving the relative position of the track. Initial tests at Ohio State University on diamond wafers produced by semi-conductor manufacturer II-IV were noisy and produced undesirably high leakage currents. More recently produced diamond samples have performed as expected and a sufficient number of diamond wafers for both Halls A and C are being procured.

Readout of the diamond strip electron detectors will be accomplished using the Calypso family of application-specific integrated circuit (ASIC) boards developed by the RD42 collaboration for low capacitance and low leakage current diamond detectors [95]. This readout can be incorporated into the existing data acquisition system used with the silicon detectors.

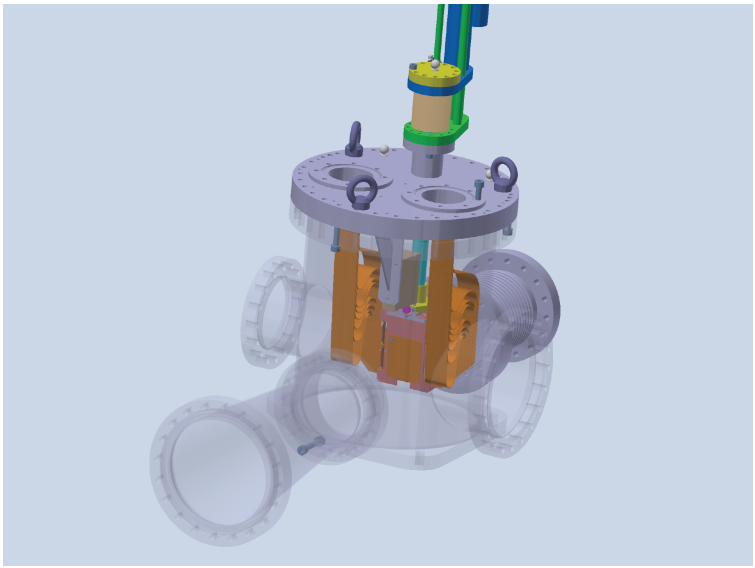

Figure 193: The four plane electron detector assembly shown inside the vacuum chamber that is connected to the beam line vacuum. This CAD model shows the existing setup, requiring many ribbon cables for readout. The chamber will be reused, but a new flange with a new set of feedthroughs will be designed, with new cable arrangement and cooling line.

The second electron detector design being developed in parallel utilizes high-voltage monolithic active pixels sensors (HVMAPS). The sensors are described in Sect. 9.5. For the Compton electron detector the same chips will be used. Figure 193 shows the four planes of current electron detectors in their holder, inside the vacuum chamber, through which the beam passes. The HVMAPS sensor implementation will replace the existing four planes, vastly reduce the number of signal lines and add active cooling. Four planes are used in the design to improve background rejection and position tracking. For each of the four planes, three

HVMAP sensors will be glued and bonded to a PCB readout board, as a vertical tile with an active area measuring 2×6 cm per plane. The corresponding assembly is shown in fig. 194.

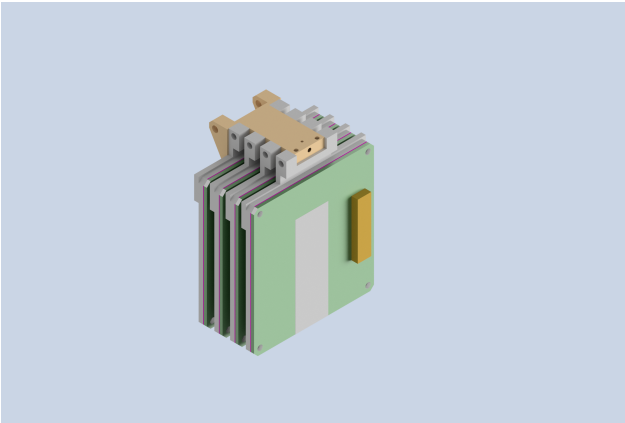

Figure 194: CAD illustration of the new four-plane electron detector assembly.

Each plane consists of a copper metal core PCB carrier board (fig. 195), bonded to a copper frame, which is attached to the four-plane assembly, which is itself suspended from the motion feedthrough (fig. 193). The HVMAPS dissipate about a 1 W of power each, for a total of 12 W for the entire electron detector. The chips can operate at up to $70°$C, but a temperature below 40 degrees is preferable for noise performance. To achieve this under beam line vacuum, the chips need to be actively cooled. This will be implemented by running LCW (low conductive water) chilled to about $4°degrees$C inside the vacuum, via a closed return loop. The loop will be run through a block of metal, used as a heat sink, mounted just above the four-plane assembly. The frames for each plane will be thermally connected to this block by short copper strips. The metal core PCB is necessary to allow efficient heat conduction from the HVMAPS chip to the heat sink. Operational and cooling tests of these sensors, under vacuum, were already performed with a simplified geometry. Cooling simulations of the new design are in progress. Figure 196 shows a simple cooling setup of the frames, with copper strips attached to the sides for the metal frames. This design will evolve in the coming weeks, but together with the already performed tests, the results suggest that cooling the sensors to the desired temperature below $40°$C should be possible. As is the case for the HVMAPS used as profile monitor in the main detector (Sect. 9.5), the Compton HVMAPS will be read out via a single flexprint ribbon cable, with the readout boards located just outside the vacuum can. The readout boards will utilize the same set of chips (CERN lpGBT and VTRX+), to serialize the signals and send them via fiber to an FPGA board. The same board will be used to facilitate slow control, trigger and gate interface, and operational bias voltages for the chips. Back-end processing of the signals for the HVMAPs is described in Sect. 10.5.4.

Expected Performance With both a functional electron detector and a photon detector, Compton scattered events can be measured with each system independently, and also using both systems together in coincidence. With the exception of the laser polarization, the potential systematic uncertainties in the measurement of the asymmetry or calibration of the experimental analyzing power are quite independent between the electron and photon analyses, so the polarimeter will provide two nearly independent measurements of the electron polarization with high precision. The goals for the systematic uncertainties from the Compton polarimeter system are shown in Tab. 34.

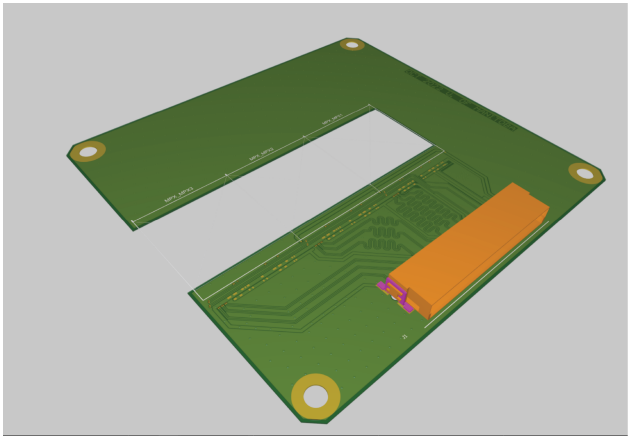

Figure 195: PCB CAD of the, as designed, carrier board for the three HVMAPS in a single detector plane. A single ribbon is sufficient to control and read out the plane.

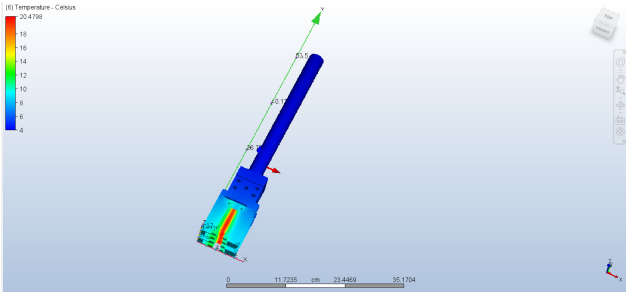

Figure 196: Preliminary CFD simulation of a single plane of the HVMAPS Compton electron detector.

Table 34: *Goals for systematic uncertainties for the Hall A Compton polarimeter at 11 GeV. Topics marked * are common systematic uncertainties between the photon and electron analyses, while the others are largely independent between the detector systems.*

Relative error (%)	electron	photon
Position asymmetries*	-	-
E_{Beam} and λ^*_{Laser}	0.03	0.03
Radiative Corrections*	0.05	0.05
Laser polarization*	0.20	0.20
Background / Deadtime / Pileup	0.20	0.20
Analyzing power Calibration / Detector Linearity	0.25	0.35
Total:	0.38	0.45

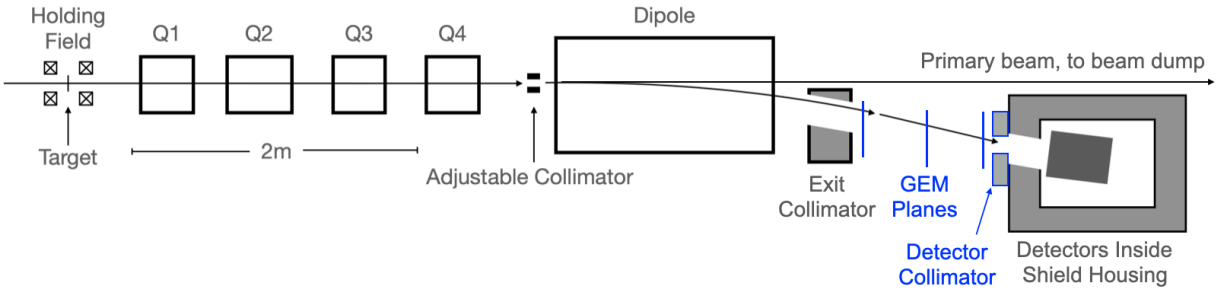

Figure 197: *Elevation view schematic of the Møller polarimeter in Hall A at Jefferson Lab. New components are show in blue.*

11.2 Møller Polarimetry

Møller polarimetry provides the second arm of our two-prong approach to the precision measurement of the beam polarization. The ultimate precision goal of this polarimeter is the same as for the Compton system, but the technique is entirely different and data will be taken in short, dedicated runs at low current. Therefore, the two measurements are complementary and will provide a convincing cross check.

This approach uses polarized Møller scattering to determine the beam polarization, that is

$$\vec{e}_{\rm Beam} + \vec{e}_{\rm Target} \rightarrow e^- + e^-$$

where both final state electrons are measured in coincidence. Reaction kinematics are kept close to 90° in the center of mass, where the analyzing power for this reaction is very large (-7/9) and perfectly calculable in quantum electrodynamics, including radiative corrections. In the Hall A Møller spectrometer, the electrons are momentum-analyzed in a QQQQD magnetic spectrometer, where the first two quadrupoles separate the pair in the horizontal plane, and the second two focus the pair into the dipole. Segmented calorimeters at the dipole exit detect the two electrons in coincidence. A schematic of the Møller polarimeter spectrometer is shown in Fig. 197.

The beam polarization $P_{\rm Beam}$ is determined by measuring the beam helicity asymmetry $A_{\rm Meas}$ in the Møller scattering reaction and using the relation

$$A_{\rm Meas} = P_{\rm Beam} P_{\rm Target} \langle A_{zz} \rangle$$

where $\langle A_{zz} \rangle$ is the analyzing power for the fundamental reaction, averaged over the spectrometer acceptance, which we determine with a thoroughly verified Monte Carlo simulation. The measured asymmetry $A_{\rm Meas}$ is determined in the same fashion as the parity-violating asymmetry. This includes running long enough to obtain sufficient statistical precision, and applying corrections for various systematic effects such as backgrounds and dead time.

11.2.1 Achieving the Systematic Uncertainty Goal

With a range of beam currents (0.5-1.5 μA) and foil thicknesses from 10-20 μm, the Møller polarimeter measurement will reach 0.2% statistical precision on the 1 hour timescale. The key to reaching the total uncertainty goal of 0.4% will be tight control of systematic uncertainty.

Experience gained during PREX-2 and CREX provided a wealth of information on how to optimize the spectrometer and the overall polarization measurement technique while also revealing the key outstanding

Table 35: *Hall A Møller polarimeter systematic uncertainties achieved in the CREX experiment and projected for MOLLER. The * denotes that it is an extrapolation error.*

Uncertainty	CREX	MOLLER
Saturation Polarization	0.28	0.24
Degree of Saturation	0.50	0.15
A_{zz}+Levchuk	0.16	0.15
Dead Time	0.15	0.10
Null Asymmetry	0.22	0.10
Accidentals	0.04	0.10
Electron Source Variation*	0.06	0.10
Current Dependence*	0.50	0.10
Aperture Transmission*	0.10	0.10
Leakage Currents*	0.18	0.00
Total	0.85	0.40

challenges. Tab. 35 provides a list of the key systematic errors for Møller polarimetry comparing what was accomplished during CREX with that expected during MOLLER. The systematic uncertainties are grouped into two types: those associated with the actual polarization measurement and extrapolation uncertainties (labeled with a * in Tab. 35) which arise when extrapolating this measurement "snapshot" to the time and conditions of the production data of the experiment.

Many of the systematic uncertainties will be reduced simply by a precise measurement campaign. For example, a series of precision measurements of the polarization as a function of target angle and magnetic field will allow us to greatly reduce the uncertainty from the degree of saturation of the target foil. Methods already have already been developed and used in the past to determine the current dependence of the polarization with low current, appropriate to the Møller target arriving in the Hall while increasing the current off the photocathode to several tens of microamperes [96]. DAQ dead time is currently determined with a LED flasher system and will be cross-checked using a dual channel detector emulator (CAEN DT5800) purchased by Temple University precisely for this purpose. This emulator will allow us to input pulses matched to the Møller energy spectrum and to set the event rate with pulses randomly spaced in time similar to real beam conditions and then to determine how many pulses are lost as a function of rate. The null asymmetry, a false asymmetry arising from beam parameters that are helicity-correlated, but do not arise from spin, is measured by inserting a copper foil with a similar thickness to the Fe foil. Measuring the null asymmetry each time the polarization is measured and to the same statistical accuracy will be sufficient to limit this systematic error to 0.1%. Accidentals are measured and the correction limited by the chosen luminosity and acceptance. Injector laser polarization changes between Møller measurements will be monitored and are expected to be negligible due to optimal setup of the source. Polarization dependence on the fractional opening of the main aperture or "chopper" in the electron source can be minimized by operating in a configuration as similar as possible to the main production, and by measurement of the dependence if required. Finally, background halo on the electron beam arising from the source laser from other experimental halls (leakage current), can be tested or eliminated by turning off other halls for 30 minutes during the key period of a Møller measurement.

A recent article [97] now published in *NIMA* provides an average of previously published world data to giving the target saturation polarization for an Fe foil along with its systematic error at 0.24%. This is expected to be the leading systematic error for Møller polarimetry.

Thus, with the exception of "A_{zz}+Levchuk" in the table, use of precision measurements taken during MOLLER and judicious use of available techniques are expected to acceptably reduce the size of most of the

systematic errors. We thus focus on this remaining systematic error where the MOLLER project additions will have their greatest impact.

Analyzing Power
The Møller longitudinal analyzing power A_{zz} is a function of the center of mass (COM) scattering angle and must be averaged over the detector acceptance. Determining A_{zz} to the required accuracy is an ongoing process that requires three modifications/improvements to the existing polarimeter, all of which are under the umbrella of the MOLLER project. These modifications are moving the Møller polarimeter target upstream 30 cm on the beam line, adding GEM tracking detectors to benchmark simulation, and adding an acceptance-limiting collimator in front of the detector.

MOLLER Beamline Modification The precise acceptance average comes from a mature GEANT4 simulation of the polarimeter and includes corrections from radiative effects, multiple scattering and the so-called Levchuk effect [98]. The Levchuk effect arises from the intrinsic momentum of the atomic target electrons. Only the outer electrons in the iron atom are polarized in the presence of an external field. The unpolarized inner electrons have higher initial-state momentum, significantly affecting the scattering angle of the outgoing scattered electron pair and typically creating a biased acceptance. This bias requires atomic wave-function models to estimate, so when Levchuk corrections are significant they introduce an atomic model dependence to the determination of A_{zz}. The recent introduction of higher quality atomic models to the determination of the Levchuk correction has led to better agreement with data and allowed a reduced uncertainty [89]. Furthermore, it is possible to limit the detector acceptance to a kinematic region where the acceptance function is not sensitive to the smearing from the initial atomic state momentum distribution. This technique was studied and successfully implemented for PREX-2and CREX to minimize the Levchuk correction and its associated uncertainty. The spectrometer optics were also chosen to be highly insensitive to the knowledge of the fields of the quadrupole magnets.

The high energy scattered electrons cannot be sufficiently focused with the existing spectrometer quadrupoles and power supplies. Simulations have verified that the existing hardware can achieve the required optics through a simple reconfiguration, moving the target upstream 30 cm to provide extra drift distance for the scattered electrons and so naturally placing the Møller-scattered electrons into the higher field region of the quadrupoles. Simulation studies have further shown that the polarimeter will be able to operate at lower beam momentum, as low as 2.2 GeV, after this reconfiguration, so the change does not limit the operability for a future physics program in Hall A. The Møller polarimeter is part of the primary beamline, upstream of the MOLLER production target. This modest reconfiguration has been incorporated into the MOLLER beamline design (see Sect. 3.4.6).

Detector Collimator A second modification is the addition of a tungsten collimator in front of the detector. As previously mentioned, our technique for controlling the Levchuk correction involves limiting the momentum acceptance which is done by physically limiting the 30 cm vertical acceptance on the detector downstream of the dipole. During PREX-2 and CREX this was accomplished by turning on only a fraction of the 4×2 array of PMTs reading out the detector. At 11 GeV, the Møller spectrum is very compressed even with the dipole nearing its upper current limit, making even a single row of PMTs (7.5 cm vertical acceptance) too large to sufficiently reduce the Levchuk correction and flatten the sensitivity to precise quadrupole field settings. A collimator has been designed to limit the vertical acceptance to 5 cm so that the existing detector can be used without modification. The collimator (see Fig. 198) will insert into the window opening of the detector shield hut and bolt into holes in the frame without modification required beyond replacing 3 of the 9 existing bolts with ones long enough to go through the collimator frame as well. The collimator acceptance window opening is slanted along the beam direction to match the particle trajectories at 11 GeV.

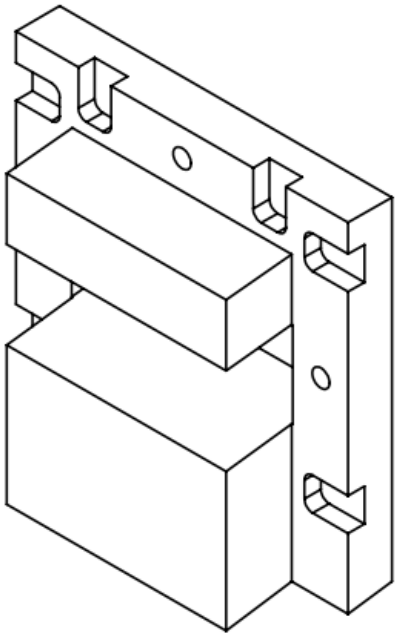

Figure 198: New tungsten collimator design will be installed in the window opening of the Møller polarimeter detector shielding hut.

The collimator is 2.5 inches thick which translates into > 15 radiation lengths for most tungsten alloys. The PMTs on the bottom half of the detector will be turned off during measurements so that the collimator length can be limited to cover only the top half of the detector, keeping material costs at a reasonable level and reducing the weight to the 25 kg level for easier installation and handling.

GEM Trackers The third modification is the addition of three gas electron multiplier (GEM) detector planes for precise tracking of the particle trajectories. The design of a single GEM plane is shown in Fig. 199 and their placement in the Møller spectrometer in Fig 200. The active region of the GEMs is 16.6 cm wide and 25.4 cm tall, much larger than the window of the collimator which is 12.9 cm wide by 5 cm tall. The larger active region was chosen to reduce sensitivity to precise alignment, to accommodate studies of backgrounds events such as those from Mott scattering outside the acceptance as well as to allow these planes to be used more generally at other energies and without the presence of the collimator. An XY readout configuration was chosen to allow independent readout of the left and right sides of the detectors. These GEMs are expected to have close to 90% efficiency.

The GEMs will be used to test key features of the simulation with special focus on the corrections from multiple scattering, radiation and the Levchuk effect. Without broadening from these corrections the Møller events would produce a well defined curved stripe on the detector plane. Signatures of the various corrections will be used to benchmark the validity of the simulation. Studies are ongoing to determine the optimal way to utilize these data to verify the simulation. The GEMs are expected to have resolution of 100 μm and with a horizontal separation of 95 cm are expected to provide an excellent angular resolution of 0.01 degrees. This resolution will be helpful in differentiating effects for example from multiple scattering,

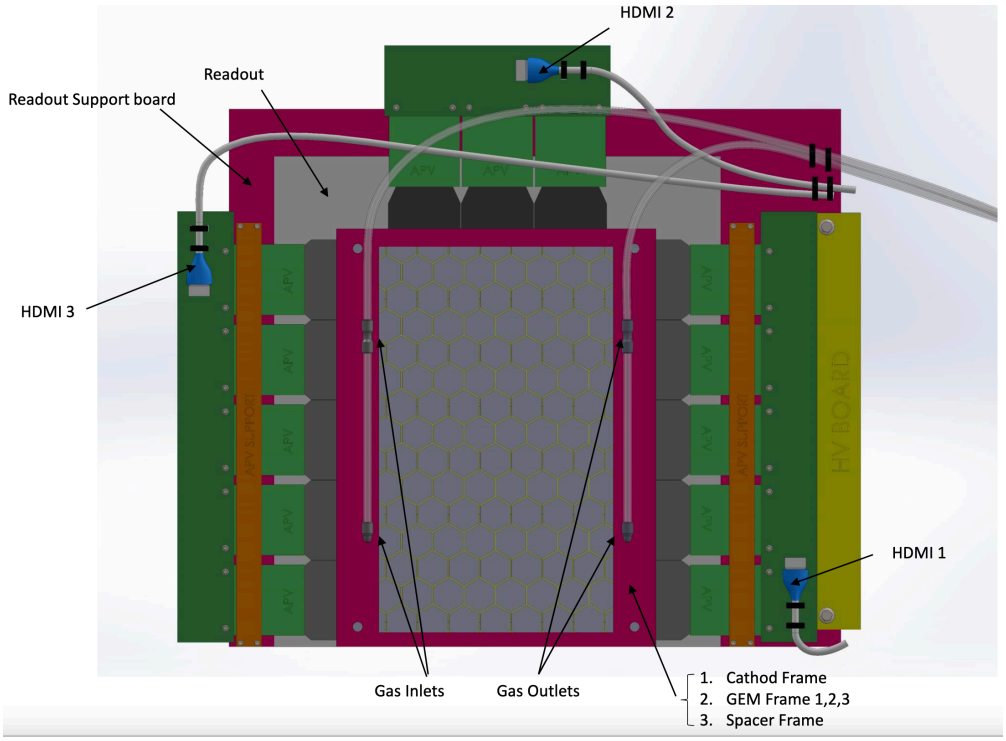

Figure 199: Design of a single GEM plane. Three planes of these will be used for tracking in the Møller polarimeter.

radiation in the target and the Levchuk effect and verifying the models used for them in the simulation. The three GEM planes will be approximately equally spaced, to optimize the ability to distinguish low energy background due to scattering in the upstream tracking plane or vacuum exit window. A fourth set of GEM planes will also be constructed to allow for swapable replacement. The GEM detectors are being developed alongside the tracking detectors for the MOLLER spectrometer (see Sect. 8). Hardware for readout of the data from the GEMs will be taken from the by-then complete SBS form factor program in Hall A.

Although the addition of the GEM tracking is expected to improve the reliability of the A_{zz} determination, we conservatively estimate only a modest improvement in systematic uncertainty relative to that achieved during CREX. Any further decrease in systematic error from use of GEMs could improve our overall systematic uncertainty beyond that shown in Tab. 35.

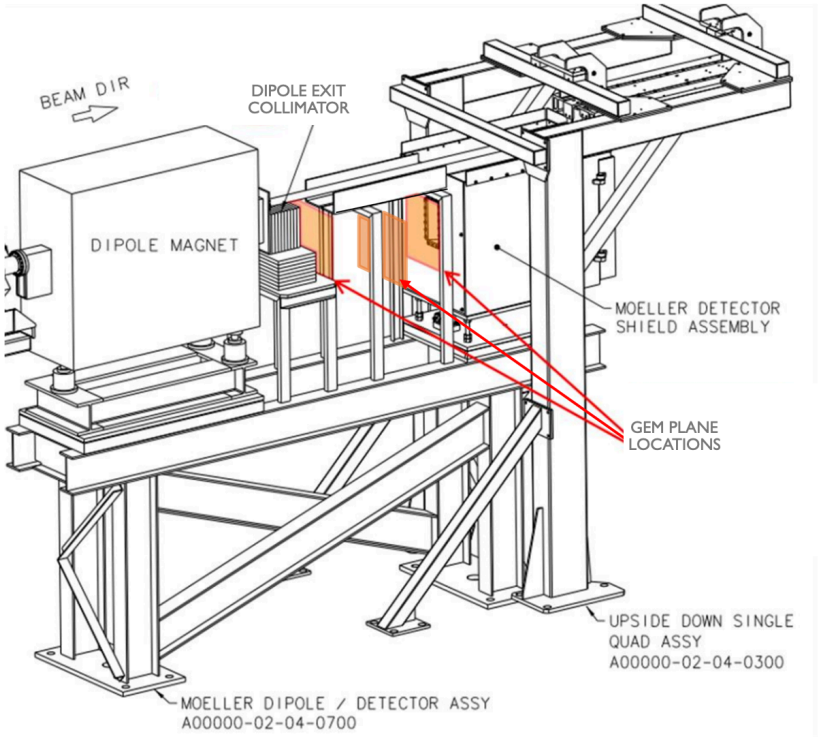

Figure 200: Placement of GEM planes in the drift region between the Møller dipole and detector.

12 Shielding and Radiation Protection

The goal of the shielding is to protect personnel and equipment throughout the lifetime of the MOLLER experiment. Personnel safety is focused on two regimes: a) outside of the hall while the experiment is taking data where the radiation is dominated by prompt sources and b) inside the hall during a maintenance access where only activated components contribute to doses. Equipment protection is focused on maintaining the operability of equipment that cannot be removed from the hall during data taking (such as data acquisition components, monitoring systems, or power supplies). The strategy employed to achieve both of these goals is to isolate locations that absorb the highest beam power (such as the target region or the upstream torus region) to reduce radiation levels in general throughout the hall and provide additional shielded enclosures for sensitive electronics that provide further protection.

12.1 Personnel radiation protection

As stated above the shielding for the MOLLER experiment has taken into account mitigation of both prompt radiation and radiation coming from activated components during times when the beam is not present inside the hall.

The activated component radiation has been modeled using FLUKA simulations in close collaboration with the Jefferson Lab Radiation Control (RadCon) group. The geometry of the major components has been integrated into the simulation and the results of the simulation are being used to establish access plans for maintenance that are in accordance with the ALARA principle. The shielding (as described below) of the areas that absorb most of the beam power plays an important role in restricting the area where harmful radiation is present and allowing access to important components in a reasonable amount of time after beam operations are stopped. The FLUKA model will be updated as the experimental design progresses and the results will be used in further planning.

Due to the high energy and power used in the MOLLER experiment, careful attention has been given to limiting the prompt radiation dose rate outside of the hall. The DOE and Jefferson Lab have mandated limits on the amount of radiation that can exit the hall during normal operations. The most stringent limit is the Jefferson Lab administrative limit of 10 mrem per calendar year as measured by monitors on the boundary of the accelerator site. These monitors are located approximately 150 to 200 meters from the center of the hall at ground level. They account for radiation from all halls, however in this document we are concerned only with radiation directly caused by the MOLLER experimental operations.

The boundary dose has been evaluated independently by two different methods: one making use of the GEANT4 framework while the other making use of FLUKA. Both methods showed consistent quantitative and qualitative results. A summary of the dose estimate per calendar year at the accelerator site boundary can be seen in Tab. 36 below. Both methods estimate that the site boundary caused by MOLLER operations will be well below the lab mandated limit.

	Boundary dose [mrem/year]
GEANT4	5.6 ± 3.0
FLUKA	6.3 ± 1.1

Table 36: Boundary dose estimates obtained from the two analysis methods.

The analysis done on the simulations in both frameworks showed that the most important sources of radiation are the target and collimator 1 (as they are the components that absorb the most beam power). While these components produce electromagnetic and hadronic radiation it is only the high energy neutrons (kinetic energy larger than $\approx$30 MeV) that have a chance to escape the hall and contribute to the boundary

dose. Furthermore, only neutrons that make their way to the roof of the hall can cross through the dirt overburden (as it is thinnest in that location) and shower in the atmosphere above the accelerator site and produce radiation detectable by the monitors. While the radiation inside and close to the hall is forward peaked (towards the hall dump) we observed that the level of radiation at the boundary monitors depends mostly on distance from the center of the hall. These findings are consistent with previous RadCon experience at the lab. The roof of the target and upstream torus enclosures are the main mitigators for the boundary dose.

12.1.1 GEANT4 results

The GEANT4 results were obtained through comparisons to previous experiments at Jefferson Lab that produced a measurable boundary dose (such as PREX, PVDIS, PREX-2, or CREX). The analysis method consisted of evaluating the high energy neutron rate at the roof of the hall for MOLLER and the comparison experiment. The ratio of these rates can then be used to scale up the measured boundary dose as observed in past experiments. This analysis method proved to be efficient as it was the basis for the estimations for the PREX-2 and CREX experiments. The observed boundary dose was within 20% of the estimated values.

Additionally, GEANT4 has been used to propagate high energy particles (electrons, positrons, photons, and neutrons) through the hall walls, the dirt overburden and finally in the atmosphere. This latter analysis proved that only neutrons have sufficient penetration power to actually contribute to the dose measured by the monitors. Additionally, the shower profile in the atmosphere above the hall was studied and showed that radiation reaching the boundary of the accelerator site does not show a clear directionality. The amount of radiation is directly proportional to the distance from the center of the hall. We set a conservative 50% uncertainty on this estimation that include both statistical uncertainties from the number of events run as well as potential systematic biases due to the modeling choices used.

12.1.2 FLUKA results

The FLUKA analysis used an advanced biasing scheme which allowed for statistically significant results to be obtained on detectors that were placed at the correct distance away from the experimental setup. This full evaluation of the boundary dose allowed for determinations of the doses seen by each monitor during the course of one full MOLLER year of data taking. Figure 201 shows a bird's-eye view of the experimental hall and the surrounding area (the background shows a map of the Jefferson Lab accelerator site around Hall A). The boundary monitor locations are shown in the 4 boxes labeled "RBM-1" through "RBM-4". The color (z-axis) of the overlayed plot shows the estimated boundary dose for this entire area. The results can be seen in Tab. 37 and are significantly below the limit imposed by the lab and in good agreement with the GEANT4 based analysis. The fluctuations between the different measurements is mostly due to their relative distance from the center of the hall (where the target and collimator 1 are located). The FLUKA results were obtained by Lorenzo Zana from the Jefferson Lab RadCon group.

	Boundary dose [mrem/year]
RBM-1	4.8 ± 1.2
RBM-2	4.9 ± 0.8
RBM-3	6.3 ± 1.1
RBM-4	4.3 ± 0.8

Table 37: Boundary dose estimates obtained from the FLUKA analysis.

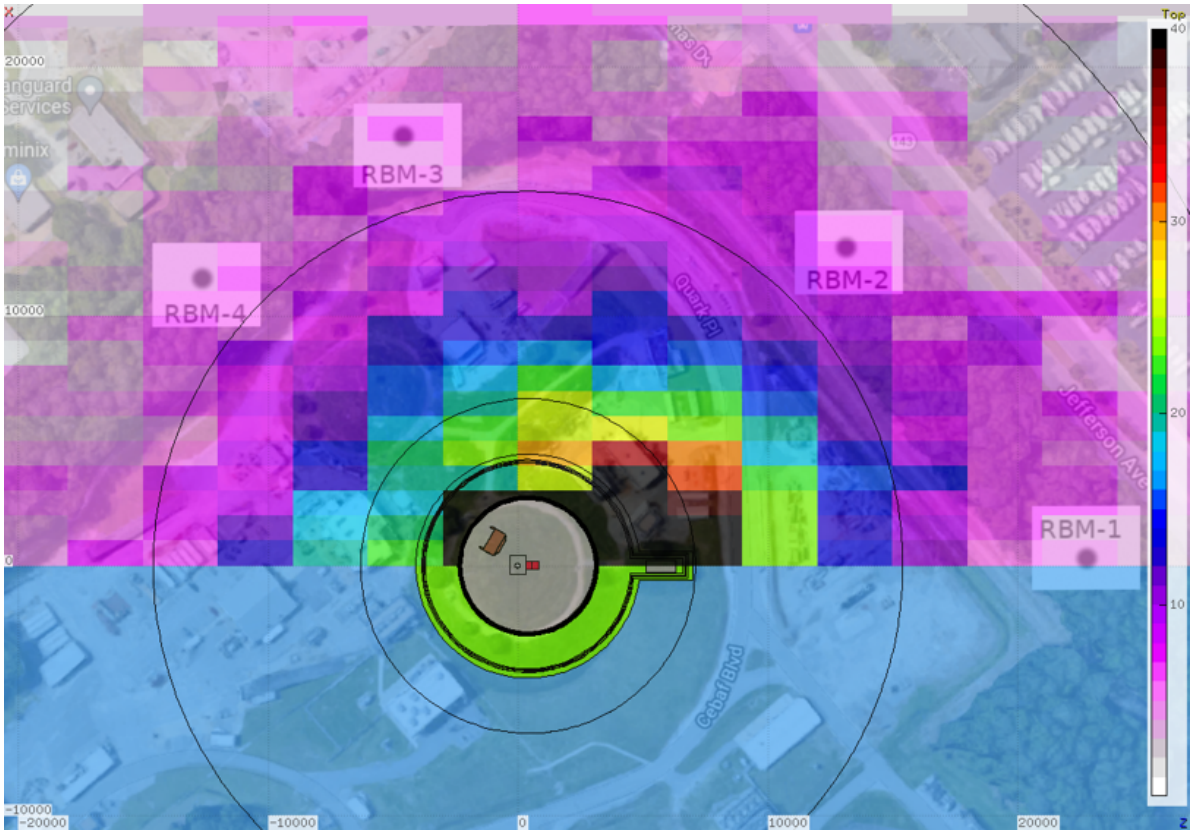

Figure 201: Radiation map for one full year of MOLLER experimental running obtained from FLUKA (color/z axis is in units of mrem).

12.2 Electronics radiation protection

To evaluate the level of potential damage that electronics could sustain during the course of the experiment we have used several standard metrics evaluated using our GEANT4 simulations. The damage can be separated into two main categories: temporary damage and permanent damage.

Temporary damage can result from interactions of high energy particles (usually hadrons) with components (such as memory chips) that result in a malfunction of the device (such as flipping of a bit). The device can be recovered through a reboot, but the experiment will incur a loss in data collection efficiency. This type of damage is evaluated by looking at the fluxes of hadrons in locations where sensitive electronics are planned to be located and comparing to the levels seen in previous experiments that ran successfully at Jefferson Lab.

The second type of radiation damage leads to significant downtime in addition to the cost of replacing parts that were permanently damaged. For this reason, the most detailed studies were performed to evaluate it at different locations throughout the hall (see details in the subsections below). We have evaluated two types of metrics: non-ionizing energy loss (NIEL) and total ionizing energy loss (TID). For the NIEL estimate, we have used look-up tables developed for the FLUKA software to convert incident particle fluxes seen in GEANT4 to NIEL depending on the species (we do this calculation for electrons, positrons, pions, protons, and neutrons) and energy. For the TID we use the in-built capability of GEANT4 to estimate energy deposition in a material and obtain the final dose by dividing the mass of the component. Both of these metrics are compared to manufacturer specifications or when those are not available we compare to results obtained from previous measurements at other laboratories around the world.

Below we describe the most important areas in our experimental setup with respect to radiation protection, however additional studies were done in collaboration with the engineering group to ensure specific components will be able to withstand the radiation field that are not all detailed here. We will maintain this capability and continue doing these studies until the project is finalized.

12.2.1 Upstream of target

In the upstream of the target region, a Compton polarimeter will be located before the entrance to the hall (at $z \approx -36$ m). The particle flux at the hall entrance location with the current target bunker design (discussed in more detail in the following section) was estimated using our GEANT4 simulation. The resulting values were found to be comparable to the other locations in the Hall where TID was estimated at 10 kRad. Based on previous experience, this level of radiation dose will not impede the continuous operation of the Compton polarimeter.

12.2.2 Target bunker

The target bunker provides crucial shielding due to the significant (≈ 3.2 kW) power deposition in the LH2 target. In order to contain the electromagnetic and neutron flux from this target, walls of 1.4 m thick concrete are used. On the downstream-side of the target bunker, within 50 cm radially to the beamline, high-density barite material is used to better absorb the high-energy electromagnetic radiation. The upstream side of the bunker will be left open in order to allow easy access to the target and beamline elements. In addition, a 2 m diameter hole in the roof provides access for the target cooling and motion mechanisms. In total, the bunker will contain 374 tons of concrete and 1 ton of barite. The analyses described in subsections 12.1 and 12.2.1 of radiation dose rates in the region upstream of the target and at the hall roof have demonstrated that this design provides sufficient shielding.

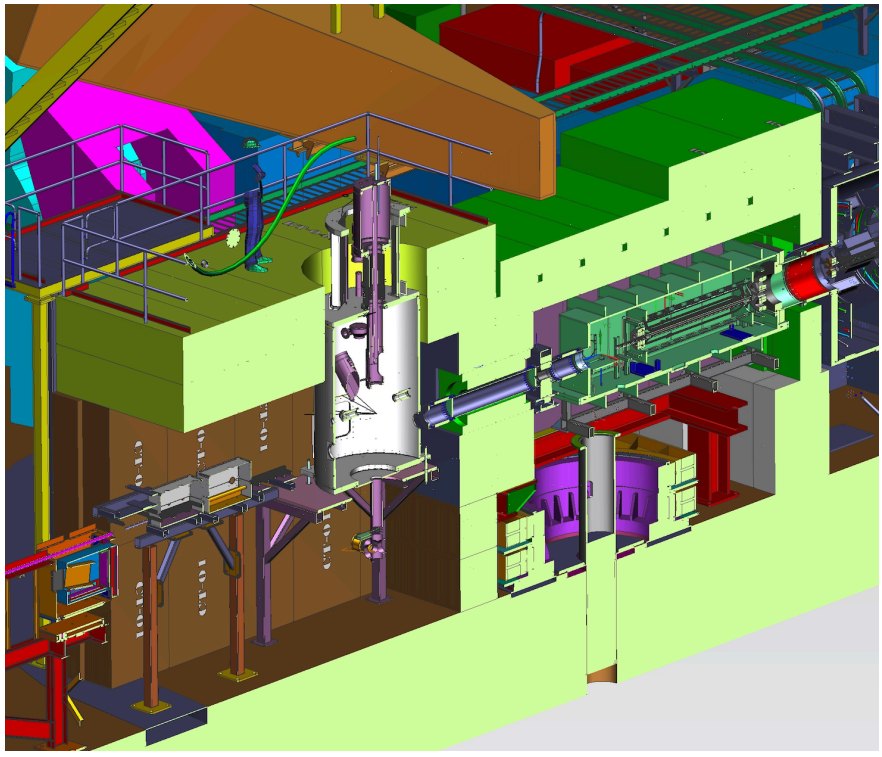

Figure 202: Illustration of the target bunker and upstream torus bunker shielding.

12.2.3 Upstream torus bunker

The upstream torus bunker surrounds the lead collar downstream of the target, the first magnet of the spectrometer, the blocker collimators, and the primary collimators 1, 2 and 4. Similar to the target bunker, the high power deposition in this region, especially that of collimators 1 and 2, requires significant shielding. The shielding of the upstream torus bunker will sit on the top of a raised platform above the Hall A pivot. The side walls of the bunker are made out of 0.8m thick concrete. The roof is made out of barite in order to minimize the amount of high-energy neutrons escaping the hall. The most upstream 0.5 m of the roof is limited to a thickness of 0.89m thick to accommodate the "nose" of the HRS, which overhangs the hall center. The remainder of the roof will be 1.4m thick. In the downstream region of the bunker, the shielding will consist of barite in the region closest to the beamline, and concrete outside that region. A rectangular opening in this wall will be covered by a "lead wall" mounted onto the upstream torus vacuum box, with a circular opening to allow for the beampipe connecting to the downstream torus vacuum box. In total, the shielding around collimators 1 and 2 will be approximately 60 tons of concrete, 120 tons of barite, and 1.5 tons of lead in the lead wall.The target bunker and the upstream torus bunker are shown in Fig. 202.

12.2.4 Electronics bunker

The readout electronics will be housed in a bunker constructed from individual iron blocks situated upstream of the target. It contains approximately 500 tons of iron. We have evaluated the re-scattering probability from this iron to the main detectors and found it within acceptable limits. The front face of the bunker will allow for approximately 1.3 m of iron shielding. This bunker has already been successfully used in previous experiments in Hall A. The top of the bunker will be shielded by approximately 5 tons of stainless steel. A GEANT4 analysis was performed in order to estimate the NIEL dose inside the bunker. The result of $2.2 \cdot 10^9$ 1-MeV neutron equivalent dose is well bellow the $1.0 \cdot 10^{13}$ limit where commercial-off-the-shelf components begin to break down and was deemed acceptable.

12.2.5 Power supply bunker

The magnet power supplies will be housed in a purpose-built bunker located beam left of the downstream torus. It will be constructed from approximately 300 tons of concrete. The height of the bunker ($\approx$3.4 m) will block all lines of sight from secondary radiation sources along the beamline to the power supplies. The bunker effectively provides $\approx$1.5 m of concrete shielding between potential sources and sensitive electronics. The simulation study was performed in order to evaluate the radiation damage to the components inside the bunker. The results show that the radiation inside the bunker will be approximately $15 \cdot 10^3$ rad which is within the limits set by the engineering group.

12.2.6 Detector wall

The detector wall will be located just downstream of the drift pipe at $z \approx 19$ m from the center of the target and will be made out of barite. This wall will support collar 2 which is composed of 2 beamline concentric lead rings totaling 0.3 tons. In conjunction with the upstream torus downstream bunker wall, this wall will help to minimize the false background asymmetry seen in the detectors from electrons rescattering off potentially magnetized elements along the beamline.In addition, this wall will reduce other backgrounds that will travel towards the tracking detectors, main detectors (and their PMTs), as well as other detectors located downstream of it.

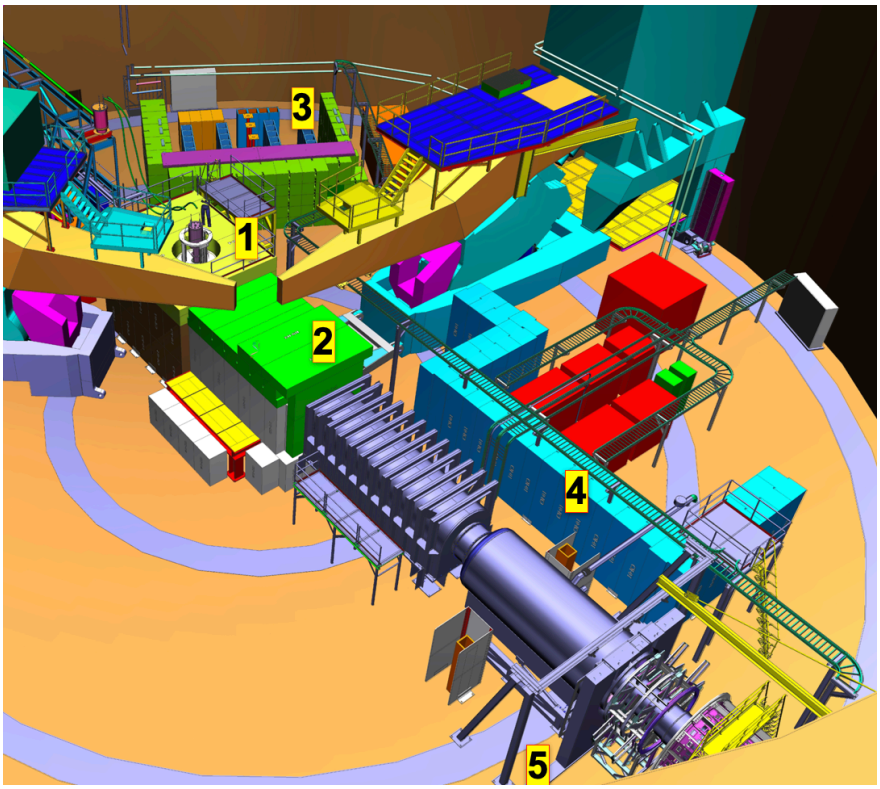

Figure 203: Illustration of the shielding configuration in the hall. 1) Target bunker, 2) Upstream torus bunker, 3) electronic bunker, 4) power supply bunker, 5) Detector wall.

13 Facility Infrastructure and MOLLER Assembly in Hall A Plan

13.1 Utilities

The MOLLER experimental apparatus requires significant cryogenic cooling for the target, low conductivity water (LCW) cooling for the spectrometer magnets and collimators, and significant electrical power for the spectrometer magnets. In this section, we describe the existing infrastructure, the upgrades that will be complete before MOLLER assembly, and the MOLLER-specific work that is part of the MOLLER infrastructure and assembly effort.

13.1.1 Cryogenics

The MOLLER target requires 3.7 kW of cryogenic cooling power. The cooling is provided by refrigerated helium provided by the End Station Refrigerator (ESR) system at the lab which provides LHe and cold GHe to Halls A, B and C. The current ESR-1 facility has a 2 kW capacity, which would limit MOLLER to operating the target at 1.7 kW of beam power. An upgrade project, ESR-2, is underway which will increase capacity to 4 kW, providing the required cooling capacity for operating MOLLER at design beam power. The electron beam will deposit 2.7 kW of beam power in the target at nominal MOLLER operating conditions of $65\ \mu A$ of beam at 11 GeV, with an expected 0.5 kW of heat load from friction losses in the LH_2 recirculation system.

The ESR-2 project schedule has the new facility operational before the start of MOLLER assembly. The MOLLER PM receives monthly status updates on the ESR-2 project. The Federal Project Director (FPD) for ESR-2 at the Thomas Jefferson Site Office is also the FPD for MOLLER.

13.1.2 Water Cooling

The Hall A low-conductivity water (LCW) system can deliver 500 gpm at 235 psi with a typical temperature of 81° F. The minimum allowable return pressure is 50 psi and the maximum allowable return temperature is 110° F. The primary heat load from MOLLER is the spectrometer magnets and power supplies. The magnet power supplies will be cooled directly from the facility LCW, while collimators and magnet coils will use closed-loop systems with water-to-water heat exchanges to transfer the heat to the facility LCW to ensure no activated material is introduced into the facility LCW system.

The nominal magnet heat load is 860 kW with a maximum load of 1100 kW during short duration calibration running at elevated current. The power supplies and leads are expected to need 300 kW based on minimum allowable power supply efficiency; actual efficiency should be higher, reducing this load. In addition, the Hall A facility LCW cools some incoming beamline elements. Though the heat load from these is quite small, the flow delivered to them currently is 120 gpm - a significant fraction of the available flow in the Hall. This leaves 380 gpm of flow for the 1200-1400 kW heat load from the MOLLER spectrometer systems. At 1400 kW the resulting temperature rise in the facility LCW would be 25° F, resulting in a return temperature 106° F, below the allowable 110° F limit.

The magnet coil closed loop system will require resin beds and filters to maintain low conductivity, a MW capacity heat exchanger to the facility LCW and manifolds to distribute flow to each of the magnet coils. The system design utilizes matched pressure drops to deliver the desired flow rates to each circuit. Flow blockages can be identified with current monitors on the coils by sensing the temperature-dependent conductivity of the copper conductors. Difference measurements between coils provide sensitivity to individual coil flow issues. System-level blockages can be sensed via temperature and flow sensors in the system. An optional chiller is being considered to stabilize the coolant temperature, i.e. to compensate for diurnal and seasonal fluctuations in the facility LCW supply temperature. The trade-off is additional system complexity and heat load on the facility LCW system.

13.1.3 Electrical Power

The main electrical load for MOLLER is the magnet power supplies. As mentioned in the previous section, the magnets run at about 1 MW. There will be five magnet power supplies, each powered by an independent 480 VAC circuit. The existing panel and switch gear in Hall A is not optimally located to provide power to the MOLLER magnet power supplies. MOLLER is responsible for assembly of a new 480 VAC panel that will feed the five power supply circuits. While the majority of the MOLLER electronics will reside in the existing electronics bunker in Hall A, some elements must be deployed close to the detectors. This will require the addition of a few new 120 VAC drops to power those electronics racks.

13.2 MOLLER Assembly

13.2.1 Assembly requirements

The MOLLER assembly includes a significant amount of large and heavy objects and requires detailed engineering, coordination and planning. The scope of the MOLLER assembly work is shown in Fig. 204 The general requirement is to position all of the MOLLER equipment in Hall A at the specified locations within the alignment tolerances. The detailed requirements are described in the MOLLER Assembly in Hall A System Requirements Document (SRD) [99]. The assembly plan will be refined as the design matures. In calendar 2023 during the scheduled accelerator down (SAD), early work will be done on hydrogen tanks and piping outside of the Hall A. Some of the upstream beamline elements modifications (see Sect. 3.4.6 and Sect. 11) are also being considered for earlier installation during a SAD. The target and spectrometer will be preassembled at Jefferson Lab. The detector subsystem preassembly and survey/alignment exercises will be performed in William and Mary high bay space prior to Hall A access. The MOLLER assembly in Hall A labor profile will peak in 2025 during the final MOLLER experimental apparatus assembly. Hall A technical staff, i.e. techs, designers, and engineers will be mainly involved in assembling the MOLLER apparatus. The alignment group, target group, magnet group engineering division and facilities will significantly contribute to the effort. The staff scientist from the detector imaging group will coordinate among all the groups due to the complexity of the process. The SBS assembly experience will be incorporated into planning.

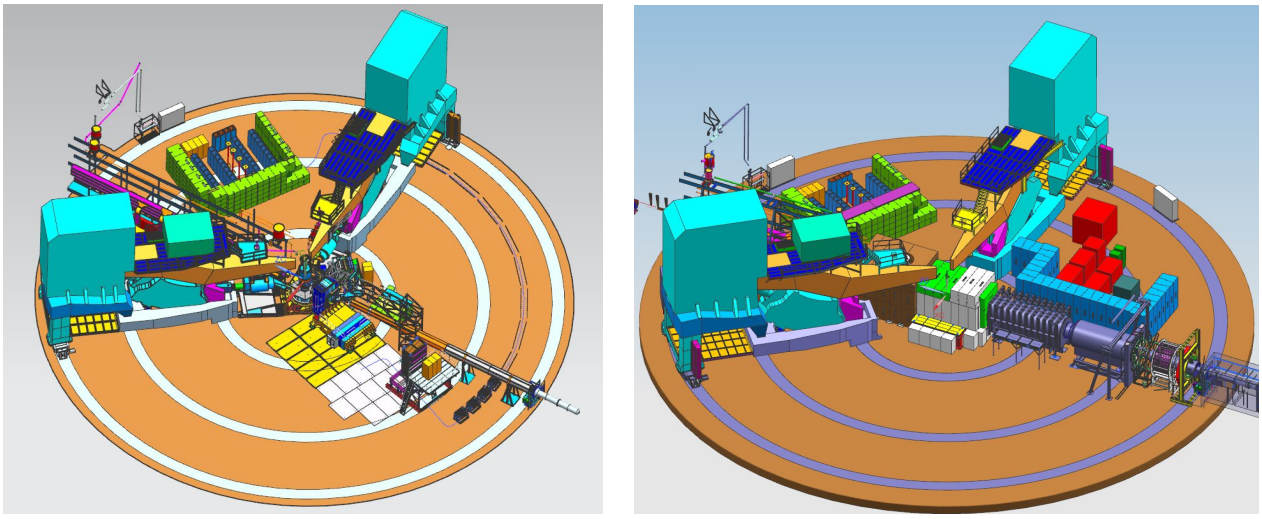

Figure 204: *The present and future configurations in the experimental Hall A. On the left is the current Hall A layout with SBS. The right figure shows the future MOLLER apparatus.*

The MOLLER experiment is very sensitive to magnetic materials that are within the particle envelope. The use of ferrous materials should be avoided in this region. Material selection is the responsibility of the sub-system delivering the component for assembly. The assembly team will have to pay attention to what materials are being used, especially for fasteners.

MOLLER assembly includes moving, lifting and other activities of the following elements. The first one is concrete shielding blocks. Typically, the concrete and high density (barite) concrete blocks will weigh 5 tons or less. Some specialty blocks such as roof spans could weigh as much as 20 tons. The second element is the liquid hydrogen target chamber. The target chamber and target lid with the target attached will be brought in separately; both units will weigh less than 5 tons. The third element is the spectrometer toroids, the downstream toroid chamber and the coil assembly. The spectrometer toroids represent significant component weights for assembly, specifically the downstream toroid. The total weight is estimated at 24 tons. This system will be attached in three parts. At the beginning the stand, weighing about 2.5 tons, will be grouted to the floor. Then the baseplate with the toroid coils will be mounted to the stand. The downstream toroid baseplate and coil assembly will be the highest single lift load at 10-12 tons. Finally, the lid object that weighs 10.5 tons will be mounted over the coil assembly. The fourth element is the detector support stands, the pion donut (lead/concrete) and the associated detector beam pipe. The detector support stands are not expected to be particularly heavy, comparatively, but the main detector support structure does include significant lead shielding. Current plans are to have this segmented into 14 sections and assembled on the structure after it is mounted on the beamline. In this case, the detector structures requiring hoisting will only weigh at most a few tons. The lead/concrete filled pion donut has a weight of about 5 tons. It will be a complicated lift with the detector beam pipe, but not overly heavy.

13.2.2 Cranes and Platforms

The Hall A overhead crane does not reach near to the wall where the detectors will be located. The plan is to mount a jib crane in the detector region for access and assembly of detectors. A jib crane is defined as a commercially available, wall mount, cantilever 2 ton crane. The target, spectrometer and detector systems require access platforms and the plan is to utilize OSHA standard commercially available roll-up stairs/platforms. For MOLLER, access platforms for the assembly have been defined.

13.2.3 Alignment and survey

The alignment goals provided in the Assembly SRD document are based on reasonably achievable values based on the survey precision and alignment mechanisms anticipated for these items rather than the accuracy required to achieve the required physics results. Achieving the target physics precision requires both alignment accuracy and knowledge of the deviations from ideal locations. In many cases, some misalignment is acceptable provided that the positions are stable and known accurately either by survey or by alignment using physics events. The Threshold Key Performance Parameters (KPP) tolerances represent the minimum required to perform the MOLLER experiment while the goal tolerances represent the desired alignment tolerance the experiment is planning to achieve. The KPP alignment tolerances are all referenced to the anticipated beam trajectory through Hall A. This implies there are a minimum of two survey steps, and often three or more, required to validate the KPPs. In all cases, one of these steps is survey of the incoming beamline relative to the Hall A survey monuments. Note that the beam raster will move the beam over a 5 mm x 5 mm area at the target to avoid boiling and achieve acceptable target density fluctuations; this initial alignment represents the alignment of the “neutral” beam trajectory with the raster off.

References

[1] J. Benesch et al. The MOLLER Experiment: An Ultra-Precise Measurement of the Weak Mixing Angle Using Moller Scattering, arXiv:1411.4088. 2014.

[2] P. L. Anthony et al. Precision measurement of the weak mixing angle in Moller scattering. *Phys. Rev. Lett.*, 95:081601, 2005.

[3] Andrzej Czarnecki and William J. Marciano. Electroweak radiative corrections to polarized Moller scattering asymmetries. *Phys. Rev. D*, 53:1066–1072, 1996.

[4] Andrzej Czarnecki and William J. Marciano. Polarized Moller scattering asymmetries. *Int. J. Mod. Phys. A*, 15:2365–2376, 2000.

[5] Jens Erler and Michael J. Ramsey-Musolf. The Weak mixing angle at low energies. *Phys. Rev. D*, 72:073003, 2005.

[6] A. G. Aleksejevs, S. G. Barkanova, Yu. M. Bystritskiy, E. A. Kuraev, and V. A. Zykunov. Two-loop electroweak vertex corrections for polarized Møller scattering. *Phys. Part. Nucl. Lett.*, 13(3):310–317, 2016.

[7] Yong Du, Ayres Freitas, Hiren H. Patel, and Michael J. Ramsey-Musolf. Parity-Violating Møller Scattering at Next-to-Next-to-Leading Order: Closed Fermion Loops. *Phys. Rev. Lett.*, 126(13):131801, 2021.

[8] The MOLLER Collaboration. Uncertainties in the Theoretical Calculation of the Parity-Violating Asymmetry in Møller Scattering. *Report submitted to U.S. Department of Energy*, 2016.

[9] P. A. Zyla et al. Review of Particle Physics. *PTEP*, 2020(8):083C01, 2020.

[10] S. C. Bennett and Carl E. Wieman. Measurement of the 6S —> 7S transition polarizability in atomic cesium and an improved test of the Standard Model. *Phys. Rev. Lett.*, 82:2484–2487, 1999. [Erratum: Phys.Rev.Lett. 82, 4153 (1999), Erratum: Phys.Rev.Lett. 83, 889 (1999)].

[11] V. A. Dzuba, J. C. Berengut, V. V. Flambaum, and B. Roberts. Revisiting parity non-conservation in cesium. *Phys. Rev. Lett.*, 109:203003, 2012.

[12] D. Androić et al. Precision measurement of the weak charge of the proton. *Nature*, 557(7704):207–211, 2018.

[13] G. P. Zeller et al. A Precise Determination of Electroweak Parameters in Neutrino Nucleon Scattering. *Phys. Rev. Lett.*, 88:091802, 2002. [Erratum: Phys.Rev.Lett. 90, 239902 (2003)].

[14] K. S. Kumar, Sonny Mantry, W. J. Marciano, and P. A. Souder. Low Energy Measurements of the Weak Mixing Angle. *Ann. Rev. Nucl. Part. Sci.*, 63:237–267, 2013.

[15] Vincenzo Cirigliano and Michael J. Ramsey-Musolf. Low Energy Probes of Physics Beyond the Standard Model. *Prog. Part. Nucl. Phys.*, 71:2–20, 2013.

[16] Jens Erler and Shufang Su. The Weak Neutral Current. *Prog. Part. Nucl. Phys.*, 71:119–149, 2013.

[17] M. J. Ramsey-Musolf and S. Su. Low Energy Precision Test of Supersymmetry. *Phys. Rept.*, 456:1–88, 2008.

[18] V. Cirigliano, A. Kurylov, M. J. Ramsey-Musolf, and P. Vogel. Lepton flavor violation without supersymmetry. *Phys. Rev. D*, 70:075007, 2004.

[19] P. S. Bhupal Dev, Michael J. Ramsey-Musolf, and Yongchao Zhang. Doubly-Charged Scalars in the Type-II Seesaw Mechanism: Fundamental Symmetry Tests and High-Energy Searches. *Phys. Rev. D*, 98(5):055013, 2018.

[20] Susan Gardner and Xinshuai Yan. Light scalars with lepton number to solve the $(g-2)_e$ anomaly. *Phys. Rev. D*, 102(7):075016, 2020.

[21] Hooman Davoudiasl, Hye-Sung Lee, and William J. Marciano. 'Dark' Z implications for Parity Violation, Rare Meson Decays, and Higgs Physics. *Phys. Rev. D*, 85:115019, 2012.

[22] Hooman Davoudiasl, Hye-Sung Lee, and William J. Marciano. Muon Anomaly and Dark Parity Violation. *Phys. Rev. Lett.*, 109:031802, 2012.

[23] E. Eichten, Kenneth D. Lane, and Michael E. Peskin. New Tests for Quark and Lepton Substructure. *Phys. Rev. Lett.*, 50:811–814, 1983.

[24] A. Kurylov, M. J. Ramsey-Musolf, and S. Su. Probing supersymmetry with parity violating electron scattering. *Phys. Rev. D*, 68:035008, 2003.

[25] Jens Erler, Paul Langacker, Shoaib Munir, and Eduardo Rojas. Z' Bosons from E(6): Collider and Electroweak Constraints. In *19th International Workshop on Deep-Inelastic Scattering and Related Subjects,*, arXiv:1108.0685, 2011.

[26] Adam Falkowski and Kin Mimouni. Model independent constraints on four-lepton operators. *JHEP*, 02:086, 2016.

[27] P. A. Souder et al. Measurement of parity violation in the elastic scattering of polarized electrons from C-12. *Phys. Rev. Lett.*, 65:694–697, 1990.

[28] D. T. Spayde et al. The Strange quark contribution to the proton's magnetic moment. *Phys. Lett. B*, 583:79–86, 2004.

[29] A. Acha et al. Precision Measurements of the Nucleon Strange Form Factors at Q**2 ˜ 0.1-GeV**2. *Phys. Rev. Lett.*, 98:032301, 2007.

[30] D. Adhikari et al. Accurate Determination of the Neutron Skin Thickness of ^{208}Pb through Parity-Violation in Electron Scattering. *Phys. Rev. Lett.*, 126(17):172502, 2021.

[31] D. Adhikari et al. Precision Determination of the Neutral Weak Form Factor of Ca48. *Phys. Rev. Lett.*, 129(4):042501, 2022.

[32] T. Allison et al. The Q_{weak} experimental apparatus. *Nucl. Instrum. Meth. A*, 781:105–133, 2015.

[33] Reza Kazimi, Arne Freyberger, Joseph Grames, John Hansknecht, Alicia Hofler, Tomasz Plawski, Matt Poelker, Michael Spata, and Yan Wang. Operational Results of Simultaneous Four-Beam Delivery at Jefferson Lab. In *10th International Particle Accelerator Conference*, page WEPMP053, 2019.

[34] P.A. Adderley, D. Bullard, Y.C. Chao, et al. An overview of how parity-violating electron-scattering experiments are performed at CEBAF. *Nucl. Instrum. Meth. A, (https://doi.org/10.1016/j.nima.2022.167710)*, 2022.

[35] T. B. Humensky *et al.* SLAC's polarized electron source laser system and minimization of electron beam helicity correlations for the E-158 parity violation experiment. *Nucl. Instrum. Meth. A*, **521**, 2004.

[36] K. D. Paschke. Controlling helicity-correlated beam asymmetries in a polarized electron source. *Eur. Phys. J. A*, **32**, 2007.

[37] Caryn Palatchi. Laser and Electron Beam Technology for Parity Violating Electron Scattering Measurements. *Doctoral Dissertation*, University of Virginia, 2019.

[38] R. Suleiman, P. Adderley, J. Grames, J. Hansknecht, M. Poelker, and M. Stutzman. High current polarized electron source. *AIP Conf. Proc.*, 1970(1):050007, 2018.

[39] Gabriel Palacios Serrano et al. High Voltage Design and Evaluation of Wien Filters for the CEBAF 200 keV Injector Upgrade. *JACoW*, IPAC2021:MOPAB324, 2021.

[40] Jay Benesch and Yves Roblin. Redesigning the Jefferson Lab Hall A beam line for high precision parity experiments. *JINST*, 16(12):T12007, 2021.

[41] Rupesh Silwal. Probing the Neutron Radius of Lead and the Strangeness Content of the Proton Using Parity-Violating Electron Scattering. *Doctoral Dissertation*, University of Virginia, 2012.

[42] Emmanouill Kargiantoulakis. A Precision Test of the Standard Model via Parity-Violating Electron Scattering in the Qweak Experiment. *Doctoral Dissertation*, University of Virginia, 2015.

[43] Kent Paschke and Caryn Palatchi. Plan to Control the Helicity-Correlated Beam Asymmetries for the MOLLER Experiment. Technical Report Moller-doc-402-v1, MOLLER Collaboration, 2019.

[44] W. Barry. A general analysis of thin wire pickups for high frequency beam position monitors. *Nucl. Instrum. Meth. A*, **301**, 1991.

[45] T. Powers, L. Doolittle, R. Ursic, and J. Wagner. Design, commissioning, and operational results of wide dynamic range BPM switched electrode electronics. *AIP Conference Proceedings*, **390**, 1997.

[46] Buddhini Waidyawansa. A 3% Measurement of the Beam Normal Single Spin Asymmetry in Forward Angle Elastic Electron-Proton Scattering using the Q_{weak} Setup. *Doctoral Dissertation*, Ohio University, 2013.

[47] John Musson. Functional Description of Algorithms Used in Digital Receivers. *JLab Technical Report JLAB-TN-14-028*, 2014.

[48] The MOLLER Collaboration. The MOLLER Project Conceptual Design Report. Technical report, MOLLER collaboration, 2021.

[49] Yuan Mei, Shujie Li, John Arrington, Joseph Camilleri, Aled Cuda, James Egelhoff, Yury Kolomensky, and Ernst Sichtermann. Development of a direct-sampling RF receiver for precision beam charge measurements in the MOLLER experiment. *JINST*, 17(04):P04006, 2022.

[50] Jay Benesch and Yves Roblin. The Hall A Beam Line at Jefferson Lab: Present and Future. *Moller-doc-711-v1*, April 2021.

[51] Jay Benesch. The Hall A Beam Line at Jefferson Lab: Present and Future. *Moller-doc-721-v1*, April 2021.

[52] David Kashy. PMAG0000-0100-S0021 MOLLER - Spectrometer Magnet Water Cooler Specification. Technical report, TJNAF, 9 2022.

[53] P. Ghoshal *et al.* Magnetic field mapping of the clas12 torus—a comparative study between the engineering model and measurements at jlab. *IEEE Transactions on Applied Superconductivity*, 29(4):1–10, 2019.

[54] M. Gericke. Stability and Excess Noise in the Integrating Detector Signal. Technical report, University of Manitoba, 2020. https://moller.jlab.org/cgi-bin/DocDB/private/ShowDocument?docid=561.

[55] S. Riordan *et al.* Study of light backgrounds from relativistic electrons in air light-guides. Technical report, 2018.

[56] Anomet. `https://anomet.com/`.

[57] S-O. Flyckt and C. Marmonier. Photomultiplier Tubes, Principles and Applications. `http://www2.pv.infn.it/~debari/doc/Flyckt_Marmonier.pdf`.

[58] ET Enterprises, Understanding Photomultipliers. `http://et-enterprises.com/images/brochures/Understanding_Pmts.pdf`.

[59] A. G. Wright. *The Photomultiplier Handbook*. Oxford University Press, 2017.

[60] Private Communication with ET representative.

[61] D. McNulty and J. Gahley. MOLLER Quartz Radiation Hardness Tests. Technical report, Idaho State University, 2022. https://moller.jlab.org/cgi-bin/DocDB/private/ShowDocument?docid=886.

[62] The MOLLER Collaboration. Report on Aluminum and Inelastic Backgrounds. `https://moller.jlab.org/DocDB/0006/000627/001/MOLLER_backgrounds.pdf`.

[63] N. L. Hall, P. G. Blunden, W. Melnitchouk, A. W. Thomas, and R. D. Young. Hadronic γZ box corrections in Møller scattering. *Phys. Lett. B*, 731:287–292, 2014. [Erratum: Phys.Lett.B 733, 380 (2014)].

[64] S. Agostinelli et al. GEANT4–a simulation toolkit. *Nucl. Instrum. Meth. A*, 506:250–303, 2003.

[65] Peter E. Bosted and M. E. Christy. New fits to inclusive electron scattering from proton, neutron, and deuteron at low Q**2. In *16th International Workshop on Deep Inelastic Scattering and Related Subjects*, page 28, 4 2008.

[66] Fabio Sauli. The gas electron multiplier (GEM): Operating principles and applications. *Nucl. Instrum. Meth. A*, 805:2–24, 2016.

[67] C. Altunbas et al. Construction, test and commissioning of the triple-GEM tracking detector for COMPASS. *Nucl. Instrum. Meth. A*, 490:177–203, 2002.

[68] Kees de Jager. The Super Bigbite Project: A Study of Nucleon Form Factors. *Int. J. Mod. Phys. E*, 19:844–855, 2010.

[69] W. Xiong et al. A small proton charge radius from an electron–proton scattering experiment. *Nature*, 575(7781):147–150, 2019.

[70] M. J. French et al. Design and results from the APV25, a deep sub-micron CMOS front-end chip for the CMS tracker. *Nucl. Instrum. Meth. A*, 466:359–365, 2001.

[71] V. Bellini et al. GEM tracker for high luminosity experiments at the JLab Hall A. *JINST*, 7:C05013, 2012.

[72] E. Noah, N. Bacchetta, D. Bisello, A. Candelori, I. Dindoyal, P. G. Fuochi, M. J. French, G. Hall, M. Raymond, and M. Vassanelli. Total dose irradiation of a 0.25-mu-m process. In *6th Workshop on Electronics for LHC Experiments*, pages 555–559, 9 2000.

[73] David E. Wiser. *Inclusive Photoproduction of Protons, Kaons, and Pions at SLAC Energies*. Other thesis, 5 1977.

[74] D. Androić et al. Parity-violating inelastic electron-proton scattering at low Q^2 above the resonance region. *Phys. Rev. C*, 101(5):055503, 2020.

[75] K. A. Aniol et al. Parity violating electroweak asymmetry in polarized-e p scattering. *Phys. Rev. C*, 69:065501, 2004.

[76] Z. Ahmed et al. New Precision Limit on the Strange Vector Form Factors of the Proton. *Phys. Rev. Lett.*, 108:102001, 2012.

[77] R. S Hicks et al. Flux profile scanners for scattered high-energy electrons. *Nucl. Instrum. Meth. A*, 553:470–482, 2005.

[78] Heiko Augustin, Ivan Perić, Andre Schöning, and Alena Weber. The mupix sensor for the mu3e experiment. *Nuclear Instruments and Methods in Physics Research Section A: Accelerators, Spectrometers, Detectors and Associated Equipment*, 979:164441, 2020.

[79] D. Becker, R. Bucoveanu, and C. et al. Grzesik. The P2 experiment. *Eur. Phys. J. A*, 54:208, 2018.

[80] EPICS: Experimental Physics and Industrial Control System. `https://epics-controls.org/`.

[81] Tom Powers. Effects of intensity and position modulation on switched electrode electronics beam position monitor systems at Jefferson Lab. *AIP Conference Proceedings*, 546:541, 2000.

[82] Linear Technology: LTC2387-18, 18-Bit, 15Msps SAR ADC. `http://www.analog.com/media/en/technical-documentation/data-sheets/238718fa.pdf`.

[83] XILINX: Zynq UltraScale+ SoCs. `https://www.xilinx.com/support/documentation/data_sheets/ds890-ultrascale-overview.pdf`.

[84] Enclustra: Mercury+ XU8 SoM. `https://www.enclustra.com/en/products/system-on-chip-modules/mercury-xu8/`.

[85] Benjamin Raydo. *VTP Manual*. Jefferson Lab Nuclear Physics Division Fast Electronics Group, Newport News, VA, 2016. `https://coda.jlab.org/drupal/system/files/pdfs/HardwareManual/VTP/VTP-HallB-Manual.pdf`.

[86] B. Raydo, S. Boyarinov, A. Celentano, C. Cuevas, R. de Vita, V. Kubarovsky, B. Moffit, S. Niccolai, R. Paremuzyan, and C. Smith. The CLAS12 Trigger System. *Nucl. Instrum. Meth. A*, 960:163529, 2020.

[87] JAPAN: Just Another Parity ANalyzer. `https://github.com/JeffersonLab/japan`.

[88] Hall A C++ Analyzer. `https://github.com/JeffersonLab/analyzer`.

[89] D. E. King et al. Precision Møller polarimetry for PREX-2 and CREX. *Nucl. Instrum. Meth. A*, 1045:167506, 2023.

[90] J. M. Grames et al. High precision 5 MeV Mott polarimeter. *Phys. Rev. C*, 102(1):015501, 2020.

[91] N. Falletto et al. Compton scattering off polarized electrons with a high finesse Fabry-Perot cavity at JLab. *Nucl. Instrum. Meth. A*, 459:412–425, 2001.

[92] S. Abrahamyan et al. Measurement of the Neutron Radius of 208Pb Through Parity-Violation in Electron Scattering. *Phys. Rev. Lett.*, 108:112502, 2012.

[93] M. Friend et al. Upgraded photon calorimeter with integrating readout for Hall A Compton Polarimeter at Jefferson Lab. *Nucl. Instrum. Meth. A*, 676:96–105, 2012.

[94] A. Narayan et al. Precision Electron-Beam Polarimetry at 1 GeV Using Diamond Microstrip Detectors. *Phys. Rev. X*, 6(1):011013, 2016.

[95] The RD42 collaboration. Development of Diamond Tracking Detectors for High Luminosity Experiments at the LHC, HL-LHC and Beyond. *CERN-LHCC-2018-015*, 2021.

[96] M. Poelker, J. Grames, J. Hansknecht, R. Kazimi, and J. Musson. Generation of electron bunches at low repetition rates using a beat-frequency technique. *Phys. Rev. ST Accel. Beams*, 10:053502, 2007.

[97] D. C. Jones, J. Napolitano, P. A. Souder, D. E. King, W. Henry, D. Gaskell, and K. Paschke. Accurate determination of the electron spin polarization in magnetized iron and nickel foils for Møller polarimetry. *Nucl. Instrum. Meth. A*, 1043:167444, 2022.

[98] L. G. Levchuk. The Intraatomic motion of bound electrons as a possible source of a systematic error in electron beam polarization measurements by means of a Moller polarimeter. *Nucl. Instrum. Meth. A*, 345:496–499, 1994.

[99] MOLLER Assembly in Hall A CAM. System Requirements Document for MOLLER Assembly in Hall A (WBS 1.08) of the MOLLER EXPERIMENT. Technical report, Jefferson Lab, 2022.